Continuum modelling of the mechanical response of paper-based materials

Borgqvist, Eric

2016

Citation for published version (APA):
Borgqvist, E. (2016). *Continuum modelling of the mechanical response of paper-based materials*. [Doctoral Thesis (compilation), Solid Mechanics].

Total number of authors:
1

Department of Construction Sciences
Solid Mechanics

ISRN LUTFD2/TFHF-16/1053-SE(1-188)
ISBN: 978-91-7623-665-9
ISBN: 978-91-7623-666-6

Continuum modeling of the mechanical response of paper-based materials

Doctoral Dissertation by

Eric Borgqvist

Printed by Media-Tryck AB, Lund, Sweden
For information, adress:
Division of Solid Mechanics, Lund University, Box 118, SE-221 00 Lund, Sweden
Homepage: http://www.solid.lth.se

Till Fang Shuai

Preface

The present work is the product of my PhD studies conducted between fall 2011 and spring 2016 at the Division of Solid Mechanics at Lund University, which has been sponsored by Tetra Pak, Stora Enso and Klabin.

First and foremost I would like to express my greatest gratitude to my main supervisor Prof. Mathias Wallin for his encouragement and support during this work. Mathias has provided me inspiration with his deep knowledge and his passion on scientific research. I am very grateful that he introduced me to this exciting research field. At a personal level, Mathias is also a friend and has provided me with help over the years (for example on my complex wooden deck). Special thanks to my co-supervisors Prof. Matti Ristinmaa and Adj. Prof. Johan Tryding for all interesting discussions and ideas during the project. Their supports have guided me in the the right direction on my research. Their commitment to this project have been invaluable. I have received much help regarding the experimental work, especially Zivorad Zivkovic, Jonas Engqvist and Erika Tudisco from LTH and Mikael Nygårds at Innventia AB in Stockholm have been very helpful. I had the pleasure as well to cooperate with Tommy Lindström, Ola Håkansson, Daniel Vojskovic and Riyam Tayeh during their master thesis projects, which have helped broaden the knowledge in the field of Paper-Mechanics. It has been a great pleasure work alongside my dear colleagues and friends that have provided such a nice atmosphere at work during these five years. I am also very grateful to my parents and siblings for the support outside my studies. Finally, I would like to give my deepest thanks to my beloved wife, Fang Shuai, for all her love.

Bunkeflostrand, February 2016

Eric Borgqvist

Abstract

Continuum based elasto-plastic-damage models for paperboard have been established in this work. The thesis begins with an introductory section that describes the mechanical properties of paperboard and some of the converting processes during forming of a package. A short review of modeling concepts that have been applied to paperboard is presented and then some key aspects and assumptions developed in this work are summarized. The main part of the thesis consists of the five papers, A, B, C, D and E. In addition to these works, a possible concept to reduce a pathological mesh-dependency is reviewed.

The thermodynamical framework is established in Paper A and a model for the in-plane response is developed. The anisotropy is handled by introducing a set of director vectors that change direction along with the continuum. A distortion hardening yield surface coupled to several scalar internal variables is introduced. The effects of pre-straining a sample in one direction and then subsequently load the sample in the perpendicular direction is studied. The model is compared to measurements obtained with Digital Image Correlation.

In Paper B, the model is further developed to model out-of-plane deformations. A normal vector is introduced to model the out-of-plane direction. Key ingredients in the model includes the specific format for the elastic part of the free energy and an expression for the plastic spin. The spin is used to control the direction of the plastic flow. Simulations are performed on the line crease setup and compared to experimental measurements. Furthermore, the industrial rotation crease setup is studied in detail using the developed model.

The Short-span Compression Test (SCT) and the line folding operation are investigated in Paper C and the deformation patterns extracted from x-ray images are studied. The model parameters are calibrated to uniaxial tests and the SCT, and then the folding of uncreased paperboard is simulated. The simulated global force-displacement/rotation curves matches the measurements and the simulated deformation patterns are similar to that observed experimentally.

A numerical scheme is presented in Paper D, where the governing equations of the elasto-plastic boundary value problem are interpreted as a Differential-Algebraic Equation (DAE) system. In particular, two material models, which includes damage variables, are investigated using the Diagonally Implicit Runge-Kutta (DIRK) scheme. The error obtained using the DIRK-method is compared to the standard implicit Euler method.

In Paper E, the continuum model that has been developed in paper A-C is further enhanced to include the effect of damage. Two damage variables are introduced in the elastic part of the free energy which is associated with out-of-plane deformations. The softening in the out-of-plane normal and shear deformations can then be recovered. The folding of creased paperboard is simulated and compared to measurements.

Sammanfattning

För att tillverka en pappersbaserad förpackning är det viktigt att materialet är tillräckligt hållfast. Förpackningsmaterial består ofta av kartong, aluminium och polymerfilmer där kartong utgör den största delen av förpackningen och bidrar mest till styvheten. Det säljs årligen mer än hundra miljarder förpackningar i världen och om kostnaden samt materialåtgång för att tillverka en kartong kan reduceras, så kan stora besparingar göras både ekonomiskt och miljömässigt. När förpackningsmaterialet spricker under konverteringen till en förpackning är anledningen till detta inte alltid helt klart. Mycket material och tid kan gå till spillo under felsökningen och det är inte alltid säkert att man finner orsaken till bristerna. Ett verktyg för att analysera hur förpackningsmaterialet belastas kan därmed vara till stor hjälp för att få en ökad förståelse av konverteringsprocessen. Ett sådant verktyg för kartongmaterialet har utvecklats i den här avhandlingen.

En materialmodell som kan beskriva relationen mellan krafter och deformationer som kartongen utsätts för har utvecklats. Kartongen består primärt av cellulosafiber som är ett par millimeter långa med en bredd och tjocklek på cirka 10-50 mikrometer. Kartongen som har betraktats i detta arbete har en tjocklek på 400 mikrometer. På grund av tillverkningsprocessen så är de flesta av fibrerna riktade åt samma håll, och fibrerna ligger väsentligen ovanpå varandra. Den riktning som fibrerna ligger staplade ovanpå varandra definieras som ut-ur-planet riktningen. Kartongens hållfasthetsegenskaper är som starkast i den riktning som fibrerna ligger i, dvs i-planet och mycket svagare ut-ur-planet. Det kan skilja en faktor hundra i styvhet mellan i-planet och ut-ur-planet. Detta är en av anledningarna som gör modellering av kartongen utmanande.

Fokus i detta arbete har varit inriktat på att simulera bignings och vikningsprocessen med hjälp av den utvecklade modellen. De mycket stora lokala deformationer som sker under dessa processer har studeras med hjälp av modellen. Viker man en obigad kartong uppkommer rynkor vilket gör det mycket svårt att vika kartongen rakt. Dessa rynkor formas på ett instabilt sätt och röntgenbilder visar att fibrerna har omorienterats inuti rynkorna. Det är därför viktigt att man först bigar kartongen så att man kan få väl definierade viklinjer. I bigprocessen pressas ett hanverktyg på kartongen så att kartongen förs in i ett honverktyg. Kartongen skjuvas och skadas genom tjockleken och en viklinje uppkommer, vilket gör att kartongen låter sig formas till en förpackning.

Denna avhandling består av fem artiklar, A-E. I artikel A etableras det termodynamiska ramverk som är basen för modellen och en i-planet modell etableras. I artikel B utökas kontinuum-modellen så att ut-ur-planet egenskaperna kan modelleras. Vikning av en obigad kartong samt i-planet kompression studeras i artikel C. För att simulera vikning av bigad kartong behövs skade-variabler införas och två olika skademodeller samt två integrationsmetoder studeras i artikel D. I artikel E införs skadevariabler i kartongmodellen och vikning av bigad kartong studeras och simuleras.

List of appended papers

This doctoral thesis is based on the following manuscripts:

Paper A
Eric Borgqvist, Tommy Lindström, Johan Tryding,
Mathias Wallin and Matti Ristinmaa (2014)
Distortional hardening plasticity model for paperboard.
International Journal of Solids and Structures, 51 (2014) 2411-2423

Paper B
Eric Borgqvist, Mathias Wallin, Matti Ristinmaa and Johan Tryding (2015)
An anisotropic in-plane and out-of-plane elasto-plastic continuum model for paperboard.
Composite Structures, 126 (2015) 184-195

Paper C
Eric Borgqvist, Mathias Wallin, Johan Tryding, Matti Ristinmaa and Erika Tudisco (2016)
Localized deformation in compression and folding of paperboard.
Under review in Packaging Technology and Science

Paper D
Eric Borgqvist and Mathias Wallin (2012)
Numerical integration of elasto-plasticity coupled to damage using a DIRK integration scheme.
International Journal of Damage Mechanics, 22 (2012) 68-94

Paper E
Eric Borgqvist, Mathias Wallin, Matti Ristinmaa and Johan Tryding,
A continuum elasto-plastic damage model for anisotropic materials with a high degree of anisotropy.
To be submitted for publication

Own Contribution The author of this thesis has had the main responsibility for the preparation and writing of all papers. The development of the model and analysis of results have in all papers been conducted in collaborations with the co-authors. The numerical implementation has been done by the author. The experimental measurements has been carried out the main author, except for the long-edge test results in Paper A, the tomograph images and the images of the paperboard in the SCT in Paper C and the shear tests in Paper E.

Contents

Paper A

Paper B

Paper C

Paper D

Paper E

1 Introduction

Paperboard is frequently used for food and beverage packaging containers. A typical paper-based package consists of metallic and polymer films and paperboard, where paperboard occupies the largest volume of the package material and provides most of the package stiffness. The number of packages produced every year in the world is several hundred billions and to avoid waste, it is important to have knowledge about the converting operations. Appropriate mechanical properties of paperboard are thereby required to obtain intact packages. It is evident that experimental testings are necessary, but it can sometimes be difficult to determine which properties of the board that are actually measured and what information to extract from the tests. Mathematical modeling can be of great aid to analyze and gain an increased understanding of the converting of packaging material. In this work, a mathematical model which can describe the mechanical behavior of paperboard during deformation has been developed.

From a mechanical modeling perspective, paperboard is a complex material and a challenge to model. Dependent upon application, many effects have to be considered, such as the high degree of anisotropy, non-linear elasticity, large plastic deformations, heterogeneity, damage, creep, etc. During the converting process of paperboard to a package, many of the above listed effects need to be considered. By the use of mathematical modeling, important information regarding the converting process can be obtained. This information might be difficult to extract from experimental measurements only. From simulations, it is possible to obtain information about the local deformation of the paperboard in the converting operations. This information can e.g. be used to design and optimize the converting tools and also provide understanding of the overall converting process.

2 Paperboard material

At the micro-level, paperboard is a fibrous material, mainly made from cellulose fibers. Starch and other chemical additives are also common constituents of paperboard. Paperboard used in packages has a thickness typically ranging from 0.2 mm to 0.5 mm and a density between 300-900 kg/m^3, which is thicker and more dense compared to normal printing paper, cf. Niskanen (2012). The dimensions of the cellulose fibers are typically 1-3 mm long and about 10-50 μm thick and wide. The structure of the paperboard is shown in Fig. 1.

The fibrous structure of paperboard is apparent from Fig. 1 and it is evident that the properties of this fiber network, such as alignment of fibers and the strength of fiber-fiber bonds, will have a major impact on the mechanical behavior of the material. As depicted in Fig. 1, the fibers are primarily arranged in planes that are stacked on top of each other. This stacking of fibers is the cause for the high difference between the in-plane and out-of-plane (ZD) directional properties. In machine produced paperboard materials, a mixture of fibers are sprayed on a traversing web from a head nozzle. The velocity difference between the web and the head nozzle results in that the majority of fibers align

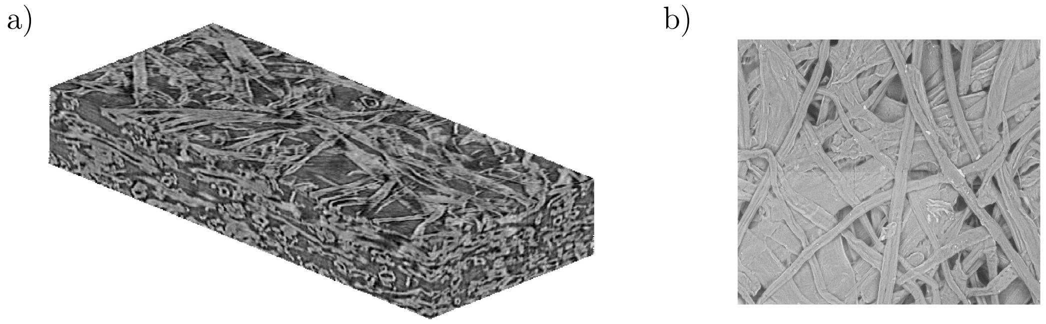

Figure 1: a) 3D-image of paperboard taken with x-ray tomograph at 4D-imaging lab, LTH. b) In-plane image obtained from Scanning Electron Microscopic technique.

in the Machine Direction (MD). As a consequence of the alignment, the stiffness in the MD direction is typically 2-3 times higher compared with the stiffness in Cross Direction (CD) and about 100 times higher compared with ZD, cf. Stenberg (2002). Due to the three distinct directions, the paperboard is typically regarded as being an orthotropic material. The three directions are marked in Fig. 2.

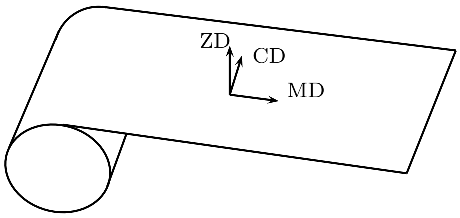

Figure 2: Illustration of the different material directions of paperboard resulting from the manufacturing process. The preferred direction are aligned with the Machine(1)-, Cross(2)- and ZD(3)-directions.

A paperboard can be either a single-ply or a multi-ply board. A multi-ply paperboard is designed as a layered fiberous structure, where each layer have different properties, such as fiber-orientation and number of fiber bonds. Normally, the middle layers are bulkier and weaker, while the outer layers contains more chemical agents and are in general stronger. The paperboard considered in this work is a single-ply board and in the modeling it has been assumed that the material properties are homogeneous through the thickness.

3 Characterization of mechanical properties

To characterize the mechanical properties of paperboard, mechanical testing needs to be performed. Since paperboard is sensitive to moisture, all tests have been performed in a climate controlled environment with 50 % relative humidity and 23° C. It is important to consider the full displacement field since the macroscopic response like force-displacement curves only provide limited information. Full field experimental techniques have therefore been utilized in this work and have been of importance for the development of the model. The full field tests have been used for verification that the deformation field predicted by the model is in agreement with the observations. Some of the full-field techniques that have been utilized are shown in Fig. 3.

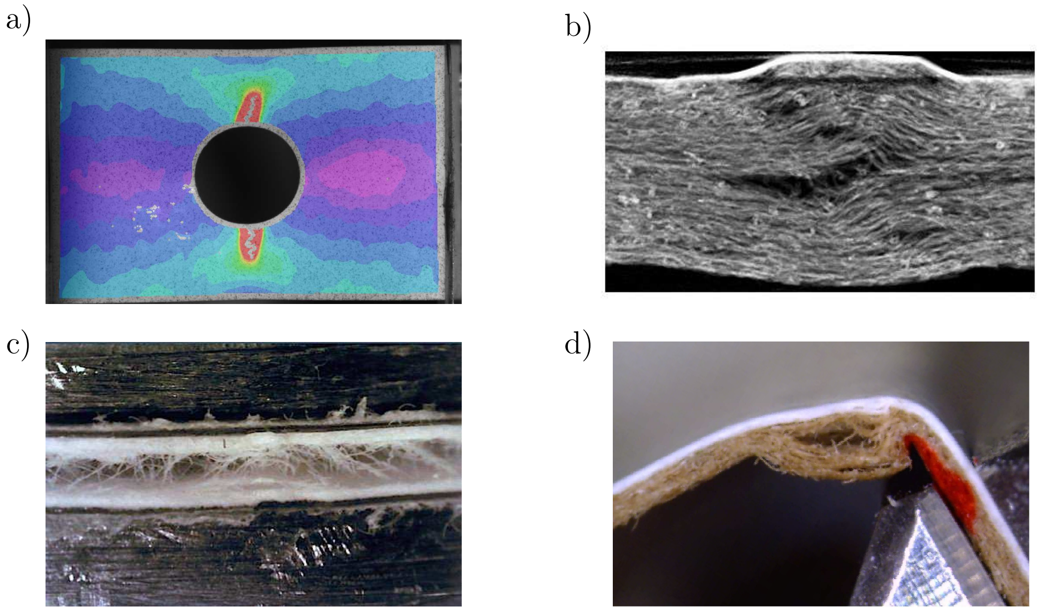

Figure 3: a) Digital image correlation during an in-plane tensile test of a paperboard with a punched hole. The magnitude of the first principal strains are indicated by the colors. b) A processed post-mortem image after a short span compression test obtained from X-ray tomograph. c) Out-of-plane tension test filmed with a microscope. d) Folding of a creased paperboard filmed with a microscope.

Within the packaging industry, there are a number of standard tests that are performed to ensure the quality of the paperboard. These standard tests have been utilized to a great extent for extracting the material properties in the developed model. Tests which induces uniaxial stress states are convenient for a modeling purposes, since they allow for a straight forward calibration of material parameters. The in-plane material properties can i.e. be extracted from an equipment following ISO:1924-3 that performs in-plane uniaxial tests.

The in-plane force-displacement curves generated from the experimental tests are shown in Fig. 4.

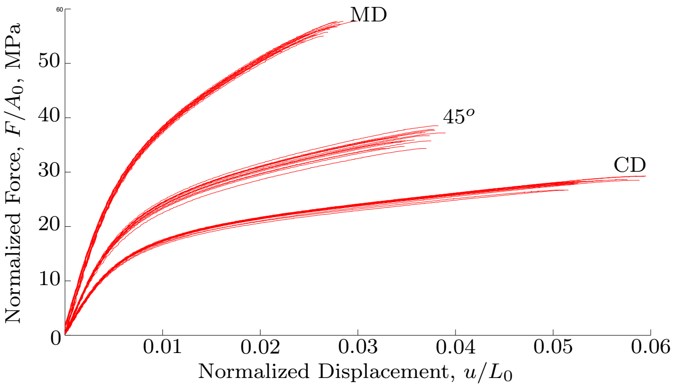

Figure 4: In-plane uniaxial tension tests in MD, CD and 45^o directions of paperboard. Displacement is normalized with the initial length, l_0 and force normalized with the initial cross section area, A_0.

The shape of the uniaxial curves in Fig. 4 are typical for paperboard materials, where the MD-test has higher stiffness, higher tensile strength and lower failure strain compared to CD. It can be observed from Fig. 4 that the degree of in-plane anisotropy is significant. The MD, CD and 45-degree tests are needed to calibrate the proposed model.

The in-plane compression response for paperboard is however challenging to determine. The difficulties stem from the fact that structural buckling occurs, since the paperboard has a slender geometry. The Short Compression Test (SCT) utilizes a short span length (0.7 mm) to compress the board. However, the clamping pressure that is applied during the test induces significant boundary effects. An alternative compression test is the long edge test, where instead a long paperboard specimen (55 mm) is used. Slender beams then acts as rigid supports on the top and bottom of the board to prevent buckling. The test does not introduce any significant boundary effects from the clamping, but the deformation state and failure are affected by the slender beams.

From the force displacement curves shown in Fig. 5, it is observed that the failure stress is lower in the long edge test compared with the SCT. The apparent stiffness in the long edge test is however very close to the stiffness measured in the tension tests, while the SCT has an apparent stiffness that is much lower. This deviation is likely due to sliding between the clamps and the paperboard in the SCT. The SCT has been investigated in detail in Paper C.

For out-of-plane testing, the situation is opposite compared with in-plane testing, i.e. it is more complicated to perform ZD-tensile testing than compression testing due to the thin geometry of paperboard. A typical force-displacement curve obtained from an out-of-plane compression test is shown in Fig. 6.

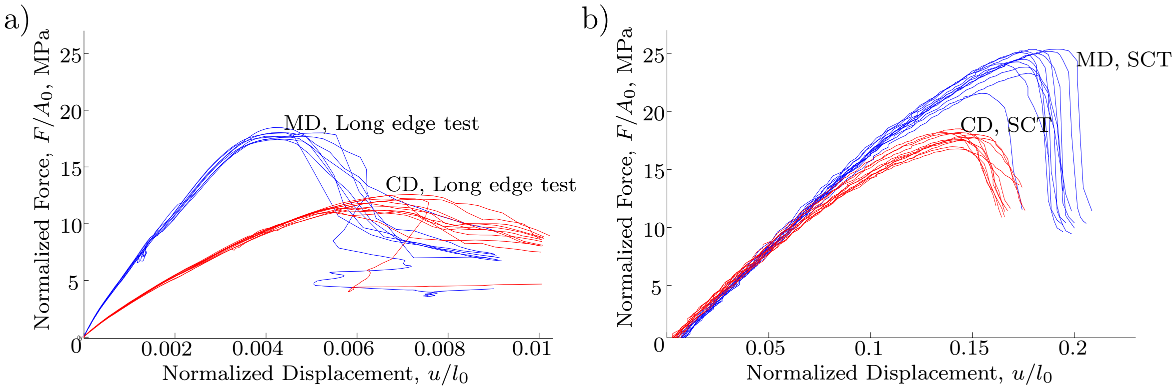

Figure 5: Force displacement curves obtained from in-plane compression tests of paperboard. a) Results from long edge tests, b) Results from SCT. Normalized force vs normalized displacement is plotted, where A_0 is the initial cross section area and l_0 the initial span-length in respective tests.

The force-displacement response in the out-of-plane compression is evidently different from the in-plane compression response, cf. Fig. 6. From the unloading curves, a nonlinear elastic material response is observed. Permanent deformations also start to develop at a relatively low stress level and a significant hysteresis can be observed in the reloading cycles. In the developed model it is assumed that permanent deformations increase linearly with respect to the stress.

Out-of-plane tension and out-of-plane shear tests are required to characterize the full orthotropic behavior of paperboard. The paperboard is much weaker in the out-of-plane direction compared to the in-plane direction. To test the paperboard in out-of-plane tension, the paperboard is glued on the top and bottom on two metal blocks, as shown in Fig. 3c. Typical out-of-plane tension curves for a paperboard are shown in Fig. 7.

As seen in Fig. 7 and Fig. 3c, the paperboard can be stretched significantly in the ZD-direction and still carry a force. The paperboard can therefore be viewed as a relatively though material. Degradation of the elastic modulus as well as permanent deformations are developed during post peak stress deformation. Hysteresis during unloading-reloading cycles are also seen in Fig. 7.

Preliminary measurements of out-of-plane shear are shown in Fig. 8 where a in-plane sample size of 20 mm × 20 mm has been used. In a) out-of-plane shear tests have been measured in the MD-ZD shear direction. Measurements of a mixed out-of-plane compression and out-of-plane shear mode are shown in Fig. 8b, where the paperboard is sheared under a constant out-of-plane pressure. This mixed mode of compression and shear is important to determine in a controlled fashion, since this mode is active in the creasing process. The tests were prepared in a climate controlled environment, but brought out to an uncontrolled testing environment during the tests. The curves are taken from Tayeh (2015) and a significant amount of tests were also performed in Håkansson (2014). The tests are conducted at a relatively slow speed of 0.5 mm/min.

If the out-of-plane shear curve in Fig. 8a is compared to the out-of plane tension curve

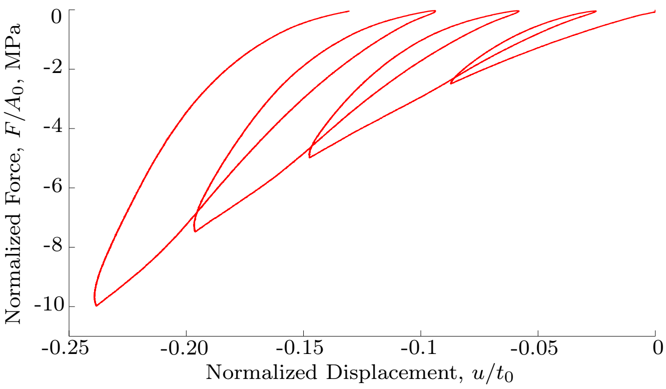

Figure 6: Out-of-plane compression test of paperboard with unloading cycles. The displacement is normalized with the initial thickness, t_0 and the force is normalized with the initial cross section area A_0.

in Fig. 7, it is noticed that the peak stress is higher in shearing. The stress also decreases faster in shear compared with tension. From Fig. 8b, it is seen that the maximum shear stress is increasing with increasing normal pressure, and that the residual stress after the peak stress is increasing. A behavior which resembles frictional type response is therefore observed for the paperboard material.

Additional tests should be performed to fully characterize the mechanical properties. It is for example important to characterize the rate-dependence, moisture dependence and temperature dependence. In this work however, a rate-independent model is proposed and all the tests and operations should preferably be performed in a climate controlled environment.

4 Converting procedures

The forming of a package is a complex process and involves several steps. To obtain straight fold lines during forming, it is important to first crease the paperboard. This is typically done by large rotating male and female cylinders as illustrated in Fig. 9. The crease patterns are complicated to ensure that corners of a package can be folded without inducing cracks. To study and isolate effects that occurs during creasing, simplified setups can be utilized. A setup where a straight male tool is pressed into the groove of a female die has been studied in this work, i.e. a line creasing operation, cf. Fig. 10.

The influence of different crease depths, crease speeds, tool geometries and web-tensions can easily be studied using the simplified setup. The paperboard is initially stretched with an initial displacement u_w and the displacement is kept fixed during the creasing process to mimic the effect of web-tension. The state in the paperboard during the line creasing process has been studied using the model developed in Paper B. Typical force-

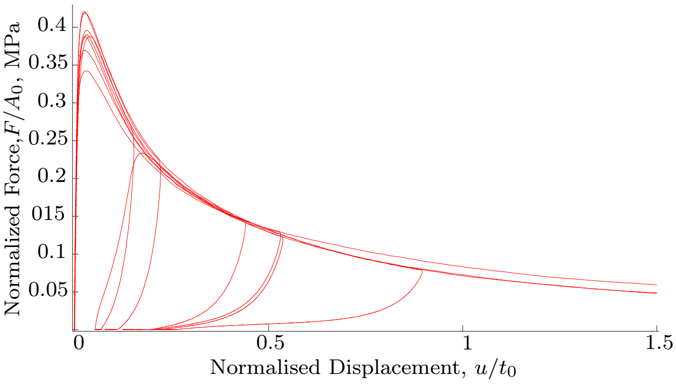

Figure 7: Out-of-plane tension test of paperboard with unloading cycles. Displacement normalized with the initial thickness, t_0 and force normalized with the initial cross section area, A_0.

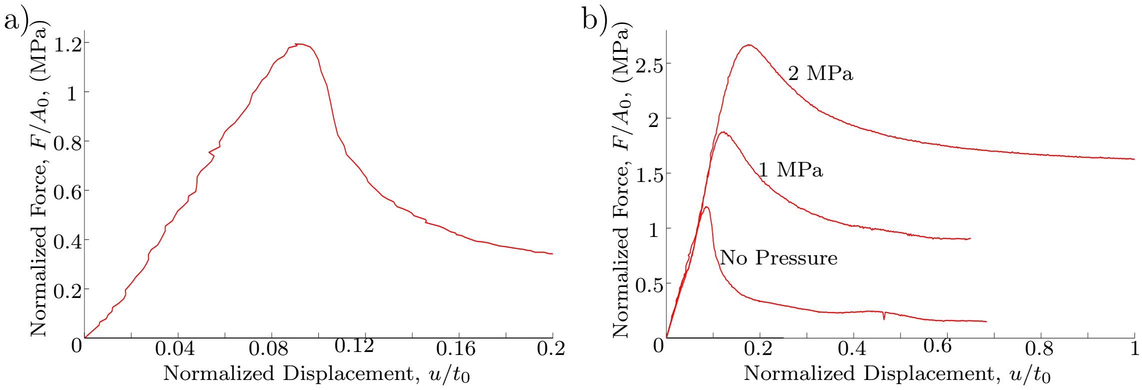

Figure 8: Out-of-plane shear test of paperboard in MD-ZD direction a) with no superimposed pressure and b) with a superimposed out-of-plane compression stress. The displacement is normalized with the initial thickness, t_0 and the force is normalized with the initial cross section area, A_0.

displacement curves from the line creasing setup are shown in Fig. 11, where a paperboard with a thickness of 0.39 mm and width of 38 mm is used. The displacement of the male die is defined as zero, when it is aligned with the female die.

In Fig. 11, the MD-crease curve means that the MD-direction is aligned in the x-direction in Fig. 10 and the x-direction is aligned with CD for the CD-crease curve. The tangent of the MD-crease curve is marked with a black line at load levels (1)-(4) in Fig. 11. It can be observed from the curves that the maximum reaction force is higher for MD compared with CD and during the initial displacement of the male die, the reaction force in MD and CD develops in a similar manner. The stiffness has a minimum at a displacement around -0.25 mm (marked at load level (2)). Upon further loading, the stiffness increases

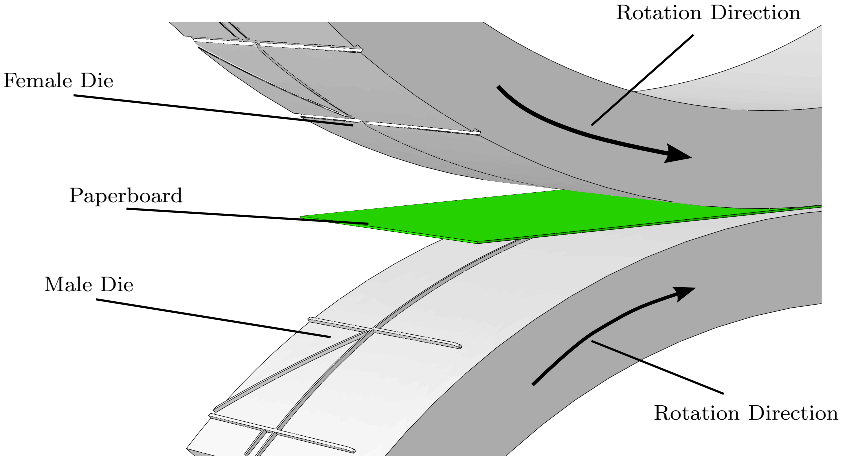

Figure 9: Rotation creasing of paperboard.

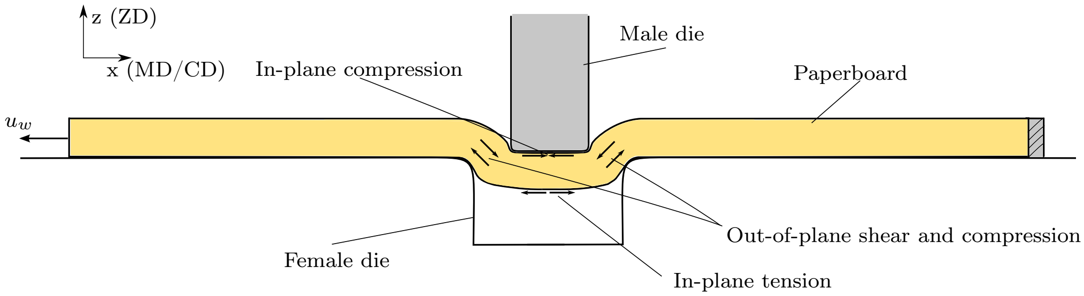

Figure 10: A schematic of the line creasing procedure. The arrows inside the paperboard indicate the dominant deformation mechanisms.

i.e. compare load level (2) with (3) and (4). From the simulations, the deformation modes can be analyzed in detail. It has been observed that between load level (1)-(2), out-of-plane shear between the male and female die is the dominant deformation mode. The simulations indicate at load level (2), the out-of-plane shear stress yield limit is reached. Upon further displacement of the male die, the ZD-compression stress increases and the paperboard is in a mixed state of ZD-compression and shear. As the male die unloads from the paperboard, it has been observed that permanent deformations in shear keeps developing.

After the creasing operation, it is much easier to obtain straight fold lines. To validate the performance of the package in the forming operations, use can be made of the simplified folding setup sketched in Fig. 12. Both creased and uncreased paperboards are tested using this setup.

The paperboard is clamped on one side with a clamping pressure of 0.2 MPa. At a distance l_0 from the clamps, a load cell is acting as rigid support. The distance l_0 is taken

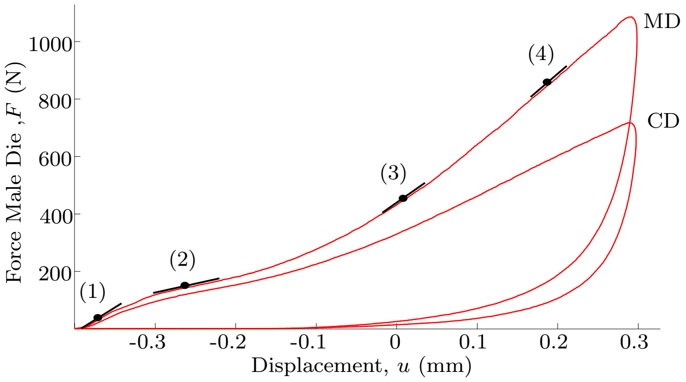

Figure 11: Force displacement curve in the line creasing operation in MD and CD. The tangent of the MD-crease curve is marked at load level (1)-(4).

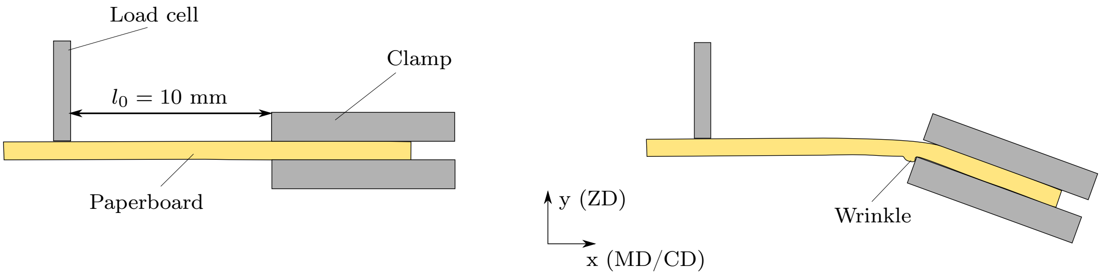

Figure 12: Schematic of line folding operation. Illustration of the folding of an uncreased paperboard.

to be $l_0 = 10$ mm in this work. The maximum bending moment is located close to the clamps and significant local deformations are triggered. The strength in compression is lower compared to the strength in tension, cf. Fig. 4 and Fig. 5 and the paperboard will fail on the side where the compression stresses are present and wrinkles will be formed.

The deformation pattern of creased paperboard, shown in Fig. 3d, is different compared to an uncreased paperboard. Due to permanent deformations and damage induced during creasing, the crease line will act as a plastic hinge where the fiber layers will become separated (delamination) during folding. The force-bending angle curve from the line folding operation of an uncreased paperboard in MD and a paperboard that has been creased 0.2 mm is shown in Fig. 13.

The maximal reaction force is significantly reduced for the creased paperboard. A common measure within the packaging industry is the Relative Crease Strength (RCS), which is often used to correlate to the behavior during the forming of a package. The

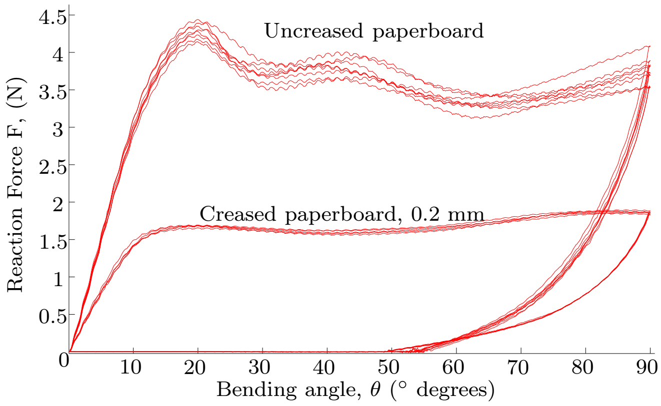

Figure 13: Force-rotation curve of folding of a creased and uncreased paperboard in MD.

RCS-value is defined as

$$\mathrm{RCS} = \frac{\text{Maximum bending force creased paperboard}}{\text{Maximum bending force uncreased paperboard}}. \tag{1}$$

For the folding curves in Fig. 13, a RCS value of about 0.39 is obtained. The folding of an uncreased paperboard is investigated in Paper C and a creased paperboard in Paper E. For folding of uncreased paperboard, it is noticed from the simulations that shear bands are forming during the simulations. It has also been noticed that the material parameters related to out-of-plane shear has a large influence on the folding curve of creased paperboard. An experimental study on the influence of crease depth on the folding behavior are found in e.g. Nagasawa et al. (2003) and Cavlin (1988).

5 Modeling of paperboard

One of the early attempts to model the response of paperboard in a unified manner was proposed in Xia (2002). The model consist of two parts, one continuum model which mainly captures the in-plane behavior and an interface model that captures the out-of-plane response, cf. Fig. 14.

Using the approach with both interfaces and continuum the delamination response of the paperboard can effectively be captured. However, the approach is associated with some limitations. The first being that the number of interfaces are somewhat arbitrary and the second is that it is necessary to apriori define where the delamination is allowed to nucleate and propagate. The third limitation is related to the calibration, which requires that the interface parameters and the continuum parameters can be experimentally distinguished.

In the original model proposed in Xia (2002), it was assumed that the continuum in the out-of-plane directions was purely elastic. This turned out to be too restrictive, since the continuum properties became too stiff, which potentially could lead to numerical

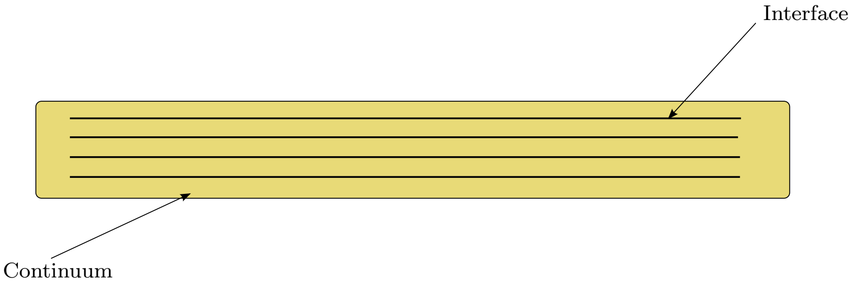

Figure 14: A paperboard model with predefined interfaces.

instability. As a remedy for this issue, three yield surfaces were utilized as well as hardening plasticity in the out-of-plane shear- and compression-directions in Nygårds et al. (2009). Models for paperboard utilizing a thermodynamic framework at finite strains were proposed in Harrysson and Ristinmaa (2008) and Ask and Ristinmaa (2008). Lately, simplified models for the mechanical response of paperboard have attracted increased interest in the research community. One disadvantage with more complex models is the number of material parameters needed to capture all the mechanical deformation modes. In Beex and Peerlings (2009), a simplified model based on the Hill criterion available in commercial softwares together with interface elements were used. It was concluded that plasticity is important to obtain a good crease. A similar approach, using the Abaqus software with Hill's yield criterion for the continuum and surface based cohesive zones for the interfaces, was established in Huang et al. (2014). It was shown that by mapping the continuum properties throughout the thickness, the macroscopic force-displacement curves obtained from experiments could be predicted. A model which accounts for the rate dependence for a high density fiberous material has been proposed recently in Tjahjanto et al. (2015).

Paperboard can also be modeled with other types of techniques rather than a continuum based approach. In Giampieri et al. (2011), a special purpose crease element was developed that can be placed between two adjacent 4 node shell finite elements of Mindlin-Reissner type, suitable for large scale forming applications. Solid-shell and cohesive elements were utilized in Pagania and Perego (2015) to model the cap opening of a carton package. In Borodulina et al. (2012) and Kulachenko (2012) paperboard was modeled using a fiber network model, where the fibers are represented by beam elements. These models are useful to investigate the influence of local micro-scale phenomenons on the mechanical properties. Micromechanical models are however computionally expensive and an alternative is to use a quasi-continuum model, cf. Beex et al. (2014), where local mirco-scale phenomena can be resolved in regions of interest, while having a coarse fiber structure elsewhere. Moisture effects were recently incorporated in a model in Bosco et al. (2015), where representative unit cell was established based on micro-scale considerations.

5.1 Continuum modeling

The continuum assumption is based on that a large number of the micro structural components of the medium are replaced with a set of representative macroscopic quantities.

The structural components for paperboard are on the microscopic scale, i.e. the cellulose fibers. For continuum modeling, the size of the specimen needs to be sufficiently large for the macroscopic observable quantities to be representative of the average behavior of the structural components. The Representative Volume Element (RVE) is defined as the smallest volume of the medium that can represent the macroscopic quantities of the entire medium. For paperboard, the size and shape of the RVE is related to the size and shape of the fibers and their bondings. It can therefore be imagined that the RVE is longer in the MD direction compared with CD and ZD, i.e. length scales varies with orientation. In Mäkelä and Östlund (2003), an investigation of the length scale effects were performed and it was concluded that length scale can matter already at the dimension at which the standardized uniaxial tests of paperboard are performed.

5.2 Kinematics framework

All tensors in this work will be considered in a Cartesian setting, i.e. following the work of Ciarlet (1988). Consider a material body in the reference configuration $\Omega_0 \in \mathbb{R}^3$ at the time instance t_0 and at the deformed configuration $\Omega \in \mathbb{R}^3$ at time instance t. The non-linear map that defines the motion is assumed to be given by $\boldsymbol{\varphi}(\boldsymbol{X}, t) : \Omega_0 \times T \to \Omega$, where $\boldsymbol{X}$ denotes the position of a particle in the reference configuration and the position of the same particle in the current configuration is found as $\boldsymbol{x} = \boldsymbol{\varphi}(\boldsymbol{X}, t)$. The mapping of vectors in the reference configuration to the current configuration is given by the deformation gradient $\boldsymbol{F} = \nabla_{\boldsymbol{X}} \boldsymbol{\varphi}$. To model permanent deformations, a multiplicative split of the deformation gradient is assumed, i.e.

$$\boldsymbol{F} = \boldsymbol{F}^e \boldsymbol{F}^p, \tag{2}$$

where $\boldsymbol{F}^e$ represents the elastic deformation and $\boldsymbol{F}^p$ the plastic deformation. The split (2), introduces a stress-free intermediate configuration, cf. Fig. 15.

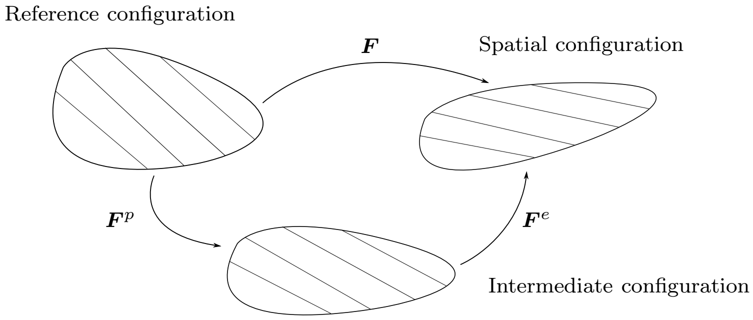

Figure 15: The three configuration introduced by the multiplicative split, i.e. the undeformed, intermediate and deformed configurations.

The evolution of the plastic deformation gradient is given by

$$\dot{\boldsymbol{F}}^p = \boldsymbol{L}^p \boldsymbol{F}^p, \tag{3}$$

where $\boldsymbol{L}^p$ is the material plastic velocity gradient. The spatial plastic velocity gradient is defined by the material time derivative of (2) and using (3),

$$\boldsymbol{l}^p = \boldsymbol{F}^e \boldsymbol{L}^p \boldsymbol{F}^{e-1}. \tag{4}$$

The models presented in this thesis are making use of quantities defined in the current configuration.

The intermediate configuration is not unique and this can be realized by a rotation of the intermediate configuration, i.e.

$$\boldsymbol{F} = (\boldsymbol{F}^e \boldsymbol{Q}^T)(\boldsymbol{Q}\boldsymbol{F}^p) = (\boldsymbol{F}^e)^*(\boldsymbol{F}^p)^*, \tag{5}$$

where $(\boldsymbol{F}^p)^*$ and $(\boldsymbol{F}^e)^*$ introduces an equivalent intermediate configuration and $\boldsymbol{Q}$ is an orthogonal tensor. The rotation operation of the intermediate configuration will leave the configuration stress free. The arbitrary rotation, $\boldsymbol{Q}$, of the intermediate configuration will in general enter in the evolution format in the skew-symmetric part of (3) i.e.

$$\mathrm{skew}(\boldsymbol{L}^p) = \mathrm{skew}(\boldsymbol{L}^p_c) + \boldsymbol{W}_c, \tag{6}$$

where $\boldsymbol{W}_c$ is referred to as the constitutive spin and is related to the choice of intermediate configuration, i.e. $\boldsymbol{Q}$. One possible choice of the intermediate configuration is the isoclinic, where $\boldsymbol{W}_c = \boldsymbol{0}$, cf. Dafalias (1998) and Harrysson and Ristinmaa (2007). The isoclinic configuration has been adopted in the work herein. Based on the isoclinic format, the plastic velocity gradient can be expressed as $\mathrm{skew}(\boldsymbol{L}^p) = \mathrm{skew}(\boldsymbol{L}^p_c)$. The spatial plastic velocity gradient can be split into a symmetric and a skew-symmetric part, i.e.

$$\boldsymbol{l}^p = \mathrm{sym}(\boldsymbol{l}^p) + \mathrm{skew}(\boldsymbol{l}^p) = \boldsymbol{d}^p + \boldsymbol{\omega}^p, \tag{7}$$

where $\boldsymbol{d}^p$ is the symmetric part of the plastic velocity gradient and $\boldsymbol{\omega}^p$ is the eulerian plastic spin.

5.3 Anisotropy framework

Since paperboard experiences large deformations in converting operations, in particular the out-of-plane directions, it is important to consider the change of the preferred directions, i.e. the MD, CD and ZD directions. Three vectors, which phenomenologically represents the preferred directions, are introduced in the undeformed configuration. Properties of paperboard is highly related to its fiberous structure and the preferred directions can therefore assumed to be embedded in the continuum. An alternative to the embedding, is to utilize an evolution of the vectors governed by a potential function, cf. Harrysson and Ristinmaa (2007) and Dafalias (1998).

A common assumption for materials with embedded fibers, is that the preferred directions evolve together with the deformation gradient, $\boldsymbol{F}$ or $\boldsymbol{F}^e$, cf. Holzapfel (2000). This choice is however not unique and an assumption needs to be made. The mapping of a phenomenological direction in the continuum can be written as

$$\boldsymbol{v} = \boldsymbol{\beta}\boldsymbol{\alpha}\boldsymbol{v}_0 = \boldsymbol{\beta}\bar{\boldsymbol{v}}, \tag{8}$$

where $\bar{\boldsymbol{v}} = \boldsymbol{\alpha}\boldsymbol{v}_0$ represents the transformation of the vector to the intermediate configuration, cf. Harrysson and Ristinmaa (2007). In this work it is assumed that $\bar{\boldsymbol{v}} = \boldsymbol{v}_0$. The director vectors are assumed to be orthogonal and of unit length in the reference configuration.

In Paper A, it is suggested that the change of the in-plane director vectors, $\boldsymbol{v}^{(\alpha)}$, follow the rotation part of the polar decomposition of the elastic deformation gradient, i.e. $\boldsymbol{R}^e$ defined from $\boldsymbol{F}^e = \boldsymbol{V}^e\boldsymbol{R}^e$. The choice will ensure that the preferred directions remain at unit length and orthogonal to each other. The drawback of the assumption is that the stress-strain relationship become somewhat complex. It is also cumbersome to derive an analytic expression for the algorithmic tangent stiffness matrix, which is needed in the numerical scheme. To simplify, the in-plane directions were taken to follow $\boldsymbol{F}^e$ in Paper B, i.e.

$$\begin{aligned} \boldsymbol{v}^{(1)} &= \boldsymbol{F}^e\boldsymbol{v}_0^{(1)} \\ \boldsymbol{v}^{(2)} &= \boldsymbol{F}^e\boldsymbol{v}_0^{(2)}. \end{aligned} \tag{9}$$

The ZD-direction is chosen to change together with the cofactor of the elastic deformation gradient in Paper B, i.e.

$$\boldsymbol{n}^{(3)} = \mathrm{cof}(\boldsymbol{F}^e)\boldsymbol{n}_0^{(3)}, \tag{10}$$

where $\mathrm{cof}(\boldsymbol{F}^e) = J^e\boldsymbol{F}^{e-T}$ is the cofactor of the elastic deformation gradient. This assumption will ensure that the ZD-direction remains perpendicular to the in-plane directions $\boldsymbol{v}^{(1)}$ and $\boldsymbol{v}^{(2)}$. The motivation for this choice in the ZD-direction stems from the idealized shearing of a deck of cards, as illustrated in Fig. 16.

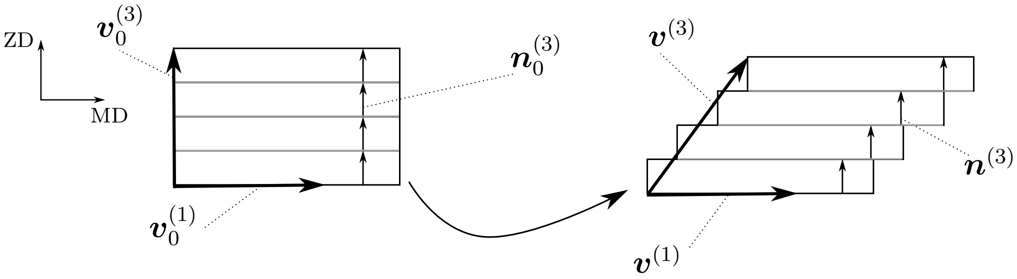

Figure 16: Out-of-plane shearing of paperboard, illustrating the idealized deformation pattern.

When defining the evolution of the director vectors, paperboard is ideally considered to be a sandwiched structure with fibers stacked on top of each other. After shear deformation, each fiber-layer normal, $\boldsymbol{n}^{(3)}$, is assumed to remain unchanged, while a director vector, $\boldsymbol{v}^{(3)} = \boldsymbol{F}^e\boldsymbol{v}_0^{(3)}$ has components in the MD-direction, cf. Fig. 16. Rather than using $\boldsymbol{v}^{(3)} = \boldsymbol{F}^e\boldsymbol{v}_0^{(3)}$, a normal vector $\boldsymbol{n}_0^{(3)}$ will be utilized for the out-of-plane behavior. This choice will ensure that the ZD-direction is always perpendicular to the in-plane directions, i.e.

$$\boldsymbol{n}^{(3)} = \boldsymbol{v}^{(1)} \times \boldsymbol{v}^{(2)}, \tag{11}$$

The alignment of $\boldsymbol{v}^{(3)}$ will imply a coupling between the in-plane and the out-of-plane response, i.e. $\boldsymbol{v}^{(3)} \cdot \boldsymbol{v}^{(1)} \neq 0$. Use of $\boldsymbol{v}^{(3)}$ instead of $\boldsymbol{n}^{(3)}$ will result in that the stronger in-plane properties will influence the weaker out-of-plane properties, whereas the choice (10) will reduce the influence of the in-plane properties on the out-of-plane response in the model.

5.4 Thermodynamic framework

The thermodynamic framework is a helpful tool when deriving relations between kinematic and kinetic quantities, as well when formulating evolution laws. A hyperelastic format is adopted in this work, which implies the existence of a potential, ψ, i.e. Helmholtz free energy. The free energy is a function of variables which characterizes the state of the system, defined as state variables. The choice of state variables are however non-trivial and depends upon which features of the system that is desired to be modeled. One typical state variable is the left elastic Cauchy-Green tensor, defined as

$$\boldsymbol{b}^{e} = \boldsymbol{F}^{e} \boldsymbol{F}^{eT}, \tag{12}$$

which characterize the deformation of the system. To model plasticity, the introduction of internal state variables, $\kappa^{(\nu)}$, are needed as well. To model anisotropy, state variables associated with the preferred directions of the material needs to be utilized. This is achieved by letting the free energy be a function of the director vectors, $\boldsymbol{v}^{(1)}, \boldsymbol{v}^{(2)}$ and the director normal $\boldsymbol{n}^{(3)}$.

The fulfillment of the dissipation inequality will ensure that the first law of thermodynamic is fulfilled. The dissipation inequality in an iso-thermal setting is given by

$$d = \boldsymbol{\tau} : \boldsymbol{l} - \rho_0 \dot{\psi} \geq 0, \tag{13}$$

where $\boldsymbol{\tau}$ is the Kirchhoff stress, $\boldsymbol{l} = \dot{\boldsymbol{F}} \boldsymbol{F}^{-1}$ is the spatial velocity gradient and ρ_0 the density in the reference configuration. By choosing appropriate evolution laws for the state variables, the dissipation inequality can be ensured to be fulfilled. Thermodynamical arguments are also important to consider if multi-physical problems are considered. In several industrial processes, high temperatures and moisture will influence the process, and the thermodynamical framework will then be crucial when developing a physical sound model. A recently proposed model where moisture and heat transport utilizing the thermodynamic framework for paperboard has been established in Alexandersson et al. (2016).

The free energy is split into an elastic part and a plastic part according to $\psi = \psi^{e} + \psi^{p}$. A novel format, suitable for materials with high degree of anisotropy, of the elastic part of the free energy is proposed in Paper B and further developed in Paper C and E. The elastic part of the free energy is split according to

$$\psi^{e} = \psi^{e}_{ip} + \psi^{e}_{cop} + \psi^{e}_{top} + \psi^{e}_{sop}. \tag{14}$$

The subscripts refer to the direction in which the energy contribution is found in the initial stiffness, i.e. *ip* in-plane directions, *top* tension-out-of-plane, *cop* compression out-of-plane and *sop* shearing out-of-plane. The additive format of the free energy enables the response between the in-plane and out-of-plane properties to be decoupled. Each term in (14) has been constructed such that the free energy is increasing for an arbitrary deformation.

5.5 Plasticity

To model an elastic domain, a yield surface, f, which determines the onset of plasticity is utilized. For $f < 0$ the response is purely elastic, while $f = 0$ implies that plastic deformations develop. In the elastic regime, the material response is reversible and no energy is dissipated, while during plastic deformations, energy is dissipated.

A range of yield surfaces for anisotropic materials were investigated in Lindström (2013). For example, a common yield surface for anisotropic materials is the Hill surface, cf. Hill (1948), which have been adopted for the modeling of paperboard, cf. Beex and Peerlings (2009) and Huang and Nygårds (2010). Assuming a fix coordinate system that is aligned with the MD, CD and ZD directions, the Hill criterion can be written as

$$f^H = \boldsymbol{\tau} : \mathbb{H} : \boldsymbol{\tau} - 1 \leq 0 \tag{15}$$

The fourth order tensor $\mathbb{H}$ can be calibrated from uniaxial tensile tests and the components of $\mathbb{H}$ are chosen such that the yield criterion becomes pressure independent. It should however be noted that paperboard is not a pressure independent material. Moreover, for the surface f^H to be convex, it is required that $\mathbb{H}$ is positive definite, cf. Ottosen and Ristinmaa (2005). The positive definiteness of $\mathbb{H}$ limits the degree of anisotropy which imposes a severe restriction in the context of paperboard modeling.

The continuum model proposed in Xia (2002), is based on a yield surface which turns out to be effective for modeling of paperboard and it has therefore been utilized in this work. The yield surface in the stress space is built up by a number of subsurfaces $\boldsymbol{n}_\nu^{(s)}$ connected by switch functions $\chi^{(\nu)}$. The explicit expression for the yield surface, which is explained in detail in the appended papers, is given by

$$f(\boldsymbol{\tau}, \boldsymbol{n}^{(\beta)}, K^{(\beta)}) = \sum_{\nu=1}^{n} \chi^{(\nu)} \left(\frac{\boldsymbol{\tau} : \boldsymbol{n}_s^{(\nu)}}{\tau^{(\nu)}} \right)^{2k} - 1 = 0 \tag{16}$$

The yield surface (16), can be used to model materials with high degree of anistropy and still remain convex. This feature stems from the fact that the location of the independent subsurfaces $\boldsymbol{n}_s^{(\nu)}$ provides flexibility which allows convexity to be preserved.

The yield surface (16), is suitable for modeling of complex hardening behavior, since the yield subsurfaces, $\boldsymbol{n}_s^{(\nu)}$, can be controlled independently of each other in the stress space. One independent internal variable $\kappa^{(\nu)}$, associated with each subsurface $\boldsymbol{n}_s^{(\nu)}$, is introduced to control the distance between each subsurface and the origin in the stress space. The decoupling also allows cross hardening to be modeled. Due to the high degree of flexibility, one yield surface can therefore be used to model both the weaker out-of-plane properties and the stronger in-plane properties. In Paper B, six additional subsurfaces, compared to the original proposed model in Xia et al. (2002), are introduced to model the out-of-plane behavior of paperboard. One disadvantage of the yield criterion is however that many parameters needs to be determined for the subsurfaces. The number of parameters can however be reduced, by apriori assumptions regarding the plastic strain ratios, which allows the subsurfaces to be calibrated from uniaxial tests.

A rate independent model is adopted in this work. It can be shown cf. Ottosen and Ristinmaa (2005), that by assuming the dissipation (13) to be at maximum during plasticity and fulfilling the constraint $f = 0$, provide the associated evolution laws

$$\begin{aligned} \boldsymbol{d}^p &= \lambda \frac{\partial f}{\partial \boldsymbol{\tau}} \\ \dot{\kappa}^{(\nu)} &= \lambda \frac{\partial f}{\partial K^{(\nu)}}, \end{aligned} \tag{17}$$

where $K^{(\nu)}$ is a conjugate stress variable. The Lagrange multiplier, λ, fulfills the Karush-Kuhn-Tucker conditions. The first equation in (17), only provides the symmetric part of the plastic velocity gradient, $\boldsymbol{l}^p$ and additional assumption need to be made for the skew symmetric part. The skew-symmetric part, i.e. the eulerian plastic spin $\boldsymbol{\omega}^p$, is an important quantity in large strain elasto-plastic constitutive models and should not be confused with the constitutive spin in (6). The plastic spin has the format

$$\boldsymbol{\omega}^p = \lambda < \cdot >, \tag{18}$$

and is related to the plastic rate of deformation, cf. Dafalias (1998). The eulerian plastic spin will not contribute to the the dissipation (13). It is however important to specify, as is shown in Paper B.

5.6 Damage

During folding of a creased paperboard, the fiber-layers in paperboard separates and the material properties in the delaminated zones are altered. In this work, Continuum Damage Mechanics (CDM), cf. Kachanov (1958) and Chaboche (1981), has been adopted to model the softening associated with out-of-plane deformations. In CDM, scalar or tensor damage variables are introduced to model the weakening of material in a macroscopic sense. In Paper D, two formats for the damage evolution are reviewed and one of the formats is adopted in Paper E for modeling of paperboard. The CDM-concept has been adopted to model the in-plane behavior of paper previously in Isaksson et al. (2004). An alternative to CDM, which has commonly been adopted to model in-plane fracture of paper, is the use of cohesive zones cf. Tryding and Gustafsson (2001), Mäkelä and Östlund (2012) and Vojskovic (2015). An excellent review on the concept of fracture mechanics applied to paper is given in Mäkelä (2002).

Scalar damage variables ϕ_α have been adopted in this work to model the weakening associated with out-of-plane deformation. The scalar damage variables are introduced into the elastic part of the free energy according to

$$\rho_0 \psi^e = \psi^e_{ip} + \psi^e_{cop} + (1 - \phi_1)^n \tilde{\psi}^e_{top} + (1 - \phi_2)^n \tilde{\psi}^e_{sop}, \tag{19}$$

Two scalar damage variables are introduced, one for the degradation of elastic properties in ZD-tension, ϕ_1, and the other for the degradation in out-of-plane shear, ϕ_2. Note that a material parameter n is introduced in (19) and that $\tilde{\psi}^e_{sop}$ and $\tilde{\psi}^e_{top}$ are functions of invariants related to the deformation only, i.e. not the damage variables. The two damage variables introduce a possibility to model softening in shear and tension independently. As seen in Fig. 8 and Fig. 7, the the post-peak part of the out-of-plane shear curve is steeper compared with ZD-tension. The energy conjugates to the damage variables are given by

$$Y_1 = \frac{\partial \psi^e_{top}}{\partial \phi_1} = n(1-\phi_1)^{n-1}\tilde{\psi}^e_{top} \qquad Y_2 = \frac{\partial \psi^e_{sop}}{\partial \phi_2} = n(1-\phi_2)^{n-1}\tilde{\psi}^e_{sop} \tag{20}$$

and are used to drive the evolution of damage, i.e. $\dot{\phi}_1 = \dot{\phi}_1(Y_1)$ and $\dot{\phi}_2 = \dot{\phi}_2(Y_2)$.

To obtain a material response with softening, the yield surface is required to function the damage variables. In the expression for the yield surface (16), the distance to respective subsurface is given by $\tau^{(\nu)}$. The distances $\tau^{(\nu)}$ belonging to ZD-tension, out-of-plane shear and MD/CD compression will be reduced according to

$$\begin{aligned}
\tau^{(\nu)} &= (1-\phi_1)^{n_c}\tau_0^{(\nu)} && \nu \in \{4,5\} \\
\tau^{(\nu)} &= (1-\phi_1)^{n_t}\tau_0^{(\nu)} && \nu = 8 \\
\tau^{(\nu)} &= (1-\phi_1)^{n_s}(1-\phi_2)^{n_s}\tau_0^{(\nu)} && \nu \in \{9,10,11,12\}
\end{aligned} \tag{21}$$

where $\nu \in \{4,5\}$ are associated with MD and CD compression, $\nu = 8$ is associated with ZD-tension and $\nu \in \{9,10,11,12\}$ are associated with out-of-plane shear. Note the three independent material constants, n_t, n_s and n_c have been introduced in (21). Other formats for how the damage variables changes the $\tau^{(\nu)}$ can be included in the framework, but the specific format proposed in (21) appears to give results in agreement with the creasing and folding processes.

Damage is however a local phenomenon and by using CDM, a solution which is dependent on the mesh is obtained. The damage will typically localize in a single element as the mesh size is reduced and consequently the results will not converge to a unique solution. Typical force-displacement curves where damage has been forced to localize in a single element for different mesh sizes are shown in Fig. 17. As clearly seen in Fig. 17, the curves do no not converge upon mesh refinement.

One method to reduce the mesh-dependency is to use a non-local formulation of the state variables, e.g. Pijaudier-Cabot and Bažant (1987), Strömberg and Ristinmaa (1996) and Jirasek (1998). By introducing a non-local formulation, a length parameter l needs to be introduced which determines the size of the localization zone. One possible choice of length parameter when it comes to paper is the width/thickness of the fiber. However, the number of fibers in the ZD-direction is estimated to be between 20-35, which is in the vicinity of the mesh size that is adopted in the simulation of creasing and folding in this work. The material parameters in Paper E have therefore been fitted to the folding curves for a fixed mesh of 25 elements through the the thickness. However, as an alternative, the non-local technique described in the next section can be adopted.

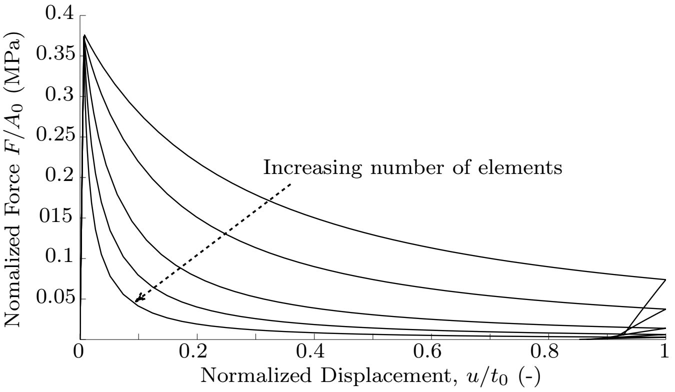

Figure 17: ZD-tension test where the number of elements through the thickness has varied according to 1,4,10,20 and 40. Only one element is used in the in-plane dimension. The displacement is normalized with the initial thickness t_0 and the force with the initial cross section area A_0

6 Non-local formulation

The implicit gradient enhancement, proposed in Peerlings et al. (1996) has been adopted below. This approach has been implemented in the software Abaqus via the UMAT and UMATHT user subroutines, cf. Abaqus User's Manual. (2013), together with proposed elasto-plastic damage model for paperboard. The driving force for the damage in ZD-direction has been made non-local, i.e. Y_1. However, the subscript is dropped from here on to keep the notation simple . The non-local field $\bar{Y}$ is obtained by solving an additional field equation, given by

$$\bar{Y} - \frac{l^2}{2}\Delta\bar{Y} = Y. \tag{22}$$

where Δ denotes the spatial Laplace operator. A similar non-local technique was adopted in Isaksson et al. (2004) for modeling of paper. In the evolution of damage, the local quantity Y will be replaced with the non-local $\bar{Y}$. The length parameter l introduced in (22), will control the size of the localization zone of $\bar{Y}$. The length parameter l can also be defined in an anisotropic manner, but for illustrating the concept, it is defined as an isotropic quantity. The boundary condition $\nabla\bar{Y} \cdot \boldsymbol{n} = 0$, where $\boldsymbol{n}$ is the boundary of the body has been adopted.

The weak form of (22) is the basis for the finite element formulation and is given by

$$\int_v \frac{l^2}{2}(\delta\nabla\bar{Y}) \cdot (\nabla\bar{Y})dv = \int_v (\delta\bar{Y})(Y - \bar{Y})dv \tag{23}$$

where v is the volume in the spatial configuration. Equation (23) has been implemented in the commercial software ABAQUS, by utilizing the subroutine UMATHT. The subroutine UMATHT is actually intended for solving the heat equation with a user-defined constitutive relation for the heat flux and heat generation. However, by reinterpreting the temperature as the non-local variable $\bar{Y}$ and by defining the heat generation in a specific manner, equation (23) can be reattained. The weak form of the heat equation is given by

$$\int_v (\delta\theta)\rho\dot{U}dv - \int_v (\delta\nabla\theta)\cdot\boldsymbol{q}dv = \int_v (\delta\theta)rdv + \int_s (\delta\theta)\boldsymbol{q}\cdot\boldsymbol{n}ds. \tag{24}$$

In (24), s denotes the surface area of the structure in the spatial configuration. The temperature is denoted by θ, heat generation by U, the heat flux by $\boldsymbol{q}$, the body flux by r and the density by ρ. By performing a time-discretization, using the boundary condition $\boldsymbol{q}\cdot\boldsymbol{n} = 0$ and setting $r = 0$, the following equation is obtained.

$$-\int_v (\delta\nabla\theta)\cdot\boldsymbol{q}dv = \frac{1}{\Delta t}\int_v (\delta\theta)\rho(U_{t+\Delta t} - U_t)dv \tag{25}$$

The subroutine UMATHT requires $U_{t+\Delta t}$ and $\boldsymbol{q}$ as output from the subroutine. By defining the quantities according to

$$\begin{aligned} \boldsymbol{q} &= -\tfrac{l^2}{2}\nabla\theta \\ U_{t+\Delta t} &= \tfrac{\Delta t}{\rho}(Y-\theta) + U_t, \end{aligned} \tag{26}$$

the heat equation is then given according to

$$\int_v \frac{l^2}{2}(\delta\nabla\theta)\cdot(\nabla\theta)dv = \int_v (\delta\theta)(Y-\theta)dv. \tag{27}$$

If the temperature θ is reinterpreted as the non-local variable $\bar{Y}$, then the exact form of the differential equation (23) used in the regularization is recovered.

6.1 Test of non-local implementation

To verify the implementation of the non-local driving force, $\bar{Y}$, a test with three different mesh sizes of the geometry seen in Fig. 18 has been performed. The geometry is fixed at the bottom boundary and pulled in the vertical direction with a fixed displacement at the top boundary.

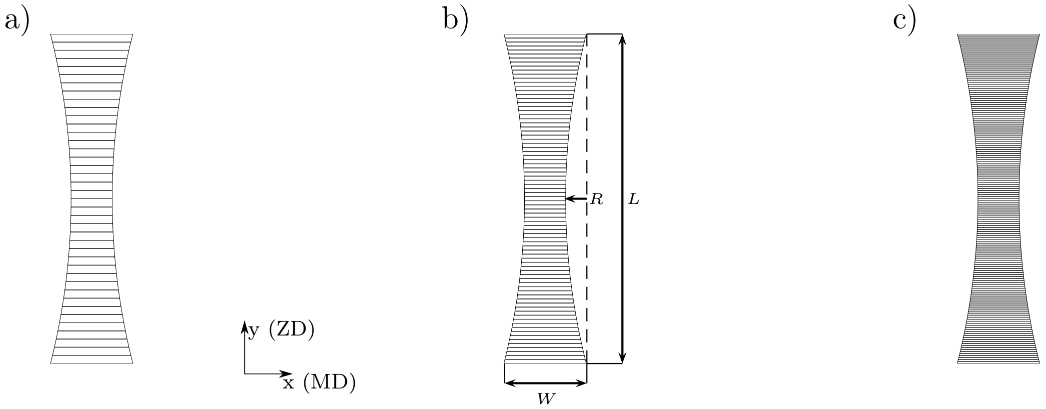

Figure 18: The geometry and meshes used to verify the implementation of the non-local damage driving force $\bar{Y}$. The dimensions are given by $L = 0.4$ mm, $W = 0.1$ mm and $R = 0.02$ mm. The number of elements used are 40, 80 and 160 respectively.

The force-displacement curves using the meshes in Fig. 18 are shown in Fig. 19. The length parameter $l^2/2 = 0.01$ mm^2 has been adopted. The red curve is the result from the coarsest mesh, while the black and blue curves are used for the medium and finest mesh. The force-displacement curves from the medium and fine mesh are hard to distinguish from each other, thereby illustrating that convergent results appears to be obtained. In Fig. 20a and b, the medium sized mesh has been adopted, but the length scale parameters have been varied according to $l^2/2 = \{0.1, 0.01, 0.001\}$. The force-displacement curves are shown in Fig. 20a while in Fig. 20b the distribution of the conjugate damage force $\bar{Y}$ as a function of the vertical position y is shown. The $\bar{Y}$ has been extracted at a displacement of $u = 0.04$ mm.

Clearly, the length scale parameter influences the response in Fig. 20. The lower the value of the length parameter, the more the non-local conjugate damage force $\bar{Y}$ localizes in the center of the geometry. The magnitude of $\bar{Y}$ also increases as the length parameter decreases.

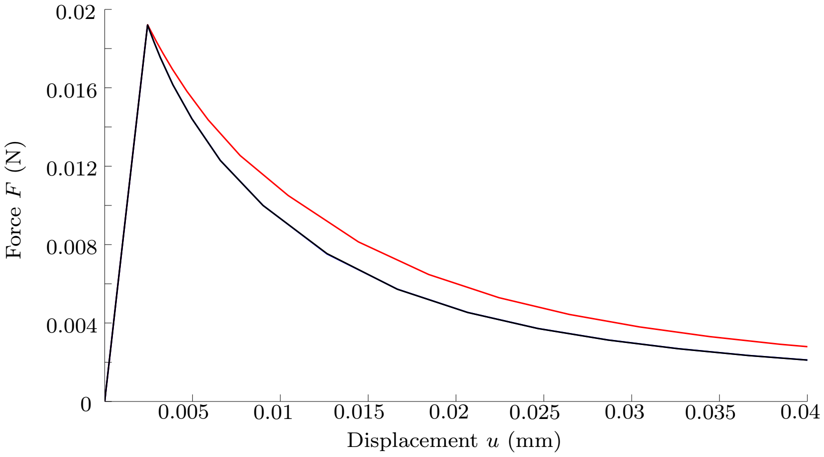

Figure 19: Force displacement curves using the different meshes seen in Fig. 18 using the $l^2/2 = 0.1$ mm^2. The red curve is for the coarsest mesh, blue for medium and black for finest mesh. The black and blue curves are however difficult to distinguish from each other.

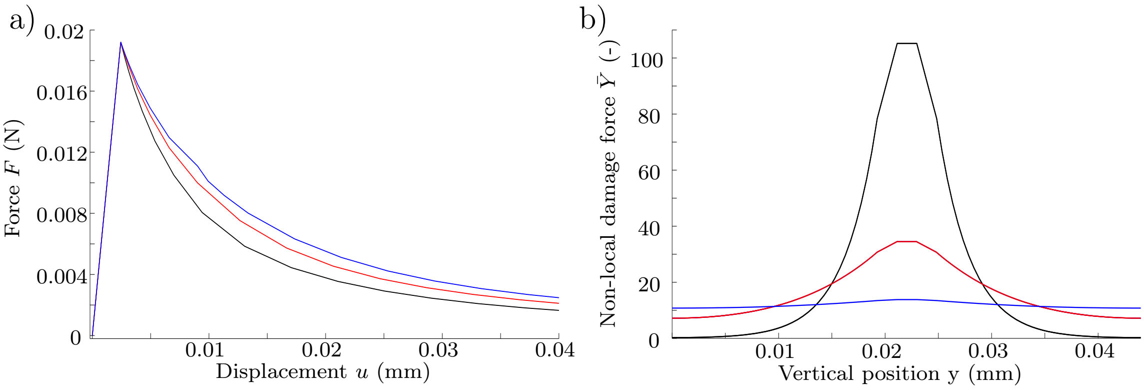

Figure 20: Force displacement curve and distribution of the non-local conjugate damage variable $\bar{Y}$ using the mesh Fig. 18b. The blue, red and black curves have been obtained using the parameters $l^2/2 = 0.1, 0.01$ and 0.001 mm^2 respectively.

7 Implementation

The introduction of damage variables causes the governing equations to become sensitive to the numerical integration scheme. Accurate integration algorithms are therefore required to properly model the softening caused by the damage. In Paper D, a numerical scheme which resembles the radial-return method is adopted to solve the balance of linear momentum and the constitutive equations. This method is also applied in Paper A.

In the reference configuration, Ω_0, the balance of linear momentum can be expressed as

$$R^w(\boldsymbol{u}, \delta\boldsymbol{w}, \boldsymbol{z}, t) = \int_{\partial\Omega_{0t}} \delta\boldsymbol{w} \cdot \boldsymbol{T} dS + \int_{\Omega_0} \delta\boldsymbol{w} \cdot \boldsymbol{b} dV - \int_{\Omega_0} \delta\boldsymbol{E} : \boldsymbol{S} dV = 0 \tag{28}$$

which should be satisfied for all admissible virtual displacements $\delta\boldsymbol{w}$. In (28), $\partial\Omega_{0t}$ denotes the part of the boundary where the traction vector, $\boldsymbol{T}$, is prescribed and the body force vector in the reference configuration is denoted by $\boldsymbol{b}$. The second Piola Kirchhoff stress is given by $\boldsymbol{S}$ and the virtual strain is denoted $\delta\boldsymbol{E}$ and defined as $\delta\boldsymbol{E} = 1/2\left(\delta\boldsymbol{F}^T\boldsymbol{F} + \boldsymbol{F}^T\delta\boldsymbol{F}\right)$. The explicit time dependence present in (28) is due to the applied load and essential boundary conditions are in general time dependent. By collecting the internal variables in a vector $\boldsymbol{z}$, i.e. $\boldsymbol{z} = [\boldsymbol{F}^p, \kappa^{(\nu)}, \phi_1, \phi_2]$, the evolution laws of the internal variables can be expressed as

$$\begin{aligned} &R^w = R^w(\boldsymbol{u}, \delta\boldsymbol{w}, t, \boldsymbol{z}) = 0 \qquad \forall\delta\boldsymbol{w} \\ &\dot{\boldsymbol{z}} = \dot{\lambda}\boldsymbol{N}(\boldsymbol{z}, \boldsymbol{F}) \\ &f(\boldsymbol{z}, \boldsymbol{F}) = 0. \end{aligned} \tag{29}$$

during plastic loading. For elastic response, i.e. $f(\boldsymbol{z}, \boldsymbol{F}) \leq 0$ the system (29) is modified such that $\dot{\lambda} = 0$, i.e. $\dot{\boldsymbol{z}} = \boldsymbol{0}$. The system described in (29) can be interpreted as a Differential Algebraic Equation (DAE) system, where the system consists both of ordinary differential equations (the evolution laws) and algebraic equations (the yield criterion and balance of linear momentum). The system is spatially discretized using the finite element method and temporal discretized with the DIRK-method, where a time interval $[t_n, t_{n+1}]$ is considered and the state of the system is assumed to be known at t_n. The unknowns (i.e. nodal displacements in this work) are computed at certain time points, called stages, denoted by $T_{n1}, T_{n2}, T_{n3}\ldots$ in the time interval. Due to the adopted Runge-Kutta scheme being diagonally implicit, the unknowns can be retrieved by solving an equation system that depends only on the current and previously computed stages. This allows the sparsity of the stiffness matrix from the finite element scheme to be reattained. If a code using the radial return method is at hand, it is then a small task to add an extra loop over the code where the displacements are computed at the stages, $T_{n1}, T_{n2}, ...$ instead of t_{n+1}. Since an embedded Runge-Kutta scheme is adopted, an error estimate is obtained at virtually no extra cost which can be used to control the size of the time step. More details on this topic can be also be found in i.e. Ellsiepen and Hartmann (2001).

Except for Paper A and D, the material model has been implemented in the commercial software Abaqus, using the a user material subroutine UMAT. The subroutine requires the Cauchy stresses and the spatial tangent stiffness matrix, given by

$$\boldsymbol{\mathcal{D}} = J\frac{\partial\boldsymbol{\tau}}{\partial\boldsymbol{F}}\boldsymbol{F}^T \tag{30}$$

as output. The quantity $\frac{\partial\boldsymbol{\tau}}{\partial\boldsymbol{F}}$ has been computed by utilizing that the stress is a function of $\boldsymbol{b}^e, \boldsymbol{m}^{(1)}, \boldsymbol{m}^{(2)}, \boldsymbol{m}^{(3)}$ and $\boldsymbol{z}$ and applying the chain rule. The evolution equations have been discretized using the implicit Euler scheme and the resulting equation system is solved using the Newton-Raphson method. The Jacobian required in the Newton-Raphson scheme has been computed using numerical differentiation in Paper A but in the remaining papers, an analytical format has been derived. Some derivations related to the Jacobian and tangent stiffness matrix is found in Appendix B in Paper B.

8 Future work

Evidently much more work remains to obtain reliable and efficient models of paperboard. To gain more knowledge about the paperboard, full-field measurements could be utilized to greater extent, i.e. X-ray tomographs, ultrasonic measurements, Digital Image Correlations, etc. These techniques could be utilized to carry out in-situ studies of deformation patterns and extract information such as the change of fiber-orientation. These could be important inputs for further development of the model of paperboard.

There are also several effects missing in this model. It is well-known that paperboard is a rate-dependent material and this is important to consider in converting operations. There is in general a desire to make the converting machines run faster. In addition, the influence of moisture and temperature in the mechanical properties should be in included for a complete model of paperboard.

Additional work related to the modeling of damage in paperboard, both in-plane fractures and out-of-plane delamination should be carried out. The CDM-concept can be utilized to a greater extent, i.e. tensor valued damage variables could be introduced and the techniques for the regularization can be improved upon. More investigations using the cohesive zone concept and extended finite elements are interesting to pursue.

The presented continuum model might be too computationally expensive for simulating the actual converting processes that are adopted in the industry. The use of shell elements is an interesting topic which could reduce the computational cost. In addition, investigation of different types of finite elements might be interesting to study in conjunction with the model.

9 Summary of the Papers

Paper A: The thermodynamic framework for the model is established. A polyconvex free energy with a parameter representing the fiber distribution is employed. It is revealed that when the paperboard has been first pre-strained in e.g. CD and then loaded in MD, a softer response is obtained compared to when only loading in MD. Several internal variables are therefore introduced such that the yield surface can harden distortionally in the stress space. It is shown that the softening of a perpendicular pre-strained paperboard can be predicted with the model. Digital Image Correlation (DIC) experiments are performed on a specimen with a central hole. It is shown that despite the heterogenous structure of paperboard, that the continuum approach for modeling the in-plane behavior is able to represent the inhomogeneous strain field from the DIC-measurements.

Paper B: In Paper B, the established framework in Paper A is extended such that the out-of-plane deformations are taken into account by the continuum model. The evolution of the anisotropy is modeled with the use of two in-plane director vectors and an out-of-plane director normal. It is shown that the plastic spin is important to specify and is chosen such that an ideal plastic response in a simple shear situation is recovered. The line creasing operation is modeled and compared to experimental results. The rotation creasing procedure present in the industry is modeled to show the potential applications for the model.

Paper C: The localized deformation developed during in-plane compression and folding of paperboard is studied using the developed continuum model in Paper B. By tuning the in-plane yield parameters to the SCT response, it is shown that the global response in folding can be predicted. The simulations are able to predict the formation of wrinkles and deformation fields that are in agreement with the measured deformation patterns. The model predicts a response associated with localized deformation into bands in both the SCT and folding.

Paper D: The numerical sensitivity of two damage evolution laws and two numerical integration schemes are investigated. An integration scheme based on a Diagonal Implicit Runge-Kutta (DIRK) is investigated. The DIRK scheme is applied to the balance of momentum as well as the constitutive evolution equations. The presented numerical examples reveal that a significant increase in accuracy can be obtained at virtually no extra cost using the DIRK scheme.

Paper E: The continuum model is enhanced using the concept of Continuum Damage Mechanics to model the softening associated with out-of-plane deformations. Two scalar damage variables are introduced for the degradation in out-of-plane tension and shear. The creasing and subsequent folding operations are investigated utilizing the model and compared with measurements.

References

Abaqus User's Manual., 2013. Dassault Systemes. Abaqus Inc. providence, RI, USA, 6.13 edition.

Alexandersson, M., Askfelt, H., Ristinmaa, M., 2016. Triphasic model of heat and moisture transport with internal mass exchange in paperboard. Transport in Porous Media (Submitted).

Ask, A., Ristinmaa, M., 2008. Simulation Model for anisotropic fibrous materials. Proceedings in Applied Mathematics and Mechanics 8, 10399–10400.

Beex, L., Peerlings, R., Geers, M., 2014. A multiscale quasicontinuum method for lattice models with bond failure and sliding. Comput. Methods Appl. Mech. Engrg 269, 108–122.

Beex, L. A. A., Peerlings, R. H. J., 2009. An experimental and computational study of laminated paperboard creasing and folding. International Journal of Solids and Structures 46, 4192–4207.

Borodulina, S., Kulachenko, A., Galland, S., Nygårds, M., 2012. Stress-strain curve of paper revisted. Nordic Pulp and Paper Research Journal 27, 318–328.

Bosco, E., Peerlings, R. H., Geers, M. G., 2015. Predicting hygro-elastic properties of paper sheets based on an idealized model of the underlying fibrous network. International Journal of Solids and Structures 56-57, 43–52.

Cavlin, S., 1988. The unique Convertibility of Paperboard. Packaging Technology and Science 10, 77–92.

Chaboche, J.-L., 1981. Continous damage mechanics - a tool to describe phenomena before crack initiation. Nuclear Engineering and Design 64, 233–247.

Ciarlet, P. G., 1988. Mathematical Elasticity. Elsevier Science Publishers B.V.

Dafalias, Y. F., 1998. Plastic spin: necessity or redundancy? International Journal of Plasticity 04, 909–931.

Ellsiepen, P., Hartmann, S., 2001. Remarks on the interpretation of current non-linear finite element analyses as differential equations. International Journal for Numerical Methods in Engineering 51, 679–707.

Giampieri, A., Perego, U., Borsari, R., 2011. A constitutive model for the mechanical response of the folding of creased paperboard. International Journal of Solids and Structures 48, 2275–2287.

Håkansson, O., 2014. Experimental study and analysis of out-of-plane shear of paperboard. Master's thesis, Lund Institute of Technology.

Harrysson, A., Ristinmaa, M., 2008. Large strain elasto-plastic model of paper and corrugated board. International Journal of Solids and Structures 45, 3334–3352.

Harrysson, M., Ristinmaa, M., 2007. Description of evolving anisotropy at large strains. Mechanics of Materials 39, 267–282.

Hill, R., 1948. A theory of the yielding and plastic flow of anisotropic materials. Proceedings of the Royal Society of London A193, 281–297.

Holzapfel, G. A., 2000. Nonlinear solid mechanics, a continuum approach for engineering. John Wiley & Sons Ltd.

Huang, H., Hagman, A., Nygårds, M., 2014. Quasi static analysis of creasing and folding for three paperboards. Mechanics of Materials 69, 11–34.

Huang, H., Nygårds, M., 2010. A simplified material model for finite element analysis of paperboard creasing. Nordic Pulp & Paper Research Journal 25, 505–512.

Isaksson, P., Hägglund, R., Gradin, P., 2004. Continuum damage mechanics applied to paper. International Journal of Solids and Structures 41, 4731–4755.

Jirasek, M., 1998. Nonlocal models for damage and fracture: comparision of approaches. International Journal of Solids and Structures 35, 4133–4145.

Kachanov, L. M., 1958. Rupture time under creep conditions. Izv. Akad. Nauks SSSR Otd. Tech. Nauk 8, 26–31 (In russian). English translation: *Rupture time under creep conditions*. International Journal of Fracture, Vol. 97, No 1–4 , pp. xi–xviii, 1999.

Kulachenko, A., 2012. Direct simulations of fiber network deformation and failure. Mechanics of Materials 51, 1–14.

Lindström, T., 2013. In-plane paperboard model. Master's thesis, Lund Institute of Technology.

Mäkelä, P., 2002. On the fracture mechanics of paper. Nordic Pulp and Paper Research Journal 17, 254–274.

Mäkelä, P., Östlund, S., 2003. Orthotropic elastic-plastic material model for paper materials. International Journal of Solids and Structures 40, 5599–5620.

Mäkelä, P., Östlund, S., 2012. Cohesive crack modelling of thin sheet material exhibiting anisotropy, plasticity and large-scale damage evolution. Engineering Fracture Mechanics 79, 50–60.

Nagasawa, S., Fukuzawa, Y., Yamaguchi, T., Tsukatani, S., Katayama, I., 2003. Effect of crease depth and crease deviation on folding deformation characteristics of coated paperboard. Journal of Materials Processing Technology 140, 157–162.

Niskanen, K., 2012. Mechanics of paper products, Chapter 2. De Gruyter.

Nygårds, M., Just, M., Tryding, J., 2009. Experimental and numerical studies of creasing of paperboard. International Journal of Solids and Structures 46, 2493–2505.

Ottosen, N., Ristinmaa, M., 2005. The mechanics of constitutive modeling, First Edition. Elsevier.

Pagania, M., Perego, U., 2015. Explicit dynamics simulation of blade cutting of thin elastoplastic shells using "directional" cohesive elements in solid-shell finite element models. Computer Methods in applied mechanics and engineering 285, 515–541.

Peerlings, R., de Borst, R., Brekelmans, W., de Vree, J., 1996. Gradient enhanced damage for quasi-brittle materials. Internation Journal for Numerical Methods in Engineering 39, 3391–3403.

Pijaudier-Cabot, G., Bažant, Z., 1987. Nonlocal damage theory. Journal of Engineering Mechanics 113, 1512–1533.

Stenberg, N., 2002. On the Out-of-Plane Mechanical Behaviour of Paper Materials. Ph.D. thesis, Department of Solid Mechanics, Royal Institute of Technology, Stockholm, Sweden.

Strömberg, L., Ristinmaa, M., 1996. FE-formulation of a nonlocal plasticity theory. Comput. Methods Appl. Mech. Engng. 136, 127–144.

Tayeh, R., 2015. Determination of the out-of-plane shear properteis of paperboard. Master's thesis, Lund Institute of Technology.

Tjahjanto, D., Girlanda, O., Östlund, S., 2015. Anisotropic viscoelastic-viscoplastic continuum model for high-density cellulose-based materials. Journal of the Mechanics and Physics of Solids 84, 1–20.

Tryding, J., Gustafsson, P., 2001. Analysis of notched newsprint sheet in mode i fracture. Journal of Pulp and Paper Science 27, 103–109.

Vojskovic, D., 2015. In-plane facture analysis of paperboard using xfem. Master's thesis, Lund Institute of Technology.

Xia, Q. S., 2002. Mechanics of inelastic deformation and delamination in paperboard. Ph.D. thesis, Massachusetts Institue of Technology.

Xia, Q. S., Boyce, M. C., Parks, D. M., 2002. A constitutive model for the anisotropic elastic-plastic deformation of paper and paperboard. International Journal of Solids and Structures 39, 4053–4071.

Paper A

Eric Borgqvist, Tommy Lindström, Johan Tryding,
Mathias Wallin and Matti Ristinmaa

Distortional hardening plasticity model for paperboard

International Journal of Solids and Structures 51 (2014), 2411-2423

Distortional hardening plasticity model for paperboard

Eric Borgqvist, Tommy Lindström, Johan Tryding,
Mathias Wallin and Matti Ristinmaa
Division of Solid Mechanics
Lund University, Box 118, S-221 00 Lund, Sweden

Abstract

A distortional hardening elasto-plastic model at finite strains suitable for modeling of orthotropic materials is presented. As a prototype material, paperboard is considered. An in-plane model is established. The model developed is motivated from non-proportional loading tests on paperboard where the paperboard is pre-strained in one direction and then loaded in the perpendicular direction. A softening effect is revealed in the pre-strained samples. The observed experimental findings can not be accurately predicted by current models for paperboard. To be able to model the softening effects, a yield surface based on multiple hardening variables is introduced. It is shown that the model parameters can be obtained from simple uniaxial experiments. The model is implemented in a finite element framework which is used to illustrate the behavior of the model at some specific loading situations and is compared with strain fields obtained from Digital Image Correlation experiments.

1 Introduction

Continuum-based constitutive models provide the macroscopic observable properties, e.g. force and stretch, resulting from the average behavior of the micro-structure. In this work, an anisotropic continuum-based material model suitable for fibrous materials is considered. Here focus is on paperboard materials, but the developed model can be used for a range of orthotropic materials. Paperboard is a heterogeneous material, where the heterogeneity stems from the manufacturing process where cellulose fibers placed on a traversing web are dried and pressed. The inhomogeneity and directional material dependence is due to the distribution and uneven drying of the fibers.

Modeling of paperboard is an active research area driven by the industry to improve converting and filling processes. In industrial converting operations, the paperboard experience complex load histories. To accurately predict the material behavior during converting operations is a challenging task. One important converting operation is the creasing process, which has been studied by several authors, and is critical for obtaining well formed liquid filled packages without defects. The creasing operation reduces the maximal bending moment and the deeper the scored line is creased, the more the maximal bending moment is reduced, cf. Cavlin (1988), Cavlin et al. (1997) and Nagasawa et al. (2003). The crease depth is limited by the occurrence of in-plane surface cracks. Modeling of the in-plane fracture process in paperboard has been based on cohesive crack mechanisms in Tryding and Gustafsson (2001), Mäkelä and Östlund (2012) and by continuum damage in Isaksson et al. (2004). During creasing the paperboard is stretched in one direction and then unloaded. In the subsequent forming process, the paperboard is stretched again, however in a direction perpendicular to the previous stretching direction. To evaluate the effect of non-proportional loading, simple non-proportional tests has been conducted on paperboard in the work herein.

Paperboard is classically characterized as an orthotropic material. The orthotropic directions are the Machine Direction (MD), Cross-machine Direction (CD) and out-of-plane direction (ZD), cf. Fig. 1. The MD and CD are referred to as the in-plane directions. The magnitude of the material properties in the MD direction are typically about 2-3 times larger compared with CD and about 100 times larger compared with ZD, cf. Stenberg (2002).

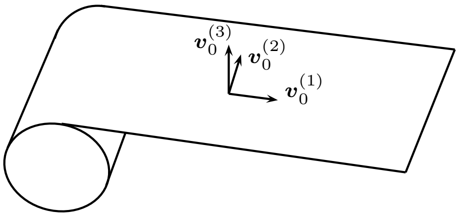

Figure 1: Illustration of the different material directions of paperboard due to the manufacturing process. The director vectors are aligned with the Machine(1)-, Cross(2)- and ZD(3)-directions.

It has previously been demonstrated that continuum based approaches are able to represent the mechanical response of paperboard, cf. Xia et al. (2002), Harrysson and Ristinmaa (2008) and Mäkelä and Östlund (2003). It has been observed by e.g. Harrysson and Ristinmaa (2008), that after unloading from the non-linear region, non-recoverable strains are obtained, and therefore the use of plasticity theory is motivated. Since the paperboard is highly anisotropic, the constitutive model is inevitable required to be anisotropic. Moreover, large rotations and relatively large strains are present in industrial applications such as creasing and forming.

A number of anisotropic models are based on the Hill (1948) criterion with proportional expansion of the yield surface cf. Huang and Nygårds (2010). Another well established yield surface for paperboard is the Tsai-Wu surface, cf. Tsai and Wu (1971) which also takes into account that the yielding in compression and tension differs. Accurate fit to uniaxial tests is usually obtained for these models, but investigations on how the actual yield surface develops in the stress space is usually not compared to experimental evidence. The experimental tests in this work reveals that the yield surface does not harden proportionally and therefore non-proportional hardening models are of importance for paperboard.

In Xia (2002), a continuum elasto-plastic model in combination with interfaces were used to model the creasing operation. This concept has been further studied in Huang and Nygårds (2010), Nygårds et al. (2009), Beex and Peerlings (2009) and Giampieri et al. (2011). The elasto-plastic model in this work is based upon the model in Xia et al. (2002) which is enhanced such that the laws of thermodynamics are fulfilled. The yield surface in Xia et al. (2002), is based upon the introduction of a set of subsurfaces in the stress-space. In this work, one internal variable is introduced for each subsurface. This is in contrast to the model by Xia et al. (2002) where only the effective plastic strain governs the hardening of all sub-surfaces. The concept of one internal variable to each subsurface allows for an anisotropic hardening of the yield surface, which is also known as distortion hardening. The derived model will allow non-proportional load histories to be taken into account, e.g. where the paperboard is stretched and unloaded in different directions. It is shown that the generalization of the yield criterion in Xia et al. (2002) to include distortion hardening can be made naturally in the thermodynamic framework. It is also shown that a calibration of the model parameters can be made using standard uniaxial tests.

To illustrate the predictive capabilities of the proposed model, the paperboard has been loaded at different angles in the plane, and also been compared with full-field measurements in two separate loading situations. The full field measurements have been obtained using Digital Image Correlation (DIC) equipment. DIC-measurements on paperboard have the potential to increase the understanding of the mechanisms present during loading of paperboard, cf. Hagman and Nygårds (2012) for a recent contribution on the topic. As a particular load situation, a paperboard with a central hole has been considered in this work. The load has been applied parallel to both the MD and CD directions of the paperboard. The strain fields have been extracted from DIC-measurements and compared with simulation results using the derived material model.

The article is organized as follows, in section 2 the experimental evidence on non-proportional tests is presented, section 3 and 4 deals with the kinematic and thermodynamic considerations, where tensors will be considered in a Cartesian setting, i.e. following the work of Ciarlet (1988). Taking into account that the first and second laws of thermodynamics should be fulfilled, physical sound models and constitutive relations is developed. Section 5 presents the specific model and in section 6 the calibration from uniaxial experiments is presented. In section 7 and 8, results and comparisions from uniaxial tests and DIC experiments are shown.

2 Experimental Evidences

Non-proportional loading situations are present in many industrial process steps related to paperboard converting. To the authors knowledge, there is a lack of experimental results reported in the literature especially for non-proportional load situations of paperboard. As the present work is aimed to predict non-proportional hardening effects, non-proportional experimental test will be presented below.

A schematic illustration of the testing procedure of pre-straining the paperboard and then the subsequent uniaxial test is shown in Fig. 2. The large test sample is pre-strained (CD/MD) until failure, which corresponded to an average strain of: 6.5 % in CD and 3.1 % in MD. Several specimen are then cut out and loaded in the direction perpendicular to the original loading direction.

The pre-straining was done with a standard MTS-tensile test machine with a 160 mm wide paperboard and 145 mm clamped length. All the tests have been performed in a climate chamber with 50 % moisture content and at room temperature 23^{o}C. The uniaxial tension tests were performed with the Th1 tensile tester (Lorentzon & Wettre Alwetron), which follows ISO 1924-3 standard, using w_0 = 15 mm wide paper and a clamped length of L_0 = 100 mm. The strain rate was 1.65 %/s. The initial thickness, t_0, of the samples was determined to t_0 = 0.38 mm. Sixteen uniaxial tension tests have been conducted in each direction for the pre-strained and non-prestrained samples.

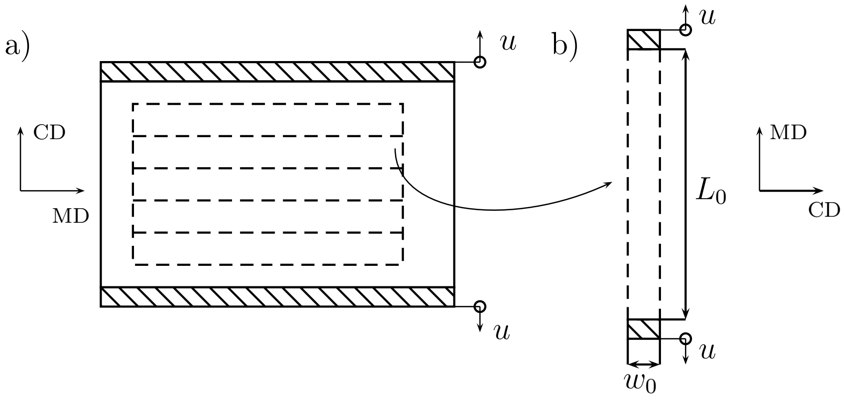

Figure 2: Illustration of the loading sequence. a) Uniaxial pre-straining of a larger test-piece in CD. b) Uniaxial loading of sample in the orthogonal direction to the pre-straining direction in MD.

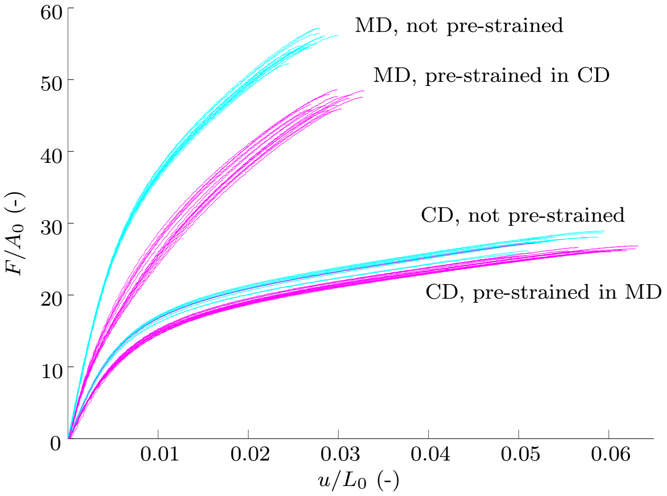

Figure 3: Uniaxial stress-strain curves in CD and MD. Light blue color is used for the experimental data obtained from samples that were not pre-strained and purple color is used for the pre-strained samples. Normalized force vs normalized displacement has been plotted, where A_0 is the initial cross section area and L_0 is the initial length.

The experimental results are shown in Fig. 3, both for the situation without pre-straining and when the samples were pre-strained. For the uniaxial MD and CD tests after pre-straining, a reduction in stiffness is observed as well as reduction in the hardening. The reduction of stiffness is approximately 25% for the MD-direction and 13% in CD. It is observed that pre-straining in MD changes the uniaxial stress-strain response in CD to a lesser extent compared with pre-straining in CD, which influences the MD response significantly. The effect of softening as shown in Fig. 3 is not well known in the literature. It should also be noted, that the thickness has been shown to remain almost constant during in-plane loading for several paperboard materials, cf. Stenberg (2002). Therefore a decoupling of the material response between the in-plane and the out-of-plane directions is assumed, i.e. zero Poisson's ratio.

The effect of non-proportional loading, as described above, can not accurately be captured by elasto-plasticity using a single internal variable (often the effective plastic strain), cf. Xia et al. (2002), Mäkelä and Östlund (2003). Orthotropic elasto-plastic models with a single internal variable, will overestimate the stress-strain response for samples that have been pre-strained in a perpendicular direction to the load direction. The overestimation stems from the fact that a single internal variable leads to an expansion of the yield surface and therefore an increased yield stress will be obtained upon reloading in a perpendicular direction. An attempt to simulate the pre-straining behavior using a standard orthotropic-elastic-plastic model with a Hill surface and isotropic hardening, cf. Abaqus (2012), is shown in. Fig 4.

The Hill-model clearly overestimates the response in MD for the pre-strained samples in CD. The experimental evidence shows a decreased yield stress for the pre-strained samples, whereas the Hill-model predicts an increased yield stress. Based on the experimental obser-

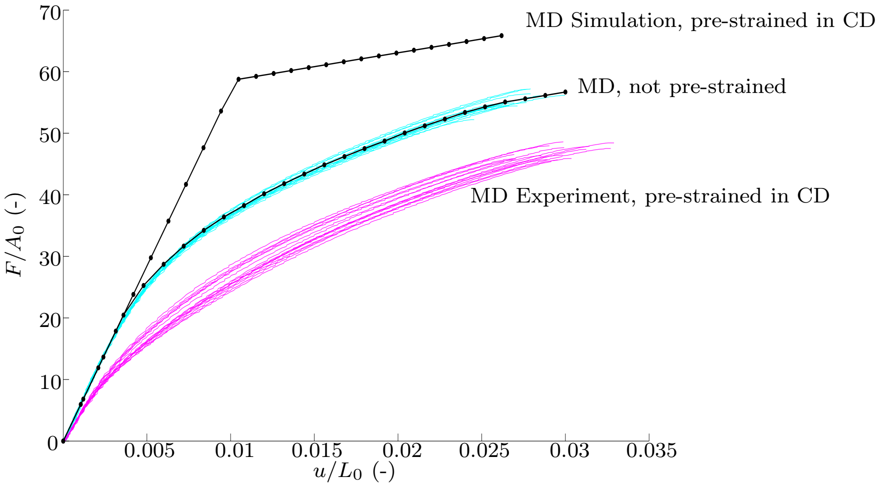

Figure 4: Uniaxial stress-strain curves in and MD together with simulation using a standard Hill-model with isotropic hardening. Light blue color is used for the experimental data obtained from samples that were not pre-strained and purple color is used for the pre-strained samples. Black color is used for the simulations. Normalized force vs normalized displacement has been plotted, where A_0 is the initial cross section area and L_0 is the initial length.

vations in Fig. 3, we propose a model in which the yield surface hardens non-isotropically in the stress-space. This effect is accomplished via the introduction of several internal variables, i.e. a form of distortion hardening. To reduce the complexity of the model, the reduction in elastic stiffness visible in the experimental tests will not be considered here.

Another approach for modeling the pre-straining is to use kinematic hardening for the evolution of the yield surface. Kinematic hardening has however not been considered here, but can also be introduced in the framework.

3 Kinematics

Consider a material body in the reference configuration $\Omega_0 \in \mathbb{R}^3$ at the time instance t_0 and at the deformed configuration $\Omega \in \mathbb{R}^3$ at time instance t. The non-linear map that defines the motion is given by $\boldsymbol{\varphi}(\boldsymbol{X}, t) : \Omega_0 \times T \rightarrow \Omega$, in the time interval $T \in [t_0, t]$ and where $\boldsymbol{X}$ denotes the position of a particle in the reference configuration and the position of the same particle in the current configuration is found as $\boldsymbol{x} = \boldsymbol{\varphi}(\boldsymbol{X}, t)$. The mapping of vectors in the reference configuration to the current configuration is given by the deformation gradient $\boldsymbol{F} = \dfrac{\partial \boldsymbol{\varphi}}{\partial \boldsymbol{X}}$. To model elasto-plasticity a multiplicative split of the deformation gradient into an elastic and a plastic part is assumed, i.e.

$$\boldsymbol{F} = \boldsymbol{F}^e \boldsymbol{F}^p, \tag{1}$$

where $\boldsymbol{F}^e$ and $\boldsymbol{F}^p$ are the elastic- and plastic-deformation gradients, respectively. The spatial velocity gradient defined as, $\boldsymbol{l} = \dot{\boldsymbol{F}}\boldsymbol{F}^{-1}$ can be additively be split into

$$\boldsymbol{l} = \boldsymbol{l}^e + \boldsymbol{F}^e\boldsymbol{L}^p\boldsymbol{F}^{e-1} = \boldsymbol{l}^e + \boldsymbol{l}^p, \tag{2}$$

where

$$\boldsymbol{l}^e = \dot{\boldsymbol{F}}^e\boldsymbol{F}^{e-1}, \qquad \boldsymbol{L}^p = \dot{\boldsymbol{F}}^p\boldsymbol{F}^{p-1}, \tag{3}$$

are referred to as the elastic and plastic velocity gradients. Further on, the polar decomposition of $\boldsymbol{F}^e$ will be exploited and is given by

$$\boldsymbol{F}^e = \boldsymbol{V}^e\boldsymbol{R}^e, \tag{4}$$

where $\boldsymbol{R}^e$ is the orthogonal elastic rotation tensor and $\boldsymbol{V}^e$ is the symmetric positive definite left elastic stretch tensor. The elastic Finger tensor, $\boldsymbol{b}^e$ is given by

$$\boldsymbol{b}^e = \boldsymbol{F}^e(\boldsymbol{F}^e)^T, \tag{5}$$

and will be used in the constitutive model. By using (2) and (5) the material time derivative of $\boldsymbol{b}^e$ can be expressed as

$$\dot{\boldsymbol{b}}^e = 2\text{sym}(\boldsymbol{l}\boldsymbol{b}^e) - 2\text{sym}(\boldsymbol{l}^p\boldsymbol{b}^e), \tag{6}$$

where sym([·]) denotes the symmetric part of [·].

The modeling framework for orthotropy will follow that outlined in Harrysson et al. (2007) and Harrysson and Ristinmaa (2007). To model orthotropy, a set of director vectors,($\boldsymbol{v}_0^{(\alpha)}, \alpha = \{1, 2, 3\}$), which are aligned with the MD, CD and ZD directions and of unit length in the reference configuration are introduced. In this work, it is postulated that the director vectors evolve with the elastic rotation (see also Ask and Ristinmaa (2008)) , i.e.

$$\boldsymbol{v}^{(\alpha)} = \boldsymbol{R}^e\boldsymbol{v}_0^{(\alpha)}, \tag{7}$$

where $\boldsymbol{v}^{(\alpha)}$ is the director vector in the spatial configuration. The choice (7), will ensure that the director vectors will remain at unit length and orthogonal to each other during deformation. Note that in contrast to Harrysson and Ristinmaa (2007), the evolution of the director vectors are postulated in a total format instead of an incremental evolution.

A set of second order structural tensors defined as a dyadic product of the director vectors are introduced as

$$\boldsymbol{m}^{(\alpha)} = \boldsymbol{v}^{(\alpha)} \otimes \boldsymbol{v}^{(\alpha)}, \quad \boldsymbol{m}_0^{(\alpha)} = \boldsymbol{v}_0^{(\alpha)} \otimes \boldsymbol{v}_0^{(\alpha)}. \tag{8}$$

The structural tensors, $\boldsymbol{m}^{(\alpha)}$, will be used to derive the free energy potential introduced in the next section. Using the symmetry of $\boldsymbol{m}^{(\alpha)}$ along with (7) allows the material time derivative of the structural tensors to be expressed as

$$\dot{\boldsymbol{m}}^{(\alpha)} = 2\text{sym}(\boldsymbol{\Omega}^e\boldsymbol{m}^{(\alpha)}), \tag{9}$$

where

$$\boldsymbol{\Omega}^e \;= \dot{\boldsymbol{R}}^e \boldsymbol{R}^{eT}, \tag{10}$$

was defined. The material time derivative of the elastic rotation tensor is found from the polar decomposition of $\boldsymbol{F}^e$. Differentiation of (4) and making use of (2) results in

$$\dot{\boldsymbol{R}}^e = \boldsymbol{V}^{e-1}(\boldsymbol{l}^e \boldsymbol{F}^e - \dot{\boldsymbol{V}}^e \boldsymbol{R}^e). \tag{11}$$

The elastic stretch tensor can be written as $\boldsymbol{V}^e = \sqrt{\boldsymbol{b}^e}$ and the time derivative of $\boldsymbol{V}^e$ can be expressed as

$$\dot{\boldsymbol{V}}^e = \frac{\partial \sqrt{\boldsymbol{b}^e}}{\partial \boldsymbol{b}^e} \dot{\boldsymbol{b}}^e = \mathbb{H}^e \dot{\boldsymbol{b}}^e. \tag{12}$$

The fourth order tensor $\mathbb{H}^e$ can be computed by taking advantage of the spectral decomposition theorem, cf. Miehe (1998). In this work however, $\sqrt{\boldsymbol{b}^e}$ is computed numerically with the Denman-Beaver square root iteration scheme, cf. Denman and Beavers (1976). The fourth order tensor $\mathbb{H}^e$ is determined by first computing $\sqrt{\boldsymbol{b}^e}$ with the Denman-Beaver scheme, followed by an analytical differentiation.

Furthermore for later purposes, the spin $\boldsymbol{\Omega}^e$ will be expressed in terms of $\boldsymbol{l}$ and $\boldsymbol{l}^p$. By using (11), (12) and (6) in (10), the tensor $\boldsymbol{\Omega}^e$ can be rewritten as

$$\boldsymbol{\Omega}^e \;=\; \boldsymbol{V}^{e-1}(\boldsymbol{l} - \boldsymbol{l}^p)\boldsymbol{V}^e - 2\boldsymbol{V}^{e-1}\mathbb{H}^e : (\mathrm{sym}(\boldsymbol{l}\boldsymbol{b}^e) - \mathrm{sym}(\boldsymbol{l}^p\boldsymbol{b}^e))\,. \tag{13}$$

The stress-strain relation will now be derived on the basis of thermodynamical arguments.

4 Thermodynamic considerations

Although the model is primarily intended for isothermal situations, it should fulfill the laws of thermodynamics. Ignoring the effects of temperature, the dissipation inequality in the spatial setting is defined as

$$d = \boldsymbol{\tau} : \boldsymbol{d} - \rho_0 \dot{\psi} \geq 0, \tag{14}$$

where $\boldsymbol{d}$ is the symmetric part of the spatial velocity gradient, $\boldsymbol{\tau}$ is the Kirchhoff stress tensor and ψ is the Helmholz free energy. The free energy is assumed to be a function of the elastic Finger tensor, $\boldsymbol{b}^e$, the structural tensors, $\boldsymbol{m}^{(\alpha)}$, and a set of internal variables, $\kappa^{(\gamma)}$, which accounts for irreversible effects, i.e. $\rho_0\psi = \rho_0\psi(\boldsymbol{b}^e, \boldsymbol{m}^{(\alpha)}, \kappa^{(\gamma)})$. The dissipation inequality then takes the form

$$d = \boldsymbol{\tau} : \boldsymbol{d} - \rho_0 \frac{\partial \psi}{\partial \boldsymbol{b}^e} : \dot{\boldsymbol{b}}^e - \rho_0 \frac{\partial \psi}{\partial \boldsymbol{m}^{(\alpha)}} : \dot{\boldsymbol{m}}^{(\alpha)} - \rho_0 \frac{\partial \psi}{\partial \kappa^{(\gamma)}} \dot{\kappa}^{(\gamma)} \geq 0. \tag{15}$$

The superscripts α and γ in the expression above should be interpreted as a summation over the indices. Using the time derivative of the elastic Finger tensor (6) and the structural tensors (9), we arrive at

$$d = \left(\boldsymbol{\tau} - 2\rho_0 \frac{\partial \psi}{\partial \boldsymbol{b}^e} \boldsymbol{b}^e\right) : \boldsymbol{d} + \left(2\rho_0 \frac{\partial \psi}{\partial \boldsymbol{b}^e} \boldsymbol{b}^e\right) : \boldsymbol{d}^p - \left(2\rho_0 \frac{\partial \psi}{\partial \boldsymbol{m}^{(\alpha)}} \boldsymbol{m}^{(\alpha)}\right) : \boldsymbol{\Omega}^e - \rho_0 \frac{\partial \psi}{\partial \kappa^{(\gamma)}} \dot{\kappa}^{(\gamma)}, \tag{16}$$

where $\boldsymbol{d}^p$ is the symmetric part of the spatial plastic velocity gradient, $\boldsymbol{l}^p$. Inserting (13) in the dissipation inequality (16) and by making use of Coleman's arguments Coleman and Gurtin (1967) the constitutive relation for the Kirchhoff stress tensor becomes,

$$\boldsymbol{\tau} = 2\rho_0 \left(\frac{\partial \psi}{\partial \boldsymbol{b}^e} \boldsymbol{b}^e + \boldsymbol{V}^{e-1} \left(\frac{\partial \psi}{\partial \boldsymbol{m}^{(\alpha)}} \boldsymbol{m}^{(\alpha)}\right) \boldsymbol{V}^e - \left(2\boldsymbol{V}^{e-1} \frac{\partial \psi}{\partial \boldsymbol{m}^{(\alpha)}} \boldsymbol{m}^{(\alpha)}\right) : (\mathbb{H}^e \cdot \boldsymbol{b}^e)\right) \tag{17}$$

The Kirchhoff stress tensor (17) is symmetric, since the Helmholz free energy is assumed to be an isotropic function of its arguments, cf. Harrysson and Ristinmaa (2007) and Menzel and Steinmann (2003). The remaining part of the dissipation inequality is given as,

$$d = \boldsymbol{\tau} : \boldsymbol{d}^p - K^{(\gamma)} \dot{\kappa}^{(\gamma)} \geq 0, \tag{18}$$

where the energy conjugates to the internal variables was defined as

$$K^{(\gamma)} = \rho_0 \frac{\partial \psi}{\partial \kappa^{(\gamma)}}. \tag{19}$$

The specific model will be discussed next.

5 The constitutive model

5.1 Elasticity

The out-of-plane response is assumed to be decoupled from the in-plane response, and as a consequence only one structural tensor is needed to capture the in-plane behavior. Decoupling of the out-of-plane has been verified to be an accurate approximation for paperboard and used by several authors, cf. Stenberg (2002), Nygårds et al. (2009). Only the in-plane model will be considered here. The Helmholz free energy is assumed to be split into an elastic and a plastic part,

$$\rho_0 \psi = \rho_0 \psi^e(\boldsymbol{b}^e, \boldsymbol{m}^{(1)}) + \rho_0 \psi^p(\kappa^{(\gamma)}). \tag{20}$$

In the Helmholz free energy, a general structural tensor for transverse isotropy will be utilized. It is defined as

$$\boldsymbol{m} = p\boldsymbol{m}^{(1)} + q(\boldsymbol{I} - \boldsymbol{m}^{(1)}), \tag{21}$$

where $\boldsymbol{I}$ is the second order identity tensor and p and q are material parameters. Note that $\boldsymbol{m}$ can not be written as a dyadic product of a vector, however it can be Cholesky decomposed as $\boldsymbol{m} = \boldsymbol{H}^T\boldsymbol{H}$, where $\boldsymbol{H}$ is a lower triangular matrix of a general structural tensor $\boldsymbol{m}$.

If the aditional requirement $p + 2q = 1$ is imposed i.e. $\mathrm{tr}(\boldsymbol{m}_0) = 1$, then it can be possible to relate q to a fiber distribution function with a normalizing condition, cf. Gasser et al. (2006). It turns out that enforcing $p + 2q = 1$ for the paperboard, that has been considered here, will give an accurate fit to experimental material data. See also Wahlström (2009) for a more thorough discussion on fiber distribution of paperboard.

A list of specific free energies that automatically fulfills stress-free reference configuration is given in Schröder et al. (2008). The free energy for the paperboard material has been chosen according to

$$\rho_0\psi^e = A\left(\frac{1}{(\alpha+1)(p+2q)^\alpha}(I_1^e)^{(\alpha+1)} + I_2^e - (p+2q)J\right), \tag{22}$$

where A and α a constitutive parameters. The strain invariants in (22) are defined as,

$$\begin{aligned} I_1^e &= \mathrm{tr}(\boldsymbol{b}^e\boldsymbol{m}) \\ I_2^e &= J^2\mathrm{tr}(\boldsymbol{b}^{e-1}\boldsymbol{m}) \\ J &= \sqrt{\det(\boldsymbol{b}^e)}. \end{aligned} \tag{23}$$

Polyconvexity implies that the free energy is a convex function in the arguments $\{\boldsymbol{F}^e, \mathrm{cof}(\boldsymbol{F}^e), \det(\boldsymbol{F}^e)\}$, where $\mathrm{cof}(\cdot)$ is defined by $\mathrm{cof}(\boldsymbol{F}^e) = \det(\boldsymbol{F}^e)\boldsymbol{F}^{e-T}$. Polyconvexity together with the growth criterion guaranties the existence of at least one minimizer to the functional of the elastic boundary value problem, cf. Ball (1977). Since the second derivative of J with respect to J is zero, it is concluded that J is convex. The invariants I_1^e, I_2^e can be split into terms involving the director vectors see Appendix A and then the proof found in Schröder and Neff (2002) can be used when $p - q > 0$. Alternatively the proof in Schröder et al. (2008) can be used, cf. also Ebbing (2010) for an extensive review of polyconvexity using crystallographic structural tensors and the Cholesky decomposition. Given that A, α, p and q are positive quantities, it is then concluded that (22) is a polyconvex free energy potential.

5.2 Plasticity

Many models are able to accurately predict the proportional stress-strain response for paperboard, whereas the predictive capability for non-proportional test are less accurate. Therefore a yield surface which hardens non-isotropically will be employed. Following the work in Xia et al. (2002), a set of yield sub-surface tensors $\boldsymbol{n}^{(\nu)}$, which are normals to the yield planes, are introduced. For this purpose a set of dyadic products defined by the director vectors are introduced as,

$$\boldsymbol{n}^{(\nu)} = n_{11}^{(\nu)}\boldsymbol{v}^{(1)} \otimes \boldsymbol{v}^{(1)} + n_{22}^{(\nu)}\boldsymbol{v}^{(2)} \otimes \boldsymbol{v}^{(2)} + n_{12}^{(\nu)}(\boldsymbol{v}^{(1)} \otimes \boldsymbol{v}^{(2)} + \boldsymbol{v}^{(2)} \otimes \boldsymbol{v}^{(1)}), \tag{24}$$

where $n_{11}^{(\nu)}, n_{22}^{(\nu)}$ and $n_{12}^{(\nu)}$ are constants. Six tensors, $\boldsymbol{n}^{(v)}$, are introduced in the model, each associated to a yield plane. The yield planes are associated to the following stress states (in order from 1 to 6): MD tension, CD tension, positive oriented shear, MD compression, CD compression and negative oriented shear.

The conjugate variables, $K^{(\nu)}$, in (19), will be used as a measure of the distance in the stress-space, which a yield plane is translated. The plastic part of the free energy is postulated to be

$$\rho_0 \psi^p = \sum_{\beta=1}^{6} \frac{a_\beta}{b_\beta} \Big((b_\beta \kappa^{(\beta)} + 1) \ln (b_\beta \kappa^{(\beta)} + 1) - b_\beta \kappa^{(\beta)} \Big). \tag{25}$$

Using (19), the conjugate quantities then takes the following form

$$K^{(\nu)} = a_\nu \ln (b_\nu \kappa^{(\nu)} + 1). \tag{26}$$

Note that according to the decoupling present in (25), each hardening variable $K^{(\nu)}$ is associated with one internal variable, $\kappa^{(\nu)}$. To allow for modeling of the non-proportional loading behavior revealed in the experimental tests, the yield surface proposed in Xia et al. (2002) will be enhanced. The enhanced part is related to the hardening behavior. The yield function is given as

$$f(\boldsymbol{\tau}, \boldsymbol{n}^{(\beta)}, K^{(\beta)}) = \sum_{\nu=1}^{6} \chi^{(\nu)} \left(\frac{\boldsymbol{\tau} : \boldsymbol{n}^{(\nu)}}{\tau^{(\nu)}} \right)^{2k} - 1, \tag{27}$$

where the stress $\tau^{(\nu)}$ is defined as

$$\tau^{(\nu)} = K_0^{(\nu)} + \sum_{\gamma=1}^{6} \omega_{\nu\gamma} K^{(\gamma)}. \tag{28}$$

In (27), k is a constant natural number and $\chi^{(\nu)}$ is a switch function, which determines if a yield plane is active for the current stress state and is defined as

$$\chi^{(\nu)} = \begin{cases} 1 & \text{if} \quad \boldsymbol{\tau} : \boldsymbol{n}^{(\nu)} > 0 \\ 0 & \quad \text{otherwise.} \end{cases} \tag{29}$$

The quantity $\omega_{\nu\gamma}$ in (28) defines a constant positive-definite matrix and it introduces a coupling between the hardening of the six different sub-yield surfaces, allowing for non-isotropic hardening. This will enable the model to capture the experimental observed behaviour shown in Fig. 3. Note that if $\omega_{\nu\gamma}$ is chosen as the identity matrix, then the yield surface proposed in Xia et al. (2002) is retained. The yield surface for the situation when $\boldsymbol{\tau}_{12} = 0$ is illustrated in Fig. 5.

The yield surface in Fig. 5 illustrates four yield plane gradients defined by the normals $\boldsymbol{n}^{(1)}, \boldsymbol{n}^{(2)}, \boldsymbol{n}^{(4)}$ and $\boldsymbol{n}^{(5)}$ together with a graphical interpretation of $\tau^{(1)}, \tau^{(2)}, \tau^{(4)}$ and $\tau^{(5)}$, i.e. the shortest distance to each yield plane from the origin. Increasing the exponent k in

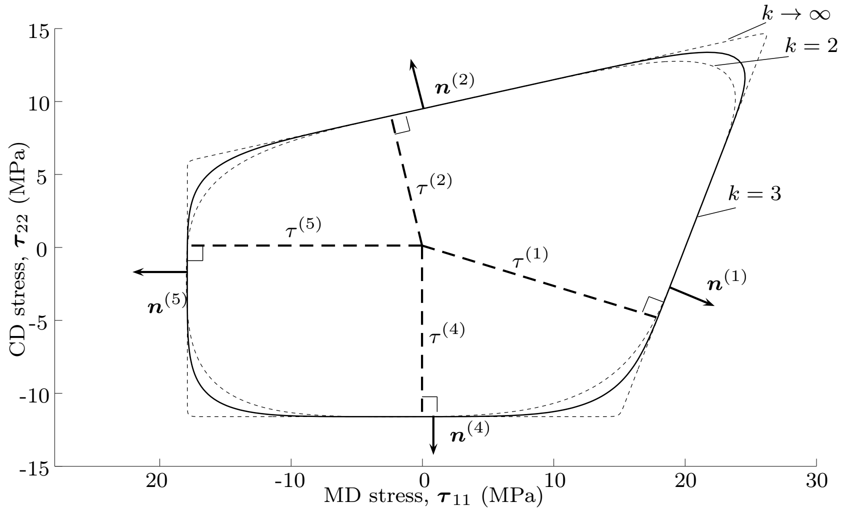

Figure 5: An illustration of the yield surface defined by (27) for $\boldsymbol{\tau}_{12} = 0$ for $k = 3$. The dotted line represents the yield surface when the exponent $k \to \infty$ and $k = 2$.

(27) will provide sharper corners in the yield surface, cf. Fig. 5. The value for k can be determined by considering biaxial stress states. The material parameters will however be derived from simple uniaxial tests and therefore a value for k has been chosen. The value $k = 3$ has been taken in this work, whereas in Xia et al. (2002) the choice $k = 2$ was made.

The evolution laws are given as

$$\begin{aligned} \boldsymbol{d}^p &= \dot{\lambda} \frac{\partial f}{\partial \boldsymbol{\tau}} \\ \dot{\kappa}^{(\nu)} &= -\dot{\lambda} \omega^{-1}_{\nu\alpha} \frac{\partial f}{\partial K^{(\alpha)}}, \end{aligned} \tag{30}$$

where α is a summation index and $\dot{\lambda}$ will be determined by enforcing $f = 0$ during elasto-plastic loading. It is further assumed that the plastic spin $\text{skew}(\boldsymbol{l}^p) = \boldsymbol{0}$. Note that the inverse of the coupling matrix, $\omega^{-1}_{\nu\gamma}$ enters the evolution law for $\kappa^{(\nu)}$ in (30). This format is chosen to obtain a physical interpretation of the internal variables in terms of the experimentally measured plastic strains. The dissipation inequality (18) with the evolution laws in (30) becomes

$$d = \sum_{\gamma=1}^{6} 2k\chi^{(\gamma)} \dot{\lambda} \Lambda_{\gamma}^{2k} \left(1 - \frac{K^{(\gamma)}}{\tau^{(\gamma)}}\right) \geq 0, \tag{31}$$

cf. Appendix B for a derivation and the definition of Λ_γ. A sufficient condition for the inequality (31) to be fulfilled, is that for all terms γ

$$K^{(\gamma)} \leq K_0^{(\gamma)} + \sum_{\alpha=1}^{6} \omega_{\gamma\alpha} K^{(\alpha)}, \tag{32}$$

where (28) was used. The criterion (32) will be discussed in detail for the specific $\omega_{\gamma\alpha}$ that has been employed in the calibration section.

6 Calibration Procedure

The number of constitutive parameters involved in an orthotropic elastic, orthotropic plastic constitutive model is inevitable large. One strategy for finding the constitutive parameters is to make use of inverse modelling in conjunction with optimization methods, cf. Garbowski et al. (2011). In the present work we will present a simple approximate fitting procedure that enables the constitutive parameters to be determined from simple uniaxial tests. It turns out that the response obtained using the estimated parameters fits well to the experimental uniaxial curves present in the calibration process.

Five uniaxial tests are used to calibrate the in-plane model, i.e. tension tests in MD, CD and 45^o and compression tests in MD and CD. The following stress states are assumed to be valid in the uniaxial tests:

$$\begin{aligned}
\boldsymbol{\tau} &= \tau^{MDt}\boldsymbol{m}_0^{(1)} && \text{MD-tension}\\
\boldsymbol{\tau} &= \tau^{CDt}\boldsymbol{m}_0^{(2)} && \text{CD-tension}\\
\boldsymbol{\tau} &= \tau^{MDc}\boldsymbol{m}_0^{(1)} && \text{MD-compression}\\
\boldsymbol{\tau} &= \tau^{CDc}\boldsymbol{m}_0^{(2)} && \text{CD-compression}\\
\boldsymbol{\tau} &= \frac{\tau^{45^o t}}{2}\left(\boldsymbol{m}_0^{(1)} + \boldsymbol{m}_0^{(2)} + \boldsymbol{v}_0^{(1)} \otimes \boldsymbol{v}_0^{(2)} + \boldsymbol{v}_0^{(2)} \otimes \boldsymbol{v}_0^{(1)}\right) && 45^o\text{-tension.}
\end{aligned} \tag{33}$$

The 45^o tension stress state in (33) is obtained by rotating a uniaxial stress state 45 degrees. Note that the director vectors are assumed to be constant in the calibration procedure, i.e. the rotations are assumed negligible. It will turn out that this assumption will provide a good fit to the uniaxial curves. The Kirchhoff stresses τ have been identified from the measured force F and the initial cross sectional area, A_0, and initial specimen length L_0, as

$$\tau = \frac{F}{A_0}(1 + \frac{u}{L_0}). \tag{34}$$

In the calibration procedure below, the elastic parameters will be considered first, and then the plastic part.

6.1 Elasticity

The initial (for small strains) orthotropic stiffness tensor, can be written as (in Voigt notation)

$$\boldsymbol{\mathcal{D}} = \frac{1}{1-\nu_{12}\nu_{21}} \begin{bmatrix} E_{11} & \nu_{12}E_{22} & 0 \\ \nu_{21}E_{11} & E_{22} & 0 \\ 0 & 0 & (1-\nu_{12}\nu_{21})G_{12} \end{bmatrix}, \tag{35}$$

where E_{11} and E_{22} are the elastic modulus in MD and CD, ν_{12} and ν_{21} are the Poisson' ratios and G_{12} is the shear modulus. Note that the symmetry condition $\nu_{12}E_{22} = \nu_{21}E_{11}$ holds. The expression (35) will be used to relate the elastic parameters present in the model. The elastic moduli in MD, CD and 45^o are deduced from the experimental uniaxial tension curves and G_{12}, can be found from a standard expression found in Lekhnitskii (1968). The contraction has been measured from uniaxial DIC-tests and it was found that

$$\sqrt{\nu_{12}\nu_{21}} \approx 0.30, \tag{36}$$

where ν_{12}, ν_{21} are the Poisson's ratios in MD and CD respectively. In the experimental investigation Baum et al. (1981) the value $\sqrt{\nu_{12}\nu_{21}} \approx 0.293$ was found for a range of paperboards. The result (36) together with the symmetry condition of the compliance tensor (35) gives that the Poisson's ratio can be found.

The stiffness tensor resulting from the strain energy (22), for $\boldsymbol{F} = \boldsymbol{I}$, i.e. initial stiffness, has been computed numerically with the constraint $q = (1-p)/2$. The difference of the matrix components in $\boldsymbol{\mathcal{D}}$ from (35) and from the stiffness resulting from the free energy (22) has been minimized in a least square sence to obtain the material data. The result of the fitting procedure is found in table 1.

Elastic parameters	
A (MPa)	950
p (-)	0.49
α (-)	4.8

Table 1: Numerical values of the elastic parameters

6.2 Plasticity

The calibration of the plastic parameters is a bit more involved. From the experimental evidences in Fig. 3, it can be concluded that the pre-strained samples display a softer response than non-prestrained samples. By decreasing the yield stress perpendicular to the pre-strained direction, a softening effect can be achieved, cf. Fig. 6.

In Fig. 6 the evolution of the yield surface is shown for uniaxial tension in CD. During loading in CD-tension, the distance to the yield sub-surface belonging to MD-tension is decreasing. It turns out that the distortion hardening illustrated in Fig. 6 can be captured by fitting the $\omega_{\nu\gamma}$ parameters present in the yield surface (27). However, first the components of the yield subsurfaces, $n_{ij}^{(\nu)}$, defined in (24) needs to be determined.

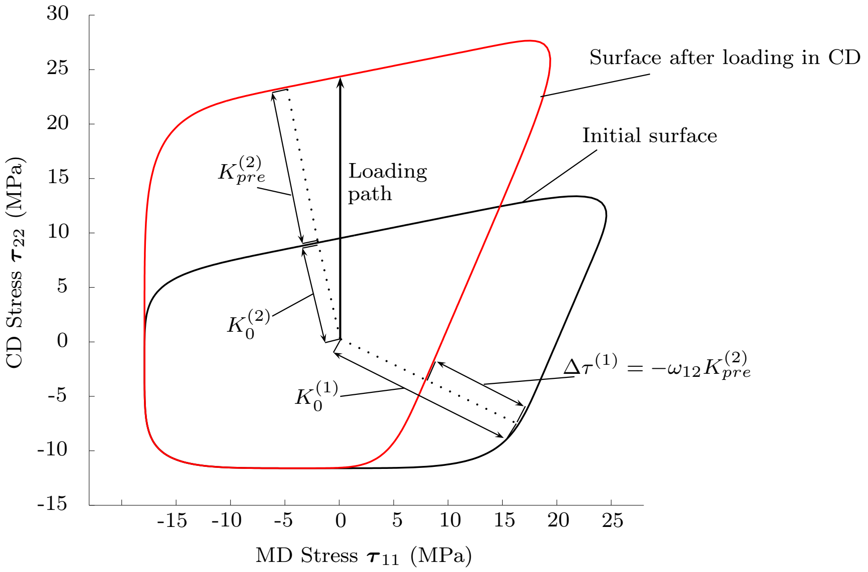

Figure 6: Evolution of yield surfaces for uniaxial tension in CD for $\boldsymbol{\tau}_{12} = 0$.

6.2.1 Yield subsurfaces, $n_{ij}^{(\nu)}$

The yield plane normals $n_{ij}^{(\nu)}$ determines the shape of the yield surface. Consider first the MD-tension stress state given in (33). Insertion of (33a) into (30) provides the plastic velocity gradient. Projection of the plastic velocity gradient on $\boldsymbol{m}_0^{(1)}$ and $\boldsymbol{m}_0^{(2)}$ gives

$$\begin{aligned} d_{11}^p &= \frac{\dot{\lambda} 2k \Lambda_1^{2k-1} n_{11}^{(1)}}{\tau^{(1)}} \\ d_{22}^p &= \frac{\dot{\lambda} 2k \Lambda_1^{2k-1} n_{22}^{(1)}}{\tau^{(1)}}. \end{aligned} \tag{37}$$

The axial and lateral strain ratio d_{11}/d_{22} has been shown for many paperboard materials to remain approximately constant, cf. Xia et al. (2002) and Harrysson and Ristinmaa (2008). For paperboard, the experimental data available for the yield-surface shape is limited and therefore the calibration of the $n_{ij}^{(\nu)}$ will be based on the assumption that the plastic strain rate ratio equals the total strain rate,

$$\frac{d_{11}^p}{d_{22}^p} = \frac{n_{11}^{(1)}}{n_{22}^{(1)}} = \nu_{12}, \tag{38}$$

i.e. the approximation (38) that was adopted in cf. Xia et al. (2002) has been employed. Note also that (36) has been utilized in (38). Using the following normalizing condition

$$\sqrt{(n_{11}^{(\nu)})^2 + (n_{22}^{(\nu)})^2 + 2(n_{12}^{(\nu)})^2} = 1, \tag{39}$$

and assuming no coupling to the shearing, i.e. $n_{12}^{(1)} = n_{12}^{(2)} = 0$, gives that $n_{11}^{(1)}$ and $n_{22}^{(1)}$ can be determined. A similar procedure for the CD-stress state can then be made. In summary, the yield plane normals for the MD- and CD-tension are obtained as,

$$\left.\begin{aligned} n_{11}^{(1)} &= \frac{1}{\sqrt{1+\nu_{12}^2}} \\ n_{22}^{(1)} &= -\sqrt{1-(n_{11}^{(1)})^2} \end{aligned}\right\} \text{MD} \qquad \left.\begin{aligned} n_{22}^{(2)} &= \frac{1}{\sqrt{1+\nu_{21}^2}} \\ n_{11}^{(2)} &= -\sqrt{1-(n_{22}^{(2)})^2} \end{aligned}\right\} \text{CD} \tag{40}$$

For the sub-surfaces associated with the compression states in (33), it has been assumed that there is no coupling between the axial and lateral plastic strains due to lack of experimental evidence, therefore $n_{11}^{(4)} = n_{22}^{(5)} = 1$ and $n_{22}^{(4)} = n_{11}^{(5)} = n_{12}^{(5)} = n_{12}^{(4)} = 0$ is adopted. For the yield plane normals associated with the positive and negative shear, it is assumed $n_{11}^{(3)} = n_{22}^{(3)} = n_{11}^{(6)} = n_{22}^{(6)} = 0$, i.e. the shear sub-surfaces are assumed decoupled from the normal components. The normalizing condition (39) gives then $n_{12}^{(3)} = 1/\sqrt{2}$ and $n_{12}^{(6)} = -1/\sqrt{2}$. The numerical values for the yield plane subsurfaces are summarized in Table 2.

Subsurface, ν	$n_{11}^{(\nu)}$	$n_{22}^{(\nu)}$	$n_{12}^{(\nu)}$
1	0.92	-0.40	0
2	0.20	0.98	0
3	0	0	0.71
4	-1	0	0
5	0	-1	0
6	0	0	-0.71

Table 2: Numerical values of subsurface parameters

6.2.2 The coupling components $\omega_{\nu\gamma}$

To achieve the distortional hardening as illustrated in Fig. 6, both ω_{12} and ω_{21} must be negative. Since no experimental data exists for the other directions, it is for simplicity assumed that the remaining cross terms $\omega_{\gamma\nu} = 0, \{\nu \neq \gamma\}$. Without loss of generality, the diagonal terms are further assumed to be normalized such that $\omega_{\gamma\gamma} = 1$. For uniaxial tension loading in MD and CD, it follows from (33) and (27) that

$$\begin{aligned} \tau^{(1)}(\kappa^{(1)},\kappa^{(2)}) &= K_0^{(1)} + K^{(1)} + \omega_{12}K^{(2)} &= \tau^{MDt} n_{11}^{(1)} \\ \tau^{(2)}(\kappa^{(1)},\kappa^{(2)}) &= K_0^{(2)} + \omega_{21}K^{(1)} + K^{(2)} &= \tau^{CDt} n_{11}^{(2)}. \end{aligned} \tag{41}$$

Furthermore from (30) it follows that,

$$\dot{\kappa}^{(\nu)} = \dot{\lambda} 2k \chi^{(\nu)} \frac{\Lambda_\nu^{2k}}{\tau^{(\gamma)}}, \qquad K^{(\nu)} = K^{(\nu)}(\kappa^{(\nu)}). \tag{42}$$

The coupling term ω_{12} is found by considering the yield function (27) for the pre-straining in CD-tension followed by MD-tension. During uniaxial pre-straining in CD, the evolution law (30) provides $K^{(1)}(\kappa^{(1)}) = K^{(1)}(0) = 0$, due to $\chi^{(1)} = 0$, cf. (42). The state obtained after the pre-strain loading in CD is given as

$$\begin{aligned} \tau^{(1)}(0, \kappa^{(2)}_{pre}) &= K^{(1)}_0 + \omega_{12} K^{(2)}_{pre} \\ \tau^{(2)}(0, \kappa^{(2)}_{pre}) &= K^{(2)}_0 + K^{(2)}_{pre}. \end{aligned} \tag{43}$$

where the subscript '*pre*' denotes the value obtained during this loading. The experimental evidence when loading in MD, i.e. the perpendicular direction, indicates that $\tau^{(1)}(0,0) \geq \tau^{(1)}(0, \kappa^{(2)}_{pre})$ cf. also Fig. 6, which requires that yielding starts earlier for the pre-strained sample. The difference is denoted by

$$\Delta\tau^{(1)} = \tau^{(1)}(0,0) - \tau^{(1)}(0, \kappa^{(2)}_{pre}) = -\omega_{12} K^{(2)}_{pre} \tag{44}$$

where (43) was used. Since $\Delta\tau^{(1)}$ can be obtained from the experimental data it follows that

$$\omega_{12} = \frac{\Delta\tau^{(1)}}{-K^{(2)}_{pre}}, \tag{45}$$

A similar procedure for ω_{21} is found by considering the yield function (27) for the MD-tension stress state followed by CD,

$$\omega_{21} = \frac{\Delta\tau^{(2)}}{-K^{(1)}_{pre}}. \tag{46}$$

The parameters are identifed as $\omega_{12} = -0.59$ and $\omega_{21} = -0.071$.

Returning to the condition for fullfilling the dissipation inequality, (32), it is required that

$$\begin{aligned} K^{(1)} &\leq K^{(1)}_0 + K^{(1)} + \omega_{12} K^{(2)}, \\ K^{(2)} &\leq K^{(2)}_0 + K^{(2)} + \omega_{21} K^{(1)}. \end{aligned} \tag{47}$$

Consider now uniaxial tension in CD, i.e. (33b). For this stress state, the evolution laws provides $K^{(1)} = 0$, which implies that (47b) is automatically fullfilled and only (47a) needs to be considered. Rewriting (47a) and using (44) gives

$$\Delta\tau^{(1)} \leq K^{(1)}_0 \tag{48}$$

indicating that the decrease of MD-yield subsurface when loading in CD (left hand side), must be be less than the initial distance to the MD-subsurface (right hand side). A similar interpretation can be made for ω_{21}.

6.2.3 Hardening parameters

The hardening, $K^{(\nu)}$, can be identified from the experimental tests using the stress states in (33). Considering tensile loading in MD it follows from (27) that

$$\tau^{(1)} = K_0^{(1)} + K^{(1)} = \tau^{MDt} n_{11}^{(1)}. \tag{49}$$

From the evolution laws (30), the following relations are then obtained,

$$\begin{aligned} d_{11}^{p,MDt} &= \dot{\lambda} 2k \frac{n_{11}^{(1)} \Lambda_1^{2k-1}}{\tau^{(1)}} \\ \dot{\kappa}^{(1)} &= \dot{\lambda} 2k \frac{\Lambda_1^{2k}}{\tau^{(1)}}, \end{aligned} \tag{50}$$

where $d_{11}^{p,MDt}$ is the component of the symmetric plastic velocity gradient $\boldsymbol{d}^p$ projected on $\boldsymbol{m}_0^{(1)}$. Assuming negligible rotations enables the spatial velocity gradient to be expressed in terms of the plastic stretch tensor $\boldsymbol{V}^p$, cf. (3), as

$$\dot{\overline{\ln V^{p,MDt}}} = d_{11}^{p,MDt}, \tag{51}$$

where $V^{p,MDt}$ is the plastic stretch in the MD-tension stress state projected on $\boldsymbol{m}_0^{(1)}$. Time integration of $d_{11}^{p,MDt}$ will then give a relation to the logarithmic plastic stretch tensor. Then the ratio $d_{11}^{p,MDt}/\dot{\kappa}^{(1)}$ from (50) together with (51) and (49) enables the internal variables of $\kappa^{(1)}$ to be determined as

$$\kappa^{(1)} = \frac{\ln V^{p,MDt}}{n_{11}^{(1)}}. \tag{52}$$

Thus allowing for $\tau^{MDt} = \tau^{MDt}(\ln V^{p,MDt})$ to be established; which has been measured in the experimental tests. A similiar procedure can be made for the remaining stress states in (33). To determine the hardening parameters a_ν and b_ν, a least square fit in the MD, CD and 45^o tension tests has been made. The numerical values are summarized in table 3.

Subsurface, ν	$K_0^{(\nu)}$ (MPa)	a_ν, (MPa)	b_ν, (-)
1	17	13	710
2	7.8	5.0	1200
3	9.3	5.1	1100
4	18	0	0
5	11.6	0	0
6	9.3	5.1	1100

Table 3: Hardening parameters

7 Numerical Implementation

The backward Euler method is used for the update of the state variables. Consider a time interval $\Delta t \in [t_n, t_{n+1}]$ between loadstep n and $n+1$, where $\boldsymbol{F}_{n+1}$ is given. First a trial step is made to check whether plasticity takes place in the elapsed time interval,

$$\begin{aligned} \boldsymbol{F}^e_{trial} &= \boldsymbol{F}_{n+1}\boldsymbol{F}^{p-1}_n \\ \boldsymbol{v}^{(\alpha)}_{trial} &= \boldsymbol{R}^e_{trial}\boldsymbol{v}^{(\alpha)}_0 \\ \kappa^{(\nu)}_{trial} &= \kappa^{(\nu)}_n. \end{aligned} \tag{53}$$

where $\boldsymbol{R}^e_{trial}$ is obtained from the polar decomposition of $\boldsymbol{F}^e_{trial}$. Using (53), the trial value of the yield surface is computed according to $f^{trial}\big(\boldsymbol{\tau}\big(\boldsymbol{F}^e_{trial}, \boldsymbol{v}^{(\alpha)}_{trial}\big), \boldsymbol{n}^{(\gamma)}\big(\boldsymbol{v}^{(\alpha)}_{trial}\big), K^{(\nu)}(\kappa^{(\gamma)}_{trial})\big)$. For the situation $f^{trial} < 0$, the updated variables are equal to the trial quantities otherwise an update is made according to (30). Using the backward Euler scheme, the discrete evolution equation becomes

$$\begin{aligned} \boldsymbol{F}^p_{n+1} &= \boldsymbol{F}^p_n + \Delta\lambda \boldsymbol{F}^{-1}_{n+1}\boldsymbol{F}^p_{n+1}\left.\frac{\partial f}{\partial \boldsymbol{\tau}}\right|_{n+1}\boldsymbol{F}^{p-1}_{n+1}\boldsymbol{F}_{n+1} \\ \kappa^{(\nu)}_{n+1} &= \kappa^{(\nu)}_n - \Delta\lambda\omega^{-1}_{\nu\alpha}\left.\frac{\partial f}{\partial K^{(\alpha)}}\right|_{n+1} \\ 0 &= f\big|_{n+1} \end{aligned} \tag{54}$$

A summation is done over the index α in the (54). The equation system (54) is solved using the Newton-Raphson algorithm.

For the numerical treatment of the model, the Algorithmic Tangent Stiffness (ATS) matrix is needed. The algorithm allows us to derive an implicit expression for $\boldsymbol{F}^p$ as a function of $\boldsymbol{F}$, i.e. the Kirchhoff stress can be written as $\boldsymbol{\tau} = \boldsymbol{\tau}(\boldsymbol{F}^e) = \boldsymbol{\tau}(\boldsymbol{F}, \boldsymbol{F}^p(\boldsymbol{F}))$. The ATS matrix is then given as

$$\boldsymbol{\mathcal{D}} = -\big[\boldsymbol{I}\overline{\otimes}\boldsymbol{\tau}\big] - \big[\boldsymbol{I}\underline{\otimes}\boldsymbol{\tau}\big] + \frac{\partial \boldsymbol{\tau}}{\partial \boldsymbol{F}}\boldsymbol{F}^T, \tag{55}$$

cf. Harrysson and Ristinmaa (2007) for a derivation. The non-standard dyadic notation $\big[\boldsymbol{A}\underline{\otimes}\boldsymbol{B}\big] : \boldsymbol{C} = \boldsymbol{A}\cdot\boldsymbol{C}^T\cdot\boldsymbol{B}^T$ and $\big[\boldsymbol{A}\overline{\otimes}\boldsymbol{B}\big] : \boldsymbol{C} = \boldsymbol{A}\cdot\boldsymbol{C}\cdot\boldsymbol{B}^T$ have been introduced above.

To improve the accuracy of the solution procedure, the Ellsiepens 2-stage Diagonally Implicit Runge-Kutta (DIRK) method has been utilized cf. Hartmann (2005) and Borgqvist and Wallin (2012) .

8 Verification of calibration and uniaxial response

The model is fitted to uniaxial tension in the MD, CD and 45^o directions, as well as uniaxial compression in MD and CD. The Long Compression Test (LCT) apparatus were used for compression tests, which has lateral support to prevent buckling, cf. Cavlin and Fellers (1975). The paperboard used in the compression tests were, $w_0 = 25$ mm wide and had a clamp length $l_0 = 55$ mm. The uniaxial tests and pre-straining where performed according to the description in section 2. To test the calibration procedure, uniaxial finite element simulations have been performed. One element FEM-simulation where the internal force and the displacement has been extracted is shown in Fig. 7 for different angles.

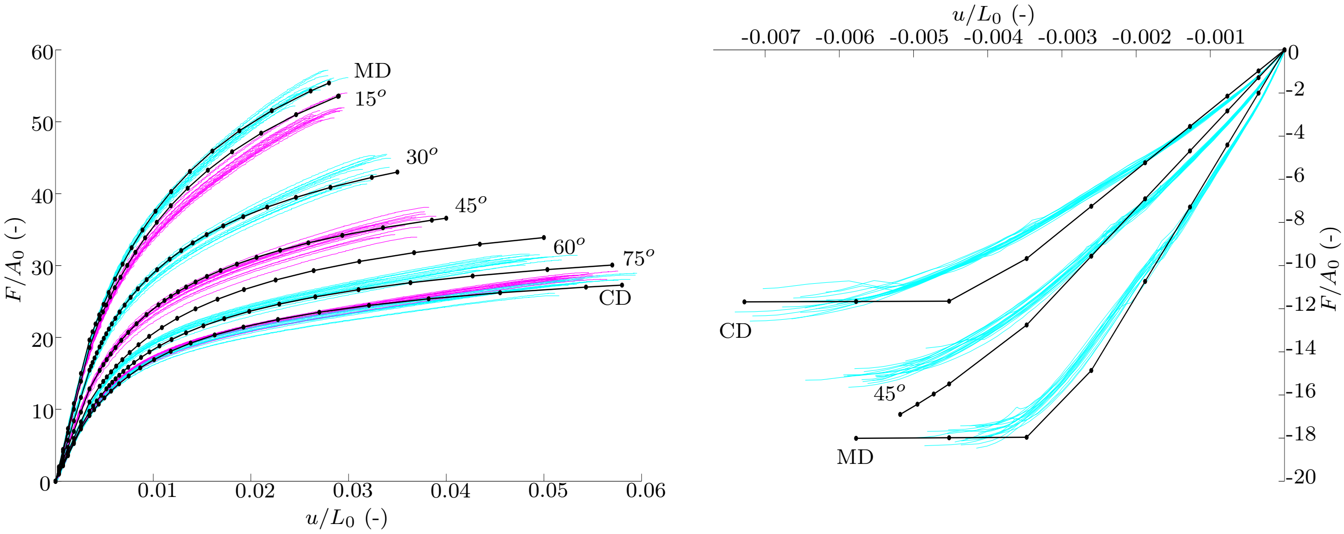

Figure 7: Uniaxial stress-strain curves in CD and MD. Light blue and purple color is used for the experimental data obtained from samples that were not pre-strained and black for the simulations. Normalized force vs normalized displacement has been plotted, where A_0 is the initial cross section area and L_0 is the initial length.

As observed from Fig. 7, despite the approximative assumptions in the calibration procedure, an accurate fit to the uniaxial curves is obtained. Note too that no fitting has been made for the the intermediate angles, $\{15^o, 30^o, 60^o, 75^o\}$ in tension and 45^o in compression, indicating that the model provides realistic predictions in uniaxial loading situations. Note that the simplifying assumption of ideal plasticity for the compressive subsurfaces in MD and CD has been made, even though the slopes of the curves are not constant up to failure.

The predicted response for the non-proportional situations are shown in Fig. 8, where it is concluded that the presented model allows the hardening response of the pre-strained samples to be predicted. Note that the distortion hardening reduces the yield stress for the pre-strained samples and the simulated hardening response is then predicted by the model. The change in the initial stiffnesses present in the experiements are not captured by the proposed elasto-plastic model. Notice also the variation in the response increases when the samples are pre-strainend. The pre-strained samples fail, however, at approximately the same displacement as the non-prestrained samples.

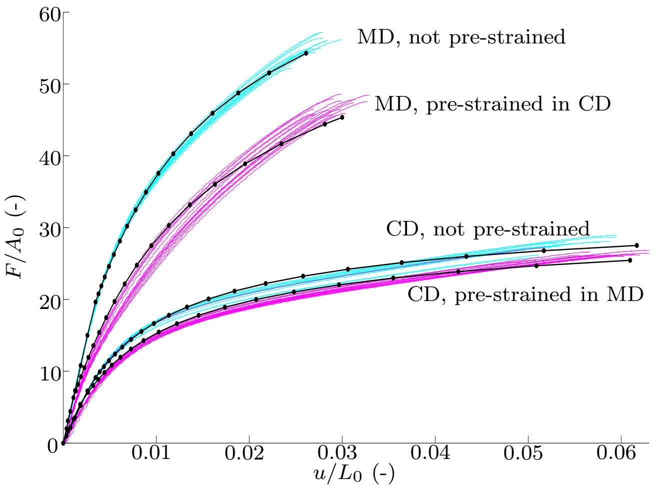

Figure 8: Uniaxial stress-strain curves in CD and MD. Light blue color is used for the experimental data obtained from samples that were not pre-strained, purple color is used for the pre-strained samples and black for the simulations. Normalized force vs normalized displacement has been plotted, where A_0 is the initial cross section area and L_0 is the initial length.

9 DIC comparision

Digital Image Correlation (DIC) measurements have been performed with a single camera on a sample with a central hole. Tests have been conducted when the loading direction is parallel to CD and when it is parallel to MD. The boundary conditions are given in Fig. 9a. The resulting strain field from the experimental setup has been compared to the strain field obtained from the simulations.

The dimensions of the geometry are given by $R = 10$ mm, $2w = 50$ mm, $2L = 80$ mm. The tests has been conducted on a standard MTS-tensile machine with a displacement rate of 2mm/min. The tests have been performed in climate chamber with moisture content RH=50% and temperature T=23^{o}C.

Four-node Lagrangian isoparametric elements have been used in the simulations. The DIC-field have been obtained by using the software VIC-2d (Correlated solutions Inc.). One high speed camera Gazelle GZL-CL-22C5M-C (Point Grey Inc.), with a resolution of 2048 times 1088 at 280 frames per second has been used. Before examining the DIC results, the macroscopic load-displacement curve will be discussed.

The force-displacement curves in the MD and CD directions for both the experiments (blue) and simulations (red) are shown Fig. 10. The experimental force-displacement curves are recorded up to the state when a complete fracture occurs. During the softening part of the force-displacement curve fracture occurs in the samples, and since fracture is not considered in the current model, the simulation are stopped when the softening is initiated. A total of 14 experiments were performed in CD and 12 in MD. The boxplots in the Fig. 10

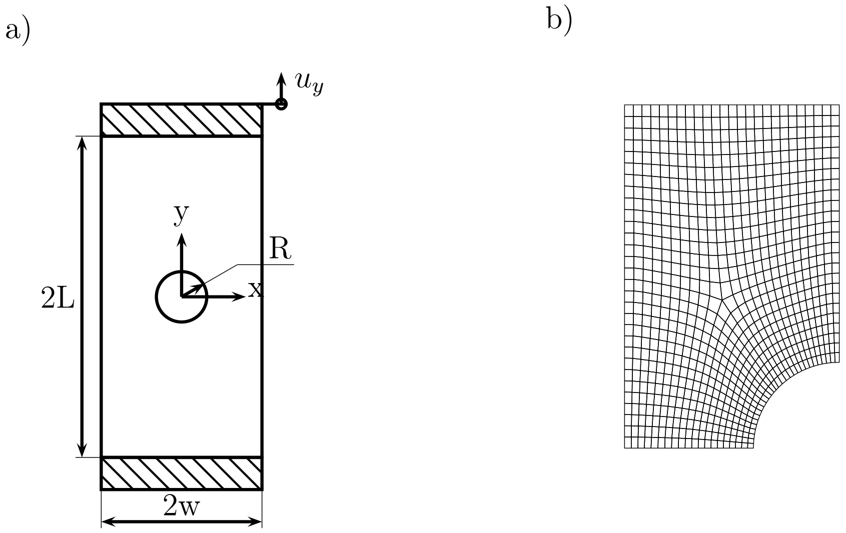

Figure 9: a) Illustration of the boundary value problem used in the experiments and numerical simulation. The top and bottom boundaries are constrained at zero displacement in the x-direction. b) The finite element mesh used in simulations consists of 825 plane stress elements with 4 nodes. Due to the symmetry, only a quarter of the structure has been considered in the finite element simulation.

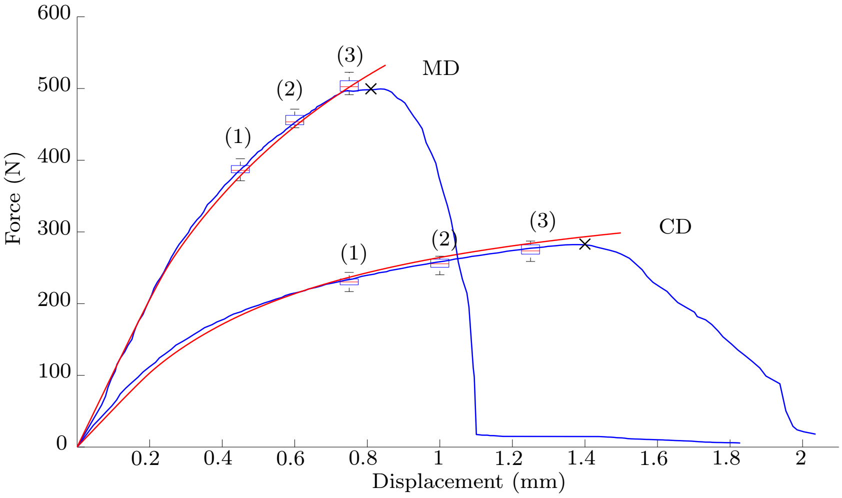

Figure 10: Force-displacement curves for both the experiments (blue) and simulations (red) of the global response of the plate with hole when the loading direction is parallel to MD and CD. The strain fields present in Fig. 11 and Fig. 12 have been taken at the displacement levels marked with (1)-(3) (same position as the boxplots). The × indicates the load level where a visible crack is observed in the sample.

indicate the variation of the global-force response for the different samples that have been tested. A visual comparison between the experiment and simulation curves, shows that the simulations provide a good prediction of experiments within expected experimental variation.

Contour plots of the largest principal Green-Lagrange strain from the simulated strain fields and experimental DIC-strain fields are shown in Figs. 11a and 12a, respectively. Typical DIC-fields when loading is applied parallel to CD and MD are shown. The comparisons are made at the displacement levels, $u_y = \{0.75, 1.00, 1.25\}$ in CD and $u_y = \{0.45, 0.60, 0.75\}$ in MD. In Fig. 10 the displacement levels are marked from (1) to (3) in the force-displacement curves.

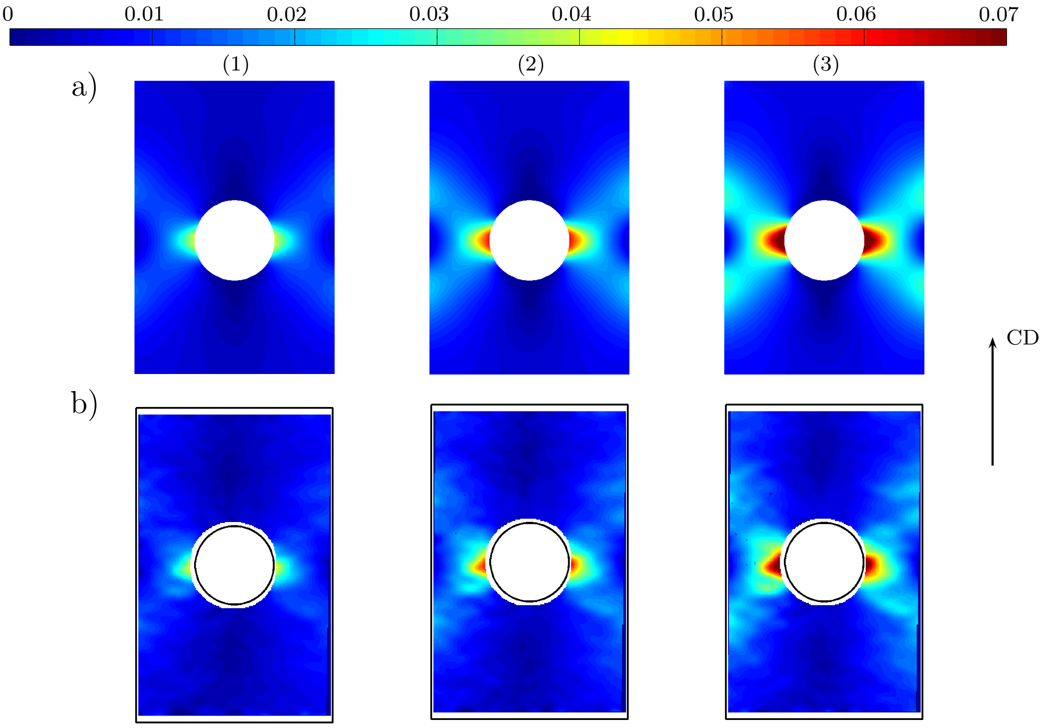

Figure 11: Contour plots of largest principal Lagrangian strain for loading in the CD-direction at the displacement levels $u_y = \{0.75, 1, 1.25\}$. a) Simulation values b) DIC values

From the DIC-strain fields in Figs. 11b and 12b the black contour indicates the full geometry of the samples. The experimental strain fields in Figs. 11b and 12b has been extracted from a single test, and thus some variations in the strain-field arising from the inherent inhomogeneity of the paperboard are visible in the figures. It is concluded from Figs. 11 and 12 that the overall strain fields obtained between the simulations and the experiments are similar. The strain level and distribution at the different displacements are about the same in the experiments and simulations. In MD, it is noticed that the strain-field is smeared out more in the vertical direction, whereas in CD the strain field is smeared more in the horizontal direction. These effects are noticed both in the simulations and in the experiments.

The inhomogeneity of paperboard was investigated in Hagman and Nygårds (2012) using DIC for uniaxial testing, where localized strain fields were observed for the uniaxial load tests. The DIC tests conducted here shows that a continuum model can capture the

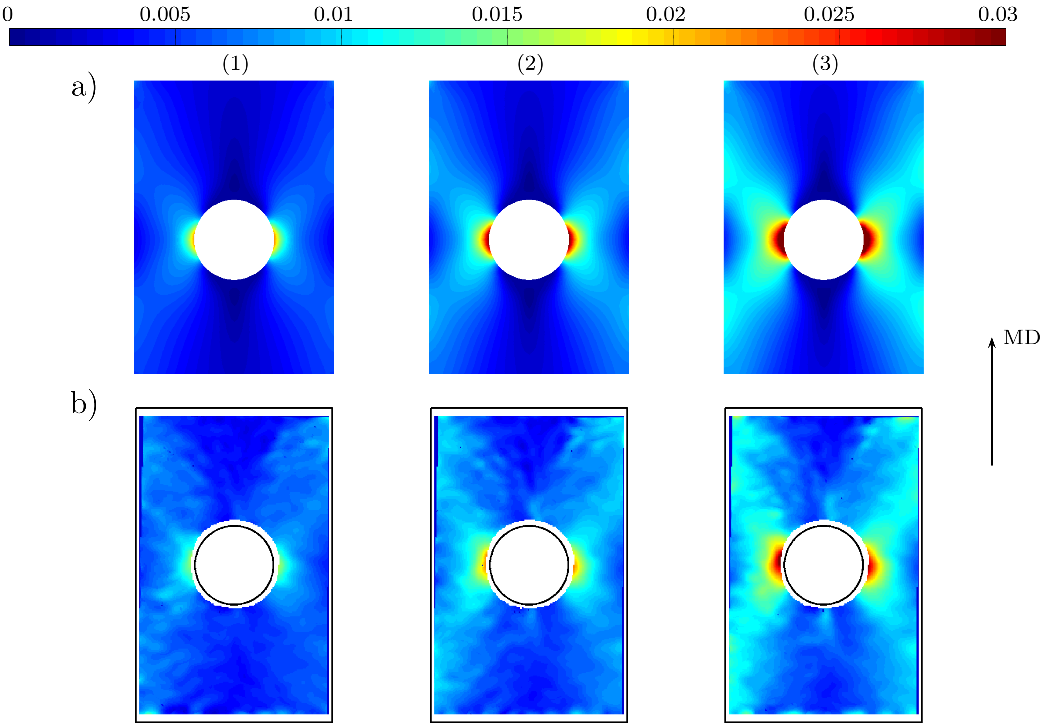

Figure 12: Contour plots of the largest principal Lagrangian strain for loading in the MD direction at the displacement levels $u_y = \{0.45, 0.6, 0.75\}$. a) Simulation values b) DIC values

overall strain fields, even though the paperboard is heterogeneous. The inherent inhomogeneity of paperboard does not appear to be crucial for the overall strain field in the load cases considered here, when comparing the simulations and experiments. Note that typical fiber lengths are around 1-3 mm with a witdh and thickness around 10-50 μm.

The error between the DIC-samples and the simulations have also been investigated. The absolute error and a relative error have been defined as

$$\varepsilon_{abs} = e_1^{(sim)} - e_1^{(DIC)}, \quad \varepsilon_{rel} = \frac{|e_1^{(sim)} - e_1^{(DIC)}|}{e_1^{DIC}} \tag{56}$$

where $e_1^{(sim)}$ and $e_1^{(DIC)}$ are the largest principal strains from the simulations and DIC respectively. The principal strains are compared at approximately the same positions in the DIC and simulations by averaging the strains at the nodes from simulations within a radius of $r = 1$ mm from the corresponding coordinates in the DIC test. The error have been plotted at the displacement level (3) marked in Fig. 10 for MD and CD.

A similar tendency for the error are observed for MD as well as for CD. The largest absolute error occurs at the horizontal sides of the holes. This implies that the strain field at the hole is not perfectly captured. The error plots suggests that at the sides of the hole along a horizontal central line, the simulation overestimates the principal strains. The relative error at the same positions, indicates that the relative error next to the hole along

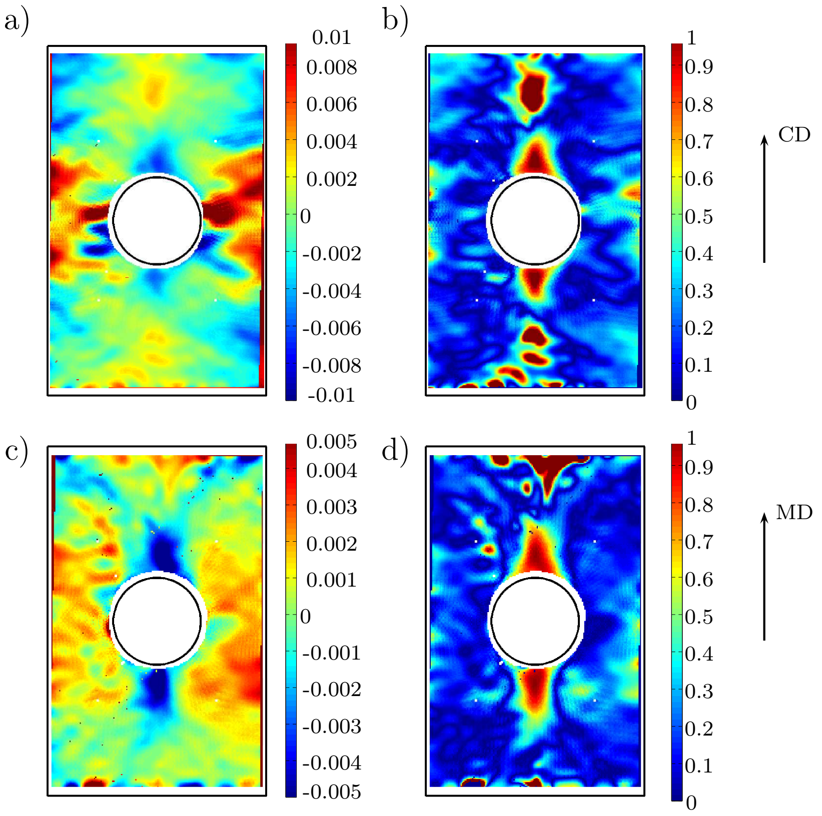

Figure 13: Contour plot of the error in CD and MD at the displacement level (3) a) Absoulte error, ε_{abs}, for CD loading b) Relative error, ε_{rel}, for CD loading c) Absoulte error, ε_{abs} , for MD loading d) Relative error, ε_{rel}, for MD loading

the horizontal line is relatively small. Considering now the relative error along the vertical symmetry line, it is at maximum at the top and bottom of the hole. From the error plots it can be concluded that the simulations predicts smaller magnitude of the strains at the top and bottom location of the hole. This might possible be due to out-of-plane deformation (buckling) which is not visible when using a single camera for the DIC tests or boundary effects.

10 Conclusions

A distortional hardening elasto-plastic model at finite strains applicable for paperboard has been presented within a thermodynamically consistent frame work. Non-proportional experiments have been performed, which shows that paperboard pre-loaded in a perpendicular direction displays a softened response. It is shown that this effect can be modeled by introducing coupling effects such that a softening takes place in the direction perpendicular to the loading direction.

The elastic part of the model, utilizes an polyconvex free energy. This introduces physical parameters p and q, related to the fiber distribution of the material. In this work however, the parameters was determined by fitting to the uniaxial force-displacement response.

For the description of the plastic part of the model, the yield surface in Xia et al. (2002) is chosen. To allow for a general coupling between the hardening response, multiple hardening variables together with a coupling matrix between the hardening variables is introduced. The coupling matrix allows the yield surface to harden distortionally. The yield surface remains convex despite large distortion of the yield surface during hardening. It is shown that the dissipation inequality sets constraints on the choice of parameters for the coupling matrix which are physically logical.

The calibration procedure for the plastic part of the model is shown to be straightforward and after that some approximations are introduced, the experimental comparison does not compromise the predicted response. Only uniaxial tests is needed in the calibration which significantly reduce the experimental complexity. The subsurface parameters has been calibrated by assuming the total strain ratio equals the plastic strain ratio. This assumption needs to be experimentally verified and more investigations are needed to determine the exact shape shape of the yield surface.

Validation experiments of a sample with a central hole has been performed to investigate performance of the model, i.e. a non-homogeneous strain field. Digital Image correlation measurements were performed on the samples to allow comparisons of the strain fields between the simulations and the experiments. The results revealed that a qualitative match between the simulated strain field and the experimental DIC-field was obtained. The error between the simulated strain field and the DIC strain field were also compared. The error was largest at the top and bottom of the holes at the final stages of loading. The deviation in the strain field can be due to the constitutive model but it can also be explained by out-of-plane behavior or boundary effects. However, the overall shape of the strain field from a single plate-hole test is captured. It is concluded that the continuum approach for the modeling of the in-plane behavior, is able to represent the inhomogeneous strain field from the DIC-measurements, despite the inherent inhomogeneous structure of paperboard.

Acknowledgements

The help from Innventia AB for support with the laboratory equipment is gratefully acknowledged. Help and suggestions on the experimental setup on the pre-straining tests from Mikael Nygårds at Innventia AB is highly appreciated. The financial support from the Crafoord foundation (grant no. 20120632) for funding of the DIC system is greatly acknowledged.

A Polyconvexity of the free energy

First, it is noticed that I_1^e can be written as

$$I_1^e = \mathrm{tr}(\boldsymbol{b}^e \boldsymbol{m}) = p\mathrm{tr}(\boldsymbol{b}^e \boldsymbol{m}^{(1)}) + q\mathrm{tr}(\boldsymbol{b}^e \boldsymbol{m}^{(2)}) + q\mathrm{tr}(\boldsymbol{b}^e \boldsymbol{m}^{(3)}). \tag{57}$$

A similar expression can be obtained for I_2^e and since a sum of convex functions is convex, it is therefore sufficient to prove that

$$\begin{aligned} \tilde{I}_1^{e,\alpha} &= \mathrm{tr}(\boldsymbol{b}^e \boldsymbol{m}^{(\alpha)}) \\ \tilde{I}_2^{e,\alpha} &= J^2 \mathrm{tr}(\boldsymbol{b}^{e-1} \boldsymbol{m}^{(\alpha)}) \end{aligned} \tag{58}$$

are convex for $\alpha = \{1, 2, 3\}$. From the polar decomposition theorem, (7) and the symmetry of $\boldsymbol{V}^e$, it follows that the invariants can be expressed as

$$\begin{aligned} \tilde{I}_1^{e,\alpha} &= \mathrm{tr}((\boldsymbol{V}^e)^2 \boldsymbol{m}^{(\alpha)}) = (\boldsymbol{V}^e \boldsymbol{v}^{(\alpha)}) \cdot (\boldsymbol{V}^e \boldsymbol{v}^{(\alpha)}) \\ &= (\boldsymbol{F}^e \boldsymbol{v}_0^{(\alpha)}) \cdot (\boldsymbol{F}^e \boldsymbol{v}_0^{(\alpha)}) = |\boldsymbol{F}^e \boldsymbol{v}_0^{(\alpha)}|^2 \\ \tilde{I}_2^{e,\alpha} &= J^2 \mathrm{tr}((\boldsymbol{V}^{e-1})^2 \boldsymbol{m}^{(\alpha)}) = J^2 (\boldsymbol{V}^{e-1} \boldsymbol{v}^{(\alpha)}) \cdot (\boldsymbol{V}^{e-1} \boldsymbol{v}^{(\alpha)}) = \\ &= (J \boldsymbol{F}^{e-T} \boldsymbol{v}_0^{(\alpha)}) \cdot (J \boldsymbol{F}^{e-T} \boldsymbol{v}_0^{(\alpha)}) = |J \boldsymbol{F}^{e-T} \boldsymbol{v}_0^{(\alpha)}|^2 = |\mathrm{cof}(\boldsymbol{F}^e) \boldsymbol{v}_0^{(\alpha)}|^2 \end{aligned} \tag{59}$$

These invaraints were shown to be polyconvex in Schröder and Neff (2002).

B Derivation of dissipation inequality

Inserting the evolution laws (30) into the dissipation inequality (18) provides

$$d = \boldsymbol{\tau} : \dot{\lambda} \frac{\partial f}{\partial \boldsymbol{\tau}} + K^{(\gamma)} \dot{\lambda} \omega_{\gamma\nu}^{-1} \frac{\partial f}{\partial K^{(\nu)}} \geq 0 \tag{60}$$

where summation is done over γ and ν. To simplify the notation Λ_ν is defined as

$$\Lambda_\nu = \frac{\boldsymbol{\tau} : \boldsymbol{n}}{\tau^{(\nu)}}. \tag{61}$$

The derivatives are then given by

$$\begin{aligned} \frac{\partial f}{\partial \boldsymbol{\tau}} &= 2k\chi^{(\gamma)} \frac{\Lambda_\gamma^{2k-1}}{\tau^{(\gamma)}} \boldsymbol{n} \\ \frac{\partial f}{\partial K^{(\nu)}} &= -2k\chi^{(\gamma)} \omega_{\nu\gamma} \frac{\Lambda_\gamma^{2k}}{\tau^{(\gamma)}} \end{aligned} \tag{62}$$

Insertion into (60) gives

$$\begin{aligned} d &= \boldsymbol{\tau} : \dot{\lambda} 2k\chi^{(\gamma)} \frac{\Lambda^{2k-1}}{\tau^{(\nu)}} \boldsymbol{n} - \dot{\lambda} 2k\chi^{(\gamma)} \frac{K^{(\gamma)}\Lambda^{2k}}{\tau^{(\gamma)}} \\ &= 2k\chi^{(\gamma)} \dot{\lambda} \Lambda^{2k} (1 - \frac{K^{(\gamma)}}{\tau^{(\gamma)}}), \end{aligned} \tag{63}$$

where summation is done over γ.

References

Abaqus User's Manual. Dassault Systemes. Abaqus Inc, Providence, RI, USA, 6.12 edition

Ask, A., Ristinmaa, M., 2008. Simulation Model for anisotropic fibrous materials. Proceedings in Applied Mathematics and Mechanics 8, 10399–10400.

Ball, J. M., 1977. Convexity Conditions and Existence Theorems in nonlinear elasticity. Symposium on Non-Well posed Problems and Logarithmic Convexity Springer, Lecture Notes in Math 316, 337–403.

Baum, G. A., Brennan, D. C., Haberger, C. C., 1981. Orthotropic elastic constants of paper. Tappi 64, 97–101.

Beex, L. A. A., Peerlings, R. H. J., 2009. An experimental and computational study of laminated paperboard creasing and folding. International Journal of Solids and Structures 46, 4192–4207.

Borgqvist, E., Wallin, M., 2012. Numerical integration of elasto-plasticity using a diagonal implicit Runge-Kutta integration scheme. International Journal of Damage Mechanics 22, 68–94.

Cavlin, S., 1988. The unique Convertibility of Paperboard. Packaging Technology and Science 10, 77–92.

Cavlin, S., Dunder, I., Edholm, D., 1997. Creasability testing by inclined rules a base for standardized specification of paperboard. Packaging Technology and Science 10(4), 191–207.

Cavlin, S., Fellers, C., 1975. A new method for measuring the edgewise compression properties of paper. Svensk papperstidning 78, 329–332.

Ciarlet, P. G., 1988. Mathematical Elasticity. Elsevier Science Publishers B.V.

Coleman, B. D., Gurtin, M. E., 1967. Thermodynamics with internal state variables. J. Chem. Phys. 47, 597–613.

Denman, E., Beavers, A., 1976. The matrix sign function and computations in systems. Applied Mathematics and Computation 2, 63–94.

Ebbing, V., 2010. Design of polyconvex Energy Functions for All Anisotropy Classes. Ph.D. thesis, Universität Duisburg-Essen, Essen, Germany.

Garbowski, T., Maier, G., Novati, G., 2011. On calibration of orthotropic elastic-plastic constitutive models for paper foils by biaxial tests and inverse analyses. Structural and Multidisciplinary Optimization 46, 111–128.

Gasser, T. C., Ogden, R. W., Holzapfel, G. A., 2006. Hyperelastic modelling of arterial layers with distributed collagen fibre orientations. Journal of the Royal Society Interface 3, 15–35.

Giampieri, A., Perego, U., Borsari, R., 2011. A constitutive model for the mechanical response of the folding of creased paperboard. International Journal of Solids and Structures 48, 2275–2287.

Hagman, A., Nygårds, M., 2012. Investigation of sample-size effects on in-plane tensile testing of paperboard. Nordic Pulp and Paper Research Journal 27, 295–304.

Harrysson, A., Ristinmaa, M., 2008. Large strain elasto-plastic model of paper and corrugated board. International Journal of Solids and Structures 45, 3334–3352.

Harrysson, M., Harrysson, A., Ristinmaa, M., 2007. Spatial representation of evolving anisotropy at large strains. International Journal of Solids and Structures 44, 3514–3532.

Harrysson, M., Ristinmaa, M., 2007. Description of evolving anisotropy at large strains. Mechanics of Materials 39, 267–282.

Hartmann, S., 2005. A remark on the application of the Newton-Raphson method in nonlinear finite element analysis. Comp. Mech. 36, 100–116.

Hill, R., 1948. A theory of the yielding and plastic flow of anisotropic materials. Proceedings of the Royal Society of London A193, 281–297.

Huang, H., Nygårds, M., 2010. A simplified material model for finite element analysis of paperboard creasing. Nordic Pulp & Paper Research Journal 25, 505–512.

Isaksson, P., Hägglund, R., Gradin, P., 2004. Continuum damage mechanics applied to paper. International Journal of Solids and Structures 41, 4731–4755.

Lekhnitskii, S. G., 1968. Anisotropic Plates. Gordon and Breach Science Publishers Ltd.

Mäkelä, P., Östlund, S., 2003. Orthotropic elastic-plastic material model for paper materials. International Journal of Solids and Structures 40, 5599–5620.

Mäkelä, P., Östlund, S., 2012. Cohesive crack modelling of thin sheet material exhibiting anisotropy, plasticity and large-scale damage evolution. Engineering Fracture Mechanics 79, 50–60.

Menzel, A., Steinmann, P., 2003. On the spatial formulation of anisotropic multiplicative elasto-plasticity. Computional Methods in Applied Mechanics and Engineering 192, 3431–3470.

Miehe, C., 1998. Comparison of two algorithms for the computation of fourth-order isotropic tensor functions. Computers & Structures 66, 37–43.

Nagasawa, S., Fukuzawa, Y., Yamaguchi, T., Tsukatani, S., Katayama, I., 2003. Effect of crease depth and crease deviation on folding deformation characteristics of coated paperboard. Journal of Materials Processing Technology 140, 157–162.

Nygårds, M., Just, M., Tryding, J., 2009. Experimental and numerical studies of creasing of paperboard. International Journal of Solids and Structures 46, 2493–2505.

Schröder, J., Neff, P., 2002. Invariant formulation of hyperelastic transverse isotropy based on polyconvex free energy functions. International Journal of Solids and Structures 40, 401–445.

Schröder, J., Neff, P., Ebbing, V., 2008. Anisotropic polyconvex energies on the basis of crystallographic motivated structural tensors. Journal of the Mechanics and Physics of Solids 56, 3486–3506.

Stenberg, N., 2002. On the Out-of-Plane Mechanical Behaviour of Paper Materials. Ph.D. thesis, Department of Solid Mechanics, Royal Institute of Technology, Stockholm, Sweden.

Tryding, J., Gustafsson, P., 2001. Analysis of notched newsprint sheet in mode i fracture. Journal of Pulp and Paper Science 27, 103–109.

Tsai, S. W., Wu, E. M., 1971. A general theory of strength for anisotropic materials. Journal of Composite Materials 5, 58–80.

Wahlström, T., 2009. Preduction of fibre orientation and stiffness Distributions in Paper - an engineering approach. In: The 14th Fundamental Research Symposium Advances in Pulp and Paper Research,Oxford, UK.

Xia, Q. S., 2002. Mechanics of inelastic deformation and delamination in paperboard. Ph.D. thesis, Massachusetts Institue of Technology.

Xia, Q. S., Boyce, M. C., Parks, D. M., 2002. A constitutive model for the anisotropic elastic-plastic deformation of paper and paperboard. International Journal of Solids and Structures 39, 4053–4071.

Paper B

Eric Borgqvist, Mathias Wallin, Matti Ristinmaa and Johan Tryding

An anisotropic in-plane and out-of-plane elasto-plastic continuum model for paperboard

Composite Structures, 126 (2015) 184-195

An anisotropic in-plane and out-of-plane elasto-plastic continuum model for paperboard

Eric Borgqvist, Mathias Wallin, Matti Ristinmaa and Johan Tryding
Division of Solid Mechanics
Lund University, Box 118, S-221 00 Lund, Sweden

Abstract

A continuum model of paperboard material possessing a high degree of anisotropy is established. To handle the anisotropy, three vectors are introduced which phenomenologically represent the preferred directions of the material. The in-plane director vectors deform as line segments and the out-of-plane direction deforms as a normal vector. This allows for a decoupling of the in-plane and the out-of-plane responses in shearing. The model is developed for large plastic strains and consequently an expression for the plastic spin has been proposed. The choice of plastic spin allows for a control of the direction in which permanent deformations will occur. To show the predictive capabilities of the model, the important industrial process of creasing is simulated. Both the simplified line crease setup, as well as the actual rotation crease setup used in industrial applications are studied.

1 Introduction

Paperboard is a material with a high degree of anisotropy, which stems from the manufacturing process where the fibers becomes aligned in preferred directions, which results in a highly anisotropic structure. In this work, a 3D-continuum elasto-plastic model for paperboard is established, i.e. a model that captures the in-plane as well as the out-of-plane responses is developed. Classically, paperboard is characterized as an orthotropic material where the normals to the symmetry planes are denoted as Machine Direction (MD), Cross Direction (CD) and out-of-plane direction (ZD), cf. Fig. 1. The magnitude of the failure stress in the MD direction is typically 2-3 times higher compared with CD and about 100 times higher compared with the failure stress in the ZD-direction, cf. Stenberg (2002). Different modeling concepts have traditionally been employed for the modeling of the in-plane and the out-of-plane responses, such as using a combination of continuum and cohesive elements, cf. Xia (2002), Beex and Peerlings (2009) and Nygårds et al. (2009b). In this work, a model, which is able to handle the large degree of anisotropy using a purely continuum based model, is presented.

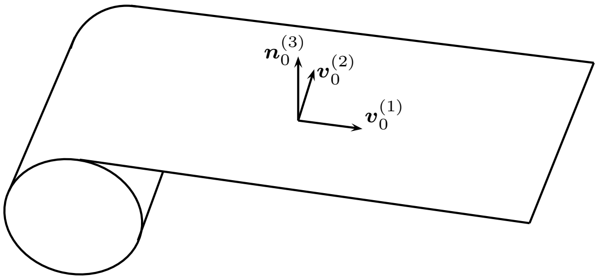

Figure 1: Illustration of the different material directions of paperboard resulting the manufacturing process. The preferred directions are aligned with the Machine(1)-, Cross(2)- and ZD(3)-directions.

Paperboard can be designed as a single-ply or multi-ply material, where the fibers in the plies are processed mechanically or chemically from wood fibers. The plies are designed to obtain desired properties through the thickness of the paperboard. The multi-ply board is a sandwiched structure, which is used to obtain a light weight construction with as high stiffness as possible without compromising other functionalities such as strength and convertability. The multi-ply design utilizes strong outer plies with higher bending resistance to prevent cracks to form, while the middle plies are made weaker such that the material can easily be folded to form a package. If a single-ply board is used, a combination of chemical additives can be pressed into the top and bottom ply to obtain a layered structure. In this work however, focus will be on the modeling of materials with a high degree of anisotropy, and for that sake the inhomogeneous properties of paperboard in the thickness direction has not been taken into account. The inhomogenous material properties can easily be included in the framework by a mapping of the material properties, cf. Huang et al. (2014). The different through thickness shear properties can be identified by using a notched shear test, as developed in Nygårds et al. (2009a) and Nygårds and Malnory (2010) or by grinding off the plies and testing the material properties of individual plies cf. Nygårds (2008). Several mechanical characteristics for the in-plane behavior of paperboard were determined in Allaoui et al. (2009), such as visco-elastic effects, plasticity and damage. Rate-dependence and damage have not been considered in the current work.

To obtain well formed packages without defects, creasing is an important industrial converting process and it is crucial for the subsequent folding operation. Creasing has been studied experimentally by several authors e.g. Cavlin (1988), Cavlin et al. (1997) and Nagasawa et al. (2003) and also in numerical studies in Beex and Peerlings (2009), Huang and Nygårds (2010), Nygårds et al. (2009b). The creasing operation reduces the initial maximal bending moment and the deeper the scored line is creased, the more the maximal bending moment is reduced. Earlier studies have modeled the simplified 2-dimensional line crease setup, whereas in this work a rotation crease with a 3-dimensional pattern is simulated as well. The modeling of the subsequent folding operation of paperboard has been investigated in Barbier et al. (2005), Huang et al. (2014) and Giampieri et al. (2011).

There exist several modeling techniques for the modeling of fiberous structures such as paperboard. Network models have been proposed in e.g. Borodulina et al. (2012) and Kulachenko (2012) where the fiber network was built up by beam elements. Insights about the mechanics present at the meso- and micro-scale of the fiber-network can be obtained by using network models. To reduce the computional cost of network models, the quasicontinuum approach was applied to fiberous materials such as paperboard in Beex et al. (2014). Continuum models for paperboard have previously been suggested, e.g. the in-plane models defined in Sawyer et al. (1998) and Mäkelä and Östlund (2003). Combined continuum and delamination models have been proposed in Beex and Peerlings (2009), Nygårds et al. (2009b), Huang and Nygårds (2010) and Xia (2002).

The in-plane yield surface in Xia et al. (2002) and further developed in Borgqvist et al. (2014) has been extended in the present work to take the out-of-plane properties into account. The yield surface is based on a set of subsurfaces in the stress-space, where each subsurface is associated with an internal variable. This approach allows the yield surface to harden distortionally in the stress-space. The yield surface in this work is equipped with additional subsurfaces such that out-of-plane plasticity is accounted for. It was observed in Stenberg et al. (2001) and Stenberg (2003), that dilation in the ZD-direction is obtained as the paperboard is sheared, and that increased shear yield stress is obtained as the material is compressed. This feature is included in the proposed model. Ideal plasticity will be assumed at the onset of failure in the out-of-plane direction.

The article is organized as follows, in sections 2 and 3 the kinematic description and the evolving anisotropy is presented. The thermodynamic framework is established in section 4, where tensors will be considered in a Cartesian setting, i.e. following the work of Ciarlet (1988). In section 5, the specific model is presented and in section 6, aspects related to the calibration are discussed. The model is implemented in a finite element framework and the results from creasing operations are shown in sections 7 and 8.

2 Kinematics

The motion of a material body from the reference configuration, $\Omega_0 \in \mathbb{R}^3$, to the current configuration $\Omega \in \mathbb{R}^3$ in the time interval $T \in [t_0, t]$, is given by $\boldsymbol{\varphi}(\boldsymbol{X}, t) : \Omega_0 \times T \rightarrow \Omega$. It is assumed that the mapping $\boldsymbol{\varphi}$ is sufficiently smooth. The vector $\boldsymbol{X}$ denotes the position of a particle in the reference configuration and the position of the same particle at time t in the current configuration is given by $\boldsymbol{x} = \boldsymbol{\varphi}(\boldsymbol{X}, t)$. The mapping of vectors in the reference configuration to the current configuration is given by the deformation gradient $\boldsymbol{F} = \nabla \boldsymbol{\varphi}$. To separate the deformation into an elastic and a plastic deformation, a multiplicative split of the deformation gradient is assumed, i.e.

$$\boldsymbol{F} = \boldsymbol{F}^e \boldsymbol{F}^p, \tag{1}$$

where $\boldsymbol{F}^e$ and $\boldsymbol{F}^p$ are the elastic and plastic deformation gradients, respectively. The split (1) introduces a stress-free intermediate configuration, which is not unique. A rigid body rotation of the intermediate configuration will leave the intermediate configuration stress free and therefore the intermediate configuration must be defined with respect to an arbitrary constitutive spin, cf. Dafalias (1998) and Harrysson and Ristinmaa (2007). For simplicity in this paper, this constitutive spin is set equal to zero, i.e. an isoclinic configuration is adopted, as introduced in Mandel (1971). Further on, the elastic deformation will be defined by the elastic Finger tensor, $\boldsymbol{b}^e = \boldsymbol{F}^e (\boldsymbol{F}^e)^T$.

Using (1), the spatial velocity gradient defined as, $\boldsymbol{l} = \dot{\boldsymbol{F}} \boldsymbol{F}^{-1}$, can be additively split into

$$\boldsymbol{l} = \boldsymbol{l}^e + \boldsymbol{F}^e \boldsymbol{L}^p \boldsymbol{F}^{e-1} = \boldsymbol{l}^e + \boldsymbol{l}^p, \tag{2}$$

where

$$\boldsymbol{l}^e = \dot{\boldsymbol{F}}^e \boldsymbol{F}^{e-1}, \qquad \boldsymbol{L}^p = \dot{\boldsymbol{F}}^p \boldsymbol{F}^{p-1}, \tag{3}$$

are referred to as the elastic and material plastic velocity gradients, respectively. The plastic velocity gradient in (2) can further be split into a symmetric part and a skew-symmetric part, i.e.

$$\boldsymbol{l}^p = \mathrm{sym}(\boldsymbol{l}^p) + \mathrm{skew}(\boldsymbol{l}^p) = \boldsymbol{d}^p + \boldsymbol{\omega}^p, \tag{4}$$

where $\boldsymbol{d}^p$ is the plastic rate of deformation tensor and $\boldsymbol{\omega}^p$ is the Eulerian plastic spin, cf. Dafalias (1998). The plastic spin, $\boldsymbol{\omega}^p$, is important to specify for anisotropic materials that undergo large plastic deformations, cf. Harrysson et al. (2007). For later purposes, the symmetric part of the spatial velocity gradient is defined as $\boldsymbol{d} = \mathrm{sym}(\boldsymbol{l})$.

3 Evolving anisotropy

The modeling framework for the anisotropy follows the format outlined in Borgqvist et al. (2014). To model the in-plane behavior, two director vectors of unit length, $\boldsymbol{v}_0^{(1)}$ and $\boldsymbol{v}_0^{(2)}$, aligned in the MD- and CD-directions in the reference configuration are introduced. These two vectors are assumed to phenomenologically represent the in-plane preferred directions of the material. The director vectors are assumed to be embedded in the continuum (i.e. the fiber-network) and are chosen to follow the elastic deformation gradient i.e.

$$\begin{aligned} \boldsymbol{v}^{(1)} &= \boldsymbol{F}^e \boldsymbol{v}_0^{(1)} \\ \boldsymbol{v}^{(2)} &= \boldsymbol{F}^e \boldsymbol{v}_0^{(2)}. \end{aligned} \tag{5}$$

Note that due to the intermediate configuration being isoclinic, the director vectors in the intermediate configuration become equal to $\boldsymbol{v}_0^{(1)}$ and $\boldsymbol{v}_0^{(2)}$, i.e. an identity mapping between the director vectors in the reference configuration to the intermediate configuration. Rather than using $\boldsymbol{v}^{(3)} = \boldsymbol{F}^e \boldsymbol{v}_0^{(3)}$, a normal vector $\boldsymbol{n}_0^{(3)}$ will be utilized for the out-of-plane behavior. The normal vector $\boldsymbol{n}_0^{(3)}$ in the reference configuration is expressed as

$$\boldsymbol{n}_0^{(3)} = \boldsymbol{v}_0^{(1)} \times \boldsymbol{v}_0^{(2)}, \tag{6}$$

i.e. a vector normal to the in-plane directions. A normal vector evolve according to the cofactor of the elastic deformation gradient,

$$\boldsymbol{n}^{(3)} = J^e \boldsymbol{F}^{e-T} \boldsymbol{n}_0^{(3)}, \tag{7}$$

where J^e is the determinant of the elastic deformation gradient, i.e. $J^e = \det(\boldsymbol{F}^e)$. The use of (7) is motivated by the fact that paperboard in essence is a sandwiched structure, consisting of layers of fibers stacked on top of each other. It can be imagined that during shearing, the paperboard response is mechanically similar to that of a deck of cards, as depicted in Fig. 2.

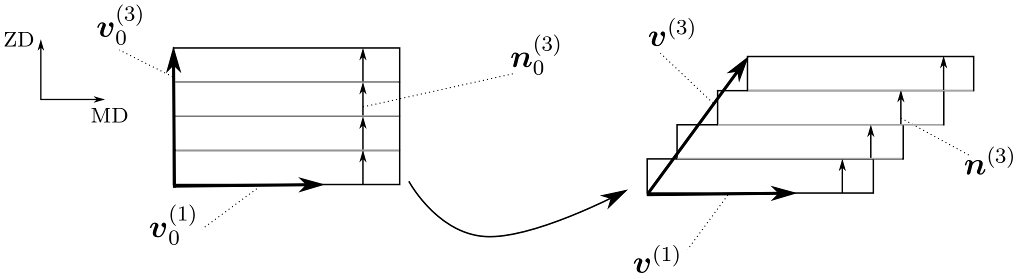

Figure 2: Out-of-plane shearing of paperboard, illustrating the idealized deformation pattern.

After the shear deformation, each fiber-layer normal, $\boldsymbol{n}^{(3)}$, is assumed to remain unchanged, while a director vector, $\boldsymbol{v}^{(3)} = \boldsymbol{F}^e \boldsymbol{v}_0^{(3)}$ has components in the MD-direction, cf. Fig. 2. The projection of $\boldsymbol{n}^{(3)}$ on the in-plane directions is therefore zero, i.e. $\boldsymbol{n}^{(3)} \cdot \boldsymbol{v}^{(1)} = 0$. The alignment of $\boldsymbol{v}^{(3)}$ will imply a coupling between the in-plane and the out-of-plane response, i.e. $\boldsymbol{v}^{(3)} \cdot \boldsymbol{v}^{(1)} \neq 0$. Use of $\boldsymbol{v}^{(3)}$ instead of $\boldsymbol{n}^{(3)}$ will result in that the stronger in-plane properties will influence the weaker out-of-plane properties, whereas the choice (7) will reduce the influence of the in-plane properties on the out-of-plane response in the model.

In the subsequent derivations, it is convenient to define a set of second order structural tensors, which are given as dyadic products of the director vectors and the normal, i.e.

$$\boldsymbol{m}^{(1)} = \boldsymbol{v}^{(1)} \otimes \boldsymbol{v}^{(1)}, \quad \boldsymbol{m}^{(2)} = \boldsymbol{v}^{(2)} \otimes \boldsymbol{v}^{(2)}, \quad \boldsymbol{m}^{(3)} = \boldsymbol{n}^{(3)} \otimes \boldsymbol{n}^{(3)}. \tag{8}$$

Later on, the evolution of the structural tensors are needed. It is therefore noted that taking the material time derivative of (5) and (7) and taking advantage of the definition of (8) and using (2) results in

$$\begin{aligned} \dot{\boldsymbol{m}}^{(1)} &= 2\text{sym}(\boldsymbol{l}^e \boldsymbol{m}^{(1)}) \\ \dot{\boldsymbol{m}}^{(2)} &= 2\text{sym}(\boldsymbol{l}^e \boldsymbol{m}^{(2)}) \\ \dot{\boldsymbol{m}}^{(3)} &= 2\big(\text{tr}(\boldsymbol{l}^e)\boldsymbol{m}^{(3)} - \text{sym}(\boldsymbol{l}^{eT} \boldsymbol{m}^{(3)})\big). \end{aligned} \tag{9}$$

The evolution of the elastic Finger tensor is needed as well and by using (2), the material time derivative of $\boldsymbol{b}^e$ can be expressed as

$$\dot{\boldsymbol{b}}^e = 2\text{sym}(\boldsymbol{l}\boldsymbol{b}^e) - 2\text{sym}(\boldsymbol{l}^p \boldsymbol{b}^e). \tag{10}$$

In the next section, the dissipation inequality will be considered when deriving expressions for the constitutive relations.

4 Dissipation inequality

The dissipation inequality in the spatial setting under isothermal conditions is given by

$$d = \boldsymbol{\tau} : \boldsymbol{d} - \rho_0 \dot{\psi} \geq 0, \tag{11}$$

where $\boldsymbol{\tau}$ is the Kirchhoff stress tensor and ψ is the Helmholz free energy per unit mass and ρ_0 is the density in the reference configuration. The free energy is assumed to be a function of the elastic Finger tensor, $\boldsymbol{b}^e$, the structural tensors, $\boldsymbol{m}^{(\alpha)}$, and a set of internal variables, $\kappa^{(\gamma)}$, which characterize the plastic response, i.e. $\rho_0\psi = \rho_0\psi(\boldsymbol{b}^e, \boldsymbol{m}^{(\alpha)}, \kappa^{(\gamma)})$. Insertion of this format of the free energy in the dissipation inequality (11) results in,

$$d = \boldsymbol{\tau} : \boldsymbol{d} - \rho_0 \tfrac{\partial \psi}{\partial \boldsymbol{b}^e} : \dot{\boldsymbol{b}}^e - \rho_0 \tfrac{\partial \psi}{\partial \boldsymbol{m}^{(\alpha)}} : \dot{\boldsymbol{m}}^{(\alpha)} - \rho_0 \tfrac{\partial \psi}{\partial \kappa^{(\gamma)}} \dot{\kappa}^{(\gamma)} \geq 0. \tag{12}$$

In (12), summation convention applies to the superscripts α and γ. Using the time derivatives of the elastic Finger tensor (10) and the structural tensors (9) as well as using arguments by Coleman and Gurtin (1967), it is concluded that

$$\boldsymbol{\tau} = 2\rho_0 \left(\frac{\partial \psi}{\partial \boldsymbol{b}^e} \boldsymbol{b}^e + \frac{\partial \psi}{\partial \boldsymbol{m}^{(1)}} \boldsymbol{m}^{(1)} + \frac{\partial \psi}{\partial \boldsymbol{m}^{(2)}} \boldsymbol{m}^{(2)} - \frac{\partial \psi}{\partial \boldsymbol{m}^{(3)}} \boldsymbol{m}^{(3)} + (\frac{\partial \psi}{\partial \boldsymbol{m}^{(3)}} : \boldsymbol{m}^{(3)}) \boldsymbol{I} \right), \tag{13}$$

where $\boldsymbol{I}$ represents the second order identity tensor. Assuming the Helmholz free energy to be an isotropic function of its arguments leads to the Kirchhoff stress tensor (13) being symmetric, cf. Menzel and Steinmann (2003) and Harrysson and Ristinmaa (2007). Insertion of (13) into (12) allows the dissipation inequality to be written as

$$d = \boldsymbol{\tau} : \boldsymbol{d}^p - K^{(\gamma)}\dot{\kappa}^{(\gamma)} \geq 0, \tag{14}$$

where the thermodynamic forces, $K^{(\gamma)}$, are energy conjugates to the internal variables, $\dot{\kappa}^{(\gamma)}$, and defined as

$$K^{(\gamma)} = \rho_0 \frac{\partial \psi}{\partial \kappa^{(\gamma)}}. \tag{15}$$

Based on the presented framework, the specific model will be discussed in the next section.

5 Model

The proposed Helmholz free energy is assumed to be additively split into an elastic and a plastic part, where the elastic part, in turn, is split into a part associated with the in-plane properties $\rho_0\psi^{ip}$, and one part, $\rho_0\psi^{op}$, associated with the out-of-plane properties, i.e.

$$\rho_0\psi^e = \rho_0\psi^{ip} + \rho_0\psi^{op}. \tag{16}$$

The invariants that will be utilized to define the model are given by

$$\begin{aligned} &I_{11} = \sqrt{\boldsymbol{m}^{(1)} : \boldsymbol{I}}, \quad I_{12} = \sqrt{\boldsymbol{m}^{(2)} : \boldsymbol{I}}, \quad I_{13} = \tfrac{1}{J^e}\sqrt{\boldsymbol{m}^{(3)} : \boldsymbol{b}^e\boldsymbol{b}^e} \\ &I_{23} = \sqrt{\boldsymbol{m}^{(3)} : \boldsymbol{I}} \quad\;\; J^e = \sqrt{\det(\boldsymbol{b}^e)}. \end{aligned} \tag{17}$$

To interpret the invariants in (17), a transformation to quantities related to the intermediate configuration can be made. Consider e.g. the invariants I_{13} and I_{23}, using the transformation of the normal vector (7) together with the definition of the structural tensor (8), provides that I_{13} and I_{23} in (17) can be written as

$$I_{13} = |\boldsymbol{F}^e\boldsymbol{n}_0^{(3)}|, \qquad I_{23} = |J^e\boldsymbol{F}^{e-T}\boldsymbol{n}_0^{(3)}| \tag{18}$$

where the Euclidean 2-norm denoted $|\cdot|$ is defined as $|\cdot| = \sqrt{[\cdot]\cdot[\cdot]}$. Since the elastic deformation gradient maps tangent vectors from the intermediate configuration to the spatial configuration, I_{13} will therefore represent the stretch of the vector $\boldsymbol{n}_0^{(3)}$. The term $J^e\boldsymbol{F}^{e-T}$ is the cofactor of the elastic deformation gradient, which maps normals to surface elements between the configurations, i.e. the Nanson's relation. Similar arguments for the remaining invariants in (17) can be made. The invariants I_{11}, I_{12} and I_{13} therefore characterize the stretches in the directions MD, CD and ZD, respectively and the invariant I_{23} represents the deformation of an area element with the normal in the ZD direction. The invariant J^e represents the deformation of a volume element. For a detailed discussion of this topic, the reader is referred to e.g. Schröder and Neff (2002). To define the elastic in-plane behavior of the material, the in-plane contribution to the energy, ψ^{ip} is postulated to have the format

$$\begin{aligned}\rho_0\psi^{ip} \;=\; & A_1\left(I_{11}+\tfrac{1}{I_{11}}\right)+A_2\left(I_{12}+\tfrac{1}{I_{12}}\right)+\\ & A_4\Big(I_{11}+I_{12}\Big)\Big(\tfrac{1}{I_{11}}+\tfrac{1}{I_{12}}\Big)+A_5\left(I_{11}+I_{12}+\tfrac{1}{I_{23}}\right),\end{aligned} \tag{19}$$

where A_1, A_2, A_4 and A_5 are elastic material parameters. The specific format (19) ensures that the parameters A_1, A_2 ,A_4 and A_5 are positive for the material considered in this work and that a stress free configuration is obtained for $\boldsymbol{F}^e = \boldsymbol{I}$. The energy is defined such that it will only contribute to the in-plane components for the initial tangent stiffness. The out-of-plane part of the free energy, $\rho_0\psi^{op}$, is assumed to be given by

$$\rho_0\psi^{op} = H^+\rho_0\psi^{top} + (1-H^+)\rho_0\psi^{cop} + \rho_0\psi^{sop}, \tag{20}$$

where the superscripts top, cop and sop refers to the tension, compression and shearing out-of-plane parts. The H^+ is a switch function, given by

$$H^+ = \begin{cases} 1 & \text{if } (I_{13}-1)\geq 0\\ 0 & \text{otherwise}\end{cases} \tag{21}$$

Due to the large difference in the material behavior in ZD-tension and ZD-compression, a switch is introduced in the free energy, (20). This is an approximation to the actual smooth transition between compression and tension, however the assumption does not introduce a significant error. A switching approach was successfully utilized in Nygårds et al. (2009b). The specific form for $\rho_0\psi^{top}$ and $\rho_0\psi^{cop}$ governing the tensile and compressive behavior are assumed to be given as

$$\rho_0\psi^{top} = A_3\left(I_{13}+\frac{1}{I_{13}}\right) \qquad \rho_0\psi^{cop} = A_7\left((I_{13})^2+\frac{1}{A_8}e^{-A_8((I_{13})^2-1)}\right), \tag{22}$$

respectively. For the compression, the exponential utilized in (22), will provide a stiffening as the material is compressed. Finally, for the out-of-plane shear part, the model is given by

$$\rho_0\psi^{sop} = A_6\Big(I_{11}+I_{12}+I_{13}-J^e\Big). \tag{23}$$

The specific forms (22) and (23) will similar to the in-plane format (19), provide positive values for the material constants A_3, A_6, A_7 and A_8 for the considered material and a stress-free state will be obtained for $\boldsymbol{F}^e = \boldsymbol{I}$. The specific form for the stress can now be established. On the basis of (19), (22) and (23) along with (13), the Kirchhoff stress is obtained as

$$\boldsymbol{\tau} = P_1\boldsymbol{m}^{(1)} + P_2\boldsymbol{m}^{(2)} + P_3\boldsymbol{m}^{(3)} + P_4\boldsymbol{I} + P_5\frac{1}{(J^e)^2}\boldsymbol{b}^e\boldsymbol{m}^{(3)}\boldsymbol{b}^e \tag{24}$$

where

$$\begin{aligned}
P_1 &= \tfrac{1}{I_{11}}\Big(A_1 + A_5 + A_6 + A_4(\tfrac{1}{I_{11}} + \tfrac{1}{I_{12}})\Big) - \tfrac{1}{(I_{11})^3}\Big(A_1 + A_4(I_{11} + I_{12})\Big) \\
P_2 &= \tfrac{1}{I_{12}}\Big(A_2 + A_5 + A_6 + A_4(\tfrac{1}{I_{12}} + \tfrac{1}{I_{11}})\Big) - \tfrac{1}{(I_{12})^3}\Big(A_2 + A_4(I_{12} + I_{11})\Big) \\
P_3 &= \tfrac{A_5}{(I_{23})^3} \\
P_4 &= -\tfrac{A_5}{I_{23}} - A_6 J^e \\
P_5 &= \tfrac{A_6}{I_{13}} + H^+ A_3\left(\tfrac{1}{I_{13}} - \tfrac{1}{(I_{13})^3}\right) + (1 - H^+)2A_7\left(1 - e^{-A_8((I_{13})^2-1)}\right)
\end{aligned} \tag{25}$$

Note that the stress-strain relationship (24) can be represented as a map $\boldsymbol{\tau} : \mathbb{R}^9 \to \mathbb{R}^6$, i.e.

$$\boldsymbol{\tau} = \boldsymbol{\tau}(\boldsymbol{F}^e, \boldsymbol{v}^{(1)}(\boldsymbol{F}^e), \boldsymbol{v}^{(2)}(\boldsymbol{F}^e), \boldsymbol{n}^{(3)}(\boldsymbol{F}^e)). \tag{26}$$

To illustrate the stiffness, the initial material tangent has been determined by assuming $\boldsymbol{F} = \boldsymbol{F}^e$. The initial stiffness is given by

$$\boldsymbol{\mathcal{D}} = \tfrac{\partial \boldsymbol{\tau}}{\partial \boldsymbol{F}}\boldsymbol{F}^T\Big|_{\boldsymbol{F}=\boldsymbol{I}}, \tag{27}$$

cf. Harrysson et al. (2007) for a derivation. Consider the split

$$\boldsymbol{\mathcal{D}} = \boldsymbol{\mathcal{D}}^{ip} + \boldsymbol{\mathcal{D}}^{op}, \tag{28}$$

of the initial tangent matrix. The $\boldsymbol{\mathcal{D}}^{ip}$ provide the stiffnesses for the in-plane components, i.e. it is obtained from the energy (19) as,

$$[\boldsymbol{\mathcal{D}}^{ip}] = \begin{pmatrix}
2A_1 + 2A_4 + 2A_5 & A_5 - 2A_4 & 0 & & & \\
A_5 - 2A_4 & 2A_2 + 2A_4 + 2A_5 & 0 & & & \\
0 & 0 & 0 & & & \\
 & & & A_5 & & \\
 & & & & 0 & \\
 & & & & & 0
\end{pmatrix} \tag{29}$$

The stiffness tensor (29) is expressed using Voigt notation with the order (MD,CD,ZD) in the indices. It is seen that the elastic parameters, A_1, A_2, A_4 and A_5 are decoupled from the out-of-plane components of $[\boldsymbol{D}^{ip}]$. The free energies (23) and (22) provide the initial stiffness $\boldsymbol{\mathcal{D}}^{op}$ that is given by

$$[\boldsymbol{\mathcal{D}}^{op}] = \begin{pmatrix} 0 & -A_6 & -A_6 & & & \\ -A_6 & 0 & -A_6 & & & \\ -A_6 & -A_6 & 2A_3H^{+} + 4A_7A_8H^{-} & & & \\ & & & A_6 & & \\ & & & & A_6 & \\ & & & & & A_6 \end{pmatrix} \tag{30}$$

As a consequence of (23), the elastic stiffness in MD-ZD and CD-ZD shearing are identical in the model. Experimental out-of-plane shear tests in MD-ZD and CD-ZD reveal that the stiffness for the two loading cases are difficult to distinguish one from the other, cf. Nygårds (2008). The contribution (23) will give rise to a negative Poisson effect between the in-plane and out-of-plane directions. Negative Poisson ratios have been experimentally observed for paperboard in Stenberg and Fellers (2002).

The elastic parameters A_i can be obtained by performing tests in the preferred directions MD, CD and ZD. The calibration procedure is similar to that of standard orthotropic models, cf. Borgqvist et al. (2014) for a recent example of the calibration procedure.

5.1 Plasticity

The yield-surface proposed in Xia et al. (2002) and further developed in Borgqvist et al. (2014) will be used to model the plasticity. The proposed yield surface consists of 12 subsurfaces, where six subsurfaces belong to the in-plane stress states and six new subsurfaces belong to the out-of-plane stress states, i.e.

$$f(\boldsymbol{\tau}, \boldsymbol{n}_s^{(\beta)}, K^{(\beta)}) = \sum_{\nu=1}^{12} \chi^{(\nu)} \left(\frac{\boldsymbol{\tau} : \boldsymbol{n}_s^{(\nu)}}{\tau^{(\nu)}} \right)^{2k} - 1. \tag{31}$$

The subsurfaces are defined by the yield-plane normals $\boldsymbol{n}_s^{(\nu)}$. The yield-plane normals are defined as the dyadic products of the director vectors and director normal according to

$$\boldsymbol{n}_s^{(\nu)} = \sum_{i=1}^{3} \sum_{j=1}^{3} N_{ij}^{(\nu)} \bar{\boldsymbol{v}}^{(i)} \otimes \bar{\boldsymbol{v}}^{(j)} \tag{32}$$

where $N_{ij}^{(\nu)}$ are the coefficients of the yield normals and $\bar{\boldsymbol{v}}^{(i)}$ represent the normed director vectors and the normed director normal, i.e.

$$\bar{\boldsymbol{v}}^{(1)} = \tfrac{1}{|\boldsymbol{v}^{(1)}|}\boldsymbol{v}^{(1)}, \quad \bar{\boldsymbol{v}}^{(2)} = \tfrac{1}{|\boldsymbol{v}^{(2)}|}\boldsymbol{v}^{(2)}, \quad \bar{\boldsymbol{v}}^{(3)} = \tfrac{1}{|\boldsymbol{n}^{(3)}|}\boldsymbol{n}^{(3)}. \tag{33}$$

The coefficients $N_{ij}^{(\nu)}$ are chosen such that the normalizing condition,

$$\sqrt{\boldsymbol{n}_s^{(\nu)} : \boldsymbol{I}} = 1, \tag{34}$$

is fulfilled in the reference configuration when the coordinate system is aligned with the MD, CD and ZD-directions. The stress $\tau^{(\nu)}$, in (31) associated with each yield-plane is defined as

$$\tau^{(\nu)} = K_0^{(\nu)} + K^{(\nu)}. \tag{35}$$

The parameter $K_0^{(\nu)}$ is related to the initial yield stress and geometrically represent the initial distance to the subsurface in the stress space. The change in distance of the subsurface is associated with the hardening variable $K^{(\nu)}$. Each hardening variable is associated with a conjugate internal variable $\kappa^{(\nu)}$, which allows the subsurfaces to be translated independently of each other in the stress space. By introducing a coupling matrix as in Borgqvist et al. (2014), a connection between the subsurfaces can be introduced. This coupling allows for modeling of the cross-softening effects, e.g. the softening in the MD-direction due to previous loading in the CD-direction. However, for simplicity the effects of pre-straining is ignored in the present model. In (31), k is a constant natural number and $\chi^{(\nu)}$ is a switch function, which determines whether a yield-plane is potentially active,

$$\chi^{(\nu)} = \begin{cases} 1 & \text{if} \quad \boldsymbol{\tau} : \boldsymbol{n}_s^{(\nu)} > 0 \\ 0 & \quad \text{otherwise.} \end{cases} \tag{36}$$

In the formulations of Xia et al. (2002) and Borgqvist et al. (2014), the yield surface was used to model in-plane plasticity, i.e. only six subsurfaces were used. In this work, additional six subsurfaces are introduced. As an example, the yield subsurface connected to the positive oriented MD-ZD out-of-plane shear is assumed to have the following format

$$\boldsymbol{n}_s^{(\nu)} = N_{13}^{(\nu)} \bar{\boldsymbol{v}}^{(1)} \otimes \bar{\boldsymbol{v}}^{(3)} + N_{33}^{(\nu)} \bar{\boldsymbol{v}}^{(3)} \otimes \bar{\boldsymbol{v}}^{(3)}. \tag{37}$$

The subsurface (37) will introduce a coupling between the shear stress and the normal stress in ZD-direction, i.e. the slope $\hat{m}$ in Fig. 3b. This frictional behavior implies that the material starts to yield at a higher shear stress when simultaneously subjected to a compression in ZD. The coupling also implies that there will be dilation in ZD-direction when the material is sheared and associated plasticity is adopted, see also Xia (2002). Note that $N_{ij}^{(\nu)}$ in (37) is not symmetric. This non-symmetry is important for specifying the evolution of the direction of the plastic flow, which will be discussed later on. The remaining yield surface parameters are summarized in the Appendix. The shape of the yield surface, (31), is shown in the MD-CD stress space in Fig. 3a and in the ZD and MD-ZD-shear stress space in Fig. 3b.

The coupling of the ZD-stress, $[\boldsymbol{\tau}]_{33}$, to the out-of-plane shear stress, $[\boldsymbol{\tau}]_{13}$, is critical for modeling of many industrial processes. In the creasing process, both compressive stresses in the ZD-direction and out-of-plane shearing are present simultaneously, cf. also Beex and Peerlings (2012) for a discussion on the frictional influences on paperboard.

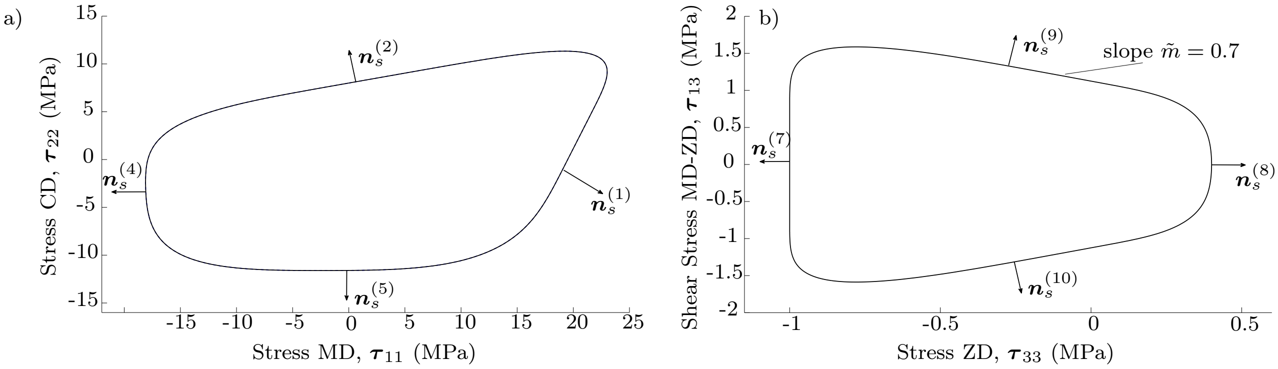

Figure 3: a) Typical shape of the yield surface in MD stress-CD stress space, b) Typical shape of the yield surface in ZD stress-MD-ZD shear stress space.

Hardening variables, $\kappa^{(\nu)}$, are introduced for the in-plane subsurfaces associated with tension and shear, $\nu = \{1, 2, 3, 6\}$, as well as for the subsurface associated with the ZD-compression $\nu = 7$, see Appendix for the abbreviation of ν. For the remaining subsurfaces, ideal plasticity is used. The conjugate hardening variables are given by

$$\begin{aligned} K^{(\nu)} &= a_\nu \ln\left(b_\nu \kappa^{(\nu)} + 1\right) \qquad && \nu = \{1, 2, 3, 6\} \\ K^{(\nu)} &= a_\nu \kappa^{(\nu)} && \nu = 7 \end{aligned} \tag{38}$$

which can easily be derived from a potential ψ^p. Associated plasticity is assumed for the evolution laws, which yields

$$\begin{aligned} \boldsymbol{d}^p &= \dot{\lambda}\frac{\partial f}{\partial \boldsymbol{\tau}} &&= \textstyle\sum_{\gamma=1}^{12} \chi^{(\gamma)} \frac{\dot{\lambda} 2k \Lambda_\gamma^{2k-1}}{\tau^{(\gamma)}} \operatorname{sym}(\boldsymbol{n}_s^{(\gamma)}) \\ \dot{\kappa}^{(\nu)} &= \dot{\lambda}\frac{\partial f}{\partial K^{(\nu)}} &&= -\chi^{(\nu)} \frac{\dot{\lambda} 2k \Lambda_\nu^{2k}}{\tau^{(\nu)}} \end{aligned} \tag{39}$$

where

$$\Lambda_\nu = \frac{\boldsymbol{\tau} : \boldsymbol{n}_s^{(\nu)}}{\tau^{(\nu)}} \tag{40}$$

was introduced to simplify the notation.

5.2 Eulerian plastic spin

During e.g. the creasing process, large plastic deformations take place and therefore the eulerian plastic spin $\boldsymbol{\omega}^p$ needs to be specified. The eulerian plastic spin is used to control the direction of the permanent deformation and is chosen as

$$\boldsymbol{\omega}^p = \sum_{\gamma=1}^{12} \chi^{(\gamma)} \frac{\dot{\lambda} 2k \Lambda_\gamma^{2k-1}}{\tau^{(\gamma)}} \operatorname{skew}(\boldsymbol{n}_s^{(\gamma)}). \tag{41}$$

The $N_{ij}^{(\nu)}$ associated with the in-plane shear ($\nu = 3, \nu = 6$) are symmetric, while the out-of-plane shear, $N_{ij}^{(\nu)}$, are not, cf. (37). The plastic deformation in the out-of-plane shearing is assumed to represent the permanent displacement of the fiber layers relative to each other, cf. Fig. 2. From (37), the symmetric and skew-symmetric plastic velocity gradients are proportional to

$$\begin{aligned} \boldsymbol{d}^p &\propto N_{13}^{(\nu)}\tfrac{1}{2}(\bar{\boldsymbol{v}}^{(1)} \otimes \bar{\boldsymbol{v}}^{(3)} + \bar{\boldsymbol{v}}^{(3)} \otimes \bar{\boldsymbol{v}}^{(1)}) \\ \boldsymbol{\omega}^p &\propto N_{13}^{(\nu)}\tfrac{1}{2}(\bar{\boldsymbol{v}}^{(1)} \otimes \bar{\boldsymbol{v}}^{(3)} - \bar{\boldsymbol{v}}^{(3)} \otimes \bar{\boldsymbol{v}}^{(1)}). \end{aligned} \tag{42}$$

By using (32) and the subsurface parameters provided in the Appendix, it can be shown that plastic velocity gradient $\boldsymbol{l}^p$ is independent of $\bar{\boldsymbol{v}}^{(3)} \otimes \bar{\boldsymbol{v}}^{(1)}$. The plastic velocity gradient is however proportional to

$$\boldsymbol{l}^p \propto N_{13}^{(\nu)}\bar{\boldsymbol{v}}^{(1)} \otimes \bar{\boldsymbol{v}}^{(3)}. \tag{43}$$

In a simple shear state, this will imply that the stacked fiber layers are permanently sheared as they slide over each other $\bar{\boldsymbol{v}}^{(1)} \cdot \boldsymbol{l}^p\bar{\boldsymbol{v}}^{(3)} \propto N_{13}^{(\nu)}$, but can not be plastically sheared in the direction in which they are stacked, i.e. $\bar{\boldsymbol{v}}^{(3)} \cdot \boldsymbol{l}^p\bar{\boldsymbol{v}}^{(1)} = 0$.

To illustrate the effect of the plastic spin for the situation depicted in Fig. 2, consider the deformation gradient

$$\dot{\boldsymbol{F}} = \dot{\gamma}\bar{\boldsymbol{v}}^{(1)} \otimes \bar{\boldsymbol{v}}^{(3)}. \tag{44}$$

Note that $\bar{\boldsymbol{v}}^{(1)}$ and $\bar{\boldsymbol{v}}^{(3)}$ are orthonormal and will not change during this specific deformation, as depicted in Fig. 2. To simplify the derivations, it is assumed that the only active subsurface in (31), is given by

$$\boldsymbol{n}_s^{(9)} = \bar{\boldsymbol{v}}^{(1)} \otimes \bar{\boldsymbol{v}}^{(3)}. \tag{45}$$

If $\dot{\boldsymbol{F}}^e = \boldsymbol{0}$, the Kirchhoff stress (26) will be constant and an ideal plastic response can be obtained. Using that at the onset of plasticity $\boldsymbol{F} = \boldsymbol{F}^e$ and $\boldsymbol{F}^p = \boldsymbol{I}$, and using (2), (3) gives

$$\dot{\boldsymbol{F}}^e = \dot{\boldsymbol{F}} - \boldsymbol{F}^e\dot{\boldsymbol{F}}^p. \tag{46}$$

The deformation gradient provided in (44) together with (4) results in

$$\dot{\boldsymbol{F}}^e = \dot{\gamma}\bar{\boldsymbol{v}}^{(1)} \otimes \bar{\boldsymbol{v}}^{(3)} - (\boldsymbol{d}^p + \boldsymbol{\omega}^p)\left(\boldsymbol{I} + \gamma\bar{\boldsymbol{v}}^{(1)} \otimes \bar{\boldsymbol{v}}^{(3)}\right). \tag{47}$$

With the choice $\boldsymbol{\omega}^p = \boldsymbol{0}$, (47) and taking advantage of (39) and (45) it follows that

$$\dot{\boldsymbol{F}}^e = \left(\dot{\gamma} - \frac{\dot{\lambda}C}{2}\right)\bar{\boldsymbol{v}}^{(1)} \otimes \bar{\boldsymbol{v}}^{(3)} - \frac{\dot{\lambda}C}{2}\left(\bar{\boldsymbol{v}}^{(1)} \otimes \bar{\boldsymbol{v}}^{(1)} + \gamma\bar{\boldsymbol{v}}^{(3)} \otimes \bar{\boldsymbol{v}}^{(1)}\right) \tag{48}$$

where it was used that $\bar{\boldsymbol{v}}^{(1)}$ and $\bar{\boldsymbol{v}}^{(3)}$ are orthonormal and $C = \frac{2k\Lambda_9^{2k-1}}{\tau^{(9)}}$ was defined. From (48) it is apparent that $\dot{\boldsymbol{F}}^e \neq \boldsymbol{0}$ at the onset of plasticity for the choice $\boldsymbol{\omega}^p = \boldsymbol{0}$. For the choice (41) however, a similar computation with (47), (39) and (45) yields

$$\dot{\boldsymbol{F}}^e = \left(\dot{\gamma} - \dot{\lambda}C\right)\bar{\boldsymbol{v}}^{(1)} \otimes \bar{\boldsymbol{v}}^{(3)}. \tag{49}$$

The plastic multiplier $\dot{\lambda}$ can be obtained from the consistency condition $\dot{f} = 0$. Using that for this particular load situation that there are no evolution of the director vectors and director normal gives

$$\dot{f} = \frac{\partial f}{\partial \boldsymbol{\tau}} : \frac{\partial \boldsymbol{\tau}}{\partial \boldsymbol{b}^e} : \dot{\boldsymbol{b}}^e = 0. \tag{50}$$

Using the expression for $\frac{\partial \tau_{ij}}{\partial b^e_{kl}}$ provided in the appendix (56), together with (39), (41), (10) and $\boldsymbol{b}^e = \boldsymbol{F}^e \boldsymbol{F}^{eT}$, yields

$$\dot{f} = 4C \left(\frac{(3A_3 + A_6)\gamma^2 + A_6}{(\gamma^2 + 1)^{5/2}} \right) \left(\dot{\gamma} - \dot{\lambda} C \right) = 0 \tag{51}$$

which provides $\dot{\lambda} = \frac{\dot{\gamma}}{C}$ and as a consequence (49) provides

$$\dot{\boldsymbol{F}}^p = \dot{\boldsymbol{F}}. \tag{52}$$

The out-of-plane shear load situation for the generalization when all subsurfaces exists has been simulated. In the simulation, there is no constraint for the displacement in ZD-direction and the plastic spin has been chosen according to (41) and $\boldsymbol{\omega}^p = \boldsymbol{0}$ and the results are shown in Fig. 4.

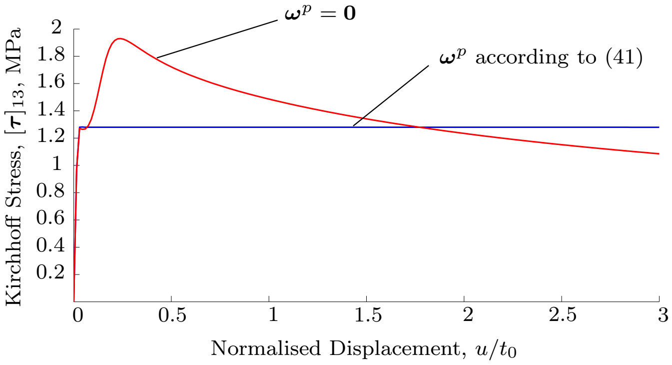

Figure 4: Result from the out-of-plane shear simulation. The red curve is obtained by choosing the plastic spin as $\boldsymbol{\omega}^p = \boldsymbol{0}$ whereas $\boldsymbol{\omega}^p$ according to (41) generates the blue curve.

With the choice $\boldsymbol{\omega}^p = \boldsymbol{0}$, a rapid increase in the shear stress will initially take place, cf. Fig. 4, while the choice (41) results in that ideal plasticity is obtained. Clearly the choice of plastic spin has a significant impact on the results.

6 Calibration

A single-ply paperboard, which is assumed to be homogeneous has been used for evaluating the model, i.e. the same material parameters are used throughout the thickness. A total of nine tests are needed to calibrate the model and to extract all material parameters. The tests include: 3 in-plane tensile tests (MD, CD and 45^o), two in-plane compression tests (MD,CD), two out-of-plane shear tests (ZD-MD, ZD-CD) and out-of-plane tests in tension and compression (ZD). This set of calibration tests are typical for orthotropic materials. The calibration procedure outlined in Borgqvist et al. (2014) and Xia et al. (2002) was used to calibrate the in-plane part of the model. The results from the in-plane calibration are shown in Fig. 5.

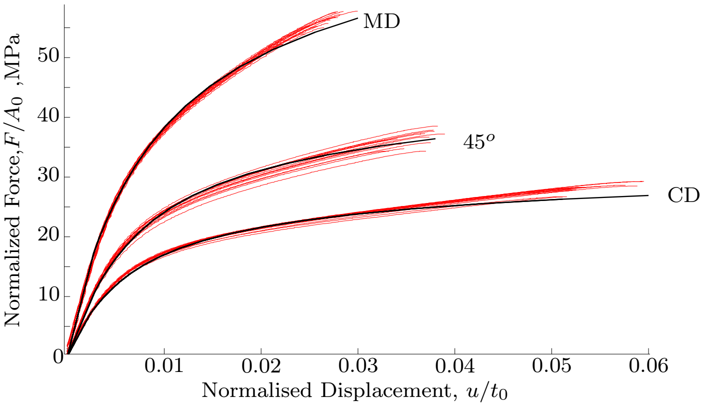

Figure 5: Uniaxial tests used for calibration of the model, tension tests in MD, CD and 45^o directions. Simulation results obtained from the calibrated model are indicated by black lines and red lines indicate measured data.

The in-plane compression strengths were determined to be -17.9 MPa in MD and -11.6 MPa in CD, using the Long Compression Test (LCT) apparatus, which is equipped with lateral support to prevent buckling, cf. Cavlin and Fellers (1975). These values have been used as the yield strengths in compression. The in-plane strain ratios between MD and CD have been determined by using digital image correlation in the uniaxial MD and CD tests.

The calibration to the out-of-plane compression is shown in Fig. 6. A small hysteresis is present during unloading cf. Fig. 6, which is not taken into account by the current model. The hysteresis is however not crucial for the simulations presented in the work herein.

Remaining parameters related to the out-of-plane properties can be found by performing ZD-tension tests and out-of-plane shear tests. The ZD-tension failure strength was determined to be 0.4 MPa in a uniaxial ZD-tension test. Due to lack of reliable data for the out-of-plane shear strength, the initial yield stress has been chosen to fit the force-displacement curve in creasing. A value of 2.5 MPa for both the MD and CD initial shear yield stress have been employed. The parameter $\tilde{m}$ related to the paper-paper friction in Fig. 3b can be found by performing experiments were first an initial ZD-compression state is applied to the material and then the paperboard is subsequently sheared, cf. Stenberg et al. (2001). The parameter governing the compression-shear coupling, has been estimated from Stenberg et al. (2001) to $\tilde{m} = 0.7$, which is similar to the paper-paper friction coefficient found in Rättö (2012) and Anna Johansson and Haugen (1998).

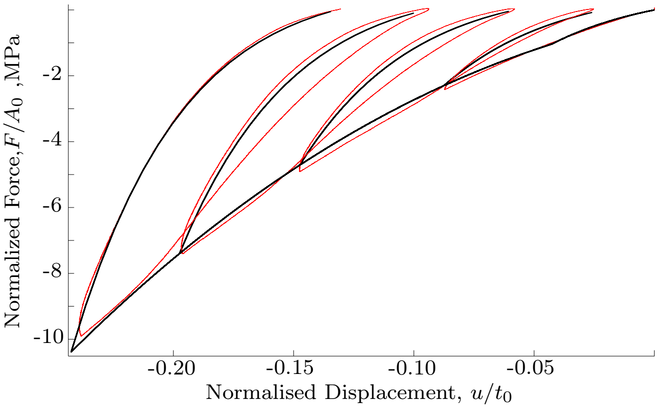

Figure 6: Uniaxial test in ZD-compression. Simulation results obtained from FEM-analysis are indicated by black lines and red lines indicate measured data.

The response under combined compression and shear has been simulated and the result is illustrated in Fig. 7. A paperboard with intial thickness t_0 is compressed in the ZD-direction with a constant stress and then sheared while keeping the ZD-stress fixed. The

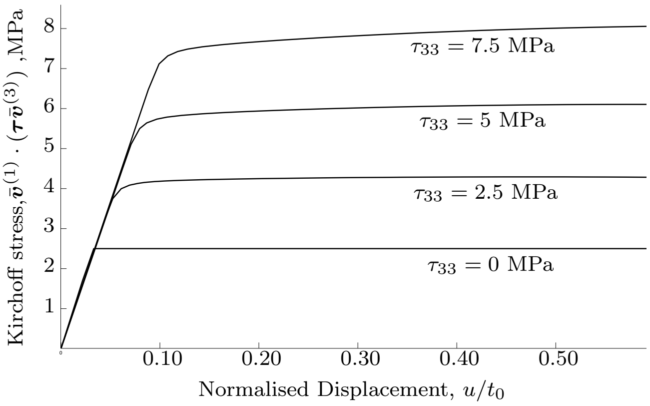

Figure 7: Simulation of out-of-plane shear subjected to superimposed compression in ZD, i.e. $\tau_{33} = \bar{\boldsymbol{v}}^{(3)} \cdot (\boldsymbol{\tau}\bar{\boldsymbol{v}}^{(3)})$.

response is similar to that previously reported in the literature. As seen in Fig. 7, the material can withstand higher stresses as it is compressed, which is typical for frictional materials like paperboard. The pressure dependent friction parameter, $\tilde{m}$, is important for the creasing processes, as have been reported in Beex and Peerlings (2012). The elastic and plastic parameters are summarized in the Appendix.

7 Line Creasing

Creasing is an important industrial process that is essential for the quality of folded package material. The creasing process reduces the resistance to bending and prevents surface cracks from being generated during the subsequent folding process. A simplified creasing process is often used in the industry to study the behavior of the paperboard, cf. Nagasawa et al. (2003) and Cavlin (1988). The setup can for instance be used to study the relation between the crease depth and surface cracks. The line crease setup previously used in Nygårds et al. (2009b), is depicted in Fig. 8.

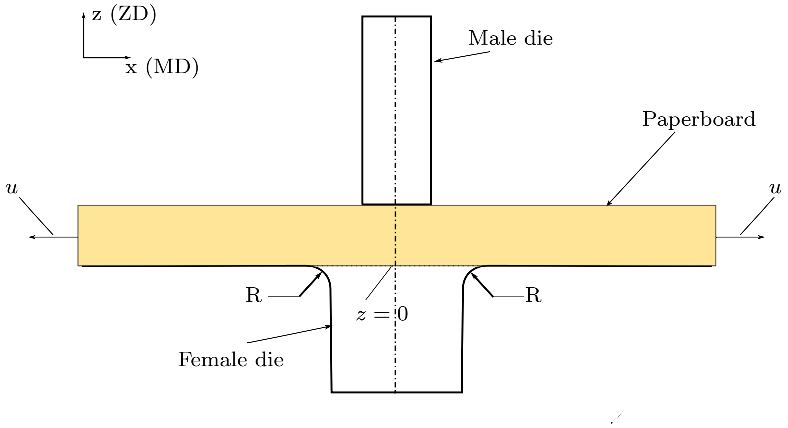

Figure 8: A schematic of the line creasing procedure.

The webtension is applied by introducing a prescribed displacement, u, as shown in Fig. 8, such that a certain initial force is obtained. The male die is then moved into contact with the paperboard and the creasing operation starts. The male die presses the paperboard into the groove of the female die and when the male die has moved such that it is aligned with the female die, the displacement of the male die is defined as zero. The width of the male die is 0.7 mm and the width of the female die is 1.7 mm. The board is 110 mm long, 38 mm wide and 0.39 mm thick and the strip has been cut out in the 45^o-direction.

The material model has been implemented in the commercial software ABAQUS Abaqus User's Manual. Dassault Systemes. Abaqus Inc (2013), via the subroutine option UMAT. The problem is solved using the standard ABAQUS-direct solver, with the linesearch algorithm activated. The evolution equations given by the plastic deformation gradient (3), the internal variables (39) and the yield condition (31) have been discretized using the backward Euler scheme. The resulting equation has been solved using the Newton-Raphson algorithm and the algorithmic tangent stiffness has been implemented. The derivation of the algorithmic tangent stiffness tensor is straight-forward but lengthy and is therefore included in the appendix. The paperboard has been discretized using eight node 3d-brick elements with full integration and 29 elements through the thickness. For the contact between the tools and the paperboard, an exponential over-closure relationship has been utilized. To reduce the computational cost, the width of the paperboard specimen was taken as 2 mm in the simulation, where 5 elements were used through the width. Symmetry boundary condition has been applied at the center of the male die. The small radius R, depicted in Fig. 8, has been taken to be 0.05 mm. A static Coulomb friction model between the tools and the paperboard has been utilized with the friction coefficient 0.4, cf. also Back (1991). The force applied to the male tool vs the displacement of the tool and the in-plane forces vs the displacement of the male tool are shown in Fig. 9.

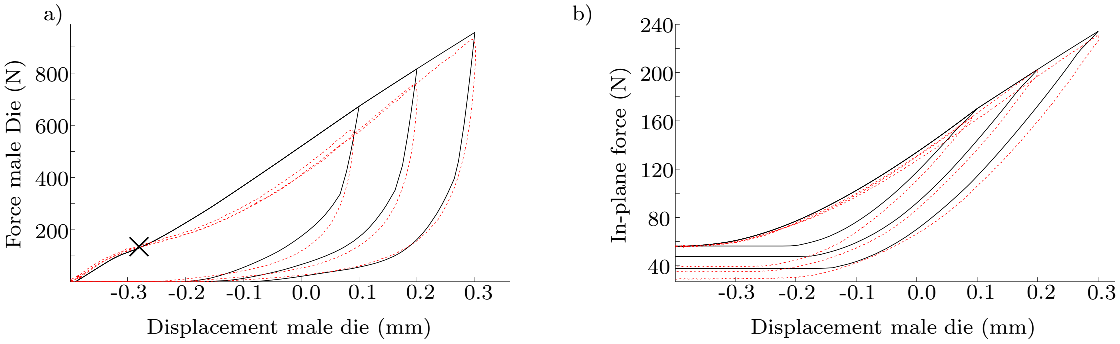

Figure 9: Simulation (black) and experimental (red-dashed) force displacement curves of a) Reaction force from male die vs displacement of male die b) In-plane force vs male die displacement.

From Fig. 9, it can be concluded that the overall shape of the macroscopic force-displacement curves can be captured. The simulated peak forces correspond well to the experimental results, however the simulations can not capture the pronounced decrease in stiffness observed at load level marked with X in Fig. 9a. The decrease in stiffness is due to the shear failure of the material, but as there is no damage incorporated in the model, this drop in stiffness can not be captured. The subsequent increase in stiffness after the initial drop in Fig. 9a, is due to the ZD compression becoming more dominant as the crease displacement increases. The in-plane forces in Fig. 9b is however captured by the model. The residual in-plane force after the male die is unloaded, is slightly larger compared with measured force, indicating that the ideal plastic assumption overestimates the amount of permanent deformation and as a consequence the paperboard can not be fully relaxed.

As the inclusion of the paper-paper friction parameter $\tilde{m}$ for the continuum is a new feature in the model compared with previous models cf. e.g. Nygårds et al. (2009b), a sensitivity analysis with respect to the parameter $\tilde{m}$ has been performed, cf. Fig. 10.

As seen in Fig. 10, the paper-paper friction parameter $\tilde{m}$ has a significant impact on the macroscopic force-displacement curves. The drop in stiffness in Fig. 10a, becomes more pronounced as $\tilde{m}$ is decreased, which is due to the magnitude of the shear stresses decreases. With decreasing $\tilde{m}$, the in-plane forces also increases. It can also be noted that the in-plane forces after unloading, increases with a decreasing $\tilde{m}$. In addition, it has been

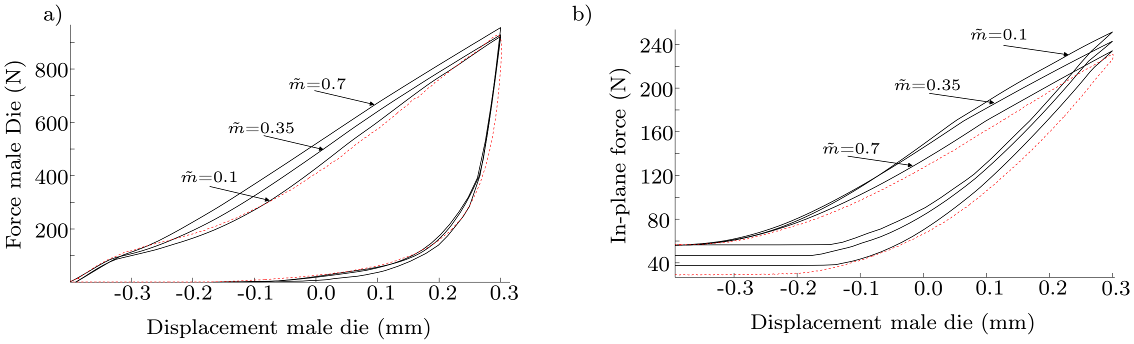

Figure 10: Sensitivity analysis with respect to material parameter $\tilde{m}$. Dashed red line indicate measurement data. a) Reaction force from male die vs Displacement of male die b) In-plane force vs male die displacement.

noted that increasing the friction coefficient between the tools and the paper, gives a softer response for the in-plane force curve.

To illustrate the shear induced permanent deformations of paperboard, contour plots of an effective plastic shear strain measure, defined from

$$\dot{\kappa}^s_{eff} = \sqrt{(\dot{\kappa}^{(9)})^2 + (\dot{\kappa}^{(10)})^2 + (\dot{\kappa}^{(11)})^2 + (\dot{\kappa}^{(12)})^2}, \tag{53}$$

is shown in Fig. 11. Note that the indices 9-12 indicate the out-of-plane shear deformations, cf. Appendix.

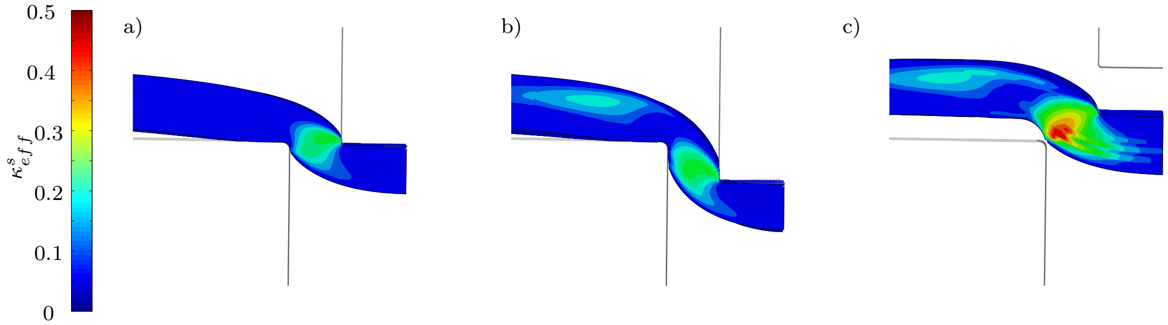

Figure 11: Simulation of line-crease at the displacement levels a) 0mm, b) 3mm (fully loaded) and c) unloaded. The effective plastic shear strain, κ^s_{eff}, is illustrated.

In Fig. 11c, the final shape of the paperboard after the crease operation is shown. The shape of the paperboard is similar to that obtained from the physical tests. There is significant amount of shear induced in the paperboard in Fig. 11, i.e. indicating maximum plastic shear strains at the order of 50 %. The effective plastic shear strain also develops during the unloading phase of the male die, cf. Fig. 11c, as was observed in Nygårds et al.

(2009b) as well. The figure indicates that shear is induced outside the groove of the female die, as the displacement of the male die becomes greater than 0 mm.

8 3D-Rotation Creasing

Previous studies on creasing have been restricted to the simplified 2-dimensional line crease setup. To demonstrate the capabilities and numerical robustness of the proposed model, the industrial relevant rotation creasing operation of paperboard has been simulated. The modeling of the rotation crease procedure is important for understanding of the complex interaction between the paperboard and the tools in the actual industrial process. An illustration of the simulated geometry is shown in Fig. 12.

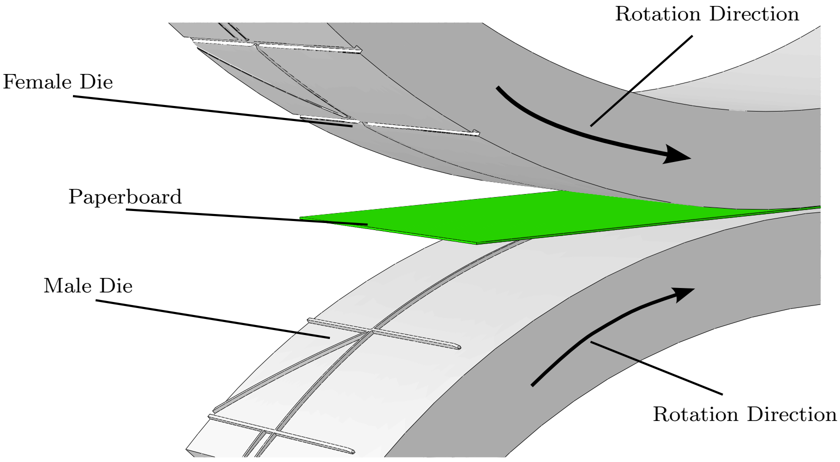

Figure 12: The simulation of the rotation creasing of paperboard.

To fold a corner of a package, a 2-dimensional crease pattern is needed, in contrast to the line crease examined in section 7. Referring to Fig. 12, it can be seen that the three line creases that meet defines a K-shaped crease pattern. The crease width of the male die is 0.7 mm whereas the width of the female die is 1.6 mm. A static analysis has been performed using the material model implemented in ABAQUS. Five elements are used through the thickness of the paperboard, cf. Fig. 13 for a close up at the mesh in the vicinity of the crease region. An exponential-overclosure relationship is used for the contact. The male and female dies have been modeled using rigid body shell elements with the same friction coefficient as in the line crease simulation, i.e. 0.4 between the paperboard and tools. The dimensions of the paperboard has been taken as 60 × 28.25 × 0.4 mm, which has been meshed with 101520 elements. The same material parameters as those in the line crease setup has been used in the simulation. In the first step of the simulation, a constant traction of 5 MPa is applied at the edges of the paperboard to mimic the web-tension present in the process. The magnitude of the applied traction is in the elastic regime and of similar magnitude to the initial applied in-plane traction examined in section 7. The cylinders are then moved vertically into position until a crease depth of 0.2 mm is obtained and then the crease operation starts by rotating the cylinders in the direction shown in Fig. 12.

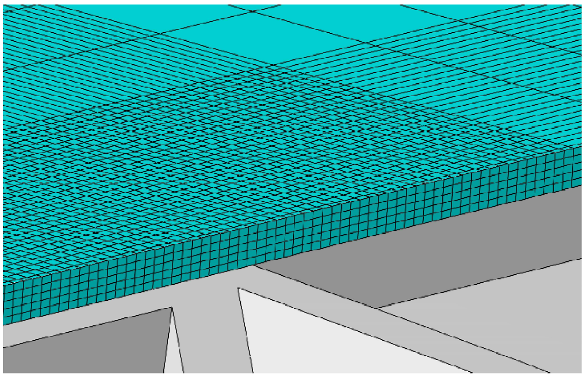

Figure 13: A zoomed section of the mesh around the crease region. Five elements are used through the thickness and a total of 101520 elements have been used for the paperboard.

With the 2-dimensional crease pattern used in the rotation creasing procedure, significant deformations are induced and the stress distribution in the paperboard is not obvious. Due to the complex stress state, the out-of-plane shear stress distribution has been studied in detail. The shear-stress field is related to the induced delamination and therefore the quality of the subsequent fold. The stress-field has been studied at sections with normal in the MD-direction of the paperboard. A close up of the female die around the corner crease is shown in Fig. 14. The location of the sections in the paperboard, at which the out-of-plane shear stresses are studied, are marked in Fig. 14 by the positions (a)-(f). The CD-out-of-plane shear stresses, $\bar{\boldsymbol{v}}^{(2)} \cdot (\boldsymbol{\tau}\bar{\boldsymbol{v}}^{(3)})$, through the thickness of the paperboard are shown in Fig. 15. The snapshots corresponds to instants when the male die is fully penetrated at the positions (a)-(f).

At position (a) in Fig. 15, the out-of-plane shear stress field distribution is similar to the effective plastic shear strain field, κ^s_{eff}, resulting from the line-crease, cf. section 7. Note that there is a negative (blue) shear stress field on the left side and a positive (red) on the right side, which is expected due to the load situation is similar to the line crease studied in section 7. At position (b), only the right-side of the female die is in contact with the paperboard and there are only significant shear stresses at that side. The stress zone is also wider compared with (a), but the magnitude is less. In (c), there are virtually no shear stresses induced in the paperboard, despite the severe deformation. The shear stresses have been unloaded, which might be due to that the paperboard is not in contact with the female die. Thereafter in (d), the paperboard is in contact with the female die on the left side and shear stresses are being generated close to the contact point. Further more, it is noticed that the width of the stress zone in (d) is approximately the same as

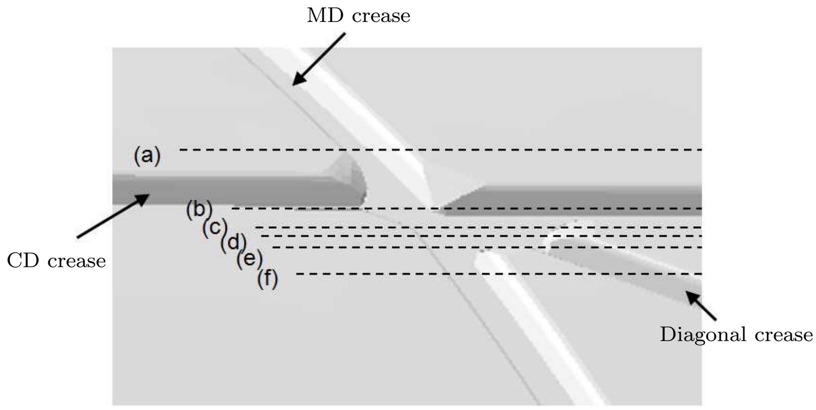

Figure 14: Female die around corner crease used in simulation. The dashed lines, (a)-(f), indicate the position of the cuts in the contour plots of the out-of-plane shear stress in Fig. 15.

the width in field (b). In (e), the diagonal crease just start to penetrate the board and there are stresses to the left and right. In (f) again a similar stress distribution as for the line crease simulation is obtained, both for the diagonal crease and the MD-crease. Due to the cut for the view, the diagonal crease appears a bit wider than the MD crease in (f).

9 Conclusions

A continuum based model for paperboard consistent with the laws of thermodynamics is established. The evolution of the anisotropy is modeled with the use of three structural tensors of which two are associated with the MD and CD directions, and a third which is associated to an out-of-plane normal vector. A free energy is proposed, which initially gives rise to a decoupled in-plane and out-of-plane response. This assumption allows the large difference in the in-plane and out-of-plane elastic parameters to be modeled.

The structural tensors are assumed to be embedded in the continuum and it is shown that the plasic spin is of importance when large plastic strains are present. The plastic spin is chosen such that no plastic deformation occurs in the direction $\boldsymbol{n}^{(3)} \otimes \boldsymbol{v}^{(1)}$ during shearing, i.e. the stacking direction of the fibers. The plastic deformation in out-of-plane shearing is assumed to be the result of sliding of the fiber layers.

In contrast to many other models for paperboard, plasticity is modeled using only one distortional hardening yield surface. For the ZD-compression, linear hardening plasticity is assumed, while the elasticity has an exponential format. For the in-plane directions a logarithmic relationship is used for the hardening variables. A good description of the material response is obtained, despite no degradation of the material properties or rate dependence are included in the present framework.

To illustrate the performance of the model, the creasing operation has been simulated and compared to experimental results. It is concluded that the macroscopic force-

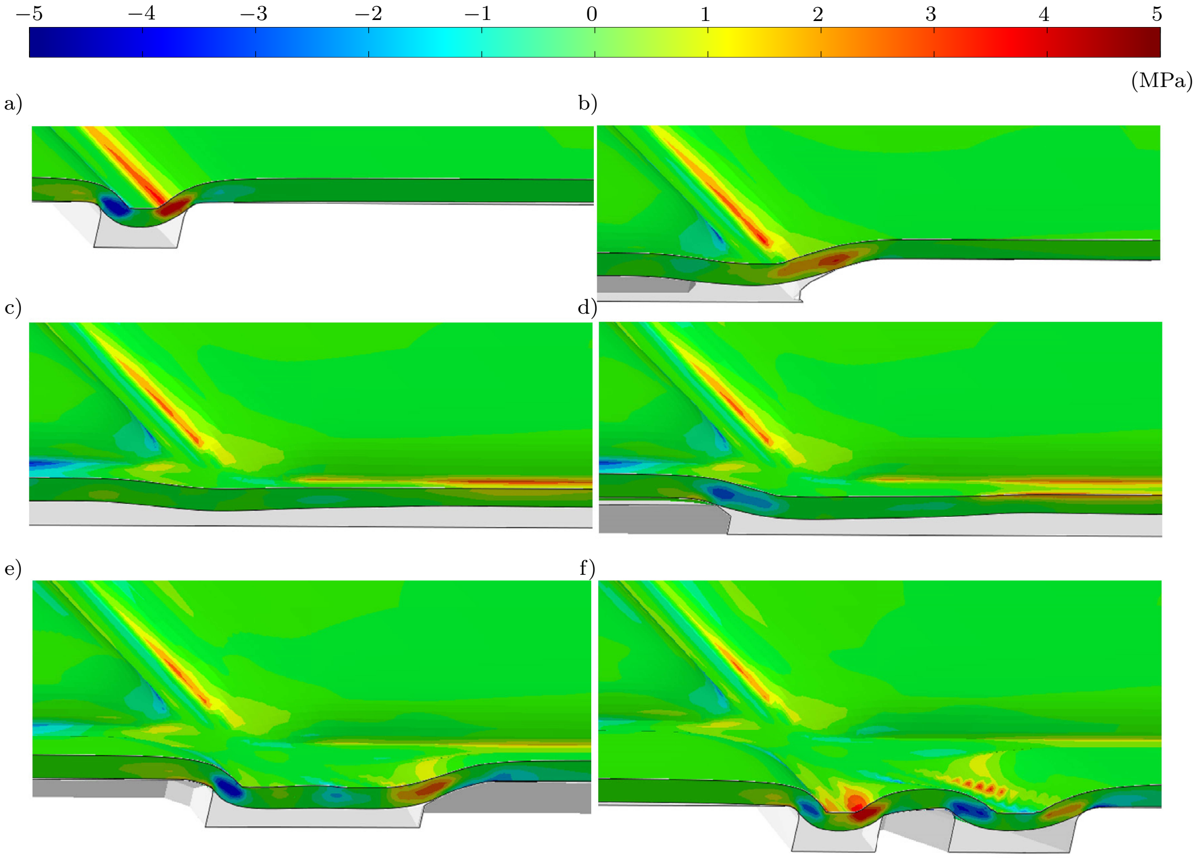

Figure 15: The out-of-plane CD-shear stress field, $\bar{\boldsymbol{v}}^{(2)} \cdot (\boldsymbol{\tau}\bar{\boldsymbol{v}}^{(3)})$, at the positions (a)-(f) marked in Fig. 14. The snapshots are taken when the male die is fully penetrated.

displacement curves from experiments can match the simulated field by using a pure continuum based model. The influence of the paper-paper friction parameter $\tilde{m}$ of the paperboard on the force-displacement curve is investigated in detail. In addition to the line crease, the rotation creasing procedure has been modeled as well. The out-of-plane shear stress field induced in the rotation creasing was studied in detail and it can be concluded that both the male and female die need to be in contact with the paperboard for a shear stress to be generated.

Acknowledgements

The help from Innventia AB for the support with the laboratory equipment is gratefully acknowledged.

A Material Parameters

The material parameters used in this work are presented in Table. 1, Table. 2 and Table. 3. The non-zero coefficients of $N_{ij}^{(\nu)}$ are summarized in Table. 1. The exponent $k = 3$ has been used in (31).

Stress-state,	Subsurface, ν	Subsurface component $N_{ij}^{(\nu)}$
MD-tension	1	$N_{11}^{(1)} = 0.9174, N_{22}^{(1)} = -0.3979$
CD-tension	2	$N_{11}^{(2)} = -0.2032, N_{22}^{(2)} = 0.9791$
MD-CD shear	3	$N_{12}^{(3)} = 0.7071, N_{21}^{(3)} = 0.7071$
MD-compression	4	$N_{11}^{(4)} = -1$
CD-compression	5	$N_{22}^{(5)} = -1$
MD-CD shear	6	$N_{12}^{(6)} = -0.7071, N_{21}^{(6)} = -0.7071$
ZD-compression	7	$N_{33}^{(7)} = -1$
ZD-tension	8	$N_{33}^{(8)} = 1$
MD-ZD-shear	9	$N_{33}^{(9)} = 0.704, N_{13}^{(9)} = 1.01$
MD-ZD-shear	10	$N_{33}^{(10)} = 0.704, N_{13}^{(10)} = -1.01$
CD-ZD shear	11	$N_{33}^{(11)} = 0.704, N_{23}^{(11)} = 1.01$
CD-ZD shear	12	$N_{33}^{(12)} = 0.704, N_{23}^{(12)} = -1.01$

Table 1: Numerical values of the in-plane subsurface parameters

Elastic parameter	Value
A_1	2020 (MPa)
A_2	229 (MPa)
A_3	28.4 (MPa)
A_4	25.2 (MPa)
A_5	1410 (MPa)
A_6	78.0 (MPa)
A_7	0.365 (MPa)
A_8	11.5 (-)

Table 2: Numerical values of the elastic parameters.

Subsurface , ν	Initial yield, K_0 (MPa)	Hardening a_ν (MPa)	Hardening b_ν (-)
1	16.5	12.2	890
2	4.05	4.75	1570
3	8.03	5.10	1540
4	18.0	-	-
5	11.6	-	-
6	8.03	5.10	1540
7	1.00	52	-
8	0.40	-	-
9	2.51	-	-
10	2.51	-	-
11	2.51	-	-
12	2.51	-	-

Table 3: Numerical values of the plastic parameters

B Algorithmic Tangent Stiffness Matrix

Index notation where the Cartesian basis vectors are assumed to be orthogonal and fixed is utilized in the description below. The algorithmic tangent stiffness matrix, which has been used as an output in the UMAT subroutine, is given by

$$[\boldsymbol{D}^{ats}]_{ijkl} = \frac{1}{2}\left([\frac{\partial \boldsymbol{\tau}}{\partial \boldsymbol{F}}\boldsymbol{F}^T]_{ijkl} + [\frac{\partial \boldsymbol{\tau}}{\partial \boldsymbol{F}}\boldsymbol{F}^T]_{ijlk}\right) \tag{54}$$

cf. Abaqus User's Manual. Dassault Systemes. Abaqus Inc (2013). Using $\boldsymbol{\tau} = \boldsymbol{\tau}(\boldsymbol{b}^e, \boldsymbol{m}^{(\alpha)})$ and noting that $\boldsymbol{b}^e = \boldsymbol{b}^e(\boldsymbol{F}, \boldsymbol{F}^p)$ and $\boldsymbol{m}^{(\alpha)} = \boldsymbol{m}^{(\alpha)}(\boldsymbol{F}, \boldsymbol{F}^p)$ the first term of the derivative in (54) can be expressed as

$$(\frac{\partial \boldsymbol{\tau}}{\partial \boldsymbol{F}}\boldsymbol{F}^T)_{ijkl} = \frac{\partial \tau_{ij}}{\partial b^e_{rs}}\left(\frac{\partial b^e_{rs}}{\partial F_{kp}} + \frac{\partial b^e_{rs}}{\partial F^p_{tu}}\frac{\partial F^p_{tu}}{\partial F_{kp}}\right)F_{lp} + \frac{\partial \tau_{ij}}{\partial m^{(\alpha)}_{rs}}\left(\frac{\partial m^{(\alpha)}_{rs}}{\partial F_{kp}} + \frac{\partial m^{(\alpha)}_{rs}}{\partial F^p_{tu}}\frac{\partial F^p_{tu}}{\partial F_{kp}}\right)F_{lp} \tag{55}$$

A summation in the superscript (α) is assumed. The derivatives of $\frac{\partial \tau_{ij}}{\partial b^e_{rs}}$ and $\frac{\partial \tau_{ij}}{\partial m^{(\alpha)}_{rs}}$ in (55) are lengthy and they are for completeness summarized below,

$$\begin{aligned}
\tfrac{1}{2}\tfrac{\partial \tau_{ij}}{\partial b^e_{rs}} &= \tfrac{p_1}{(J^e)^2}B^{(2)}_{ij}(B^{(1)}_{rs} + B^{(1)}_{sr}) - (p_1(I_{13})^2 + \tfrac{p_2}{(J^e)^2})B^{(2)}_{ij}b^{e-1}_{rs} \\
&+ \tfrac{p_2}{2(J^e)^2}(\delta_{ir}B^{(1)}_{js} + \delta_{is}B^{(1)}_{jr} + \delta_{js}B^{(1)}_{ir} + \delta_{jr}B^{(1)}_{is}) - \tfrac{A_6}{4}J^e\delta_{ij}b^{e-1}_{rs} \\
\tfrac{1}{2}\tfrac{\partial \tau_{ij}}{\partial m^{(1)}_{rs}} &= p_3 m^{(1)}_{ij}\delta_{rs} + p_4(\delta_{ir}\delta_{js} + \delta_{is}\delta_{jr}) \\
&+ p_5 m^{(2)}_{ij}\delta_{rs} + \tfrac{(A_5+A_6)}{4}\left(\tfrac{1}{I_{11}}(\delta_{ir}\delta_{js} + \delta_{is}\delta_{jr}) - \tfrac{1}{(I_{11})^3}m^{(1)}_{ij}\delta_{rs}\right) \\
\tfrac{1}{2}\tfrac{\partial \tau_{ij}}{\partial m^{(2)}_{rs}} &= p_6 m^{(2)}_{ij}\delta_{rs} + p_7(\delta_{ir}\delta_{js} + \delta_{is}\delta_{jr}) \\
&+ p_5 m^{(1)}_{ij}\delta_{rs} + \tfrac{(A_5+A_6)}{4}(\tfrac{1}{I_{12}}(\delta_{ir}\delta_{js} + \delta_{is}\delta_{jr}) - \tfrac{1}{(I_{12})^3}m^{(2)}_{ij}\delta_{rs}) \\
\tfrac{1}{2}\tfrac{\partial \tau_{ij}}{\partial m^{(3)}_{rs}} &= \tfrac{p_1}{(J^e)^2}B^{(2)}_{ij}B^{(3)}_{rs} + \tfrac{p_2}{2(J^e)^2}(b^e_{ir}b^e_{sj} + b^e_{is}b^e_{rj}) + \tfrac{A_5}{4(I_{23})^3}\delta_{ij}\delta_{rs} - \tfrac{3A_5}{4(I_{23})^5}m^{(3)}_{ij}\delta_{rs} \\
&+ \tfrac{A_5}{4(I_{23})^3}(\delta_{ir}\delta_{js} + \delta_{is}\delta_{jr})
\end{aligned} \tag{56}$$

In (56) δ_{ij} denotes Kroneckers delta and the following tensors were introduced to simplify notation

$$\begin{aligned}
B^{(1)}_{ij} &= b^e_{ik}m^{(3)}_{kj} \\
B^{(2)}_{ij} &= b^e_{ik}m^{(3)}_{kl}b^e_{lj} \\
B^{(3)}_{ij} &= b^e_{ik}b^e_{kj}
\end{aligned} \tag{57}$$

Moreover, the scalars $p_1 - p_7$ were also introduced

$$\begin{aligned}
p_1 &= \tfrac{1}{(J^e)^2}\left(H^+ A_3\left(\tfrac{-1}{4(I_{13})^3} + \tfrac{3}{4(I_{13})^5}\right) - \tfrac{A_6}{4(I_{13})^3} + (1-H^+)A_7 A_8 e^{-A_8((I_{13})^2-1)}\right)\\
p_2 &= H^+ A_3\left(\tfrac{1}{2I_{13}} - \tfrac{1}{2(I_{13})^3}\right) + \tfrac{A_6}{2I_{13}} + (1-H^+)A_7(1 - e^{-A_8((I_{13})^2-1)})\\
p_3 &= \tfrac{A_1}{4}\left(\tfrac{3}{(I_{11})^5} - \tfrac{1}{(I_{11})^3}\right) + \tfrac{A_4}{4}\left(\tfrac{3I_{12}}{(I_{11})^5} - \tfrac{1}{(I_{11})^3 I_{12}}\right)\\
p_4 &= \tfrac{A_1}{4}\left(\tfrac{1}{I_{11}} - \tfrac{1}{(I_{11})^3}\right) + \tfrac{A_4}{4}\left(\tfrac{1}{I_{11}I_{12}} - \tfrac{I_{12}}{(I_{11})^3}\right)\\
p_5 &= \tfrac{-A_4}{4}\left(\tfrac{1}{I_{12}(I_{11})^3} + \tfrac{1}{I_{11}(I_{12})^3}\right)\\
p_6 &= \tfrac{A_2}{4}\left(\tfrac{3}{(I_{12})^5} - \tfrac{1}{(I_{12})^3}\right) + \tfrac{A_4}{4}\left(\tfrac{3I_{11}}{(I_{12})^5} - \tfrac{1}{I_{11}(I_{12})^3}\right)\\
p_7 &= \tfrac{A_2}{4}\left(\tfrac{1}{I_{12}} - \tfrac{1}{(I_{12})^3}\right) + \tfrac{A_4}{4}\left(\tfrac{1}{I_{11}I_{12}} - \tfrac{I_{11}}{(I_{12})^3}\right)
\end{aligned} \tag{58}$$

The term $\frac{\partial F^p_{tu}}{\partial F_{kp}}$ in (55) can be obtained from the inner residual system defined by the backward Euler discretization of the evolution equations given by $\dot{\boldsymbol{F}}^p$, $\dot{\kappa}^{(\nu)}$ and the yield function $f = 0$, i.e. equations (3), (39) and (31). The residual equations is defined as $\boldsymbol{R}$ and $\boldsymbol{F}^p, \kappa^{(\nu)}$ and λ are collected in a vector $\boldsymbol{Y}$. The residual equations can then be seen as a function of $\boldsymbol{F}$ according

$$\boldsymbol{R} = \boldsymbol{R}(\boldsymbol{Y}(\boldsymbol{F}), \boldsymbol{F}) = \boldsymbol{0} \tag{59}$$

The derivative $\frac{\partial F^p_{tu}}{\partial F_{kp}}$ in (55) can be obtained from

$$\frac{\partial \boldsymbol{Y}}{\partial \boldsymbol{F}} = -\left(\frac{\partial \boldsymbol{R}}{\partial \boldsymbol{Y}}\right)^{-1} \left(\frac{\partial \boldsymbol{R}}{\partial \boldsymbol{F}}\right). \tag{60}$$

where the Jacobian $\frac{\partial \boldsymbol{R}}{\partial \boldsymbol{Y}}$ is used when solving the set of residual equations defined by (59) using the Newton-Raphson algorithm. The remaining terms in (55) can be computed in a straight forward manner and they are therefore not provided herein.

References

Abaqus User's Manual. Dassault Systemes. Abaqus Inc, 2013. Providence, RI, USA, 6.13 edition.

Allaoui, S., Aboura, Z., Benzeggagh, M., 2009. Phenomena governing uni-axial tensile behaviour of paperboard and corrugated cardboard. Composite Structures 87, 80–92.

Anna Johansson, Christer Fellers, D. G., Haugen, U., 1998. Paper friction- influence of measurement conditions. Tappi Journal 81, 175–183.

Back, E. L., 1991. Paper-to-paper and paper-to-metal friction. International Paper Physics Conference, 49–165.

Barbier, C., Larsson, P.-L., Östlund, S., 2005. Numerical investigation of folding of coated papers. Composite Structures 7, 383–394.

Beex, L., Peerlings, R., Geers, M., 2014. A multiscale quasicontinuum method for lattice models with bond failure and sliding. Computer Methods in Applied Mechanics and Engineering 269, 108–122.

Beex, L. A. A., Peerlings, R. H. J., 2009. An experimental and computational study of laminated paperboard creasing and folding. International Journal of Solids and Structures 46, 4192–4207.

Beex, L. A. A., Peerlings, R. H. J., 2012. On the influence of delamination on laminated paperboard creasing and folding. Philosophical transactions of the Royal Society 370, 1912–1924.

Borgqvist, E., Lindström, T., Tryding, J., Wallin, M., Ristinmaa, M., 2014. Distortional hardening plasticity model for paperboard. International Journal of Solids and Structures 51, 2411–2423.

Borodulina, S., Kulachenko, A., Galland, S., Nygårds, M., 2012. Stress-strain curve of paper revisted. Nordic Pulp and Paper Research Journal 27, 318–328.

Cavlin, S., 1988. The unique Convertibility of Paperboard. Packaging Technology and Science 10, 77–92.

Cavlin, S., Dunder, I., Edholm, D., 1997. Creasability testing by inclined rules a base for standardized specification of paperboard. Packaging Technology and Science 10(4), 191–207.

Cavlin, S., Fellers, C., 1975. A new method for measuring the edgewise compression properties of paper. Svensk papperstidning 78, 329–332.

Ciarlet, P. G., 1988. Mathematical Elasticity. Elsevier Science Publishers B.V.

Coleman, B. D., Gurtin, M. E., 1967. Thermodynamics with internal state variables. Journal of Chemical Physics 47, 597–613.

Dafalias, Y. F., 1998. Plastic spin: necessity or redundancy? International Journal of Plasticity 04, 909–931.

Giampieri, A., Perego, U., Borsari, R., 2011. A constitutive model for the mechanical response of the folding of creased paperboard. International Journal of Solids and Structures 48, 2275–2287.

Harrysson, M., Harrysson, A., Ristinmaa, M., 2007. Spatial representation of evolving anisotropy at large strains. International Journal of Solids and Structures 44, 3514–3532.

Harrysson, M., Ristinmaa, M., 2007. Description of evolving anisotropy at large strains. Mechanics of Materials 39, 267–282.

Huang, H., Hagman, A., Nygårds, M., 2014. Quasi static analysis of creasing and folding for three paperboards. Mechanics of Materials 69, 11–34.

Huang, H., Nygårds, M., 2010. A simplified material model for finite element analysis of paperboard creasing. Nordic Pulp & Paper Research Journal 25, 505–512.

Kulachenko, A., 2012. Direct simulations of fiber network deformation and failure. Mechanics of Materials 51, 1–14.

Mäkelä, P., Östlund, S., 2003. Orthotropic elastic-plastic material model for paper materials. International Journal of Solids and Structures 40, 5599–5620.

Mandel, J., 1971. Plasticite Classique et viscoplasticity. CISM course No.97. Springer-Verlag, Udine.

Menzel, A., Steinmann, P., 2003. On the spatial formulation of anisotropic multiplicative elasto-plasticity. Computional Methods in Applied Mechanics and Engineering 192, 3431–3470.

Nagasawa, S., Fukuzawa, Y., Yamaguchi, T., Tsukatani, S., Katayama, I., 2003. Effect of crease depth and crease deviation on folding deformation characteristics of coated paperboard. Journal of Materials Processing Technology 140, 157–162.

Nygårds, M., 2008. Experimental techniques for characterization of elastic- plastic material properties in paperboard. Nordic Pulp and Paper Research Journal 23, 432–437.

Nygårds, M., Fellers, C., Östlund, S., 2009a. Development of the notched shear test. Advance in Pulp and Paper Research, Oxford, 887–898.

Nygårds, M., Just, M., Tryding, J., 2009b. Experimental and numerical studies of creasing of paperboard. International Journal of Solids and Structures 46, 2493–2505.

Nygårds, M., Malnory, J., 2010. Measuring the out-of-plane shear strength profiles in different paper qualities. Nordic Pulp and Paper Research Journal 25, 366–371.

Rättö, P., 2012. An investigation of friction mechanisms of paper-to-paper friction of coated papers. Nordic Pulp and Paper Research Journal 27, 122–129.

Sawyer, J. P., Jones, R., McKinlay, P. R., 1998. A unified constitutive theory for paper. Composite Structures 42, 93–100.

Schröder, J., Neff, P., 2002. Invariant formulation of hyperelastic transverse isotropy based on polyconvex free energy functions. International Journal of Solids and Structures 40, 401–445.

Stenberg, N., 2002. On the Out-of-Plane Mechanical Behaviour of Paper Materials. Ph.D. thesis, Department of Solid Mechanics, Royal Institute of Technology, Stockholm, Sweden.

Stenberg, N., 2003. A model for the through-thickness elastic-plastic behaviour of paper. International Journal of Solids and Structures 40, 7483–7498.

Stenberg, N., Fellers, C., 2002. Out-of-plane poisson's ratios of paper and paperboard. Nordic Pulp and Paper Research Journal 17, 387–394.

Stenberg, N., Fellers, C., Östlund, S., 2001. Plasticity in the thickness direction of paperboard under combined shear and normal loading. Journal of Engineering Materials and Technology 123, 184–190.

Xia, Q. S., 2002. Mechanics of inelastic deformation and delamination in paperboard. Ph.D. thesis, Massachusetts Institue of Technology.

Xia, Q. S., Boyce, M. C., Parks, D. M., 2002. A constitutive model for the anisotropic elastic-plastic deformation of paper and paperboard. International Journal of Solids and Structures 39, 4053–4071.

Paper C

Eric Borgqvist, Mathias Wallin, Matti Ristinmaa,
Johan Tryding and Erika Tudisco

Localized deformation in compression and folding of paperboard

Under review in Packaging Technology and Science

Localized deformation in compression and folding of paperboard

Eric Borgqvist, Mathias Wallin, Johan Tryding,
Matti Ristinmaa and Erika Tudisco
Division of Solid Mechanics
Lund University, Box 118, S-221 00 Lund, Sweden

Abstract

The localized deformation patterns developed during in-plane compression and folding of paperboard have been studied in this work. X-ray post-mortem images reveal that cellulose fibers have been reoriented along localized bands in both the compression and folding tests. In folding, the paperboard typically fails on the side where the compressive stresses exists and wrinkles are formed. The in-plane compression test is however difficult to perform due to the slender geometry of the paperboard. A common technique to determine the compression strength is to use the so called Short-Span Compression Test (SCT). In the SCT, a paperboard with a free length of 0.7 mm is compressed. Another technique to measure the compression strength is the long edge test where the motion of the paperboard is constrained on the top and bottom to prevent buckling. A continuum model that previously has been proposed by the authors is further developed and utilized to predict the occurrence of the localized bands. It is shown that the in-plane strength in compression for paperboard can be correlated to the mechanical behavior in folding. By tuning the in-plane yield parameters to the SCT response, it is shown that the global response in folding can be predicted. The simulations are able to predict the formation of wrinkles and the deformation field is in agreement with the measured deformation pattern. The model predicts an unstable material response associated with localized deformation into bands in both the SCT and folding.

1 Introduction

Paperboard is a light-weight cellulose based fibrous material, which is suitable for converting into packaging containers. During converting procedures, the paperboard undergoes a complex deformation history, which is difficult to experimentally characterize. The packaging industry has traditionally relied on correlating the response in various simplified load situations with the performance in the converting process. One such technique is the Short-Span-Compression test (SCT), where a short sample of the paperboard is compressed. The failure strength in this test, the SCT-value, is considered to be an important measure for i.e. the foldability of the material, cf. Cavlin (1988), Carlsson *et al.* (1980) and the box compression strength, cf. Ristinmaa *et al.* (2012). However, the deformation mechanisms that are active during this test have not yet been fully understood.

Paperboard is a material which possesses a high degree of anisotropy. This anisotropy is due to the manufacturing process where cellulose fibers are sprayed on a traversing web and thereby becomes stacked in planes. The stacking direction is denoted ZD (out-of-plane). The fibers are mainly aligned in the Machine Direction (MD) and the transverse direction to MD is known as the Cross-Direction (CD). The failure stress in ZD is typically two orders of magnitude smaller than the failure stress in MD, while the failure stress in CD is about 2-3 times lower than MD. To obtain a low weight, paperboard is commonly produced as a sandwiched structure, with stronger mechanical properties in the outer-plies (top and bottom) and weaker properties in the middle. Measurements and simulations have been performed for a single ply board in this work.

Good foldability implies minimum spring-back and absence of cracks along fold lines, cf. Cavlin (1988). Due to the bending state present during folding, in-plane compression strength has been attributed for being the dominant factor affecting the foldability of paperboard. However, later investigations have confirmed that the out-of-plane shear is an important mechanism to consider during converting procedures, cf. Nygårds *et al.* (2009b), Beex and Peerlings (2009) and Borgqvist *et al.* (2015). The in-plane compression strength is difficult to measure due to that structural instabilities (buckling) easily are triggered as a result of the slender geometry of the paperboard. To overcome the difficulties associated with the structural stability in compression tests, short span length can be used to prevent the buckling. An alternative experimental method is based on constraining the deflection in the out-of-plane direction using lateral support on the top and bottom of the paperboard, i.e. the long edge compression test, cf. Cavlin and Fellers (1975). In Westerlind and Carlsson (1992), the peak stress in the long edge compression test and the short-span compression test were shown to be correlated using a weakest link relation.

A common modeling technique to analyze complicated load situations for paperboard is to use combination of continuum and interface models, as proposed in Xia (2002). Using this combined approach, the SCT was simulated in Hagman *et al.* (2013) and features such as the maximum peak stress was captured using this concept. Moreover, in Hagman *et al.* (2013), the through thickness profile obtained from a notched shear test, cf. Nygårds *et al.* (2009a), was correlated to the location of the delamination. However in Hagman *et al.* (2013), the displacement at failure in the SCT was not considered in the simulated response.

A simplified model based on the Hill's yield criterion was adopted for the continuum, which does not differentiate between compression and tension. The line creasing and folding operation have been analyzed using a similar modeling technique in Huang *et al.* (2014). In Borgqvist *et al.* (2015), a pure continuum model for paperboard was established and the creasing process was investigated for a single ply board. No damage was included in the model, instead the simplifying assumption of ideal plasticity at the onset of failure was utilized. In Carlsson *et al.* (1980) it was suggested that an ideal plastic response for the in-plane compression could be used to predict the maximal bending moment in folding.

In Carlsson *et al.* (1980) it was shown that there exists a correlation between the failure stress in the SCT and the maximal bending moment in folding. In this work, the deformation during the SCT and line folding operation is investigated. Post-mortem images have been produced using x-ray tomography to characterize the deformation mechanisms that have been active during the folding and SCT. The fiber orientation and the distribution of the fibers are analyzed and the observed deformation patterns are compared to the numerical predictions.

The deformation during the SCT and the line folding operation are analyzed using the continuum model previously proposed in Borgqvist *et al.* (2015). The plastic part of the model is based on the yield surface proposed by Xia *et al.* (2002), which utilizes a set of subsurfaces in the stress-space, where each subsurface is associated with a hardening variable. The yield surface hardens non-proportionally in the stress space, cf. Borgqvist *et al.* (2014) and different yield stresses are used for tension and compression loading. An alternative is to use kinematic hardening, which was adopted in Tjahjanto *et al.* (2015) for a high density fiberous material.

The article is organized as follows, in section 2 the different techniques to measure the in-plane compression strength are examined, in section 3 the material model is reviewed, in section 4 the model is calibrated to the SCT-response and the deformation characteristics are examined, in section 5 and 6 the folding of paperboard is investigated and the response predicted by the model is presented.

2 In-plane compression of paperboard

Two alternatives to measure the in-plane compression strength are the long edge test and the SCT, where the latter is the most common technique employed in the industry. The SCT is fast and widely available since it follows the ISO-standard, cf. ISO:9895:2008 ISO:9895:2008 (2008). Boundary effects can not be neglected, due to the short sample length in the SCT. To reduce the boundary effects, the long edge test can be used where the motion is constrained in the lateral direction. The response from both the SCT and the long edge test have been considered in this work. Measurements and numerical results have been obtained for a solid bleached single ply board with a thickness of 0.4 mm in this work. The grammage of the board has been measured to be 315.2 g m^{-2}.

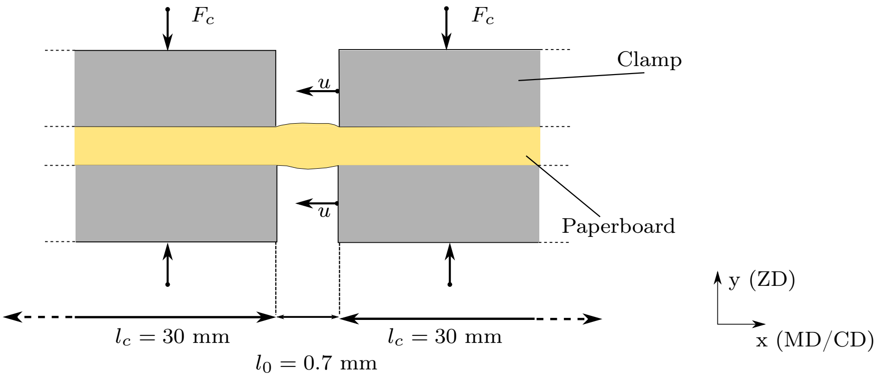

Figure 1: Schematic of the SCT.

2.1 Short-Span Compression Test

The setup for the short-span compression test is shown in Fig. 1. The clamping area is 30 mm × 15 mm in the SCT and the free span length which separates the two clamps is 0.7 mm. Initially, the two top clamps are displaced in the y-direction such that a clamp force of $F_c = 2300 \pm 500$ N is obtained. On the basis of the geometry of the clamps, this force correspond to a clamping pressure of approximately 5 MPa. Due to the applied force in the y-direction, the paperboard bulges in the free-span zone. After the clamping, the right clamps in Fig. 1 are displaced in the x-direction which thereby reduces the distance between the clamps, l_0. During the compression, sliding between the paperboard and the clamps can be observed, cf. also the ISO-standard, ISO:9895:2008 ISO:9895:2008 (2008) Annex B. As a comparison, in the short-span tensile test typical clamping pressures is in the order of 50 MPa to prevent sliding, cf.Hägglund *et al.* (2004).

The force-displacement curves generated during the SCT and tensile tests are shown in Fig. 2 for both MD and CD. The force and displacement response have been normalized with the initial cross section area A_0, and the initial span length l_0, respectively. The apparent stiffness in the SCT is significantly lower compared to the stiffness from the tensile tests. In Cavlin and Fellers (1975), the apparent stiffness in the SCT was shown to be dependent on the free-span length, the clamping pressure and the clamp length. Due to limitations in the experimental setup it was not possible to record the full force-displacement curve following the abrupt softening in the SCT. The maximum normalized peak force in Fig. 2 is 25 MPa in MD and 18 MPa in CD.

Snapshots just before and after the load drop of a typical paperboard in the SCT are shown in Fig. 3. The paperboard in Fig. 3 has similar material properties as the single ply board that is otherwise investigated in this work. The paperboard appears to be intact and no major flaws are observed before the load drop, while delamination is clearly visible after failure. Part of the energy that is released at the load drop has been consumed by the separation process of the fiber layers. In Carlsson *et al.* (1980) it was suggested that ideal plastic deformation in compression precedes the delamination and this hypothesis will be

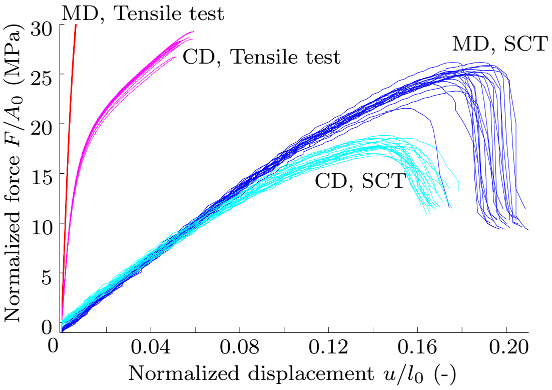

Figure 2: Normalized force vs normalized displacement for MD/CD SCT. The initial cross section area is denoted A_0 and l_0 is the initial span-length. Measurements from both tensile tests and the long edge tests are shown. Only part of the MD tensile curve is shown due to the high failure stress in MD.

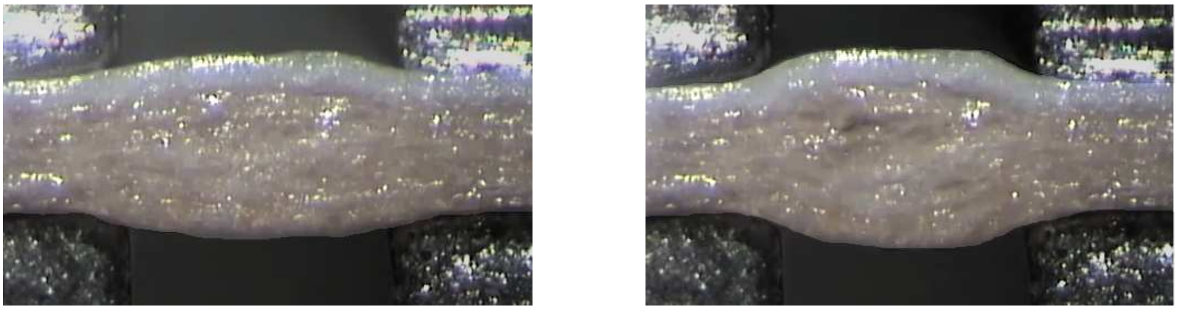

Figure 3: Snapshots of a Duplex paperboard just before and after failure (Stora Enso is gratefully acknowledged for providing the images.)

investigated further in this work using numerical techniques.

2.2 Comparison long-edge test

In the long-edge test, lateral support to prevent buckling is utilized, cf. Fig. 4. The paperboard specimens used in the compression tests are 25 mm wide and a clamp length of l_{0l} =55 mm is adopted. The same apparatus that was utilized in Hagman *et al.* (2013) has been used, cf. also Cavlin and Fellers (1975) for additional details regarding the experimental setup.

The force-displacement responses obtained during the long edge-tests for both MD and CD are shown in Fig. 5. Measurements from in-plane tensile tests are shown in the same figure. Comparing the stiffnesses in the long edge compression test with the initial stiffnesses in the tensile tests, it is noticed that they are almost identical. This indicates

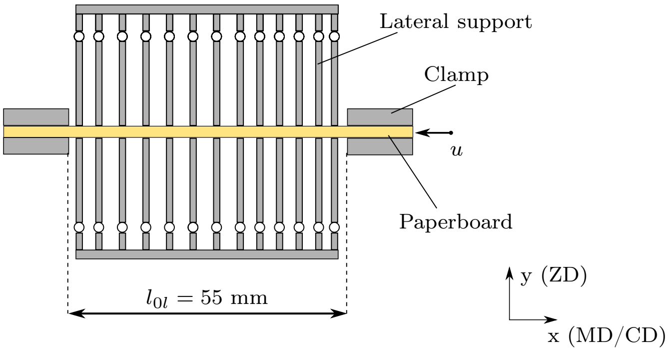

Figure 4: Schematic of the Long edge-test.

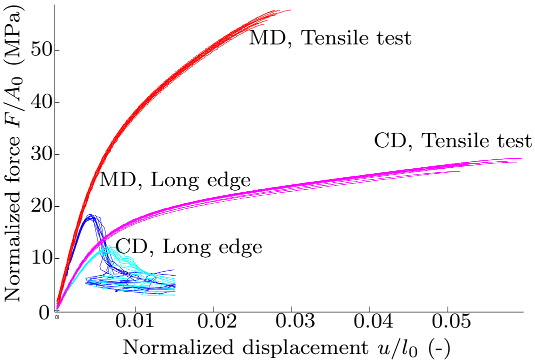

Figure 5: Normalized force vs normalized displacement has been plotted, where A_0 is the initial cross section area and l_0 the initial span-length. Measurements from both tensile tests and the long edge tests are shown.

that neither boundary effects nor sliding have a significant effect on the load-displacement curves. The long edge test predicts a failure stress of 18 MPa in MD and 12 MPa in CD, which are lower compared to the SCT. The softening in the long edge test is irregular and follows a non-unique path with snap-back behavior.

2.3 Post-mortem analysis of SCT

The single-ply paperboard has been analyzed using x-ray tomography (Zeiss Xradia XRM520) following the SCT. Low resolution images were initially obtained to identify the area of interest and then higher resolution (1 μm pixel size) images were generated. During the scan, approximately 950 images across the width of the paperboard have been generated.

A typical image of the paperboard following the SCT in MD is shown in Fig. 6. Separation of the fiber layers can be observed, i.e. delamination has occurred and reorientation of the fibers is visible. The delamination is located at the center of the paperboard and the thickness of the paperboard has increased.

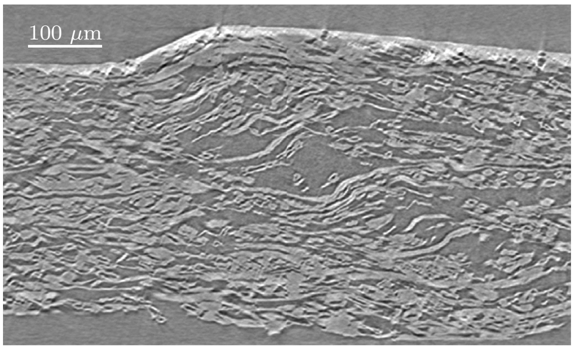

Figure 6: Typical post-mortem image obtained from the x-ray scan of the SCT.

To investigate the deformation pattern in detail, image processing using the software ImageJ, cf. Rasband (2015), has been performed. The images have first been binary processed into black and white color with a single threshold limit. A total of 40 consecutive images are then summed together at different sections through the width. On the basis of these averaged images, the fiber orientation is analyzed. The orientation of the fibers is computed by using the plugin OrientationJ cf. Rezakhaniha *et al.* (2011), available for the software ImageJ. The resulting images from the SCT is shown in Fig. 7.

It is observed that the significant reorientation of the fibers occurs in localized bands. The width of the bands ranges between 50 and 100 μm and a reorientation of approximately ± 25° degrees is observed. Two possible failure mechanisms of the fiber network are the buckling of fiber segments and plastic micro-buckling such as plastic kinking of the fibers, cf. Fleck (1997) and Christer Fellers, Richard E. Mark (Editor) (1983). From Fig. 7 it is evident that individual fibers are subjected to significant bending. It can also be noted that there is a difference in the deformation pattern through the width of the paperboard, even though the boundary conditions are almost planar .

3 Material model

The material model adopted is based on the thermodynamic consistent model proposed in Borgqvist *et al.* (2015) and is briefly summarized in this section. The deformation gradient is assumed to be multiplicative split into an elastic and a plastic part, i.e. $\boldsymbol{F} = \boldsymbol{F}^e\boldsymbol{F}^p$. The plastic velocity gradient is defined through $\boldsymbol{L}^p = \dot{\boldsymbol{F}}^p\boldsymbol{F}^{p-1}$ where the spatial plastic velocity gradient follows from $\boldsymbol{l}^p = \boldsymbol{F}^e\boldsymbol{L}^p\boldsymbol{F}^{e-1}$. To model anisotropy, three vectors of unit length are introduced which phenomenologically represent the MD, CD and ZD directions in the reference configuration. The MD, CD and ZD directions are respectively given by $\boldsymbol{v}_0^{(1)}$, $\boldsymbol{v}_0^{(2)}$ and $\boldsymbol{n}_0^{(3)}$. The transformation from the reference to the spatial configuration of the vectors

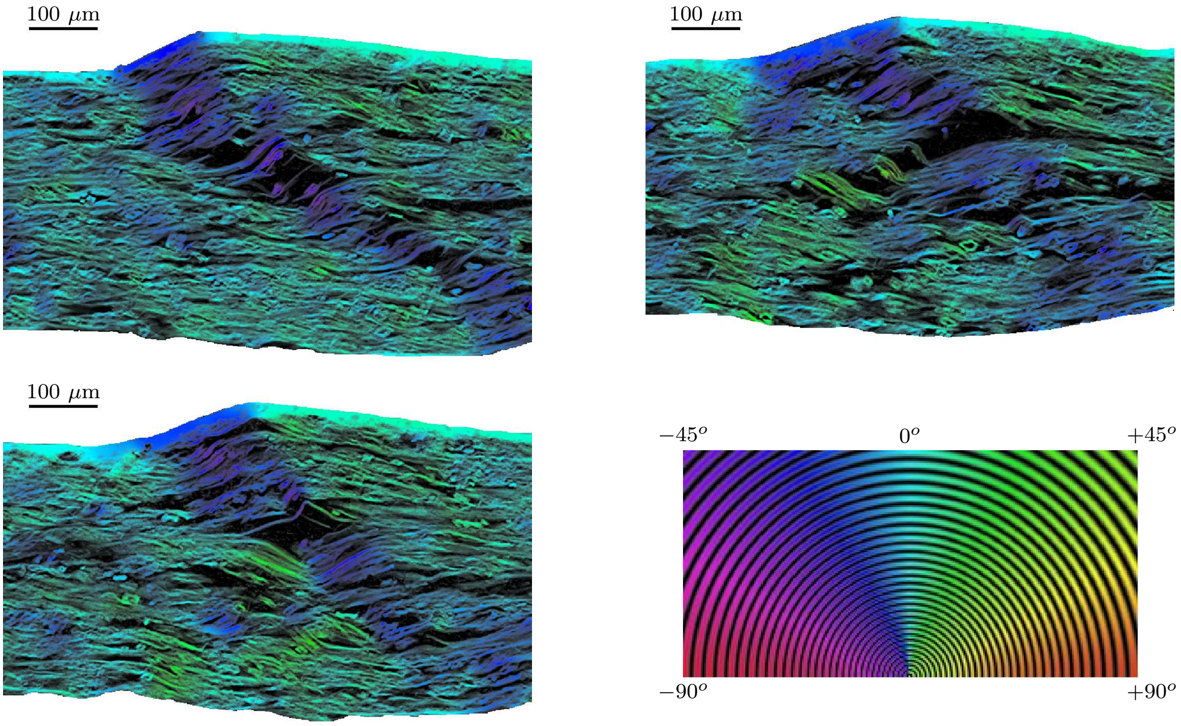

Figure 7: Processed tomograph images from SCT in MD. Images taken at different cross sections through the width of the same sample. The color map indicates the local orientation in the image according to the scale given on the bottom right.

are given by the following relations,

$$\begin{aligned} \boldsymbol{v}^{(1)} &= \boldsymbol{F}^e \boldsymbol{v}_0^{(1)} \\ \boldsymbol{v}^{(2)} &= \boldsymbol{F}^e \boldsymbol{v}_0^{(2)} \\ \boldsymbol{n}^{(3)} &= J^e \boldsymbol{F}^{e-T} \boldsymbol{n}_0^{(3)}, \end{aligned} \tag{1}$$

where J^e is the determinant of the elastic deformation gradient. On the basis of (1) it can be observed that, the ZD-direction, $\boldsymbol{n}^{(3)}$ remains orthogonal to the MD and CD directions in the spatial configuration. Structural tensors are adopted in the model and they are defined by dyadic products of the director vectors according to

$$\boldsymbol{m}^{(1)} = \boldsymbol{v}^{(1)} \otimes \boldsymbol{v}^{(1)}, \quad \boldsymbol{m}^{(2)} = \boldsymbol{v}^{(2)} \otimes \boldsymbol{v}^{(2)}, \quad \boldsymbol{m}^{(3)} = \boldsymbol{n}^{(3)} \otimes \boldsymbol{n}^{(3)}. \tag{2}$$

The following invariants will be used to define the model,

$$\begin{aligned} &I_{11} = \sqrt{\boldsymbol{m}^{(1)} : \boldsymbol{I}}, \quad I_{12} = \sqrt{\boldsymbol{m}^{(2)} : \boldsymbol{I}}, \quad I_{13} = \tfrac{1}{J^e}\sqrt{\boldsymbol{m}^{(3)} : \boldsymbol{b}^e \boldsymbol{b}^e} \\ &I_{23} = \sqrt{\boldsymbol{m}^{(3)} : \boldsymbol{I}} \quad J^e = \sqrt{\det(\boldsymbol{b}^e)}, \end{aligned} \tag{3}$$

where the left elastic Cauchy-Green tensor is defined as $\boldsymbol{b}^e = \boldsymbol{F}^e(\boldsymbol{F}^e)^T$. The potential governing the relationship between the stresses and the kinematical quantities are given by the free energy $\rho_0\psi = \rho_0\psi^{ip} + \rho_0\psi^{op}$. A slightly different format of $\rho_0\psi$ compared to Borgqvist *et al.* (2015) is proposed, such that the Poisson's effect between the in-plane and out-of-plane directions initially is zero, which will result in good agreement between the simulated and measured response in the SCT. The two parts of the free energy are proposed to be,

$$\begin{aligned} \rho_0\psi^{ip} &= A_1\left(I_{11} + \tfrac{1}{I_{11}} - 2\right) + A_2\left(I_{12} + \tfrac{1}{I_{12}} - 2\right) + A_4\left(I_{11} + I_{12} + \tfrac{1}{I_{23}} - 3\right) \\ \rho_0\psi^{op} &= HA_3\left(I_{13} + \tfrac{1}{I_{13}} - 2\right) + (1-H)A_6\left((I_{13})^2 + \tfrac{1}{A_7}e^{-A_7((I_{13})^2-1)} - 2\right) + \\ & \quad A_5\left(I_{11}I_{12}I_{13} - J^e\right) \end{aligned} \tag{4}$$

where $A_1, A_2, \ldots A_7$ are elastic material parameters and H is the step function defined as 1 when $I_{13} - 1 \geq 0$ and zero otherwise. The material parameters $A_i, \{i = 1, 2, \ldots 7\}$ should be positive to ensure that each term is increasing, i.e. the energy is increasing for an arbitrary deformation.

From thermodynamical arguments in an isothermal setting, it can be shown that the Kirchhoff stress can be obtained from the potential $\rho_0\psi$ according to

$$\boldsymbol{\tau} = 2\rho_0\left(\frac{\partial\psi}{\partial\boldsymbol{b}^e}\boldsymbol{b}^e + \frac{\partial\psi}{\partial\boldsymbol{m}^{(1)}}\boldsymbol{m}^{(1)} + \frac{\partial\psi}{\partial\boldsymbol{m}^{(2)}}\boldsymbol{m}^{(2)} - \frac{\partial\psi}{\partial\boldsymbol{m}^{(3)}}\boldsymbol{m}^{(3)} + \left(\frac{\partial\psi}{\partial\boldsymbol{m}^{(3)}} : \boldsymbol{m}^{(3)}\right)\boldsymbol{I}\right), \tag{5}$$

where $\boldsymbol{I}$ represents the second order identity tensor. Utilizing that the initial stiffness is given by (cf. Harrysson *et al.* (2007)),

$$\boldsymbol{\mathcal{D}} = \tfrac{\partial\boldsymbol{\tau}}{\partial\boldsymbol{F}}\boldsymbol{F}^T\Big|_{\boldsymbol{F}=\boldsymbol{I}}, \tag{6}$$

the following stiffness tensor for the energy (4) is obtained (in Voigt notation with the order MD,CD,ZD)

$$[\boldsymbol{\mathcal{D}}] = \begin{pmatrix} 2A_1 + 2A_4 & A_4 & & & & \\ A_4 & 2A_2 + 2A_4 & & & & \\ & & 2HA_3 + 4(1-H)A_6A_7 & & & \\ & & & A_4 + A_5 & & \\ & & & & A_5 & \\ & & & & & A_5 \end{pmatrix}. \tag{7}$$

A zero entry is indicated by a blank space in (7).

To model the threshold for the irreversible deformations of the material, a yield surface is utilized, where $f < 0$ defines the elastic domain. The explicit format for f is given by

$$f(\boldsymbol{\tau}, \boldsymbol{n}_s^{(\beta)}, K^{(\beta)}) = \sum_{\nu=1}^{12} \chi^{(\nu)} \left(\frac{\boldsymbol{\tau} : \boldsymbol{n}_s^{(\nu)}}{\tau^{(\nu)}} \right)^{2k} - 1, \tag{8}$$

where the subsurfaces $\boldsymbol{n}_s^{(\nu)}$ are given as dyadic products of the normed director vectors,

$$\boldsymbol{n}_s^{(\nu)} = \sum_{i=1}^{3} \sum_{j=1}^{3} N_{ij}^{(\nu)} \bar{\boldsymbol{v}}^{(i)} \otimes \bar{\boldsymbol{v}}^{(j)}. \tag{9}$$

The parameters $N_{ij}^{(\nu)}$ in (9) are the coefficients of the yield normals and $\bar{\boldsymbol{v}}^{(i)}$ are given by

$$\bar{\boldsymbol{v}}^{(1)} = \tfrac{1}{|\boldsymbol{v}^{(1)}|} \boldsymbol{v}^{(1)}, \quad \bar{\boldsymbol{v}}^{(2)} = \tfrac{1}{|\boldsymbol{v}^{(2)}|} \boldsymbol{v}^{(2)}, \quad \bar{\boldsymbol{v}}^{(3)} = \tfrac{1}{|\boldsymbol{n}^{(3)}|} \boldsymbol{n}^{(3)}. \tag{10}$$

The abbreviation for the terms given by index ν is summarized in Table. 1 in Appendix A, along with the calibrated material parameters. In (8), k is a constant natural number and $\chi^{(\nu)}$ is a switch function, which for a given stress state $\boldsymbol{\tau}$ determines if a subsurface is potentially active,

$$\chi^{(\nu)} = \begin{cases} 1 & \text{if} \quad \boldsymbol{\tau} : \boldsymbol{n}_s^{(\nu)} > 0 \\ 0 & \quad \text{otherwise.} \end{cases} \tag{11}$$

The distance to each subsurface in (8) is given by $\tau^{(\nu)}$ where

$$\tau^{(\nu)} = \tau_0^{(\nu)} + K^{(\nu)}. \tag{12}$$

The initial distance from the origin in the stress space, to the subsurface is given by $\tau_0^{(\nu)}$, indicating the initial yield stress in a certain loading direction (e.g. MD-tension for $\nu = 1$). The conjugate hardening variables, $K^{(\nu)}$, represents the change in distance from the origin to a subsurface due to plastic loading. The non-zero conjugate hardening variables are functions of internal variables, $\kappa^{(\nu)}$, according to

$$\begin{aligned} K^{(\nu)} &= a_\nu \ln(b_\nu \kappa^{(\nu)} + 1) \qquad && \nu = \{1, 2, 3, 6\} \\ K^{(\nu)} &= a_\nu \kappa^{(\nu)} && \nu = 7. \end{aligned} \tag{13}$$

where a_ν and b_ν are material parameters. The distance from the origin in the the stress-space to the sub-surfaces corresponding to tension in MD/CD, in-plane shear and compression in ZD will increase according to (13). The remaining sub-surfaces, $\nu \in \{4, 5, 8, 9, 10, 11, 12\}$ are associated with the out-of-plane directions and the in-plane compression and the corresponding sub-surfaces will remain fixed. As a consequence an ideal plastic response will be obtained for the corresponding uniaxial stress states.

Finally, the evolution laws governing the irreversible deformation behavior are postulated as

$$\begin{aligned} \boldsymbol{l}^p &= \textstyle\sum_{\gamma=1}^{12} \dot{\lambda} H_\gamma \boldsymbol{n}_s^{(\gamma)} \\ \dot{\kappa}^{(\nu)} &= \dot{\lambda} H_\nu \left(\frac{\boldsymbol{\tau}:\boldsymbol{n}_s^{(\nu)}}{\tau^{(\nu)}} \right), \end{aligned} \tag{14}$$

where

$$H_\nu = \frac{2k\chi^{(\nu)}}{\tau^{(\nu)}} \left(\frac{\boldsymbol{\tau} : \boldsymbol{n}_s^{(\nu)}}{\tau^{(\nu)}} \right)^{2k-1}, \tag{15}$$

and $\dot{\lambda}$ is a Lagrange multiplier.

The model parameters associated with the out-of-plane directions and the tensile in-plane directions have been calibrated from uniaxial tests following the procedure in Borgqvist *et al.* (2015) and Borgqvist *et al.* (2014). The parameters related to in-plane plastic compression has been chosen to fit the response in the SCT described in the next section.

4 Numerical investigation of SCT

The SCT has been numerically simulated using the material model presented in the previous section. The model has been implemented in the commercial software ABAQUS Abaqus User's Manual (2013), via the subroutine option UMAT. Details regarding the numerical implementation of the model is provided in Borgqvist *et al.* (2015). In the numerical model, the paperboard is homogeneous and therefore possess constant material parameters through the width and thickness. The geometry of the SCT is shown in Fig. 8.

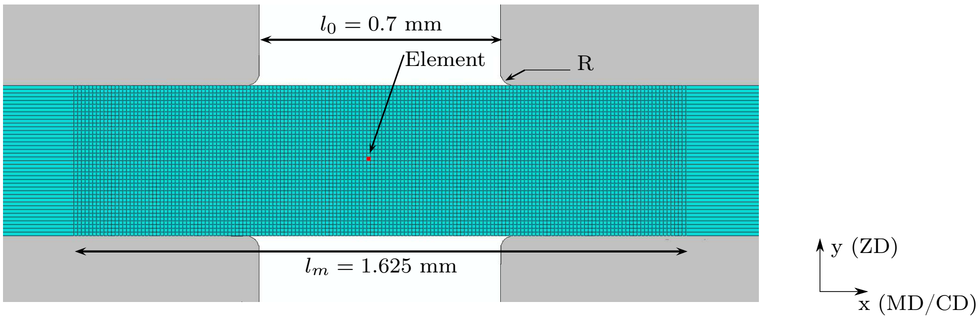

Figure 8: Finite element mesh of the SCT at the center of the specimen. Element size is 0.01mm ×0.01 mm in the finer meshed region. The marked position indicates the element in which the stress state has been examined in Fig. 12. All four clamps have been rounded with a small radius $R = 0.02$ mm.

The problem is modeled using 3D fully integrated 8-node bi-linear continuum elements. To reduce the computational cost, the width of paperboard has been taken as 3 mm and meshed with one element. A structured mesh is originally generated where the size of the elements in the x and y directions are 0.01 mm×0.01 mm in the finer meshed region of the paperboard and 0.5 mm×0.01 mm in the other regions, cf. Fig. 8. The clamps have been modeled as rigid analytic bodies. To capture the observed steady sliding between the clamps and the paperboard, a linear relationship between the friction force and displacement is initially assumed (elastic slip) before gross sliding occurs, cf. Oden and Pires (1983). The friction law is available in ABAQUS, cf. Abaqus User's Manual (2013). The maximum allowed elastic slip has been taken as 0.085 mm and an anisotropic static coefficient of friction equal to 0.16 in MD and 0.21 in CD has been adopted. The standard ABAQUS-direct solver is utilized, with a quasi-static solution procedure.

Material instability effects make the problem mesh dependent and therefore a perturbation field has been added to the geometry. The nodes in the finer meshed region, cf. Fig. 8, have been given initial y-coordinates according to

$$y = y_0 + h\sin\left(\frac{N2\pi x}{l_m}\right) \tag{16}$$

where y_0 is the original y-coordinate of the node from the structured mesh without the perturbation, $N = 5$ is the period, $h = 0.0005$ mm the magnitude of the perturbation and l_m the length defined in Fig. 8.

In the SCT simulation, the clamps are initially displaced such that a clamping force $F_c = 460N$ is obtained. The applied force has been adjusted to take into account that only 3 mm of the width of the paperboard is used in the simulation. The clamps on the right side in Fig. 8 are in the next step displaced until a drop in the force displacement curve occurs. The simulated force-displacement responses are compared to the experimental data in Fig. 9.

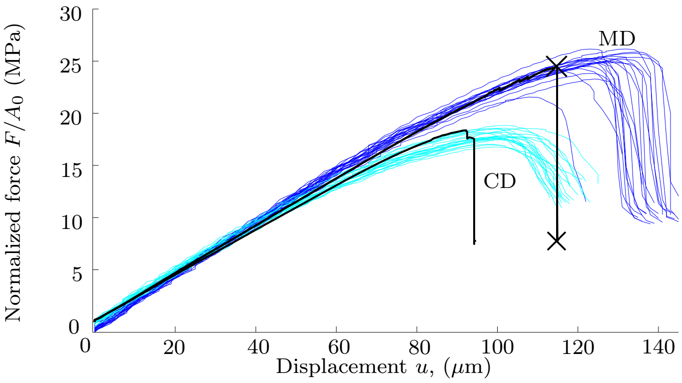

Figure 9: Force-displacement curves obtained from the SCT- simulation and measurements. Reaction force on the clamps normalized with the initial cross-section area of the paperboard and the displacement are shown.

Both the MD and the CD simulation tests in Fig. 9 shows good agreement with the experimental data. To fit the data, the in-plane compression strength is taken as $\tau_0^{(4)} = 29$ MPa in MD and $\tau_0^{(5)} = 21$ MPa in CD, which are slightly higher compared to the failure

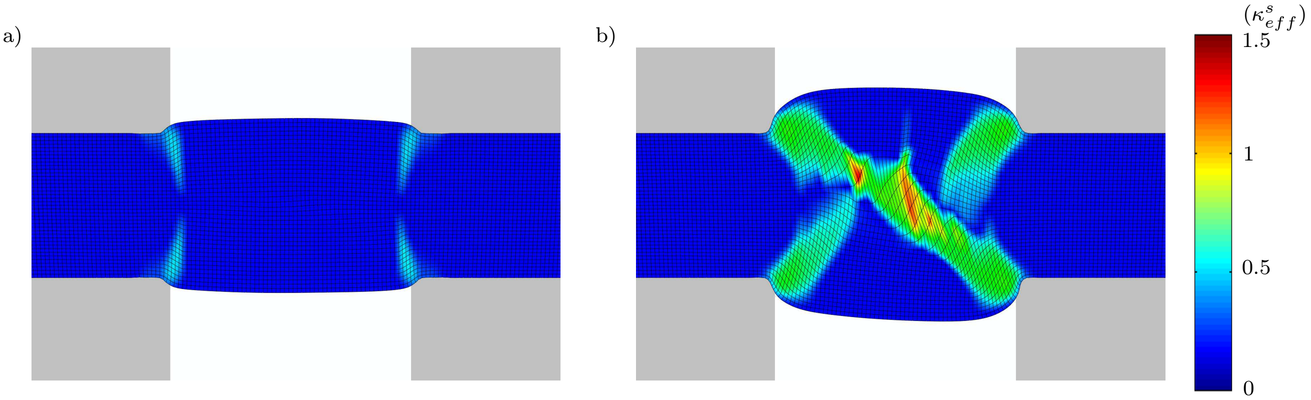

Figure 10: Deformation fields in MD at the marked load levels in the global force-displacement response in Fig. 9. In a) the deformation field before failure is shown and in b) after failure.

stresses observed in the global response of the SCT. The apparent modulus between the tests and the simulations are matched as well as the maximum peak force. The displacement at failure is however slightly underestimated by the simulation. The failure is due to the local material instability and is possible to be predicted by the model, even though no explicit damage variable is included in the modeling framework.

The deformation patterns predicted by the simulation are illustrated in Fig. 10 and corresponds to the two points marked in the force-displacement curve, cf. Fig. 9. To visualize the localized shear deformation, a contour plot indicating the accumulated effective plastic shear, defined from

$$\dot{\kappa}^s_{eff} = \sqrt{(\dot{\kappa}^{(9)})^2 + (\dot{\kappa}^{(10)})^2 + (\dot{\kappa}^{(11)})^2 + (\dot{\kappa}^{(12)})^2}, \tag{17}$$

is shown in Fig. 10. The superscript (9)-(12) in (17) are related to permanent deformations in out-of-plane shear, cf. Table 1 in Appendix A. Before the initiation of failure (cf. Fig. 10a), the deformation is relatively uniform and only limited permanent shear in the vicinity of the edges of the clamps can be observed. After the failure point, cf. Fig. 10b, a sudden change in the deformation pattern is observed, where localized shear bands have been formed, cf. also the states shown in Fig. 3. Some elements along the band running from top-left to bottom right have been severely stretched, resembling a delamination type of deformation.

The predicted reorientation of the MD-direction, i.e. $\phi = \arccos(\bar{\boldsymbol{v}}^{(1)} \cdot \boldsymbol{v}_0^{(1)})$ is shown in Fig. 11 at the unloaded state in a similar color map as was shown for the post-mortem tomograph images in Fig. 7. The width and location of the plastic shear bands in Fig. 11 are similar to that of the fiber-orientation bands measured in the tomograph images. The magnitude of the rotation is however slightly overestimated in the simulation compared to the x-ray tomograph images. However, the paperboard might have been affected during the transfer from the SCT device to the x-ray tomograph. The main deformation features are captured by the model, such as the localized bands of fiber-reorientation.

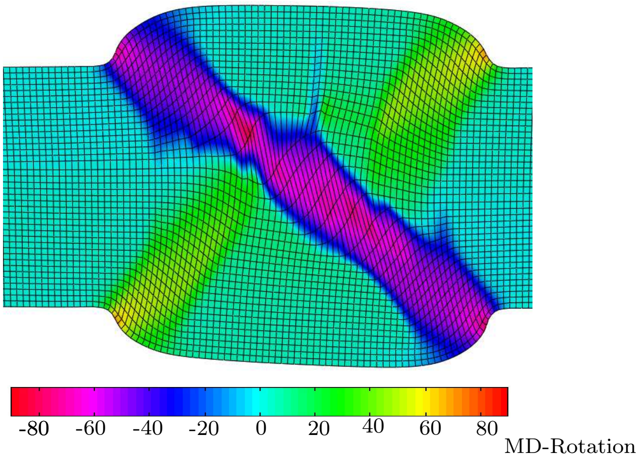

Figure 11: Rotation of the MD-direction at the unloaded state of the SCT. The color map coincides with the color map used in Fig. 7.

The in-plane and out-of-plane stress states at the center of the paperboard, indicated in Fig. 8, have been examined to determine the state of the paperboard during the simulation. The in-plane and out-of-plane stresses are defined by projecting the Kirchhoff stress tensor on the in-plane and out-of-plane directions respectively, i.e. $\tau_{ip} = \boldsymbol{v}^{(1)} \cdot \boldsymbol{\tau} \cdot \boldsymbol{v}^{(1)}$ and $\tau_{op} = \boldsymbol{v}^{(3)} \cdot \boldsymbol{\tau} \cdot \boldsymbol{v}^{(3)}$. The stresses τ_{ip} and τ_{op} are shown in Fig. 12 for the MD simulation.

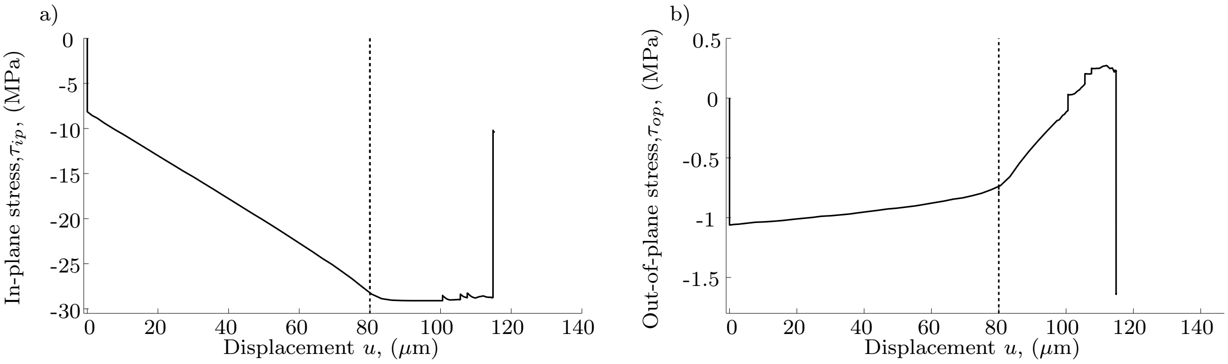

Figure 12: The in-plane Kirchhoff stress a) $\tau_{ip} = \boldsymbol{v}^{(1)} \cdot \boldsymbol{\tau} \cdot \boldsymbol{v}^{(1)}$ and the out-of-plane Kirchhoff stress b) $\tau_{op} = \boldsymbol{v}^{(3)} \cdot \boldsymbol{\tau} \cdot \boldsymbol{v}^{(3)}$ at the center of the board indicated in Fig. 8 as a function of the displacement of the clamps. The dashed line at displacement of $u_y = 80$ μm indicates the onset of plastic deformation in compression for the element.

Due to the clamping procedure, the in-plane stress τ_{ip} in Fig. 8a, is negative at zero displacement ($u = 0$ μm). The clamping pressure used in the test is therefore important to consider. As the distance between the clamps is decreased, the in-plane stress decreases until the limit $\tau_0^{(4)} = 29$ MPa is reached at a displacement of $u_y = 80$ μm, which is well before the failure displacement at $u_f = 115$ μm.

Referring to the ZD-stress τ_{op} in Fig. 8b, it is observed that also a compression stress state is induced due to the clamping procedure. The stress then increases slightly until the displacement $u_y = 80$ μm is reached. Upon further loading, the stress changes rapidly from a compression state to a tension state where a stress of 0.32 MPa is reached which is very close to the ZD-initial yield stress $\tau_0^{(8)} = 0.4$ MPa. The stress state in the element therefore becomes associated with both plastic deformation in out-of-plane tension and in-plane compression. At this stress state, unstable material response is obtained and the deformation becomes localized into bands. The strength in ZD can therefore have an influence on the failure displacement u_f but it is also clear that the in-plane stress has a significant influence.

To further illustrate how the stress state is associated with plastic deformations, the in-plane stress τ_{ip} vs out-of-plane stress τ_{op} of the element is shown in Fig. 13. The yield surface is shown in the same figure with a dashed line. It is noted that due to the clamping procedure, the stress state reaches the yield sub-surface associated with ZD-compression. Further on, when the clamps are displaced in the x-direction, the stress path is in the elastic regime until the stress state reaches the subsurface belonging to MD-compression, i.e. $u_y = 80$ μm. Upon further loading, the stress state moves along the MD-compression subsurface until it reaches the corner of the yield surface that is connected by the MD and ZD subsurface. The final stress state prior to the material instability is marked with an $\times$ in Fig. 13. At this stress state, the out-of-plane stress τ_{op} cannot increase anymore without decreasing the in-plane stress τ_{ip}.

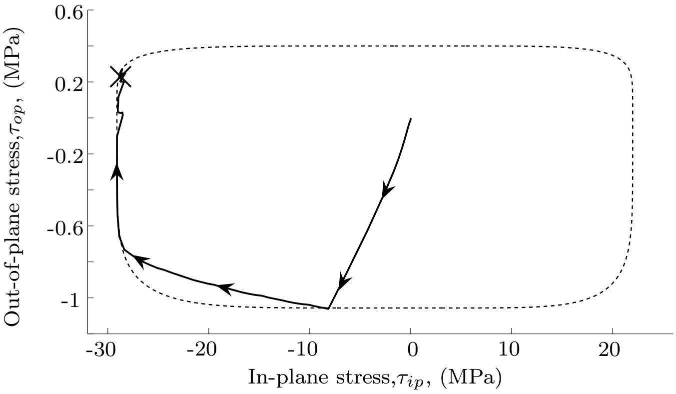

Figure 13: The stress path during SCT belonging the element marked in Fig. 8. The in-plane Kirchhoff stress $\tau_{ip} = \boldsymbol{v}^{(1)} \cdot \boldsymbol{\tau} \cdot \boldsymbol{v}^{(1)}$ and the out-of-plane Kirchhoff stress $\tau_{op} = \boldsymbol{v}^{(3)} \cdot \boldsymbol{\tau} \cdot \boldsymbol{v}^{(3)}$ is shown. The dashed line indicates the yield surface.

5 The line folding operation

In the 3-dimensional mechanical modeling of paperboard, the in-plane and out-of-plane response have typically been separated by using a combination of continuum and interface elements, cf. i.e. Xia (2002), Beex and Peerlings (2009), Nygårds *et al.* (2009b), Huang *et al.* (2014) and Hagman *et al.* (2013). This approach works well to study the typical deformation in folding of creased paperboards. However, the out-of-plane permanent deformations are controlled by the interface elements. Another approach was adopted in Borgqvist *et al.* (2015), by instead allowing the continuum elements to deform plastically in the out-of-plane directions and allowing more localized type of deformations to be predicted that is not restricted to the location of interface elements. The formation of wrinkles during folding can then be predicted, which to the authors knowledge have not previously been modeled for paper-based materials.

In the experimental setup for the line-folding operation, the paperboard is clamped at one side with a pressure of 0.2 MPa whereas the other side is constrained by a load-cell acting as a rigid support. A bending moment is applied by rotating the clamps. The width of the paperboard is 38 mm and the distance between the clamps and the rigid support is 10 mm. The paperboard is folded until an angle of 90 degrees is reached and then unloaded. The force as well as the bending angle are measured during the test. This folding apparatus is commonly used to correlate the performance of paperboard in converting processes. The L & W creasability tester (AB Lorentzen & Wettre, Stockholm, Sweden) has been utilized in this work.

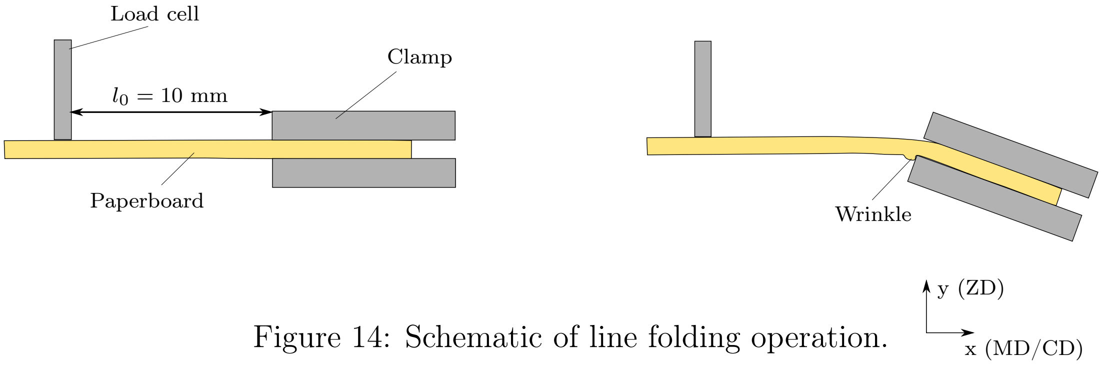

Figure 14: Schematic of line folding operation.

The bending moment varies linearly in the paperboard with respect to the position from the load cell, cf. Fig. 14. For small bending angles, before plasticity is initiated, the in-plane stress will vary linearly through the thickness of the sample (if the material properties are homogeneous). Evidently, the top side and bottom side are subjected to tension and compression respectively and the difference in strength between tension and compression for paperboard is therefore of importance to consider during folding, cf. Cavlin (1988).

5.1 Post-mortem analysis of folded samples

A post-mortem x-ray analysis has been performed after folding a sample in MD. Again approximately 950 images have been acquired across the width of the paperboard with a 1 μm pixel size. A typical post-mortem image of a folded sample is shown in Fig. 15. A distinct wrinkle is seen in Fig. 15 with delamination at the center of the wrinkle. The

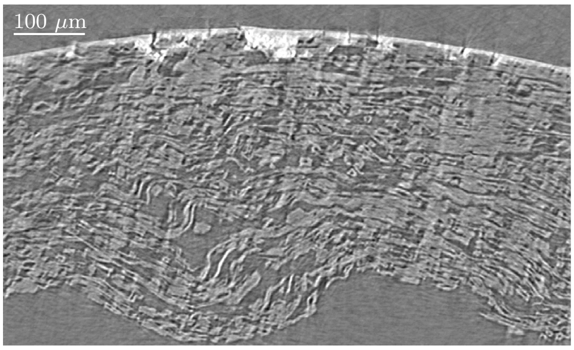

Figure 15: Typical post-mortem image obtained from the x-ray scan of the folding.

fiber-orientation field has been analyzed using the same technique as for the SCT images in Fig. 7 and the resulting images are shown in Fig. 16.

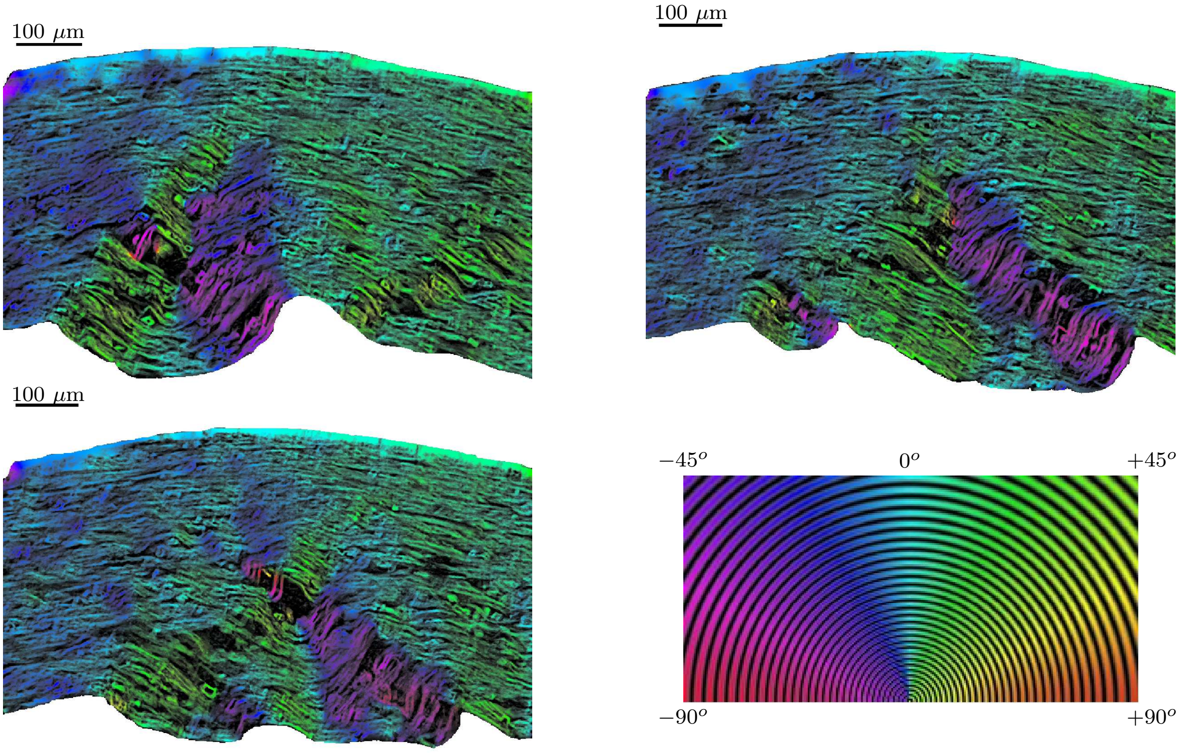

Figure 16: Processed tomograph images from the folding test. The images are taken at different cross sections through the width of the same sample. The local reorientation is indicated according to the color map given on the bottom right.

Localized bands where the fibers haven been reoriented can be observed in Fig. 16. As expected, wrinkles occur only on the side of the paperboard that has been subjected to compression. The reorientation appears somewhat larger compared with the post-mortem images from the SCT, around ± 45° with a band width typically ranging between 75-150 μm. Note too that the wrinkles do not have the same shape and size at the different sections through the width. In the top left image in Fig. 16 one distinct wrinkle is observed and then a gradual transition into a two wrinkles on the top right image has occurred and finally only a single large wrinkle is visible, indicating that folding is actually a fully 3-dimensional event. The fibers inside the wrinkle have become bent similar as to the fibers in the SCT.

6 Predictions of the line folding operation

In the following simulation, the same type of elements as in the SCT is used with similar mesh size, i.e. one element used through the width of a 3 mm wide specimen and 0.01mm×0.01 mm mesh size in an area close to the clamps and a 0.5mm ×0.01mm otherwise. The initial geometry is shown in Fig. 17, where the location of the center of rotation is marked by a red cross. The clamps and the load cell are modeled as rigid analytic surfaces and the corners of the clamps and load cell have been rounded with a small radius $R = 0.02$ mm, i.e. same radius as in the SCT has been used. The distance between the load cell and the clamps is 10 mm. Similar to the SCT, the geometry has been perturbed according to (16) but now with l_m replaced by $l_m^f = 2.75$ mm and $N = 10$.

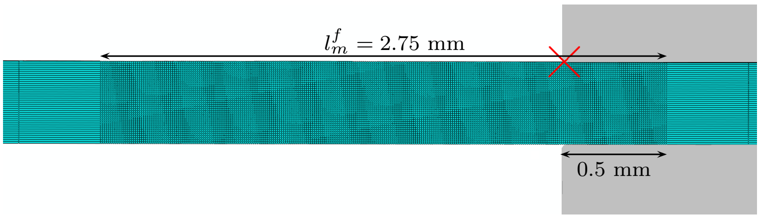

Figure 17: Geometry of simulated line folding zoomed in around the finer meshed region.

The clamps are initially vertically displaced such that a pressure of 0.2 MPa is obtained in the board and then the clamps are rotated an angle of 90 degrees. The resulting moment-rotation response is shown in Fig. 18. The simulated response (solid line) shows good agreement with the experimental results in the CD-direction. The stiffness as well as the maximum bending moment are reasonable predicted by the model. The simulated MD response displays a more serrated shape compared to the experiments. The serrated shape can be correlated to the formation of unstable shear bands, i.e. the force drop when a shear band is formed after an incremental increase in the bending angle. The bending force for the MD-simulation is overestimated at bending angles in the span 30-60 degrees, however in this region the bending moment is sensitive to where the wrinkles are triggered. The bending stiffness and moment are insensitive to the choice of perturbation but the size, shape and the number of wrinkles are influenced by the perturbations. In the simulation it assumed that the paperboard is homogeneous through the width, which likely has an influence on the results. If the in-plane compression threshold is chosen to fit the maximal compression strength from the long edge test, the dashed curve in Fig. 18b is obtained. The dashed line underestimates the measured response and it is clear that the in-plane plastic parameters have a large influence on the bending moment.

The deformation patterns of the folded paperboards in the MD and CD directions are shown in Fig. 19 at the positions marked in Fig. 18. The model is able to predict the formation of wrinkles and shear bands on the compression side. The predicted deformation fields in MD and CD display many similarities but also some differences. Shear bands are formed both in the MD and CD simulations and they are formed in either a stable or an unstable manner. The shear band either grows continuously as the bending angle increases, or instantaneously after an incremental increase in the bending angle. The instantaneous shear band formation is associated with a drop in the moment-rotation curve, cf. Fig. 18. Referring to Fig. 19 at load level (1) for CD, a single shear band is propagating in a stable manner, but at load level (2) after the slight drop in the bending moment has occurred, a distinct wrinkle has formed and a second shear band is observed. Elements inside the wrinkle have stretched several hundreds of percents, resembling a delamination type of deformation. At load level (3) the wrinkle has grown in size.

Examining the deformation field for MD, it is noticed that at load level (1) two shear bands are propagating close to the corner of the lower clamp. The paperboard is compressed and bends inwards at the junction where the two shear bands are in contact on the bottom side. This in-plane compression deformation is not observed in the CD-simulation. At load level (2) a wrinkle and several shear bands have been formed which explains the serrated response in MD. At load level (3) the bending moment has dropped compared to load level (2) and a second larger wrinkle has been formed.

The reorientation of MD direction after the line folding is shown in Fig. 20. From the

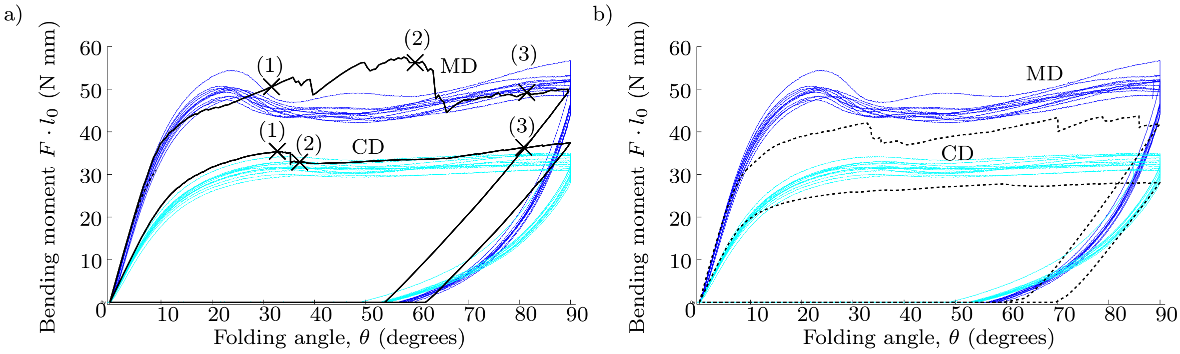

Figure 18: Simulated and measured rotation-moment curves of paperboard. In a) (solid line) have been obtained by fitting the in-plane compression yield thresholds,$\tau_0^{(4)} = 29$ MPa and $\tau_0^{(5)} = 21$ MPa such that the measured SCT response is captured. In b) (dashed lines) the yield thresholds have been chosen to match the maximal peak forces from the long edge test $\tau_0^{(4)} = 18$ MPa and $\tau_0^{(5)} = 12$ MPa.

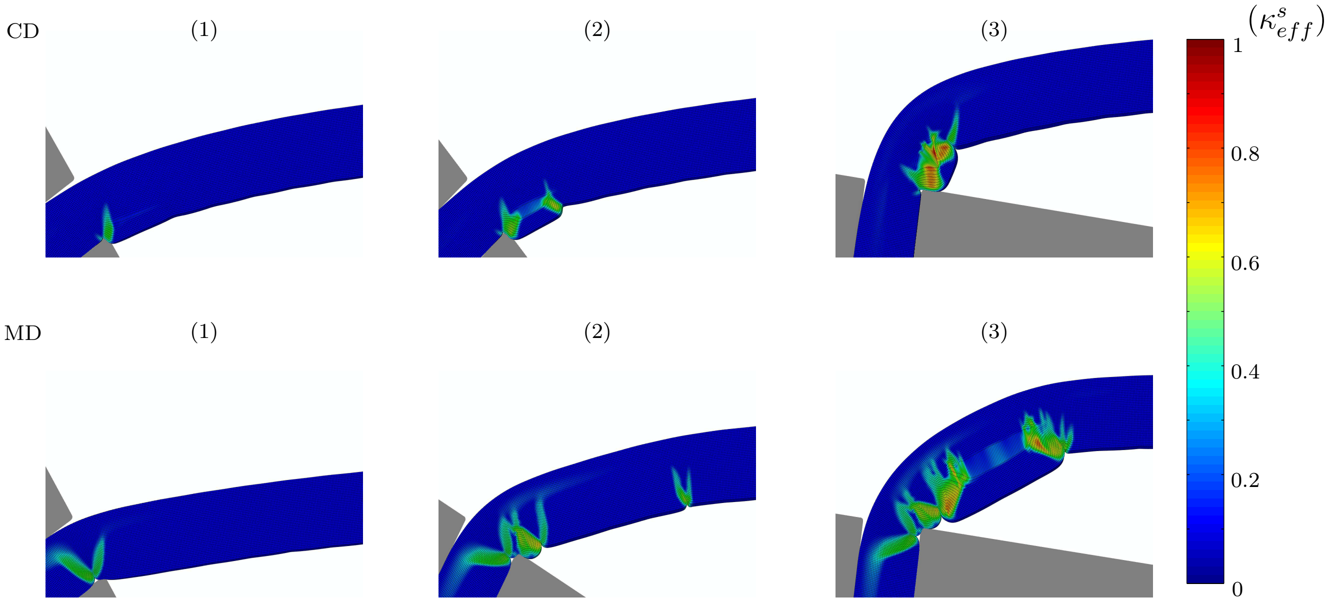

Figure 19: Deformation in line folding operation. The accumulated effective plastic shear is shown at three load levels marked in Fig. 18a for MD (bottom) and CD(top) .

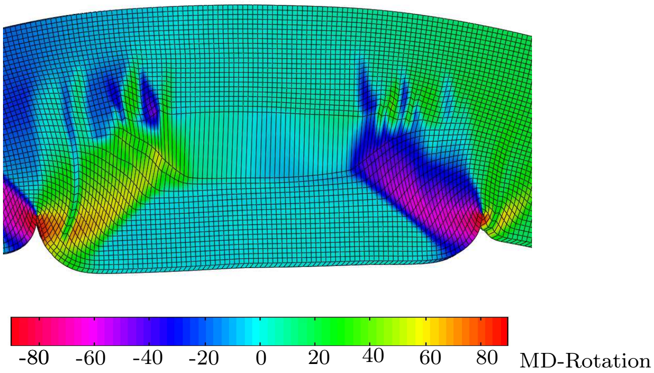

Figure 20: The rotation of the MD-direction is plotted at the unloaded state of the folding in MD. A similar color map as that in Fig. 16 is used.

figure it is seen that the reorientation of the fibers is similar to that observed in the bottom left tomograph image in Fig. 16. The wrinkle and the delamination pattern is slightly overestimated by the model, but the shape and the fiber reorientation angles are similar. Since the material is assumed to be homogeneous, the post-mortem tomograph images, cf. Fig. 16, can not be expected to be exactly captured at the different cross-sections through the width. The model is however able to predict the localized deformation into bands, the formation of the wrinkles and the global moment-rotation curves when calibrated to fit the response in the SCT.

7 Conclusions

The SCT-value is a common measure to characterize the quality of paperboards during industrial packaging applications. The deformation mechanisms that are active during the SCT has therefore been identified and highlighted in this paper. It has been shown that a continuum model can be used to predict the localized deformation patterns occurring in both the SCT and folding. A continuum model has been enhanced such that a free energy with no initial Poisson effect between the in-plane and out-of-plane directions is obtained. Prior to failure in the simulated SCT, a stress state that is associated with permanent deformations in both in-plane compression and out-of-plane tension is occurring. It is therefore important to consider both the in-plane and the out-of-plane yielding. After the maximum out-of-plane stress is reached, an unstable material response is predicted by the model, where the deformation becomes localized into bands. Similar localized deformation fields are revealed from the post-mortem x-ray tomograph images.

The deformation mechanisms that become active during folding is evidently important for forming packages. The model predicts that the shear bands either grow in a stable or an unstable fashion. Formation of wrinkles in the model is associated with the instantaneous growth of the shear bands. From the x-ray tomograph images it is observed that the deformation localizes into bands inside the wrinkles, which is also predicted by the model. The in-plane material parameters related to yielding in compression has a significant influence on the folding response. By fitting the in-plane compression parameters to the SCT response, the model is able to predict the folding process. Inside the wrinkle, the elements are severely stretched in the out-of-plane direction, resembling a delamination type of deformation.

The simplifying assumption of ideal plasticity is used both for the in-plane compression response and out-of-plane response in the model. This assumption allows the unstable material behavior observed both in the SCT and folding to be predicted. In addition, the bending moment measured from the folding operation is in agreement with the simulated response with this assumption. However, the ideal plastic assumption in the out-of-plane direction overestimates the internal forces in the delaminated zones. By including out-of-plane softening into the model, it is expected that the delamination will be in better agreement with experimental results, which will be of importance when folding creased paperboards.

Acknowledgements

The images of the SCT conducted by Björn Hansson and Göran Niklasson at Stora Enso in Karlstad is gratefully acknowledged. The support from Innventia AB with the laboratory equipment related to the long edge and tensile tests is gratefully acknowledged. The x-ray tomography was performed at the 4D-Imaging Lab at the Division of Solid Mechanics, Lund University (financed by the Faculty of Engineering -Lund University). E. Tudisco was supported by the Swedish strategic research programme eSSENCE.

A Material parameters and calibrations

The material parameters used in this work are presented in Tables. 1, 2 and 3. The non-zero components of $N_{ij}^{(\nu)}$ are summarized in Table. 1. The exponent $k = 3$ has been used in (8). The density for the paperboard is 788 kg/m^3.

Stress-state,	Subsurface, ν	Subsurface component $N_{ij}^{(\nu)}$ (-)
MD-tension	1	$N_{11}^{(1)} = 0.925, N_{22}^{(1)} = -0.379$
CD-tension	2	$N_{11}^{(2)} = -0.215, N_{22}^{(2)} = 0.977$
MD-CD shear	3	$N_{12}^{(3)} = 0.7071, N_{21}^{(3)} = 0.7071$
MD-compression	4	$N_{11}^{(4)} = -1$
CD-compression	5	$N_{22}^{(5)} = -1$
MD-CD shear	6	$N_{12}^{(6)} = -0.7071, N_{21}^{(6)} = -0.7071$
ZD-compression	7	$N_{33}^{(7)} = -1$
ZD-tension	8	$N_{33}^{(8)} = 1$
MD-ZD-shear	9	$N_{33}^{(9)} = 0.704, N_{13}^{(9)} = 0.502$
MD-ZD-shear	10	$N_{33}^{(10)} = 0.704, N_{13}^{(10)} = -0.502$
CD-ZD shear	11	$N_{33}^{(11)} = 0.704, N_{23}^{(11)} = 0.502$
CD-ZD shear	12	$N_{33}^{(12)} = 0.704, N_{23}^{(12)} = -0.502$

Table 1: Numerical values of the in-plane subsurface parameters

Elastic parameter	Value
A_1	1690 (MPa)
A_2	292 (MPa)
A_3	28.4 (MPa)
A_4	1333 (MPa)
A_5	78.0 (MPa)
A_6	0.365 (MPa)
A_7	11.5 (-)

Table 2: Numerical values of the elastic parameters.

Subsurface , ν	Initial yield, K_0 (MPa)	Hardening a_ν (MPa)	Hardening b_ν (-)
1	20.4	12.2	690
2	11.7	5.10	435
3	9.91	6.63	334
4	29.1	-	-
5	21.0	-	-
6	9.91	6.63	435
7	1.00	49	-
8	0.40	-	-
9	2.51	-	-
10	2.51	-	-
11	2.51	-	-
12	2.51	-	-

Table 3: Numerical values of the plastic parameters

References

Abaqus User's Manual (2013). Dassault Systemes. Abaqus Inc providence, RI, USA, 6.13 edition.

Beex, L. A. A. and Peerlings, R. H. J. (2009). An experimental and computational study of laminated paperboard creasing and folding. *International Journal of Solids and Structures*, **46**, 4192–4207.

Borgqvist, E., Lindström, T., Tryding, J., Wallin, M., and Ristinmaa, M. (2014). Distortional hardening plasticity model for paperboard. *International Journal of Solids and Structures*, **51**, 2411–2423.

Borgqvist, E., Wallin, M., Ristinmaa, M., and Tryding, J. (2015). An anisotropic in-plane and out-of-plane elasto-plastic continuum model for paperboard. *Composite Structures*, **126**, 184–195.

Carlsson, L., Fellers, C., and de Ruvo, A. (1980). The mechanism of failure in bending of paperboard. *Journal of material science*, **15**, 2636–2642.

Cavlin, S. (1988). The unique Convertibility of Paperboard. *Packaging Technology and Science*, **10**, 77–92.

Cavlin, S. and Fellers, C. (1975). A new method for measuring the edgewise compression properties of paper. *Svensk papperstidning*, **78**, 329–332.

Christer Fellers, Richard E. Mark (Editor) (1983). *Handbook of physical and mechanical testing of paper and paperboard Vol.1, Chapter 8*. Marcel Dekker inc, first edition.

Fleck, N. A. (1997). Compressive failure of fiber composites. *Advances in applied Mechanics*, **33**, 43–117.

Hägglund, R., Gradin, P., and Tarakameh, D. (2004). Some aspects on the zero-span tensile test. *Experimental Mechanics*, **44**, 365–374.

Hagman, A., Huang, H., and Nygårds, M. (2013). Investigation of shear induced failure during sct loading of paperboards. *Nordic Pulp & Paper Research Journal*, **28**, 415–429.

Harrysson, M., Harrysson, A., and Ristinmaa, M. (2007). Spatial representation of evolving anisotropy at large strains. *International Journal of Solids and Structures*, **44**, 3514–3532.

Huang, H., Hagman, A., and Nygårds, M. (2014). Quasi static analysis of creasing and folding for three paperboards. *Mechanics of Materials*, **69**, 11–34.

ISO:9895:2008 (2008). Paper and board– compressive strength – short-span test.

Nygårds, M., Fellers, C., and Östlund, S. (2009a). Development of the notched shear test. *Advance in Pulp and Paper Research, Oxford*, pages 887–898.

Nygårds, M., Just, M., and Tryding, J. (2009b). Experimental and numerical studies of creasing of paperboard. *International Journal of Solids and Structures*, **46**, 2493–2505.

Oden, J. T. and Pires, E. B. (1983). Nonlocal and nonlinear friction laws and variational principles for contact problems in elasticity. *Journal of Applied Mechanics*, **50**, 67–76.

Rasband, W. (1997-2015). ImageJ, U.S. National Institutes of Health, Bethesda, Maryland, USA. *http://imagej.nih.gov/ij/*.

Rezakhaniha, R., Agianniotis, A., Schrauwen, J. T. C., A. Griffa, D. S., Bouten, C. V. C., van de Vosse, F. N., Unser, M., and Stergiopulos, N. (2011). Experimental investigation of collagen waviness and orientation in the arterial adventitia using confocal laser scanning microscopy. *Biomechanics and modeling in mechanobiology, DOI 10.1007/s10237-011-0325-z*.

Ristinmaa, M., Ottosen, N. S., and Korin, C. (2012). Analytical prediction of package collapse loads–basic considerations. *Nordic Pulp & Paper Research Journal*, **27**, 806–813.

Tjahjanto, D., Girlanda, O., and Östlund, S. (2015). Anisotropic viscoelasticâĂŞviscoplastic continuum model for high-density cellulose-based materials. *Journal of the Mechanics and Physics of Solids*, **84**, 1–20.

Westerlind, B. S. and Carlsson, L. A. (1992). Compressive response of corrugated board. *Tappi Journal*, **75**, 145–154.

Xia, Q. S. (2002). *Mechanics of inelastic deformation and delamination in paperboard*. Ph.D. thesis, Massachusetts Institue of Technology.

Xia, Q. S., Boyce, M. C., and Parks, D. M. (2002). A constitutive model for the anisotropic elastic-plastic deformation of paper and paperboard. *International Journal of Solids and Structures*, **39**, 4053–4071.

Paper D

Eric Borgqvist and Mathias Wallin

Numerical integration of elasto-plasticity coupled
to damage using a DIRK integration scheme

International Journal of Damage Mechanics, 22 (2012) 68-94

Numerical integration of elasto-plasticity coupled to damage using a DIRK integration scheme

Eric Borgqvist and Mathias Wallin
Division of Solid Mechanics
Lund University, Box 118, S-221 00 Lund, Sweden

Abstract

The present paper is concerned with the numerical integration of finite strain continuum damage models. The numerical sensitivity of two damage evolution laws and two numerical integration schemes are investigated. The two damage models differ in that one of the models includes a threshold such that the damage evolution is suppressed until a certain effective plastic strain is reached. The classical integration scheme based on the implicit Euler scheme is found to suffer from a severe step-length dependence. An alternative integration scheme based on a Diagonal Implicit Runge-Kutta (DIRK) scheme originally proposed by Ellsiepen (1999) is investigated. The DIRK scheme is applied to the balance of momentum as well as the constitutive evolution equations. When applied to finite strain multiplicative plasticity the DIRK scheme destroys the plastic incompressibility of the underlying continuum evolution laws. Here, the evolution laws are modified such that the incompressibility of the plastic deformation approximately is preserved. The presented numerical examples reveal that a significant increase in accuracy can be obtained at virtually no cost using the DIRK scheme. It is also shown that for the model including a discontinuous evolution law the superiority of the DIRK scheme over the IE-scheme is reduced.

Introduction

The material degradation associated with ductile fracture can be modeled using micromechanical approaches (Gurson (1975)) or Continuum Damage Mechanics (CDM) (cf. Kachanov (1958)) based approaches or a combination thereof (cf. Wallin *et al.* (2008)). In both approaches the degradation of the material is modeled using an internal state variable that captures the influence of micro-voids, micro-cracks and other micro-defects. Since micro-defects nucleate and evolve when subjected to applied load an originally isotropic material can after loading attain an anisotropic micro-structure, cf. Hayhurst (1972). The development of anisotropic damage models is an active research field and an early approach is given by Chow and Wang (1987). Some more recent approaches employing anisotropic Gurson type models are given by e.g. Leblond *et al.* (1994); Steglich *et al.* (2008, 2010) whereas anisotropic continuum damage models have been considered by Menzel *et al.* (2005); Benzerga *et al.* (2002); Menzel and Steinmann (2001). Anisotropic damage models requires the internal state variable being represented by a dyadic product of vectors or higher order tensors. The complexity of anisotropic damage models is significantly higher than that of isotropic damage models where the damage is represented by a scalar internal variable. Since anisotropic damage models are associated with the same numerical difficulties as the isotropic damage models we will here restrict ourselves to consider isotropic damage models only. We refer to Besson (2010) for an extensive review on the state of the art of damage models and their predictive capability.

The elasto-plastic boundary value problem is governed by balance of momentum and constitutive evolution equations that control the material response locally. The numerical solution of the balance of momentum is exclusively based on the finite element method. Depending on load duration, problem size etc., the time integration can be implicit or explicit. The implicit solution procedure is typically based on a multi-level Newton scheme where the solution of the 'global level' requires the sensitivity of the 'local level'. The sensitivity is denoted the algorithmic tangent stiffness tensor (cf. Runesson and Booker (1982), and Simo and Taylor (1985)). An alternative to the multi-level approach is to adopt the Schur's complement approach (cf. Hartmann (2005) and Kulkarni *et al.* (2007)) where the local constitutive iterations are eliminated thus leading to significant speedups for complex constitutive models. The time steps in the Newton procedure is typically governed by the number of Newton iterations in the previous step using a heuristic rule. This rule is evidently not related to the accuracy of the solution of the boundary value problem.

The elasto-plastic damage evolution equations need to be integrated over a finite time step when implemented into a finite element code. Algorithms for integration of path-dependent material response is currently used and has been subject for intense research for many decades. The motivation for this research is that robust and at the same time numerically efficient algorithms are of great importance for both industry and academy. Robustness implies that the numerical scheme should produce a solution for a wide range of loading conditions without interference of the user. Efficiency is a measure of the accuracy in relation to the computational work spend. When evaluating the accuracy of an elasto-plastic boundary value problem the accuracy of the constitutive model is often separated from the accuracy of the solution of the balance of momentum.

The canonical numerical method for performing the integration of the constitutive laws was proposed by Wilkins (1964) and is based on a backward Euler approximation of the evolution equations in combination with enforcement of the yield condition at the end of the integration interval. The resulting time-discretized evolution equations comprise a set of non-linear equations that is solved using a Newton or quasi-Newton method, cf. e.g. Ekh and Menzel (2006). The Wilkins' type of integration scheme is often, due to it's geometrical interpretation, referred to as the radial return method or the closest point projection method (CPPM). The reason for the radial return method being widely used is that the method, although its simplicity, shows good accuracy and stability properties for important models like kinematic hardening von Mises plasticity models, cf. e.g. Kouhia *et al.* (2005). For complex constitutive models, e.g. finite strain anisotropic hardening models the simplicity is lost. Based on this observation alternate integration schemes have been developed.

One alternative approach is based on sub-stepping schemes where a differentiated form of the yield condition is employed (cf. Sloan (1987); Sloan and Booker (1992), Wallin and Ristinmaa (2001), Menzel and Steinmann (2001) and Wallin and Ristinmaa (2008)). The major advantages of this class of methods are its algebraic simplicity and accuracy for sensitive constitutive models. When used in an implicit finite element context these explicit algorithms suffers from having a high cost for calculating the algorithmic tangent stiffness tensor.

In contrast to the methods above where the update is obtained from a direct approximation of the evolution laws, the updating procedure can be based on variational principles. For general non-associated plasticity these algorithms are still under development and we refer to Mosler (2010) for a recent contribution on variational updates for non-associated kinematic hardening finite strain plasticity.

In the radial-return based schemes, sub-stepping schemes and the variational based schemes, the integration of the constitutive equations are considered as being independent of the balance of momentum. However, in Fritzen (1997) the elasto-plastic boundary value problem was identified as being a set of differential algebraic equations (DAE). In Ellsiepen and Hartmann (2001) it was shown that the low-order embedded Diagonally Implicit Runge-Kutta (DIRK) schemes (e.g. Ellsiepen (1999), Cash (1979)) together with the multi-level Newton-Raphson algorithm is particular suitable for solving elasto-plastic boundary value problems. This class of methods preserve the sparsity present in the canonical implicit solution procedure and it has also proven to have superior accuracy over the classical implicit solution procedure. Moreover, since the method is embedded it provides an error estimation of the local error which enables an efficient step-length control. The method has previously been successfully applied to: visco-plasticity small strains (Ellsiepen and Hartmann (2001)); finite strain viscoelasticity (Hartmann (2002)); metal powder plasticity (Hartmann and Bier (2008)) and incompressible materials (Hartmann *et al.* (2008)).

In the present work the numerical sensitivity of the classical damage evolution law proposed by Lemaitre (1985) and Lemaitre and Chaboche (1990) will be compared to the damage evolution law proposed by Bonora (1997) and Bonora and Milella (2001). It should be noted that in contrast to the Lemaitre model, the Bonora model involves a threshold for the damage evolution. This threshold poses a problem for both integration schemes and it is of particular interest to investigate the performance of the DIRK scheme for this model. To evaluate the performance of the numerical schemes and models use will be made of structural iso-error plots where the accuracy of the entire boundary value problem is evaluated. This contrasts many previous studies where iso-error plots have been used to illustrate the accuracy of the constitutive equations only. Moreover, the damage evolution in a fixed point during tensile loading is also considered.

Kinematics

To set the stage we start by considering the finite strain kinematics required to formulate the constitutive model. A particle is identified by its position $\boldsymbol{X}$ in the reference configuration, $\Omega_0 \in \mathbb{R}^3$. The position $\boldsymbol{x}$ of the particle $\boldsymbol{X}$ in the current configuration, $\Omega \in \mathbb{R}^3$, is obtained from the mapping $\boldsymbol{\chi} : \Omega_0 \times \mathbb{R} \rightarrow \Omega$ which can be expressed as $\boldsymbol{x} = \boldsymbol{\chi}(\boldsymbol{X}, t) = \boldsymbol{X} + \boldsymbol{u}$ $\boldsymbol{X}$ from Ω_0 to Ω, i.e. $\boldsymbol{u} = \boldsymbol{x} - \boldsymbol{X}$. The deformation gradient, $\boldsymbol{F} : \Omega_0 \times \mathbb{R} \rightarrow \Omega$ that defines the deformation in the neighborhood of $\boldsymbol{x} \in \Omega$ is defined as

$$\boldsymbol{F} = \frac{\partial \boldsymbol{\chi}}{\partial \boldsymbol{X}} = \boldsymbol{1} + \frac{\partial \boldsymbol{u}}{\partial \boldsymbol{X}}. \tag{1}$$

To define the elastic and plastic portion of the deformation we make use of the multiplicative split (cf. Kröner (1960)) of the deformation gradient, $\boldsymbol{F}$, into an elastic and a plastic part, i.e.

$$\boldsymbol{F} = \boldsymbol{F}^e \boldsymbol{F}^p \tag{2}$$

where $\boldsymbol{F}^e$ and $\boldsymbol{F}^p$ represent the elastic and plastic deformation gradients, respectively. Due to notational simplicity, the inner product of the two second order tensors in (2) was not explicitly indicated. This format will be employed in the following. The elastic Cauchy-Green deformation tensor is defined as $\boldsymbol{C}^e = (\boldsymbol{F}^e)^T \boldsymbol{F}^e$, where the superscript T indicates transpose. The irreversible evolution laws are formulated as rate quantities and, based on (2), the spatial velocity gradient, $\boldsymbol{L} = \dot{\boldsymbol{F}} \boldsymbol{F}^{-1}$, can be decomposed into

$$\boldsymbol{L} = \boldsymbol{l}^e + \boldsymbol{F}^e \boldsymbol{l}^p \boldsymbol{F}^{e-1} \tag{3}$$

where the elastic and plastic velocity gradients $\boldsymbol{l}^e$ and $\boldsymbol{l}^p$ are defined as

$$\boldsymbol{l}^e = \dot{\boldsymbol{F}}^e \boldsymbol{F}^{e-1} \text{ and } \boldsymbol{l}^p = \dot{\boldsymbol{F}}^p \boldsymbol{F}^{p-1}. \tag{4}$$

In the relations above a superposed $\cdot$ denotes the material time derivative and the superscript -1 the inverse. The degradation of the material is characterized by a scalar damage variable α which in a macroscopic sense represents the ratio of damaged material to the undamaged material. To define the kinematic hardening use is a made of a deformation gradient $\boldsymbol{F}^k$ associated with the micro-structure.

The evolution law for the kinematic hardening is defined as

$$\dot{\boldsymbol{F}}^k = \boldsymbol{F}^k \boldsymbol{\beta} \tag{5}$$

where $\boldsymbol{\beta}$ can be interpreted as a velocity gradient to $\boldsymbol{F}^k$. For further details regarding the evolution law (5), we refer to Wallin *et al.* (2003) and Wallin and Ristinmaa (2005). Furthermore, the Cauchy-Green deformation tensor associated with the kinematic hardening is defined as $\boldsymbol{C}^k = (\boldsymbol{F}^k)^T \boldsymbol{F}^k$. The effective plastic strain ε^p_{eff} defined as

$$\dot{\epsilon}^p_{eff} = \frac{1}{1-\alpha}\sqrt{\frac{2}{3}\boldsymbol{l}^p : \boldsymbol{l}^p} \tag{6}$$

will be used to define the damage evolution. It should be noted that ϵ^p_{eff} can be used to define isotropic hardening. This effect is, however, without loss of generality omitted in the present study.

To separate the volumetric deformation from the isochoric deformation the deformation gradient is split into

$$\boldsymbol{F} = (J)^{1/3}\, \boldsymbol{F}_i \tag{7}$$

where $J = det(\boldsymbol{F})$ represents the volumetric deformation and where the isochoric deformation gradient $\boldsymbol{F}_i$ fulfills $det(\boldsymbol{F}_i) = 1$. Note that the volumetric/isochoric decoupling (7) applies to all deformation gradient type variables present in the formulation, i.e.

$$\boldsymbol{F}^p = (J^p)^{1/3}\, \boldsymbol{F}^p_i, \quad \boldsymbol{F}^e = (J^e)^{1/3}\, \boldsymbol{F}^e_i, \quad \boldsymbol{F}^k = \left(J^k\right)^{1/3} \boldsymbol{F}^k_i \tag{8}$$

where $J^p = \det(\boldsymbol{F}^p)$, $J^e = \det(\boldsymbol{F}^e)$ and $J^k = \det(\boldsymbol{F}^k)$.

Governing equations

The elasto-plastic boundary value problem is governed by the equilibrium as well as the constitutive model governing the local material behavior. The equilibrium will be expressed in terms of the principle of virtual work whereas the constitutive equations are formulated in terms of evolution equations.

Constitutive model for damage coupled to elasto-plasticity

The damage model presently explored is an extension of the finite strain kinematic hardening model proposed by Wallin *et al.* (2003) and Wallin and Ristinmaa (2005). That model is in the present work augmented such that the effect of elastic degradation caused by plasticity induced damage evolution is included. The internal variables that defines the model are the plastic deformation gradient $\boldsymbol{F}^p$, the kinematic deformation gradient $\boldsymbol{F}^k$ and a scalar damage variable α. It is assumed that the free energy ψ can be decomposed into an elastic $\psi^e(\boldsymbol{C}^e, \alpha)$ and a plastic part $\psi^p(\boldsymbol{C}^k)$ where the damage variable, α, is restricted to only influence the elastic part of the free energy. In the present work ψ^e is chosen as

$$\rho_o \psi^e = \frac{1}{2}(1-\alpha)K(I_1^e)^2 + 2(1-\alpha)GJ_2^e \tag{9}$$

where the K and G are elastic parameters that for small strains correspond to the bulk and shear modulus respectively. The dilatational invariant I_1^e and the isochoric invariants J_2^e present in (9) are defined as

$$I_1^e = \frac{1}{2}\mathrm{tr}(\ln \boldsymbol{C}^e) = \ln J^e \quad \text{and} \quad J_2^e = \frac{1}{8}(\ln \boldsymbol{C}^e)^{dev} : (\ln \boldsymbol{C}^e)^{dev}. \tag{10}$$

From (9) it follows that the damage variable, α, degrades the elastic parameters such that no residual elastic stiffness being present for $\alpha = 1$.

Although it is straight forward to introduce ϵ^p_{eff} in the free energy it is for simplicity omitted. To ensure that the constitutive model does not violate the laws of thermodynamics the reduced isothermal dissipation inequality

$$\theta = \boldsymbol{\Sigma} : \boldsymbol{l}^p - \boldsymbol{B} : \boldsymbol{\beta} - Y\dot{\alpha} \geq 0 \tag{11}$$

must be satisfied. The Mandel stress, $\boldsymbol{\Sigma}$, the Mandel-type back-stress, $\boldsymbol{B}$ and the damage stress, or energy release rate, Y, driving the irreversible evolution are defined as

$$\boldsymbol{\Sigma} = 2\rho_o \boldsymbol{C}^e \frac{\partial \psi}{\partial \boldsymbol{C}^e}, \quad \boldsymbol{B} = 2\rho_o \boldsymbol{C}^k \frac{\partial \psi}{\partial \boldsymbol{C}^k}, \quad Y = \rho_o \frac{\partial \psi}{\partial \alpha} \tag{12}$$

where ρ_0 is the density in the reference configuration. Using (9) together with (12a) and (12c) enables the Mandel stress, $\boldsymbol{\Sigma}$, and the damage stress, Y, to be identified as

$$\boldsymbol{\Sigma} = K_d \ln J^e \boldsymbol{1} + G_d \ln \boldsymbol{C}_i^e, \quad Y = -\frac{\psi^e}{1-\alpha} \tag{13}$$

where $K_d = (1-\alpha)K$ and $G_d = (1-\alpha)G$. Furthermore, let us also emphasize that the isochoric part of the Mandel stress is deviatoric; since $\ln \boldsymbol{C}_i^e = \ln(\boldsymbol{F}_i^{eT} \boldsymbol{F}_i^e) = (\ln \boldsymbol{C}^e)^{dev}$. The non-symmetric Mandel stress $\boldsymbol{\Sigma}$, is related to the second Piola Kirchhoff stress, $\boldsymbol{S}$, via $\boldsymbol{S} = \boldsymbol{F}^{p-1}\left(\boldsymbol{\Sigma}\boldsymbol{C}^{e-1}\right)\boldsymbol{F}^{p-T}$.

The plastic part of the free energy ψ^p per unit mass is given by

$$\rho_0 \psi^p(\boldsymbol{C}^k) = hJ_2^k \tag{14}$$

where h is a material parameter governing the kinematic hardening. The invariant J_2^k is in analogy to (10b) defined as

$$J_2^k = \frac{1}{8}(\ln \boldsymbol{C}^k)^{dev} : (\ln \boldsymbol{C}^k)^{dev} \tag{15}$$

where we similar to the elastic deformation note that $(\ln \boldsymbol{C}^k)^{dev} = \ln \boldsymbol{C}_i^k = \ln(\boldsymbol{F}_i^{k,T} \boldsymbol{F}_i^k)$. Use of (14) together with the definition of the Mandel type back-stress, (12b) results in

$$\boldsymbol{B} = \frac{1}{2} h (\ln \boldsymbol{C}^k)^{dev} \tag{16}$$

which reveals that the back-stress being purely deviatoric, i.e. $\boldsymbol{B} : \boldsymbol{1} = 0$.

Rate-independent plasticity is adopted and the yield function f that defines the elastic domain is given by

$$f = \sigma_{eff} - \sigma_y, \quad \sigma_{eff} = \left(\frac{3}{2} \bar{\boldsymbol{\Sigma}} : \bar{\boldsymbol{\Sigma}} \right)^{1/2} \tag{17}$$

where σ_y represents the yield stress and where the effective stress $\bar{\boldsymbol{\Sigma}}$ is defined as

$$\bar{\boldsymbol{\Sigma}} = \frac{\boldsymbol{\Sigma}^{dev}}{1 - \alpha} - \boldsymbol{B} \tag{18}$$

Note that the damage is assumed to not influence the backstress and as a consequence $\bar{\boldsymbol{\Sigma}}$ does not vanish when the material has fully degraded. A similar choice can for example be found in Besson (2010) and the work by Nayebi and Abdi (2008). During plastic response $f = 0$ whereas elastic response takes place for $f \leq 0$. To ensure that the dissipation inequality (11) is satisfied, the evolution laws are chosen as

$$\boldsymbol{l}^p = \dot{\lambda} \frac{\partial g}{\partial \boldsymbol{\Sigma}} = \dot{\lambda} \boldsymbol{N}^p, \quad \boldsymbol{\beta} = -\dot{\lambda} \frac{\partial g}{\partial \boldsymbol{B}} = \dot{\lambda} \boldsymbol{N}^k, \quad \dot{\alpha} = -\dot{\lambda} \frac{\partial g}{\partial Y} = \dot{\lambda} N^\alpha \tag{19}$$

where g is convex a potential function satisfying $g(\boldsymbol{\Sigma}, \boldsymbol{B}, \alpha) - g(\boldsymbol{0}, \boldsymbol{0}, 0) \geq 0$. This choice for g ensures the dissipation defined in (11) being fulfilled, i.e. $\theta \geq 0$. The plastic multiplier, $\dot{\lambda}$, introduced in (19) is assumed to be given by the Karush-Kuhn-Tucker (KKT) conditions

$$\dot{\lambda} \geq 0, \quad f \leq 0, \quad f \dot{\lambda} = 0. \tag{20}$$

The potential function g is split into one plastic part, g^p, and one part, g^d, that governs the damage evolution, i.e. $g = g^p + g^d$. Two different damage models will be considered. The first model (Model A) is due to Lemaitre (1985) and Lemaitre and Chaboche (1990) and is given by

$$g^d = \frac{S_A}{(1 + m_A)(1 - \alpha)} \left(-\frac{Y}{S_A} \right)^{1 + m_A} \tag{21}$$

where S_A and m_A are material parameters. Based on (19) and (21) we conclude that the evolution law for the damage variable takes the following form in Model A

$$\dot{\alpha} = \dot{\lambda} \frac{1}{(1 - \alpha)} \left(-\frac{Y}{S_A} \right)^{m_A}. \tag{22}$$

The second model (Model B) that will be considered was proposed by Bonora (1997); Bonora and Milella (2001) and is defined by

$$g^d = \frac{1}{2} \left(-\frac{Y}{S_B} \right)^2 \frac{S_B}{1 - \alpha} \frac{(\alpha_{cr} - \alpha)^{(m_B - 1)/m_B}}{(\epsilon_{eff}^p)^{(2+n)/n}} H(\epsilon_{eff}^p - \epsilon_{th}^p) \tag{23}$$

where H represents the Heaviside step function and $S_B, m_B, \alpha_{cr}, \epsilon^p_{th}$ and n are material constants. This form for g^d leads to that the damage evolution in Model B takes the form

$$\dot{\alpha} = -\dot{\lambda}\frac{Y}{S_B(1-\alpha)}\frac{(\alpha_{cr}-\alpha)^{(m_B-1)/m_B}}{(\epsilon^p_{eff})^{(2+n)/n}}H(\epsilon^p_{eff}-\epsilon^p_{th}). \tag{24}$$

The two formats (22) and (24) differ in that Model B includes the effective plastic strain, ϵ^p_{eff} and that it also includes the critical amount of damage, α_{cr} at failure. Moreover, in the latter model (Model B) the damage evolution is suppressed until the effective plastic strain reaches the threshold value ϵ^p_{th}. Although other formats for the damage evolution exist (cf. e.g. Pires *et al.* (2004)), the evolution laws (22) and (24) are sufficient in the present study.

In accordance with Chaboche (1986) the potential function g^p governing the plastic deformation is chosen as

$$g^p = f + \frac{3}{4B_\infty}\boldsymbol{B}:\boldsymbol{B} \tag{25}$$

where the saturation of the kinematic hardening is denoted B_∞. Using (25), (17) and (19) allow us to identify the evolution laws for $\boldsymbol{l}^p$ and $\boldsymbol{\beta}$ as

$$\boldsymbol{l}^p = \dot{\lambda}\frac{3\bar{\boldsymbol{\Sigma}}}{2\sigma_y(1-\alpha)}, \quad \boldsymbol{\beta} = \dot{\lambda}\left(\frac{3\bar{\boldsymbol{\Sigma}}}{2\sigma_y} - \frac{3\boldsymbol{B}}{2B_\infty}\right). \tag{26}$$

For completeness the constitutive model is summarized in Box 1. The evolution equations governing the material response can now be written in the compact format

$$\dot{\boldsymbol{z}} = \begin{bmatrix} \dot{\boldsymbol{F}}^p \\ \dot{\boldsymbol{F}}^k \\ \dot{\epsilon}^p_{eff} \\ \dot{\alpha} \end{bmatrix} = \dot{\lambda}\begin{bmatrix} \boldsymbol{N}^p \\ \boldsymbol{N}^k \\ N^\varepsilon \\ N^\alpha \end{bmatrix} = \dot{\lambda}\boldsymbol{N}. \tag{27}$$

Based on (19), (26), (22), (24) and (6) we conclude that the generalized direction of the plastic flow, $\boldsymbol{N}$, is a function of the internal variable $\boldsymbol{z}$ and the deformation gradient, $\boldsymbol{F}$, i.e. $\boldsymbol{N} = \boldsymbol{N}(\boldsymbol{z}, \boldsymbol{F})$. Differentiation of the yield condition $\dot{f} = 0$, enables the plastic multiplier $\dot{\lambda}$, to be expressed in terms of the state variables $\boldsymbol{z}$, the displacement field $\boldsymbol{u}$ and the rate of the displacement field $\dot{\boldsymbol{u}}$. However, instead of using $\dot{f} = 0$ the yield condition, $f = 0$, will serve as an algebraic constraint equation that sets the magnitude of $\dot{\lambda}$.

Balance of momentum

The balance of linear momentum is governed by the (static) principle of virtual work in the reference configuration, Ω_0, i.e.

$$\int_{\partial\Omega_{0t}} \delta\boldsymbol{w}\cdot\boldsymbol{T}dS + \int_{\Omega_0}\delta\boldsymbol{w}\cdot\boldsymbol{b}dV = \int_{\Omega_0}\delta\boldsymbol{E}:\boldsymbol{S}dV \tag{28}$$

- Constitutive relations:

$$\boldsymbol{\Sigma} = K_d \ln J^e \mathbf{1} + G_d \ln \boldsymbol{C}_i^e$$

$$\boldsymbol{B} = \frac{1}{2} h (\ln \boldsymbol{C}^k)^{dev}$$

$$Y = -\frac{\psi^e}{1-\alpha}$$

- Evolution laws:

$$\dot{\boldsymbol{F}}^p = \dot{\lambda} \left(\frac{3\bar{\boldsymbol{\Sigma}}}{2\sigma_y (1-\alpha)} \right) \boldsymbol{F}^p = \dot{\lambda} \boldsymbol{N}^p$$

$$\dot{\boldsymbol{F}}^k = \dot{\lambda} \boldsymbol{F}^k \left(\frac{3\bar{\boldsymbol{\Sigma}}}{2\sigma_y} - \frac{3\boldsymbol{B}}{2B_\infty} \right) = \dot{\lambda} \boldsymbol{N}^k$$

$$\dot{\alpha} = -\dot{\lambda} \frac{\partial g^d}{\partial Y} = \dot{\lambda} N^\alpha$$

$$\dot{\epsilon}_{eff}^p = \frac{\dot{\lambda}}{1-\alpha} = \dot{\lambda} N^\varepsilon$$

where $\dot{\lambda}$ is obtained from $\dot{f} = 0$

Box 1: Summary of the constitutive model.

which should be satisfied for all admissible virtual displacements $\delta \boldsymbol{w}$. In (28) $\partial\Omega_{0t}$ denotes the part of the boundary where the traction vector, $\boldsymbol{T}$, in the reference configuration is prescribed. Moreover, the body force vector in the reference configuration is denoted $\boldsymbol{b}$. The virtual strain is denoted $\delta\boldsymbol{E}$ and is defined as $\delta\boldsymbol{E} = 1/2 \left(\delta\boldsymbol{F}^T \boldsymbol{F} + \boldsymbol{F}^T \delta\boldsymbol{F} \right)$ where $\delta\boldsymbol{F} = \frac{\partial(\delta\boldsymbol{w})}{\partial\boldsymbol{X}}$. Rearranging (28) and noting that the stress depends on the internal variables $\boldsymbol{z}$ and the displacement field $\boldsymbol{u}$, results in

$$R^w(\boldsymbol{u}, \delta\boldsymbol{w}, \boldsymbol{z}, t) = \int_{\partial\Omega_{0t}} \delta\boldsymbol{w} \cdot \boldsymbol{T} dS + \int_{\Omega_0} \delta\boldsymbol{w} \cdot \boldsymbol{b} dV - \int_{\Omega_0} \delta\boldsymbol{E} : \boldsymbol{S} dV = 0 \tag{29}$$

which should hold for all admissible virtual displacements $\delta\boldsymbol{w}$. The explicit time dependence present in (29) is a manifestation of the applied load and essential boundary conditions in general being time dependent.

Numerical solution procedure

Let us now bring the balance law and the constitutive model together and form the system governing the elasto-plastic boundary value problem. From (27) and (29) we conclude that during plastic response the system is governed by

$$\begin{aligned} &R^w = R^w(\boldsymbol{u}, \delta\boldsymbol{w}, t, \boldsymbol{z}) = 0 \\ &\dot{\boldsymbol{z}} = \dot{\lambda}\boldsymbol{N}(\boldsymbol{z}, \boldsymbol{F}) \\ &f(\boldsymbol{z}, \boldsymbol{F}) = 0. \end{aligned} \tag{30}$$

For elastic response, i.e. $f(\boldsymbol{z}, \boldsymbol{F}) \leq 0$ the system (30) is modified such that $\dot{\lambda} = 0$, i.e. $\dot{\boldsymbol{z}} = \boldsymbol{0}$. The spatial discretization in (30) will be performed using the finite element method whereas an embedded Runge-Kutta scheme will be employed for the time discretization. Finally we note that the system (30) can be interpreted as a semi-explicit DAE-system of index 2.

Spatial discretization- FE formulation

A displacement based finite element formulation is adopted and the interpolation for the displacement field is expressed as $\boldsymbol{u} = \boldsymbol{N}_m\boldsymbol{a}$ where $\boldsymbol{N}_m$ represents a matrix that contains the shape functions and $\boldsymbol{a}$ the nodal displacements. A Galerkin approach is adopted, i.e. the virtual displacements are given by $\delta\boldsymbol{w} = \boldsymbol{N}_m\delta\boldsymbol{a}$ where $\delta\boldsymbol{a}$ represents the virtual nodal displacements. Inserting $\delta\boldsymbol{w} = \boldsymbol{N}_m\delta\boldsymbol{a}$ into (29) allows the FE formulation to be established, i.e.

$$\int_{\partial\Omega_{0t}} \boldsymbol{N}_m^T\boldsymbol{T}dS + \int_{\Omega_0} \boldsymbol{N}_m^T\boldsymbol{b}dV - \int_{\Omega_0} \boldsymbol{B}_m^T\boldsymbol{S}dV = \boldsymbol{R} = \boldsymbol{0} \tag{31}$$

where $\boldsymbol{B}_m$ is defined from $\delta\boldsymbol{E} = \boldsymbol{B}_m\delta\boldsymbol{a}$. Note that in (31) and in the following we will for simplicity not distinguish between tensors and matrices. An important feature of the finite element method is that the method allows the integrals in (31) to be evaluated element-wise, i.e. the domain Ω_0 is discretized into N_{elm} elements, i.e. $\Omega_0 = \cup_{\alpha=1..N_{elm}}\Omega_0^\alpha$. The integrals over the elements, Ω_0^α, is evaluated using Gauss quadrature, i.e.

$$\int_{\Omega_0^\alpha} [\cdot]\, dV = \sum_{i=1}^{N_{gp}} w_i\, [\cdot]_i \tag{32}$$

where w_i represents the Gauss integration weights and N_{gp} is the number of integration points per element. Based on (32) it is concluded that the internal state variables, $\boldsymbol{z}$ are required in all, $N_{gp} \cdot N_{elm}$, integration points throughout the body, i.e. $\boldsymbol{z}^\alpha$. The spatially discretized form of (30) can be expressed as

$$\begin{aligned} &\boldsymbol{R} = \boldsymbol{R}(\boldsymbol{a}, \boldsymbol{z}^\alpha, t) = \boldsymbol{0} \\ &\dot{\boldsymbol{z}}^\alpha = \dot{\lambda}^\alpha\boldsymbol{N}^\alpha(\boldsymbol{z}^\alpha, \boldsymbol{a}) \\ &f(\boldsymbol{z}^\alpha, \boldsymbol{a}) = 0 \end{aligned} \tag{33}$$

where $\alpha = 1..N_{gp} \cdot N_{elm}$. To complete the solution procedure the time discretization will be addressed in the next section.

$$\begin{array}{c|cccc}
c_1 & a_{11} & 0 & \dots & 0 \\
c_2 & a_{21} & a_{22} & \dots & 0 \\
\vdots & \vdots & \vdots & \ddots & \vdots \\
c_s & b_1 & b_2 & \dots & b_s \\
\hline
 & b_1 & b_2 & \dots & b_s
\end{array}$$

Table 1: Diagonally Implicit Runge-Kutta method

Temporal discretization- Runge-Kutta based integration scheme

The temporal discretization of (33b) will be based on a Runge-Kutta based integration scheme. Let us therefore briefly recapture some of the basic features of the Runge-Kutta methods used for integration of ordinary differential equations. An approximate solution to the initial value problem $\dot{\boldsymbol{y}} = \boldsymbol{f}(\boldsymbol{y}, t)$, $\boldsymbol{y}(t_n) = \boldsymbol{y}_n$ at $t = t_{n+1}$ is given by the quadrature rule

$$\boldsymbol{y}(t_{n+1}) \approx \boldsymbol{y}_{n+1} = \boldsymbol{y}_n + \Delta t_n \sum_{i=1}^{s} b_i \boldsymbol{f}(t + c_i \Delta t_n, \boldsymbol{y}(t_n + c_i \Delta t_n)) \tag{34}$$

where b_i are weight factors and c_i coefficients that determine the location of the quadrature points, stages. The number of stages is denoted s are defined by $T_{ni} = t_n + c_i \Delta t$. To evaluate (34) the stage values $\boldsymbol{y}(t_n + c_i \Delta t_n)$ are required. The stage values are approximated in a manner similar to (34), i.e.

$$\boldsymbol{y}(t_n + c_i \Delta t_n) \approx \boldsymbol{Y}_{ni} = \boldsymbol{y}(t_n) + \Delta t_n \sum_{j=1}^{s} a_{ij} \dot{\boldsymbol{Y}}_{nj} \tag{35}$$

where a new set of weighting factors a_{ij} were introduced. The stage derivatives, $\dot{\boldsymbol{Y}}_{nj}$, present in (35) are defined as

$$\dot{\boldsymbol{Y}}_{nj} = \boldsymbol{f}(T_{nj}, \boldsymbol{Y}_{nj}) \tag{36}$$

Note that the quadrature points T_{nj} in (36) coincides with the quadrature points in (34). Insertion of (36) into (35) results in a non-linear system in the stage variables $\boldsymbol{Y}_{ni}$, i.e. $\boldsymbol{r}(\boldsymbol{Y}_{n1}, \boldsymbol{Y}_{n2}, ..., \boldsymbol{Y}_{ns}) = \boldsymbol{0}$. This system can be solved for the stage variables $\boldsymbol{Y}_{n1}$, $\boldsymbol{Y}_{n2}$, ...,$\boldsymbol{Y}_{ns}$ and once the stage variables are calculated the updated state $\boldsymbol{y}_{n+1}$ can be calculated using (34).

A general Runge-Kutta algorithm is not suitable for finite element formulations since the sparse structure of the FE method is not preserved, cf. Ellsiepen and Hartmann (2001). A group of methods that has proven to be very useful are the Diagonally Implicit Runge Kutta (DIRK) schemes, cf. Tab. 1. A DIRK method has the properties $a_{si} = b_i$ and $a_{ij} = 0$ for $i < j$. The DIRK schemes are referred to as stiffly accurate since the last stage $\boldsymbol{Y}_{ns}$ coincides with the new solution $\boldsymbol{y}_{n+1}$, a property that guarantees the algebraic constraints being fulfilled at the solution $\boldsymbol{y}_{n+1}$ (cf. Ellsiepen and Hartmann (2001)). Due to the diagonal structure of the DIRK scheme the stage i can be decoupled from the previously calculated stages, i.e.

$$\boldsymbol{Y}_{ni} = \boldsymbol{y}_n + \Delta t_n \sum_{j=1}^{i} a_{ij} \dot{\boldsymbol{Y}}_{nj} = \boldsymbol{S}_{ni} + \Delta t_n a_{ii} \dot{\boldsymbol{Y}}_{ni} \tag{37}$$

where the 'start value' $\boldsymbol{S}_{ni}$, is defined as

$$\boldsymbol{S}_{ni} = \boldsymbol{y}_n + \Delta t_n \sum_{j=1}^{i-1} a_{ij} \dot{\boldsymbol{Y}}_{nj}. \tag{38}$$

The reason for introducing the quantity $\boldsymbol{S}_{ni}$ is to emphasize that it only depends upon the stage derivatives calculated from the previous stages. This property is crucial for the use of DIRK schemes in a FE context since it decouples the stages and as a consequence of this decoupling the sparse structure of the original FE-system is preserved. Isolating $\dot{\boldsymbol{Y}}_{ni}$ from (37) results in

$$\dot{\boldsymbol{Y}}_{ni} = \frac{\boldsymbol{Y}_{ni} - \boldsymbol{S}_{ni}}{\Delta t_n a_{ii}} \tag{39}$$

i.e. once the stage value $\boldsymbol{Y}_{ni}$ is calculated the stage derivative $\dot{\boldsymbol{Y}}_{ni}$ is provided by (39). In the context of elasto-plasticity the unknown $\boldsymbol{y}$ is comprised by the displacement field $\boldsymbol{a}$ and the internal variables $\boldsymbol{z}^\alpha$. Defining $\boldsymbol{y} = \{\boldsymbol{z}^\alpha,\ \boldsymbol{a}\}$ and the stage variable $\boldsymbol{Y}_{ni} = \{\boldsymbol{Z}^\alpha_{ni},\ \boldsymbol{A}_{ni}\}$ results in that (33) for each stage can be expressed as

$$\begin{aligned}
&\boldsymbol{R} = \boldsymbol{R}(\boldsymbol{A}_{ni}, \boldsymbol{Z}^\alpha_{ni}, T_{ni}) = \boldsymbol{0} \\
&\boldsymbol{Z}^\alpha_{ni} - \boldsymbol{Z}^\alpha_{S,ni} = \Delta\lambda^\alpha_{ni} \boldsymbol{N}(\boldsymbol{Z}^\alpha_{ni}, \boldsymbol{A}_{ni}) \\
&f(\boldsymbol{Z}^\alpha_{ni}, \boldsymbol{A}_{ni}) = 0
\end{aligned} \tag{40}$$

where $\Delta\lambda^\alpha_{ni} = \Delta t_n a_{ii} \dot{\lambda}^\alpha_{ni}$ was defined. It should be noted that in load step n and stage i we associate $\boldsymbol{Y}_{ni}$, $\boldsymbol{Z}^\alpha_{ni}$ and $\boldsymbol{A}_{ni}$ with $\boldsymbol{y}$, $\boldsymbol{z}^\alpha$ and $\boldsymbol{a}$. The start values for the internal variables $\boldsymbol{Z}^\alpha_{S,ni}$, are extracted from the start values $\boldsymbol{S}_{ni} = \left\{\boldsymbol{Z}^\alpha_{S,ni}, \boldsymbol{A}_{S,ni}\right\}$. The non-linear system system (40) is solved at each stage and once the solution $\boldsymbol{Y}_{ni}$ is determined the stage derivative $\dot{\boldsymbol{Y}}_{ni}$ is calculated via (39) thus allowing the procedure to be advanced to the next stage $i+1$. Note that in general the boundary conditions are time dependent and as a consequence the starting value for the displacement field $\boldsymbol{A}_{S,ni}$ will drive the deformation in a displacement controlled problem.

In Ellsiepen and Hartmann (2001) a three stage RK-method (Cash's method) was considered. Since the underlying elasto-plastic problem is non-smooth, it was concluded that Cash's method was not able to provide third order accuracy and therefore only Ellsiepen's two stage method will be considered in this investigation. The two stage DIRK-method proposed by Ellsiepen (1999) is given in Tab. 2. Besides being an efficient higher order integration scheme the DIRK scheme also provides an error control which can be used to determine a suitable time step. Assume that $\hat{\boldsymbol{y}}_{n+1}$ is the solution at t_{n+1} from a RK-method

$$\begin{array}{c|cc} \gamma & \gamma & \\ 1 & 1-\gamma & \gamma \\ \hline & 1-\gamma & \gamma \\ & 1-\hat{\gamma} & \hat{\gamma} \end{array} \qquad \begin{array}{l} \\ \\ \gamma = 1-\frac{1}{2}\sqrt{2} \\ \hat{\gamma} = 2-\frac{5}{4}\sqrt{2} \end{array}$$

Table 2: Butcher tableau for the two stage DIRK-method proposed by Ellsiepen (1999)

of order q and that $\boldsymbol{y}_{n+1}$ is the solution from a RK-method of order $q+1$. Subtracting $\boldsymbol{y}_{n+1}$ from $\hat{\boldsymbol{y}}_{n+1}$ provides an estimate for the local integration error, i.e.

$$\boldsymbol{\kappa} = \hat{\boldsymbol{y}}_{n+1} - \boldsymbol{y}_{n+1} \tag{41}$$

The error estimation $\boldsymbol{\kappa}$ can be determined at virtually no extra cost using an embedded Runge Kutta method since $\hat{\boldsymbol{y}}_{n+1}$ is calculated using the same stages as for the lower order method $\boldsymbol{y}_{n+1}$. For Ellsiepen's method the b_i coefficients for the embedded method given in the last row of the tableau Tab 2. The error estimation for an embedded scheme is given by

$$\boldsymbol{\kappa} = \Delta t_n \sum_{i=1}^{s} (\hat{b}_i - b_i)\dot{\boldsymbol{Y}}_{ni}. \tag{42}$$

Let us now apply the presented DIRK-discretization to the system (33) explicitly. Using the Ellsiepen's method presented in Tab. 2 a system leading to the stage variable $\boldsymbol{Y}_{n1}$ can be obtained, i.e.

$$\begin{aligned} &\boldsymbol{R} = \boldsymbol{R}(\boldsymbol{A}_{n1}, \boldsymbol{Z}^{\alpha}_{n1}, T_{n1}) = \boldsymbol{0} \\ &\boldsymbol{Z}^{\alpha}_{n1} - \boldsymbol{z}^{\alpha}_{n} = \Delta\lambda^{\alpha}_{n1}\boldsymbol{N}(\boldsymbol{Z}^{\alpha}_{n1}, \boldsymbol{A}_{n1}) \\ &f(\boldsymbol{Z}^{\alpha}_{n1}, \boldsymbol{A}_{n1}) = 0 \end{aligned} \tag{43}$$

where $\Delta\lambda^{\alpha}_{n1} = \gamma\Delta t_n \dot{\lambda}^{\alpha}_{n1}$. Based on the solution $\boldsymbol{Y}_{n1} = \{\boldsymbol{Z}^{\alpha}_{n1},\ \boldsymbol{A}_{n1}\}$ to (43) the stage derivative $\dot{\boldsymbol{Y}}_{n1}$ is calculated from (39). The start value $\boldsymbol{S}_{n2}$ for stage 2 can then be formed as

$$\boldsymbol{S}_{n2} = \boldsymbol{y}_n + (1-\gamma)\Delta t_n \dot{\boldsymbol{Y}}_{n1}. \tag{44}$$

Noting that the solution of stage 2 coincides with the updated state which allows $\boldsymbol{Y}_{n2}$ to be identified as $\boldsymbol{Y}_{n2} = \{\boldsymbol{Z}^{\alpha}_{n2},\ \boldsymbol{A}_{n2}\} = \left\{\boldsymbol{z}^{\alpha}_{n+1}\ \boldsymbol{a}_{n+1}\right\}$. Based on the starting value calculated in (44) the system governing stage 2 can be formed, i.e.

$$\begin{aligned} &\boldsymbol{R} = \boldsymbol{R}(\boldsymbol{a}_{n+1}, \boldsymbol{z}^{\alpha}_{n+1}, t_{n+1}) = \boldsymbol{0} \\ &\boldsymbol{z}^{\alpha}_{n+1} - \boldsymbol{Z}^{\alpha}_{S,n2} = \Delta\lambda^{\alpha}_{n2}\boldsymbol{N}(\boldsymbol{z}^{\alpha}_{n+1}, \boldsymbol{a}_{n+1}) \\ &0 = f(\boldsymbol{z}^{\alpha}_{n+1}, \boldsymbol{a}_{n+1}) \end{aligned} \tag{45}$$

where $\Delta\lambda^{\alpha}_{n2} = \gamma\Delta t_n \dot{\lambda}^{\alpha}_{n2}$. By only considering one stage and taking the butcher tableau as $a_1 = b_1 = c_1 = 1$, the implicit Euler scheme is obtained. It can thus be concluded that the solution of the DIRK-method is obtained by solving two systems of identical structure as the implicit Euler method.

Updating of the internal variables

Let us now consider the updating procedure for the elasto-plastic damage model previously described. Referring to (40) the internal variables at stage i should be updated according to

$$\begin{aligned} &\boldsymbol{Z}^{\alpha}_{ni} - \boldsymbol{Z}^{\alpha}_{S,ni} = \Delta\lambda^{\alpha}_{ni}\boldsymbol{N}(\boldsymbol{Z}^{\alpha}_{ni}, \boldsymbol{A}_{ni}) \\ &0 = f(\boldsymbol{Z}^{\alpha}_{ni}, \boldsymbol{A}_{ni}). \end{aligned} \tag{46}$$

It should be noted that the structure in (46) is identical to the structure of the classical radial return scheme. As for the backward Euler scheme a check whether elastic or plastic response takes place must be performed. This check is performed by introducing the trial state which is obtained from the start values (38), i.e. $\boldsymbol{Z}^{\alpha}_{ni,trial} = \boldsymbol{Z}_{S,ni}$ together with the displacement field at the stage $\boldsymbol{A}_{ni}$. If $f(\boldsymbol{Z}^{\alpha}_{ni,trial}, \boldsymbol{A}_{ni}) \leq 0$ elastic response takes place and the internal variables are updated according to $\boldsymbol{Z}^{\alpha}_{ni} = \boldsymbol{Z}^{\alpha}_{n,trial}$. For the situation $f(\boldsymbol{Z}^{\alpha}_{ni,trial}, \boldsymbol{A}_{ni}) > 0$ the response is plastic and the internal variables must be updated accordingly, cf. (46).

The discontinuity in the damage evolution in Model B calls for extra attention. The damage evolution is suppressed until $\varepsilon^p_{eff} < \varepsilon^p_{th}$ and it is not possible to determine whether $\varepsilon^p_{eff} = \varepsilon^p_{th}$ is reached during a load step a priori. If the starting value for ε^p_{eff} is less than ε^p_{th} the evolution equations are first updated assuming $\dot{\alpha} = 0$. Based on the updated state, a check if the threshold value has been passed is made. If the threshold value ε^p_{th} is reached the system is solved again but using $\dot{\alpha} > 0$.

For incompressible plasticity the exponential update for the plastic deformation gradient is often preferred, (cf. Weber and Anand (1990)) since it inherently preserves the plastic incompressibility, i.e. $det(\boldsymbol{F}^p) = 1$. As noted by Hartmann *et al.* (2008) this update is not applicable for the DIRK schemes and therefore alternative approaches must be considered. Combining (26a) together with (18) reveals that $tr(\boldsymbol{l}^p) = 0$ which implies that the plastic deformation is incompressible (cf. also Box 1). With this condition let us consider the volumetric/isochoric split (cf. (8)) of $\boldsymbol{F}^p$ in detail. Based on $tr(\boldsymbol{l}^p) = \dot{\overline{ln(J^p)}}$ (4) can be formulated as

$$\dot{\boldsymbol{F}}^p = \left(\text{dev}(\boldsymbol{l}^p) + \frac{1}{3}\dot{\overline{\ln J^p}}\boldsymbol{1}\right)\boldsymbol{F}^p. \tag{47}$$

Hartmann *et al.* (2008) made use of a projection technique to preserve plastic incompressibility. In the present paper the evolution law for $\dot{\overline{\ln J^p}}$ is augmented such that incompressibility approximately is preserved. Instead of $\dot{\overline{\ln J^p}} = 0$ we will make use of $\dot{\overline{\ln J^p}} = \kappa^p$ in the evolution law for $\boldsymbol{F}^p$. For an exact integration κ^p vanishes, however, since the RK-scheme introduces numerical error, κ^p will be used to ensure the plastic incompressibility being fulfilled. The evolution law for $\boldsymbol{F}^p$ will now take the form

$$\dot{\boldsymbol{F}}^p = \left(\text{dev}(\boldsymbol{l}^p) + \kappa^p\boldsymbol{1}\right)\boldsymbol{F}^p. \tag{48}$$

The parameter κ^p can be determined from the condition $J^p = 1$. However, to avoid additional equations in the solution procedure, we will estimate κ^p in each stage. The estimation for κ^p will be based on

$$\dot{\overline{\ln J^p}} = \frac{\dot{J}^p}{J^p} \approx \frac{J^p_{ni} - J^p_S}{a_{ii}\Delta t_n J^p_{ni}}. \tag{49}$$

By making use of $J^p_{ni} = 1$, we obtain the following estimation for κ^p

$$\kappa^p = \frac{1}{3}\frac{1 - J^p_S}{a_{ii}\Delta t_n}. \tag{50}$$

From (50) we conclude that by introducing κ^p the deviation $1 - J^p_S$ is corrected such that $J^p_{ni} = 1$ is approached. The estimation (50) has been used in the current investigation and the volumetric plastic formation J^p has been monitored; the deviation $\det(\boldsymbol{F}^p) - 1$ found in the simulations is typically of the order $10^{-7} - 10^{-9}$.

Since the structure of the kinematic hardening evolution law is similar to that of $\boldsymbol{l}^p$ the concept presented in (48) is applied to the kinematic evolution laws, i.e.

$$\dot{\boldsymbol{F}}^k = \boldsymbol{F}^k\Big(\kappa^k\boldsymbol{1} + \operatorname{dev}(\boldsymbol{\beta}_\alpha)\Big). \tag{51}$$

An estimate for κ^k similar to κ^p can be obtained by replacing J^p_S by J^k_S in (49). To summarize the following system has to be solved in each stage for all gauss points

$$\begin{aligned}
\boldsymbol{\varphi}^p &= \boldsymbol{F}^p - \Big((1 - \Delta t_n\gamma\kappa^p)\boldsymbol{1} - \Delta\lambda\operatorname{dev}(\boldsymbol{N}^p)\Big)^{-1}\boldsymbol{F}^p_S = \boldsymbol{0}\\
\boldsymbol{\varphi}^k &= \boldsymbol{F}^k - \boldsymbol{F}^k_S\Big((1 - \Delta t_n\gamma\kappa^k)\boldsymbol{1} - \Delta\lambda\operatorname{dev}(\boldsymbol{N}^k)\Big)^{-1} = \boldsymbol{0}\\
\varphi^\alpha &= \alpha - \alpha_S + \Delta\lambda\frac{\partial g^d}{\partial Y}|_{\alpha=\alpha_{ni}} = 0\\
\varphi^\varepsilon &= \epsilon^p_{eff} - \epsilon^p_{eff,S} - \frac{\Delta\lambda}{1-\alpha} = 0\\
\varphi^f &= f(\boldsymbol{F}^p, \boldsymbol{F}^k, \Delta\lambda, \alpha) = 0
\end{aligned} \tag{52}$$

where subscripts S indicates start values extracted from $\boldsymbol{Z}_{S,ni}$. In (52) the subscript ni for the stage values and the index α for the gauss points have for simplicity been omitted. The system (52) may be written as

$$\boldsymbol{\varphi}(\tilde{\boldsymbol{Z}}^\alpha_{ni}; \boldsymbol{F}) = \boldsymbol{0} \tag{53}$$

where $\tilde{\boldsymbol{Z}}^\alpha_{ni}$ is defined as $\tilde{\boldsymbol{Z}}^\alpha_{ni} = \{\boldsymbol{Z}^\alpha_{ni}, \Delta\lambda^\alpha_{ni}\}$. It should be noted that ψ^ϵ can be omitted for Model A since this model has no explicit ϵ^p_{eff} dependence. The system (53) is solved using the Newton-Raphson iteration scheme, i.e.

$$\tilde{\boldsymbol{Z}}^\alpha_{ni}\big|_{k+1} = \tilde{\boldsymbol{Z}}^\alpha_{ni}\big|_k - \boldsymbol{J}^{-1}\boldsymbol{\varphi}|_k \tag{54}$$

where $\boldsymbol{J}$ denotes the Jacobian $\boldsymbol{J} = \dfrac{\partial \boldsymbol{\varphi}}{\partial \tilde{\boldsymbol{Z}}^{\alpha}_{ni}}\Big|_k$ and the subscript k the iteration number.

Let us now return to the solution of the equilibrium equations, i.e. (40a). A consistent linearization of (40a) and using $\tilde{\boldsymbol{Z}}^{\alpha}_{ni} = \tilde{\boldsymbol{Z}}^{\alpha}_{ni}(\boldsymbol{A}_{ni})$ results in the Newton-Raphson iteration scheme for the displacement field, i.e.

$$\boldsymbol{A}_{ni}\big|_{k+1} = \boldsymbol{A}_{ni}\big|_{k} - \left(\left[\frac{\partial \boldsymbol{R}}{\partial \boldsymbol{A}_{ni}} + \frac{\partial \boldsymbol{R}}{\partial \tilde{\boldsymbol{Z}}^{\alpha}_{ni}} \frac{\partial \tilde{\boldsymbol{Z}}^{\alpha}_{ni}}{\partial \boldsymbol{A}_{ni}}\right]\Bigg|_{k}\right)^{-1} \boldsymbol{R}\big|_{k}. \tag{55}$$

To obtain the sensitivity of the internal variables with respect to the displacement field we return to (53). Since $\boldsymbol{\varphi}(\tilde{\boldsymbol{Z}}^{\alpha}_{ni}; \boldsymbol{F}) = \boldsymbol{0}$ for all $\boldsymbol{F}$ we obtain

$$\frac{\partial \tilde{\boldsymbol{Z}}^{\alpha}_{ni}}{\partial \boldsymbol{F}} = -\left[\frac{\partial \boldsymbol{\varphi}}{\partial \tilde{\boldsymbol{Z}}^{\alpha}_{ni}}\right]^{-1} \frac{\partial \boldsymbol{\varphi}}{\partial \boldsymbol{F}} \tag{56}$$

Noting that $\boldsymbol{F} = \boldsymbol{F}(\boldsymbol{A}_{ni})$ we conclude that (56) provide $\frac{\partial \tilde{\boldsymbol{Z}}^{\alpha}_{ni}}{\partial \boldsymbol{A}_{ni}}$ and therefore the algorithmic tangent stiffness tensor present in (55) can be calculated.

Numerical example

To investigate the numerical sensitivity of the constitutive model in conjunction with the presented numerical integration scheme the boundary value problem depicted in Fig. 1 will be considered.
The measures of the considered structure is given by

$$\frac{\mathrm{R}}{t} = \frac{500}{12}, \quad \frac{\mathrm{w}}{\mathrm{R}} = 3, \quad \frac{\mathrm{L}}{\mathrm{w}} = 2$$

where t is the thickness. Fully integrated 4-node quadratic plane strain elements have been employed. To avoid locking due to incompressibility, a mixed formulation of the balance of momentum (29) has been used cf. Wallin and Ristinmaa (2005). It should be noted that the softening associated with the damage evolution results in mesh-dependence. To reguralize the problem a length-scale can be introduced into the formulation via a non-local formulation, cf. e.g. Håkansson *et al.* (2006). This approach is out of the scope of the present study, and is therefore not considered. The constitutive parameters used in the simulations are given in Tab. 3 and Tab. 4.

G (GPa)	K_b (GPa)	h (MPa)	B_∞ (MPa)	σ_y (MPa)	S_A (MPa)	m (-)
80	164	12000	350	400	2.67	2

Table 3: Constitutive parameters used in Model A

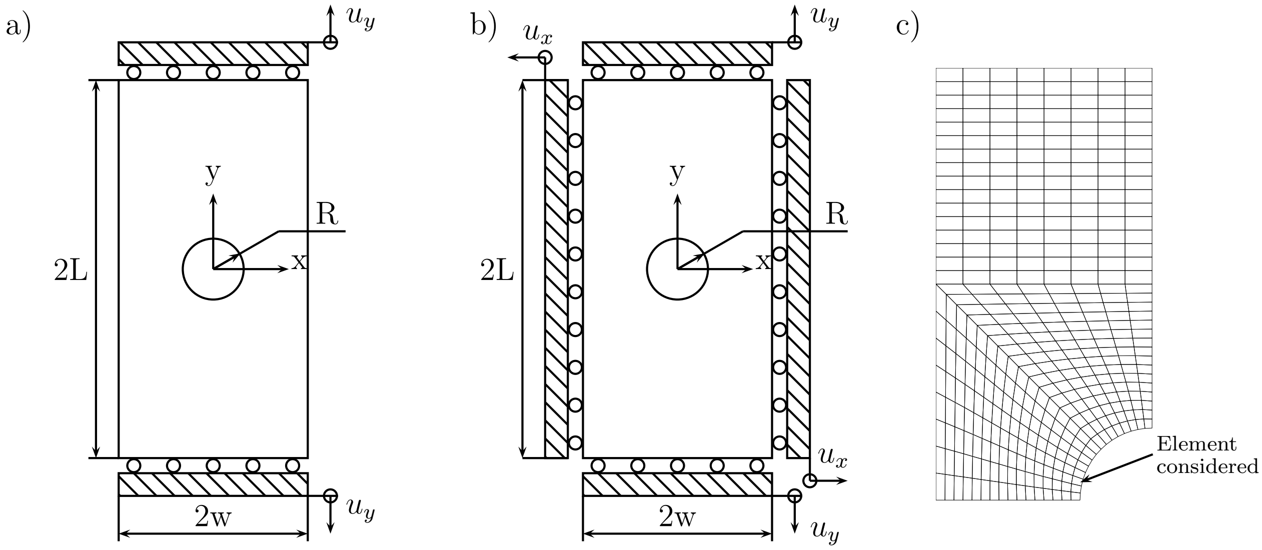

Figure 1: Illustration of the boundary value problem used in the numerical simulation. Two different boundary conditions are considered: a) Prescribed displacement in y-direction b) prescribed displacements in both x- and y-directions c) The finite element mesh used in all simulations consists of 384 plane strain elements. Due to the symmetry, only a quarter of the structure has been considered.

G (GPa)	K_b (GPa)	h (MPa)	B_∞ (MPa)	σ_y (MPa)	S_B (MPa)	m_B (-)	n (-)	ε_{th} (-)	α_{cr} (-)
80	164	12000	350	400	300	0.1	10	0.005	1

Table 4: Constitutive parameters used in Model B

For completeness the force-displacement relation following from the parameters in Tab. 3 and Tab. 4 is given in Fig. 2. The boundary conditions used in the simulation is shown in Fig. 1a. The corresponding stress and damage distributions are shown in Fig. 3 and in Fig. 4. Clearly the chosen parameters results in almost identical mechanical response.

Local damage evolution

In this example the boundary conditions shown in Fig. 1a are considered. To control the time step in the Implicit Euler-method (IE) the following heuristic rule based on the global Newton iterations has been used

$$\Delta t_{n+1} = \Delta t_n f_{inc} \left(\frac{f_{iter}}{N_{newt}} \right)^v \tag{57}$$

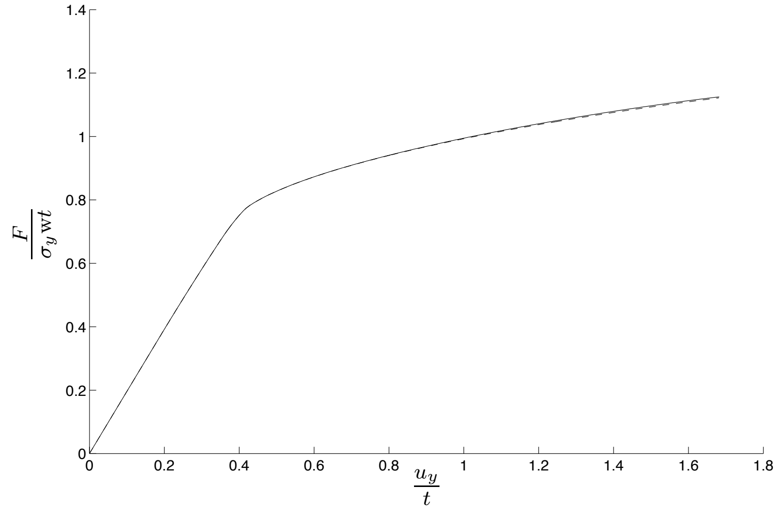

Figure 2: Total applied force along the top boundary versus displacement for Model A (dashed line) and Model B (solid line) using the boundary conditions shown in Fig. 1a. Note that the responses are almost identical and thus difficult to distinguish from each other.

where N_{newt} is the number of Newton iterations in the current load step and f_{inc}, f_{iter} and v are time stepping parameters. The heuristic rule (57) is augmented so that if the solution diverges, the load step is restarted using a time step that is reduced by a factor 2. For the RK-method we adopt the time stepping procedure presented in Ellsiepen and Hartmann (2001). The estimate for the error $\boldsymbol{\kappa}$ is separated into the displacements $\boldsymbol{\kappa}_u$ and the internal variables $\boldsymbol{\kappa}_z$. The 2-norm will be used for the displacements $\boldsymbol{\kappa}_u$ and the maximum norm for the internal variables $\boldsymbol{\kappa}_z$. Based on $\boldsymbol{\kappa}_u$ and $\boldsymbol{\kappa}_z$ the following error measure will be employed

$$e_m = \max\left(\frac{1}{N_{dof}}\sqrt{\sum_{l=1}^{N_{dof}}\left(\frac{\kappa_u^l}{R_{rel}\cdot u^l + R_u^l}\right)^2},\ \max_{k=1\ldots N_{elm}\cdot N_{gp}}\left(\left|\frac{\kappa_z^k}{R_{rel}\cdot z^k + R_z^k}\right|\right)\right) \tag{58}$$

where R_{rel} is a relative tolerance, R_u^l and R_κ^k are absolute tolerances. N_{dof} is the number of degree of freedoms in the structure. The new step size is calculated on the basis of the error measure e_m according to:

$$\Delta t_{new} = \Delta t_n \left\{\begin{array}{ll} \max(f_{min}, f_s \cdot e_m^{-1/(q+1)}) & \text{if } e_m > 1 \\ \min(f_{max}, f_s \cdot e_m^{-1/(q+1)}) & \text{if } e_m \leq 1 \end{array}\right) \tag{59}$$

The safety factor f_s prevents oscillations in the step sizes whereas f_{min} and f_{max} sets maximal step size changes.

In Fig. 5a and Fig. 6a the damage evolution in one gauss point in one element (cf. arrow in Fig. 1c) is plotted versus the displacement u_y. The reference solution (solid line)

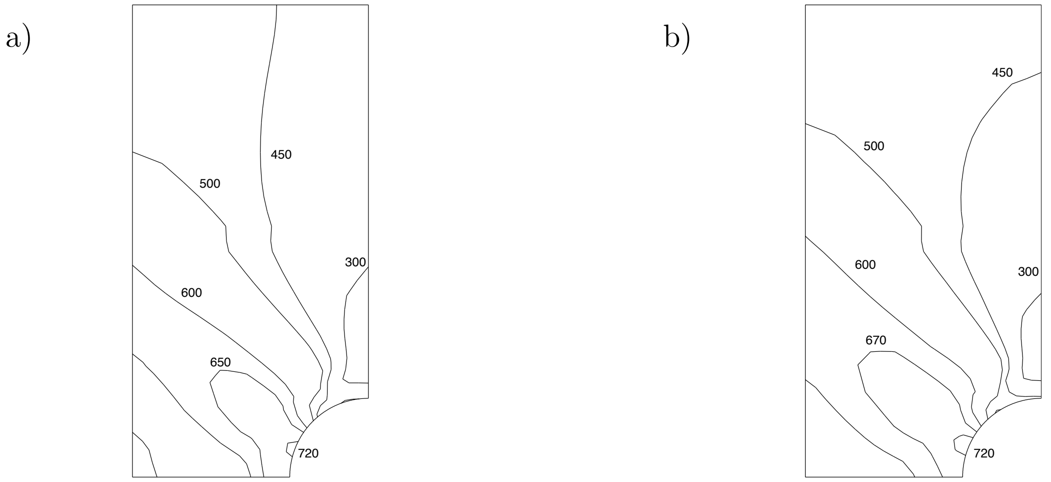

Figure 3: Contour plot of effective stress distribution with a)Model A and b) Model B at the end of the simulation. The boundary conditions given in Fig. 1a has been used.

is obtained by taking 1500 load steps using the RK-method. The difference $|\alpha - \alpha_{ref}|$, where α_{ref} is the damage obtained from the reference solution have been plotted in Fig. 5b and Fig. 6b to emphasize the difference between the integration schemes.

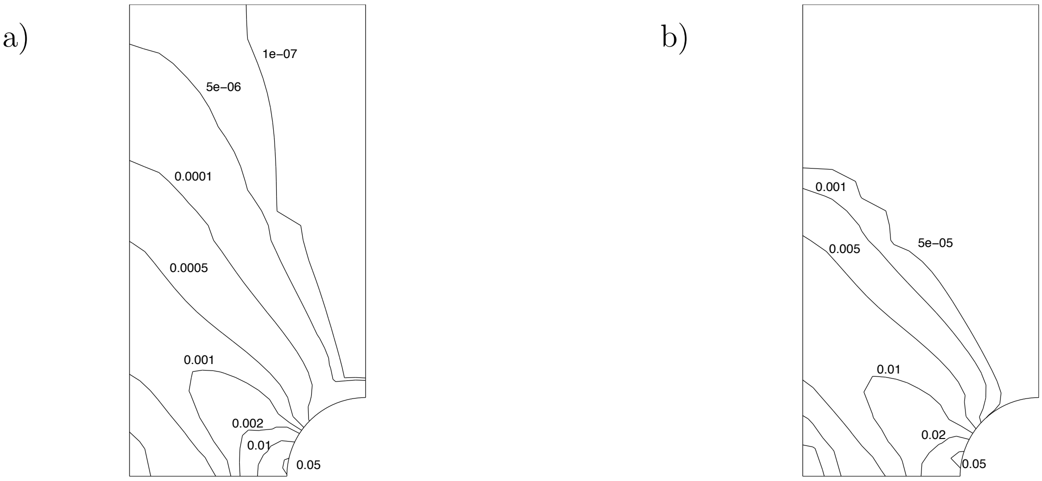

Figure 4: Contour plot of the damage distribution with a) Model A and b) Model B at the end of the simulation. The boundary conditions given in Fig. 1a has been used.

The numerical parameters used to generate Fig. 5 and Fig. 6 are given in the appendix. In Fig. 5 a distinct difference between the two integration schemes can be observed. For simulations using approximately the same number of Newton iterations the RK-scheme shows a significant higher accuracy than the IE-scheme (cf. $\times$ and $\circ$ in Fig. 5a). It is noted that the RK-scheme using 8 steps ($\circ$) shows a higher accuracy than the IE-scheme using 82 ($+$) load steps. Note too that the RK-scheme ($\Box$) completed the simulation using 3 load steps while having approximately the same accuracy as the IE-scheme using 15 load steps.

For Model B the difference in performance is less pronounced. Due to the discontinuity in the damage evolution the integration becomes highly dependent on the location of the damage initiation. As an example, the time stepping parameters used in the RK-simulations marked with $\diamond$ and $\Box$ only differ in the initial time step Δt_1 and one can conclude that this difference results in a significant different solution. Similarly for the IE-scheme one can observe that the simulation using 33 load steps ($\times$) shows less deviation from the reference solution than the simulation using 42 ($+$) load steps.

To evaluate the approximation (49) the maximum deviation from $\det \boldsymbol{F}^p - 1$ was monitored. As an example the the maximum deviation found in the simulation $\Box$ in Fig. 6 was $\det(\boldsymbol{F}^p) - 1 = 4.5 \cdot 10^{-6}$.

Iso-error plots

Iso-error plots have been generated by structurally displacing the geometry using the boundary conditions shown in Fig. 1b. The structure is initially displaced by an amount u_x and u_y in the x- and y-directions. At this level of initial deformation significant plasticity is generated and the maximum damage in the structure is about 4.4 % in Model A and 4.3 % in Model B. After this initial displacement, the structure is further displaced by an amount Δu_x and Δu_y and the internal variables together with the displacements are stored in $\boldsymbol{y}_{xy}$. During the displacement from (u_x, u_y) to $(u_x + \Delta u_x, u_y + \Delta u_y)$, one step is

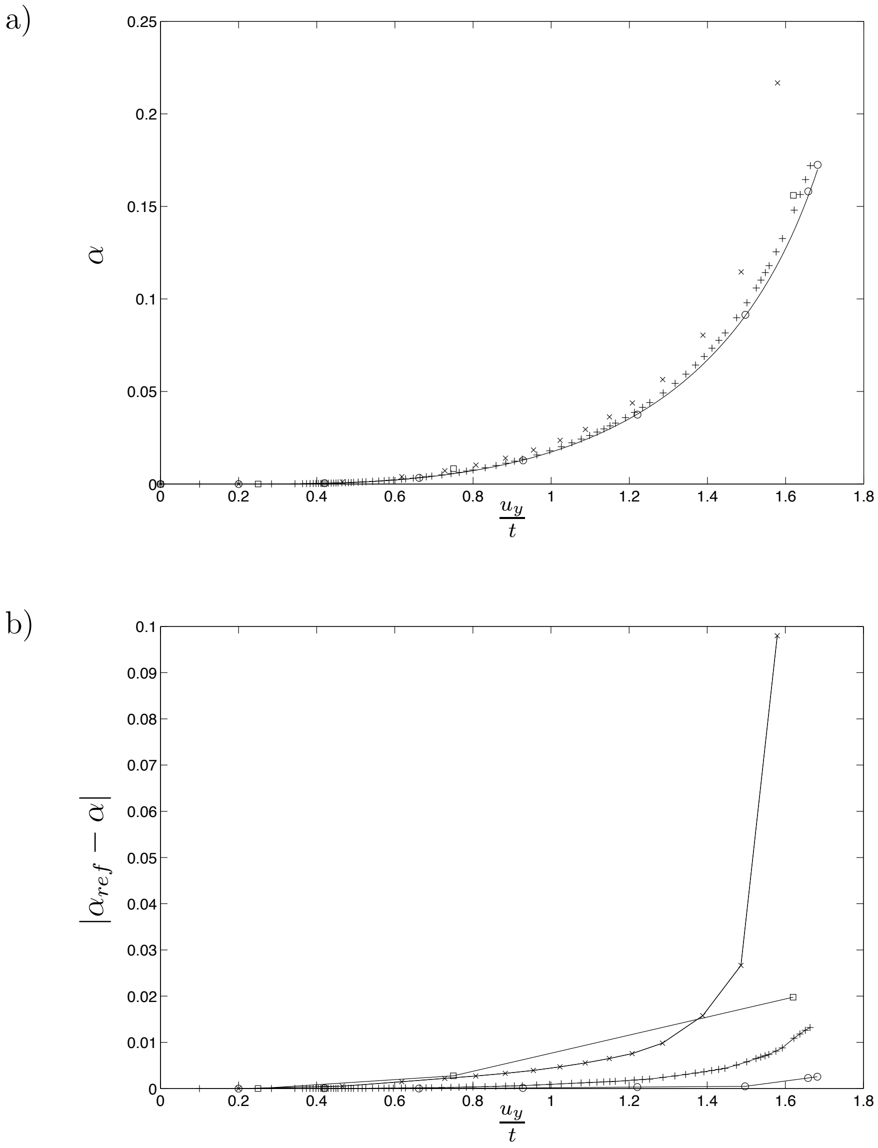

Figure 5: Damage evolution for Model A in one gauss point for the element marked in Fig. 1c. Solid line is the reference solution and solutions indicated by ○, □ are obtained from the RK-solution. The solutions × and + are obtained from the IE-solution. The difference between the reference solution and the simulations is shown in b).

a)

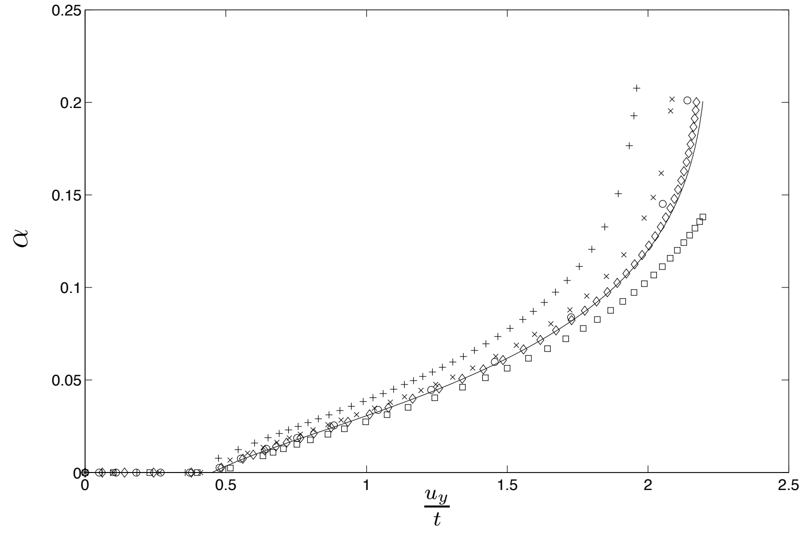

b)

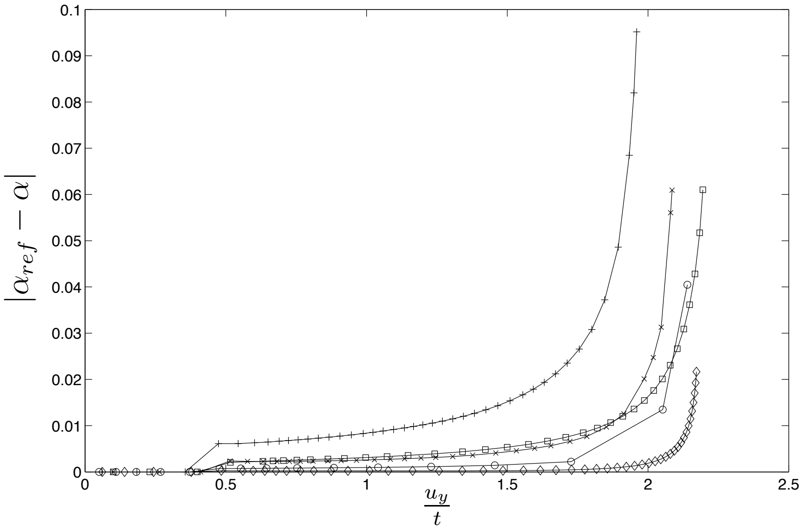

Figure 6: Damage evolution for Model B in one gauss point for the element marked in Fig. 1c. Solid line is the reference solution and solutions indicated by ○, □ , ◇ are obtained from the RK-solution. The solutions ×, + are obtained from the IE-solution. The difference between the reference solution and the simulations is shown in b).

made using the RK-method and two steps with the IE-method. This will ensure that the two methods are using approximately the same number of Newton iterations. Based on the solution at each increment $(u_x + \Delta u_x, u_y + \Delta u_y))$ a contour plot of e_{err}, defined as

$$e_{err} = \left(\int_A (\boldsymbol{y}_{xy}^{ref} - \boldsymbol{y}_{xy}) \boldsymbol{D} (\boldsymbol{y}_{xy}^{ref} - \boldsymbol{y}_{xy}) dA \right)^{\frac{1}{2}} \tag{60}$$

is made. The matrix $\boldsymbol{D}$ is chosen as a diagonal matrix and determines the weight of the variables in $\boldsymbol{y}_{xy}$. The reference solution $\boldsymbol{y}_{xy}^{ref}$ has been obtained by taking 20 steps when using the RK-method from (u_x, u_y) to $(u_x + \Delta u_x, u_y + \Delta u_y)$ and 40 steps when using the IE-method. The iso-error plots are shown in Figs. 7-8 for Model A and Figs. 9-10 for Model B.

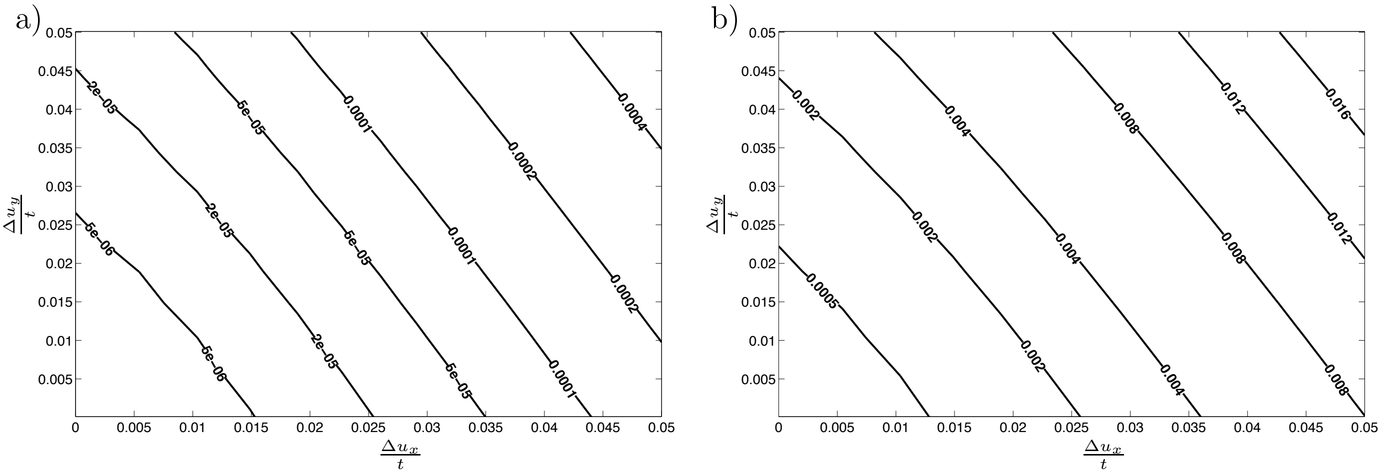

Figure 7: Iso-error plots using Model A. The matrix $\boldsymbol{D}$ is chosen so that only the damage variables are weighted. a)Runge Kutta method and b) Implicit Euler method.

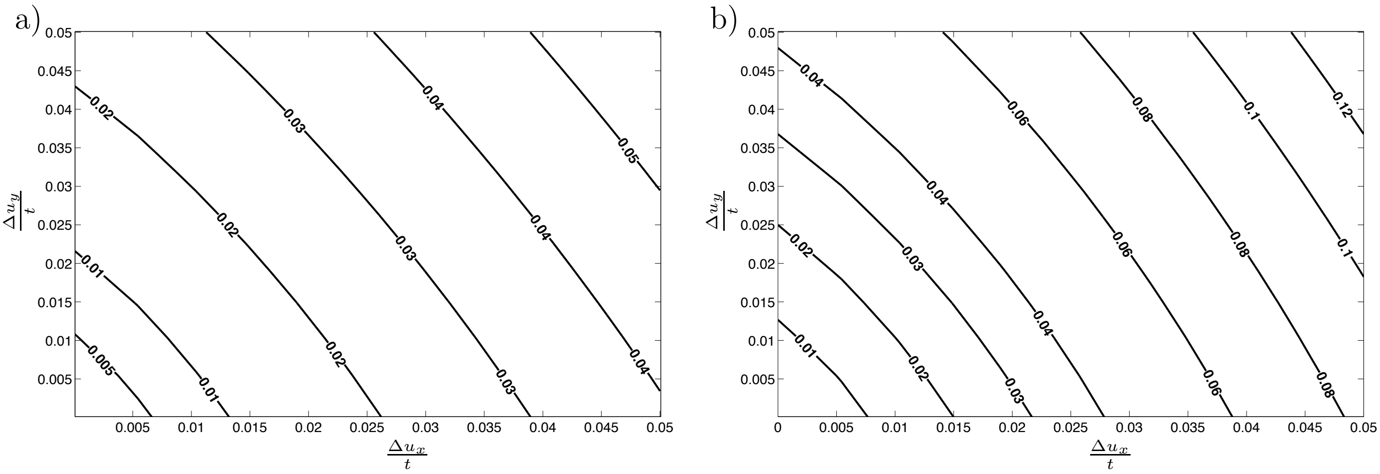

Figure 8: Iso-error plots using Model A. The matrix $\boldsymbol{D}$ is chosen so that all the variables are weighted equal. a) Runge Kutta method and b) Implicit Euler method.

Referring to Fig. 7 it can be concluded that the RK-based integration schemes shows significant higher accuracy than the IE based integration scheme; the error when only the damage distribution is considered is one magnitude lower than the IE based scheme. It is also emphasized that the computational cost is almost identical for the simulations shown in Fig. 7a and Fig. 7b. Furthermore using an error measure where the displacements and all the internal variables are considered (Fig. 8), the accuracy is improved when using the RK-scheme instead of the IE-scheme.

For Model B the improvement using the RK-scheme is reduced. Both Fig. 9a and Fig. 9b shows an error that is about the same. It is also noted that the iso-error plots for Model B is not as smooth as for Model A. This effect is due to that the error varies depending on when damage is initiated. When all the internal variables and the displacements are accounted for (Fig. 10) the RK-scheme shows a higher accuracy and the improvement using the RK-scheme is similar to that found for Model A.

Conclusions

We have presented a finite strain continuum damage kinematic hardening model. Two different forms for the damage evolution law was considered and the numerical sensitivity evaluated. It was concluded that the damage evolution is very sensitive to the step length when using classical Implicit Euler scheme. As an alternative to the canonical Implicit-Euler scheme a solution procedure based an a DIRK algorithm was considered. The efficiency and accuracy of the DIRK scheme was compared to that of the backward-Euler scheme using structural iso-error plots and also via comparison of the damage evolution at a fixed position in the material. The two methods for both models were evaluated using approximately the same number of Newton iterations and it was found that the DIRK based integration scheme is superior to the backward Euler scheme when a smooth damage evolution is considered. However, for a model involving a discontinuous damage evolution, the improvement using the RK-scheme was reduced.

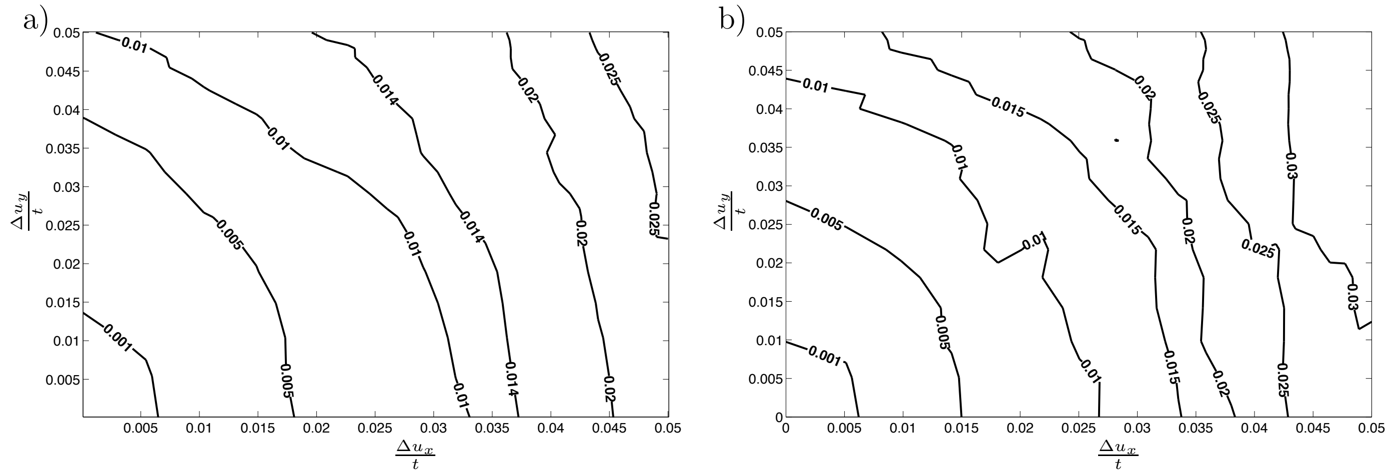

Figure 9: Iso-error plot using Model B. The matrix $\boldsymbol{D}$ is chosen so that only the damage variables are weighted. a) Runge Kutta method and b) Implicit Euler method.

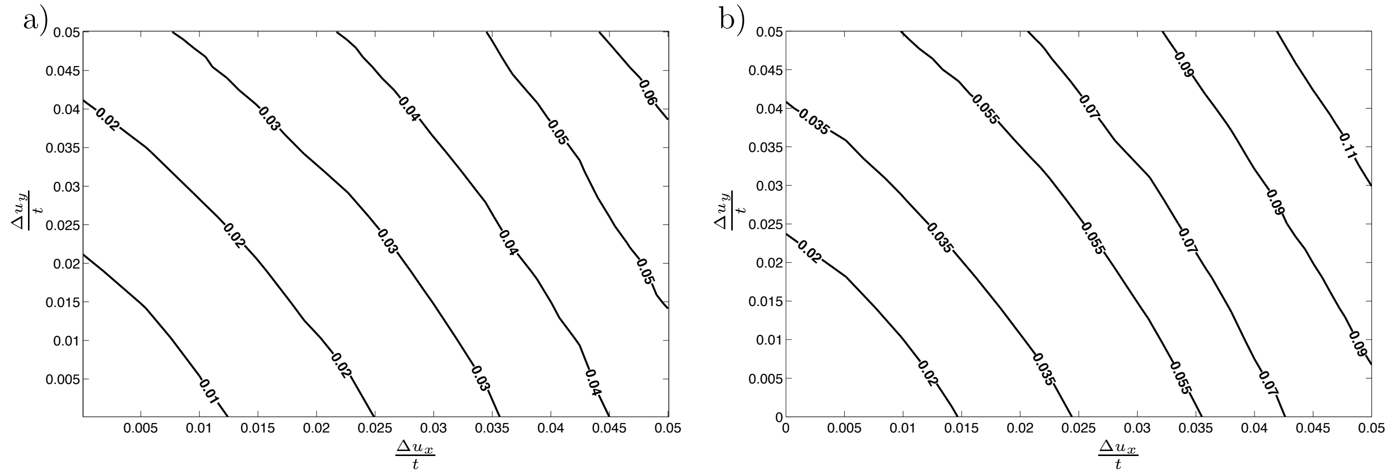

Figure 10: Iso-error plot using Model B. The matrix $\boldsymbol{D}$ is chosen so that all the variables are weighted equal. a) Runge Kutta method and b) Implicit Euler method.

Appendix: Numerical data used in the simulations

Model	Type	R_{rel}	R_u	R_{F^p}	R_{F^k}	R_ε	R_α	f_{min}	f_{max}	f_{safety}	Δt_0
A	○	0	0.1	0.1	0.1	–	0.001	0.05	1.1	0.9	0.2
A	☐	0	1	1	1	–	0.1	0.5	2	0.9	0.25
B	○	10^{-3}	0.1	0.1	0.1	10^{-4}	10^{-3}	0.4	1.2	0.9	0.05
B	☐	10^{-4}	0.01	0.01	0.01	10^{-4}	10^{-5}	0.3	1.3	0.9	0.1
B	◇	10^{-4}	0.01	0.01	0.01	10^{-4}	10^{-5}	0.3	1.3	0.9	0.061

Table 5: Time stepping parameters for RK method used to generate Fig. 5 and Fig. 6.

Damage Model	Type	f_{inc}	f_{iter}	v	Δt_1
A	×	1.01	4.8	1.5	0.2
A	+	1.02	3.8	2.5	0.1
B	×	1.01	4.5	1.2	0.1
B	+	1.01	4.1	1	0.06

Table 6: Time stepping parameters for IE method used in Fig. 5 and Fig. 6.

Damage Model	Type	Newton iterations	Load Steps
A	○ RK	79	8
A	× IE	81	15
A	☐ RK	39	3
A	+ IE	321	82
B	○ RK	146	16
B	× IE	157	33
B	☐ RK	274	36
B	◇ RK	366	49
B	+ IE	182	42

Table 7: Number of Newton iterations and load steps used to generate Fig. 5 and Fig. 6

References

Benzerga, A., Besson, J., Batisse, R., and Pineau, A. (2002). Synergistic effects of plastic anisotropy and void coalescence on fracture mode in plane strain. *Modelling Simul. Mater. Sci. Eng.*, **10**, 73–102.

Besson, J. (2010). Continuum models of ductile fracture: A review. *Int. J. Damage Mechanics*, **19**, 3–52.

Bonora, N. (1997). A non-linear CDM model for ductile failure. *Engineering Fracture Mechanics*, **58**, 11–28.

Bonora, N. and Milella, P. (2001). Constitutive modelling for ductile metals behavior incorporating strain rate, temperature and damage mechanics. *International Journal of Impact Engineering*, **26**, 53–64.

Cash, J. (1979). Diagonally implicit runge-kutta formulae with error estimates. *J. Inst. Maths Applics*, **24**, 293–301.

Chaboche, J. L. (1986). Time-independent constitutive theories for cyclic plasticity. *Int. J. Plasticity*, **2**(2), 149–188.

Chow, C. L. and Wang, J. (1987). An anisotropic theory of continuum damage mechanics for ductile fracture. *Engineering fracture mechanics*, **27**, 547–558.

Ekh, M. and Menzel, A. (2006). Efficient iteration schemes for anisotropic hyperelastoplasticity. *International Journal for Numerical Methods in Engineering*, **66**, 707–721.

Ellsiepen, P. (1999). *Zeit- und ortsadaptive Verfahren angewandt auf Mehrphasenprobleme poröser Medien*. Ph.D. thesis, University of Stuttgart, Stuttgart, Germany.

Ellsiepen, P. and Hartmann, S. (2001). Remarks on the interpretation of current non-linear finite element analyses as differential equations. *International Journal for Numerical Methods in Engineering*, **51**, 679–707.

Fritzen, P. (1997). *Numerische Behandlung nichtlinearer Probleme der Elastizitäts- und Plastizitätstheorie*. Ph.D. thesis, Universty of Darmstadt, Darmstadt, Germany.

Gurson, A. (1975). Plastic flow and fracture behavior of ductile materials incorporating void nucleation, growth, and interaction. *PhD thesis, Brown University, Applied Mechanics.*

Håkansson, P., Wallin, M., and Ristinmaa, M. (2006). Thermomechanical response of non-local porous material. *Int. J. Plasticity*, **22**, 2066–2090.

Hartmann, S. (2002). Computation in finite-strain viscoelasticity: Finite elements based on the interpretation as differential-algebraic equations. *Comput. Methods Appl. Mech. Engrg*, **191**, 1439–1470.

Hartmann, S. (2005). A remark on the application of the Newton-Raphson method in non-linear finite element analysis. *Comp. Mech.*, **36**, 100–116.

Hartmann, S. and Bier, W. (2008). High-order time integration applied to metal powder plasticity. *International Journal of Plasticity*, **24**, 17–54.

Hartmann, S., Quint, K. J., and Arnold, M. (2008). On plastic incompressibility within time-adaptive finite elements combined with projection techniques. *Comput. Methods Appl. Mech. Engng.*, **198**, 178–193.

Hayhurst, D. R. (1972). Creep rupture under multi-axial states of stress. *Journal of the Mechanics and Physics of Solids*, **20**, 381–390.

Kachanov, L. M. (1958). Rupture time under creep conditions. *Izv. Akad. Nauks SSSR Otd. Tech. Nauk*, **8**, 26–31 (In russian). English translation: *Rupture time under creep conditions.* International Journal of Fracture, Vol. 97, No 1–4 , pp. xi–xviii, 1999.

Kouhia, R., Marjamki, P., and Kivilathi, J. (2005). On the implicit integration of rate-dependent inelastic constitutive models. *Int. J. Numer. Meth. Engng.*, **62**, 1832–1856.

Kröner, E. (1960). Allgemeine kontinuumstheorie der versetzungen und eigenspannungen. *Archive for rational mechanics and analysis*, **4**, 273–334.

Kulkarni, D. V., Tortorelli, D. A., and Wallin, M. (2007). A Newton-Schur alternative to the consistent tangent approach in computational plasticity. *Comput. Methods Appl. Mech. Engng.*, **196**, 1169–1177.

Leblond, J., Perrin, G., and Devaux, J. (1994). Bifurcation effects in ductile metals with damage delocalization. *J. Appl. Mech.*, **61**, 236–242.

Lemaitre, J. (1985). A continuous damage mechanics model for ductile failure. *Journal of Engng. Mat. and Tech.*, **107**, 83–89.

Lemaitre, J. and Chaboche, J.-L. (1990). *Mechanics of solid materials.* Cambridge University press, Cambridge, United Kingdom, English edition.

Menzel, A. and Steinmann, P. (2001). A theoretical and computational framework for anisotropic continuum damage mechanics at large strains. *Int. J. Solids Structures*, **38**, 9505–9523.

Menzel, A., Ekh, M., Runesson, K., and Steinmann, P. (2005). A framework for multiplicative elastoplasticity with kinematic hardening coupled to anisotropic damage. *Int. J. Plasticity*, **21**, 397–434.

Mosler, J. (2010). Variationally consistent modeling of finite strain plasticity theory with non-linear kinematic hardening. *Computer Methods in Applied Mechanics and Engineering*, **199**, 2753–2764.

Nayebi, A. and Abdi, R. E. (2008). Shakedown analysis of beams using nonlinear kinematic hardening materials coupled with continuum damage mechanics. *International Journal of Mechanical Sciences*, **50**, 1247–1254.

Pires, F. A., de Souza Neto, E., and Owen, D. (2004). On the finite element prediction of damage growth and fracture initiation in finitely deforming ductile materials. *Computer Methods in Applied Mechanics and Engineering*, **193**, 5223–5256.

Runesson, K. and Booker, J. R. (1982). On mixed and displacement finite element methods in perfect elasto-plasticity. In *Proc. of the Fourth Int. Conf. in Australia on Finite Element Methods*, pages 85–89.

Simo, J. C. and Taylor, R. L. (1985). Consistent tangent operators for rate-independent elasto-plasticity. *Comput. Methods Appl. Mech. Engng.*, **48**, 101–118.

Sloan, S. W. (1987). Substepping schemes for the numerical integration of elastoplastic stress-strain relations. *Int. J. Numer. Meth. Engng.*, **24**, 893–911.

Sloan, S. W. and Booker, J. R. (1992). Integration of Tresca and Mohr-Coulomb constitutive relations in plane strain elasticity. *Int. J. Numer. Meth. Engng.*, **33**, 163–196.

Steglich, D., Brocks, W., and Jürgen Heerens, T. P. (2008). Anistropic ductile fracture of al 2024 alloys. *Engineering fracture mechanics*, **75**, 3692–3706.

Steglich, D., H.Wafai, and Besson, J. (2010). Interaction between anistropic plastic deformation and damage evolution in al 2198 sheet metal. *Engineering fracture mechanics*, **77**, 3501–3518.

Wallin, M. and Ristinmaa, M. (2001). Accurate stress updating algorithm based on constant strain rate assumption. *Comput. Methods Appl. Mech. Engng.*, **190**, 5583–5601.

Wallin, M. and Ristinmaa, M. (2005). Deformation gradient based kinematic hardening model. *Int. J. Plasticity*, **21**, 2025–2050.

Wallin, M. and Ristinmaa, M. (2008). An alternative method for the integration of continuum damage evolution laws. *Computational Mechanics*, **41**, 347–359.

Wallin, M., Ristinmaa, M., and Ottosen, N. S. (2003). Kinematic hardening in large strain plasticity. *Eur. J. Mech. A/Solids*, **22**(3), 341–356.

Wallin, M., Olssson, M., and Ristinmaa, M. (2008). Modeling of the degradation of elastic properties due to the evolution of ductile damage. *International Journal of Damage Mechanics*, **2**, 149–172.

Weber, G. and Anand, L. (1990). Finite deformation constitutitve equations and a time integration procedure for isotropic, hyperelastic-viscoplastic solids. *Comput. Methods Appl. Mech. Engng.*, **79**, 173–202.

Wilkins, M. L. (1964). Calculation of elasto-plastic flow. In *Methods of Computational Physics 3* ,eds., B. Alder et. al. Academic Press, New York.

Paper E

Eric Borgqvist, Mathias Wallin, Matti Ristinmaa and Johan Tryding

A continuum elasto-plastic damage model for anisotropic materials with a high degree of anisotropy

To be submitted for publication

A continuum elasto-plastic damage model for anisotropic materials with a high degree of anisotropy

Eric Borgqvist, Mathias Wallin, Matti Ristinmaa and Johan Tryding
Division of Solid Mechanics
Lund University, Box 118, S-221 00 Lund, Sweden

Abstract

An anisotropic continuum elasto-plastic-damage model has been developed. The considered material is paperboard, which possess a high degree of anisotropy between the in-plane and out-of-plane mechanical material properties. In-plane director vectors and a normal vector are utilized to model the anisotropic behavior of the material. A yield surface, which hardens and softens distortionally is adopted. The model uses two scalar internal variables to model the degradation of material properties in out-of-plane tension and shear, respectively. Using the developed model, the important industrial testing method of creasing and subsequent folding is examined. The deformation patterns are examined using the model and compared with measurements. It is shown that both out-of-plane tension and shear deformations are significant during the folding of creased paperboard.

1 Introduction

Material modeling is becoming increasingly important in product development processes. The models can be used to study specific industrial applications and thereby increase the knowledge about the process. The models need to be sufficiently advanced to represent the actual behavior of the material, but at the same time being simple enough to reduce the computational cost. A continuum based anisotropic material model that can model damage and permanent deformations at finite strains has been developed in this work. An anisotropic format for the elastic, the plastic and the damage parts of the model is utilized.

The developed model in this work is an extension of a model presented in Borgqvist *et al.* (2015). Effects of damage and degradation will be taken into account, such that the softening associated with delamination can be modeled. The specific material that will be considered is paperboard, having a layered fibrous structure and possessing a high degree of anisotropy. The developed model is however general and might be suitable for modeling of other layered structures, such as composites.

The high degree of anisotropy in paperboard stems from the manufacturing process where a fiber mixture is sprayed on a traversing web. The velocity difference between the web and the mixture (as the mixture hits the web) causes a majority of the fibers to align with the Machine Direction (MD). The fibers are typically stacked on top of each other and the stacking direction is called out-of-plane (ZD). Orthogonal to MD in the in-plane direction is the Cross Direction (CD). The stiffness in MD is typically 2-3 times higher compared to CD and about 100 times higher compared to ZD, cf. Stenberg (2002).

The industrial application that will be examined is the folding of creased paperboard. To obtain a straight fold line without in-plane cracks, it is crucial to first perform creasing. In the creasing process, a male tool presses the paperboard into the groove of a female tool. The creasing inflicts permanent deformation and damage in the paperboard, such that the crease zone will act as a plastic hinge during folding operation. To asses the quality of paperboard, it is common to measure the reduction of maximal bending moment between an uncreased and creased paperboard, cf. Nagasawa *et al.* (2003), Giampieri *et al.* (2011) and Cavlin (1988). Experimental tests of folding uncreased and creased paperboard have been performed, which have been compared to predictions obtained in simulations.

One early attempt to use continuum modeling to simulate the converting of paperboard was performed in Xia (2002), where continuum and interface elements were combined. A similar technique have been adopted in Nygårds *et al.* (2009), Beex and Peerlings (2009), Beex and Peerlings (2012), Huang *et al.* (2014) and Hagman *et al.* (2013) using the interface/continuum approach. Since the continuum elements are too stiff in the out-of-plane directions, the out-of-plane deformation is typically restricted to the interfaces, which are a-priori defined in these modeling approaches. In Borgqvist *et al.* (2015), a continuum model which takes into account the large anisotropy between the in-plane and out-of-plane directions was presented. In this work, the model presented Borgqvist *et al.* (2015) is extended such that softening in the out-of-plane directions can be modeled. This extension is important when modeling folding of creased paperboard, as the degradation obtained during the creasing process reduces the load carrying capacity of the material.

A Continuum Damage Mechanics (CDM) concept, where damage is approximated to be smeared out in the material, will be used to model the degradation of material properties. The concept was introduced in Kachanov (1958) and has since then been extensively developed, e.g. Chaboche (1981), Lemaitre (1985), and Al-Rub and Voyiadjis (2003). For general anisotropic damage evolution, second order or fourth order tensor needs to be adopted. However, to reduce the complexity in the model, only scalar damage variables are used in the work herein. An excellent review on the different damage concepts is presented in Besson (2010). The scalar damage will only weaken the material parameters associated with out-of-plane deformation, and thereby allowing softening present during delamination to be recovered. Previously, Isaksson *et al.* (2004) applied the CDM concept to model the in-plane behavior of paper.

The article is structured as follows, first the kinematical and thermodynamic frameworks are established. Tensors will be considered in a Cartesian setting, i.e. following the work of Ciarlet (1988). Section 4 presents the specific model and in section 5 it is demonstrated that the material model can be calibrated to uniaxial tests when a single element is used. The creasing and folding processes are reviewed in the final section and compared with results obtained from simulations.

2 Kinematics

The framework adopted in Borgqvist *et al.* (2014, 2015) will be used to model the anisotropic material. The vector $\boldsymbol{X}$ denotes the position of a particle in the reference configuration and the position of the same particle at time t in the current configuration is given by the mapping $\boldsymbol{x} = \boldsymbol{\varphi}(\boldsymbol{X}, t)$, defined in the time interval $T \in [t_0, t]$. The mapping of vectors in the reference configuration to the current configuration is given by the deformation gradient $\boldsymbol{F} = \nabla_{\boldsymbol{X}} \boldsymbol{\varphi}$. To separate the deformation into elastic and permanent deformations, a multiplicative split of the deformation gradient is assumed, i.e.

$$\boldsymbol{F} = \boldsymbol{F}^e \boldsymbol{F}^p. \tag{1}$$

To model the elastic response, use is made of the left Cauchy-Green tensor, given by $\boldsymbol{b}^e = (\boldsymbol{F}^e)^T \boldsymbol{F}^e$. The spatial velocity gradient is defined as, $\boldsymbol{l} = \dot{\boldsymbol{F}} \boldsymbol{F}^{-1}$ and can be additively split according to

$$\boldsymbol{l} = \boldsymbol{l}^e + \boldsymbol{F}^e \boldsymbol{L}^p \boldsymbol{F}^{e-1} = \boldsymbol{l}^e + \boldsymbol{l}^p. \tag{2}$$

The elastic and material plastic velocity gradients introduced in (2), were defined according to

$$\boldsymbol{l}^e = \dot{\boldsymbol{F}}^e \boldsymbol{F}^{e-1}, \qquad \boldsymbol{L}^p = \dot{\boldsymbol{F}}^p \boldsymbol{F}^{p-1}. \tag{3}$$

The plastic velocity gradient in (2) can further be split into a symmetric part and a skew-symmetric part, i.e.

$$\boldsymbol{l}^p = \mathrm{sym}(\boldsymbol{l}^p) + \mathrm{skew}(\boldsymbol{l}^p) = \boldsymbol{d}^p + \boldsymbol{\omega}^p, \tag{4}$$

where $\boldsymbol{d}^p$ is the plastic rate of deformation tensor and $\boldsymbol{\omega}^p$ is the Eulerian plastic spin, cf. Dafalias (1998). For later purposes, the symmetric part of the spatial velocity gradient is defined as $\boldsymbol{d} = \text{sym}(\boldsymbol{l})$.

To model anisotropy, two director vectors which phenomenologically represent the MD and CD directions are introduced. The vectors are given by $\boldsymbol{v}_0^{(1)}$ and $\boldsymbol{v}_0^{(2)}$ respectively, and they are of unit length and orthogonal. An isoclinic configuration is adopted, implying that the director vectors in the reference configuration and the intermediate configuration are identical, cf. Mandel (1971), Dafalias (1998) and Harrysson and Ristinmaa (2007). The mapping of the in-plane directions to the spatial configuration are assumed to be given by

$$\begin{aligned} \boldsymbol{v}^{(1)} &= \boldsymbol{F}^e \boldsymbol{v}_0^{(1)} \\ \boldsymbol{v}^{(2)} &= \boldsymbol{F}^e \boldsymbol{v}_0^{(2)}. \end{aligned} \tag{5}$$

Following Borgqvist *et al.* (2015), the ZD-direction is chosen such that it is normal to the in-plane directions in the deformed configuration, i.e. $\boldsymbol{n}^{(3)} = \boldsymbol{v}^{(1)} \times \boldsymbol{v}^{(2)}$. Due to the chosen format in (5), it can be shown that the transformation of the ZD-direction can be written as

$$\boldsymbol{n}^{(3)} = J^e \boldsymbol{F}^{e-T} \boldsymbol{n}_0^{(3)}, \tag{6}$$

where J^e is the determinant of the elastic deformation gradient and $J^e \boldsymbol{F}^{e-T}$ the cofactor of $\boldsymbol{F}^e$.

A set of second order structural tensors are used in the subsequent derivations, which are given as dyadic products of the director vectors and normal vector, i.e.

$$\boldsymbol{m}^{(1)} = \boldsymbol{v}^{(1)} \otimes \boldsymbol{v}^{(1)}, \quad \boldsymbol{m}^{(2)} = \boldsymbol{v}^{(2)} \otimes \boldsymbol{v}^{(2)}, \quad \boldsymbol{m}^{(3)} = \boldsymbol{n}^{(3)} \otimes \boldsymbol{n}^{(3)}. \tag{7}$$

The constitutive relations adopted in the model will be described next.

3 Constitutive framework

The dissipation inequality in an isothermal setting is given by

$$d = \boldsymbol{\tau} : \boldsymbol{d} - \rho_0 \dot{\psi} \geq 0, \tag{8}$$

where $\boldsymbol{\tau}$ is the Kirchhoff stress tensor and ψ is the Helmholtz free energy per unit mass and ρ_0 is the density in the reference configuration. Two scalar damage variable ϕ_1 and ϕ_2 are introduced to model the effect of degradation of the elastic parameters in the out-of-plane direction. In Borgqvist *et al.* (2015), the free energy, $\rho_0\psi$, is taken as a function of the elastic deformation $\boldsymbol{b}^e$, the structural tensors $\boldsymbol{m}^{(\alpha)}$ and a set of internal variables, $\kappa^{(\nu)}$ that governs the hardening. In the present work this model is extended such that the free energy also depends on the damage variables ϕ_1 and ϕ_2, i.e.

$$\psi = \psi(\boldsymbol{b}^e, \boldsymbol{m}^{(\alpha)}, \kappa^{(\nu)}, \phi_1, \phi_2), \tag{9}$$

Using arguments by Coleman and Gurtin (1967) it can be shown that the Kirchhoff stress tensor can be expressed as, (cf. Borgqvist *et al.* (2015))

$$\boldsymbol{\tau} = 2\rho_0 \left(\frac{\partial \psi}{\partial \boldsymbol{b}^e} \boldsymbol{b}^e + \frac{\partial \psi}{\partial \boldsymbol{m}^{(1)}} \boldsymbol{m}^{(1)} + \frac{\partial \psi}{\partial \boldsymbol{m}^{(2)}} \boldsymbol{m}^{(2)} - \frac{\partial \psi}{\partial \boldsymbol{m}^{(3)}} \boldsymbol{m}^{(3)} + \left(\frac{\partial \psi}{\partial \boldsymbol{m}^{(3)}} : \boldsymbol{m}^{(3)}\right) \boldsymbol{I} \right). \tag{10}$$

Making use of (8), (9) and (10) along with (2) and (4), the dissipation inequality can be reduced to

$$d = \boldsymbol{\tau} : \boldsymbol{d}^p - K^{(\gamma)} \dot{\kappa}^{(\gamma)} + Y_1 \dot{\phi}_1 + Y_2 \dot{\phi}_2 \geq 0, \tag{11}$$

where the thermodynamic forces, $K^{(\gamma)}$, Y_1 and Y_2 were introduced. The forces, $K^{(\gamma)}$, Y_1 and Y_2 are energy conjugates to the internal variables, $\dot{\kappa}^{(\gamma)}$ and damage variables $\dot{\phi}_1$ and $\dot{\phi}_2$ respectively, and defined as

$$K^{(\gamma)} = \rho_0 \frac{\partial \psi}{\partial \kappa^{(\gamma)}} \qquad Y_1 = -\rho_0 \frac{\partial \psi}{\partial \phi_1} \qquad Y_2 = -\rho_0 \frac{\partial \psi}{\partial \phi_2}. \tag{12}$$

The free energy is further assumed to be split into an elastic and a plastic part according to $\rho_0 \psi = \rho_0 \psi^e(\boldsymbol{b}^e, \boldsymbol{m}^{(\alpha)}, \phi_1, \phi_2) + \rho_0 \psi^p(\kappa^{(\gamma)})$.

4 Specific Model

The specific model that will be adopted in the simulations will be described next. First the constitutive equations governing the reversible (elastic) response are described and then the relations governing the irreversible response are introduced.

4.1 Reversible deformations

The invariants that will be utilized to define the model are given by

$$\begin{aligned} &I_{11} = \sqrt{\boldsymbol{m}^{(1)} : \boldsymbol{I}}, \quad I_{12} = \sqrt{\boldsymbol{m}^{(2)} : \boldsymbol{I}}, \quad I_{13} = \frac{1}{J^e} \sqrt{\boldsymbol{m}^{(3)} : \boldsymbol{b}^e \boldsymbol{b}^e} \\ &I_{23} = \sqrt{\boldsymbol{m}^{(3)} : \boldsymbol{I}} \quad J^e = \sqrt{\det(\boldsymbol{b}^e)}, \end{aligned} \tag{13}$$

where $\boldsymbol{I}$ represent the second order unit tensor. The invariants, $I_{1\alpha}$ can be interpreted as the stretch in the directions (α) and I_{23} represents the change of an area element with normal in the ZD-direction. The elastic part of the Helmholtz free energy is split according to

$$\rho_0 \psi^e = \rho_0 \psi^{ip} + \rho_0 \psi^{cop} + \rho_0 \psi^{top} + \rho_0 \psi^{sop}, \tag{14}$$

where the superscripts refers to ip: in-plane, cop: compression out-of-plane, top: tension out-of-plane and sop: shear out-of-plane. The first two terms in (14) are given by

$$\begin{aligned} \rho_0 \psi^{ip} &= A_1 \left(I_{11} + \frac{1}{I_{11}} - 2 \right) + A_2 \left(I_{12} + \frac{1}{I_{12}} - 2 \right) + A_4 \left(I_{11} + I_{12} + \frac{1}{I_{23}} - 3 \right) \\ \rho_0 \psi^{cop} &= (1 - H_1) A_6 \left((I_{13})^2 + \frac{1}{A_7} e^{-A_7((I_{13})^2 - 1)} - (1 + \frac{1}{A_7}) \right), \end{aligned} \tag{15}$$

where the elastic parameters are defined by $A_\alpha \geq 0$ and H_1 is a step function defined as 1 when $I_{13} - 1 \geq 0$ and zero otherwise. The scalar damage variables, ϕ_1 and ϕ_2, will enter the terms $\rho_0 \psi^{top}$ and $\rho_0 \psi^{sop}$ according to

$$\rho_0 \psi^{top} = (1-\phi_1)^n \rho_0 \tilde{\psi}^{top}, \qquad \rho_0 \psi^{sop} = (1-\phi_2)^n \rho_0 \tilde{\psi}^{sop} \tag{16}$$

where

$$\begin{aligned} \rho_0 \tilde{\psi}^{top} &= H_1 A_3 \left(I_{13} + \frac{1}{I_{13}} - 2 \right) \\ \rho_0 \tilde{\psi}^{sop} &= A_5 \Big(I_{11} I_{12} I_{13} - J^e \Big). \end{aligned} \tag{17}$$

With the format (16), the material constants that govern the initial stiffness in the out-of-plane directions will be degraded with a factor $(1-\phi_1)^n$ in out-of-plane tension and $(1-\phi_2)^n$ in out-of-plane shear and as a consequence, a softening response can be modeled. By combining (12) and (16) and due to the additive format of the free energy, the conjugated damage variables are given by

$$\begin{aligned} Y_1 &= n(1-\phi_1)^{n-1} \rho_0 \tilde{\psi}^{top} \\ Y_2 &= n(1-\phi_2)^{n-1} \rho_0 \tilde{\psi}^{sop}. \end{aligned} \tag{18}$$

The conjugated forces Y_1 and Y_2 are the driving forces for the evolution of the damage due to tension in ZD and out-of-plane shear, respectively.

To illustrate the influence of the material constants on the initial stiffness, the spatial stiffness tensor is computed according to (cf. Harrysson *et al.* (2007)),

$$\boldsymbol{\mathcal{D}} = \frac{\partial \boldsymbol{\tau}}{\partial \boldsymbol{F}} \boldsymbol{F}^T \bigg|_{\boldsymbol{F}=\boldsymbol{I}} \tag{19}$$

Using (15) and (17), the following initial stiffness tensor is obtained (in Voigt notation with the order MD, CD, ZD)

$$[\boldsymbol{\mathcal{D}}] = \begin{pmatrix} 2A_1 + 2A_4 & A_4 & & & & \\ A_4 & 2A_2 + 2A_4 & & & & \\ & & 2H_1 \bar{A}_3 + 4(1-H_1)A_6 A_7 & & & \\ & & & A_4 + \bar{A}_5 & & \\ & & & & \bar{A}_5 & \\ & & & & & \bar{A}_5 \end{pmatrix}, \tag{20}$$

where $\bar{A}_3 = (1-\phi_1)^n A_3$ and $\bar{A}_5 = (1-\phi_2)^n A_5$ and a zero entry is indicated by a blank space in (20). From (20), it can be concluded that the free energy ψ^{ip} will provide an initial stiffness for the MD and CD directions whereas the parts ψ^{cop}, ψ^{top} and ψ^{sop} of the free energy will define the initial stiffness in the out-of-plane direction.

4.2 Irreversible deformations

The yield surface originally proposed in Xia *et al.* (2002) and later used for fiberous materials in e.g. Nygårds *et al.* (2009), Tjahjanto *et al.* (2015), Garbowski *et al.* (2011) and Borgqvist *et al.* (2014), will be utilized. A set of sub-surfaces in the stress space are utilized to define the yield surface. The normals to the sub-surfaces are given by $\boldsymbol{n}_s^{(\nu)}$ where for instance $\nu = 1$ refers to the subsurface associated with positive stresses in the MD-direction. The explicit format of the yield surface is given by

$$f = \sum_{\nu=1}^{12} \chi^{(\nu)} \left(\frac{\boldsymbol{\tau} : \boldsymbol{n}_s^{(\nu)}}{\tau^{(\nu)}} \right)^{2k} - 1. \tag{21}$$

The sub-surfaces $1 \dots 7$ are associated with in-plane stresses while $8 \dots 12$ are associated with out-of-plane stresses. The normals to the sub-surfaces are given by $\boldsymbol{n}_s^{(\nu)}$ and are defined by dyadic products of the normed director vectors and normal, i.e.

$$\boldsymbol{n}_s^{(\nu)} = \sum_{i=1}^{3} \sum_{j=1}^{3} N_{ij}^{(\nu)} \bar{\boldsymbol{v}}^{(i)} \otimes \bar{\boldsymbol{v}}^{(j)}. \tag{22}$$

The parameters, $N_{ij}^{(\nu)}$ introduced in (22), define the yield normals and $\bar{\boldsymbol{v}}^{(i)}$ are given by

$$\bar{\boldsymbol{v}}^{(1)} = \frac{1}{|\boldsymbol{v}^{(1)}|}\boldsymbol{v}^{(1)}, \quad \bar{\boldsymbol{v}}^{(2)} = \frac{1}{|\boldsymbol{v}^{(2)}|}\boldsymbol{v}^{(2)}, \quad \bar{\boldsymbol{v}}^{(3)} = \frac{1}{|\boldsymbol{n}^{(3)}|}\boldsymbol{n}^{(3)}, \tag{23}$$

where $|\cdot|$ denotes the Euclidean 2-norm. The material parameters $N_{ij}^{(\nu)}$ was calibrated in Borgqvist *et al.* (2015) and are found in Table 1 in the Appendix. In (21), the exponent k is a constant natural number and $\chi^{(\nu)}$ is a switch function, which for a given stress state $\boldsymbol{\tau}$ determines if a subsurface is potentially active,

$$\chi^{(\nu)} = \begin{cases} 1 & \text{if} \quad \boldsymbol{\tau} : \boldsymbol{n}_s^{(\nu)} > 0 \\ 0 & \quad \text{otherwise.} \end{cases} \tag{24}$$

The distance from the origin to each subsurface in (21) is given by $\tau^{(\nu)}$ where

$$\tau^{(\nu)} = h_\nu(\phi_1, \phi_2)(\tau_0^{(\nu)} + K^{(\nu)}). \tag{25}$$

The initial distance from the origin to the subsurface is given by $\tau_0^{(\nu)}$, i.e. the initial yield stress in a certain loading direction. The conjugated hardening variables, $K^{(\nu)}$, represents the change in distance from the origin to a subsurface due to plastic loading and the function $h_\nu(\phi_1, \phi_2)$ represents the change in distance to the subsurface due to damage evolution. To reduce the complexity of the model, it is assumed that the distances to the sub-surfaces will either increase due to plastic loading or decrease due to the damage evolution, i.e. either hardening or softening will occur for each yield sub-surface. The hardening parameters have been chosen in a similar format as in Borgqvist *et al.* (2015), i.e.

$$\begin{aligned}
&K^{(\nu)} = a_\nu \ln\left(b_\nu \kappa^{(\nu)} + 1\right) && \nu \in \{1,2,3,6\} \\
&K^{(\nu)} = a_\nu \kappa^{(\nu)} && \nu = 7 \\
&K^{(\nu)} = 0 && \nu \in \{4,5,8,9,10,11,12\},
\end{aligned} \tag{26}$$

where a_ν and b_ν are material parameters. During plastic deformation, the sub-surfaces corresponding to tension in MD/CD, in-plane shear and compression in ZD will therefore translate in the stress-space according to (26). The functions governing the softening of the subsurfaces are chosen as

$$\begin{aligned}
h_\nu(\phi_1,\phi_2) &= (1-\phi_1)^{n_c} && \nu \in \{4,5\} \\
h_\nu(\phi_1,\phi_2) &= (1-\phi_1)^{n_t} && \nu = 8 \\
h_\nu(\phi_1,\phi_2) &= (1-\phi_1)^{n_s}(1-\phi_2)^{n_s} && \nu \in \{9,10,11,12\} \\
h_\nu(\phi_1,\phi_2) &= 1 && \nu \in \{1,2,3,6,7\}.
\end{aligned} \tag{27}$$

Note that different material constants n_t, n_s and n_c enters in (27). The specific choice in (27) is motivated from finite element simulations and tests of the creasing and folding operation. The subsurfaces associated with tension in ZD, out-of-plane shear and compression in MD/CD will as a consequence of (27) give rise to a softening response as damage evolves.

Projections of the yield surface in the ZD-MD/ZD shear stress space for different values of the damage variables ϕ_1 and ϕ_2 are given in Fig. 1. The out-of-plane stress, τ_{op} and the out-of-plane shear stress τ_{sop} are defined according to $\tau_{op} = \boldsymbol{v}^{(3)} \cdot \boldsymbol{\tau} \cdot \boldsymbol{v}^{(3)}$ and $\tau_{sop} = \boldsymbol{v}^{(1)} \cdot \boldsymbol{\tau} \cdot \boldsymbol{v}^{(3)}$ in Fig. 1. The yield surface approaches a Coulomb type surface when ϕ_α increases, as illustrated in Fig. 1. The shape of the yield surface in Fig. 1 will ensure that the material can withstand increasing shear stresses as the compressive stresses τ_{op} increases, i.e. frictional type behavior is modeled. A slope of $\eta = 0.7$ has been adopted in the simulations, which remains constant as the damage increases.

To simplify the notation the quantity Λ_ν is introduced as

$$\Lambda_\nu = \frac{\boldsymbol{\tau} : \boldsymbol{n}_s^{(\nu)}}{\tau^{(\nu)}}. \tag{28}$$

A non-associated format is adopted for the evolution laws. The potential which governs the evolution of the internal variables and damage is assumed to be given by

$$g = \sum_{\nu \in \Omega_\nu} \chi^{(\nu)} \Lambda_\nu^{2k} + c_{op} \chi^{(8)} \Lambda_8^{2k} + H_2 \frac{S_1}{m+1} \left(\frac{Y_1}{S_1}\right)^{m+1} + \frac{S_2}{m+1} \left(\frac{Y_2}{S_2}\right)^{m+1} \tag{29}$$

A set $\Omega_\nu = \nu \in \{1, 2, \ldots 12\} \backslash \{8\}$ is defined in (29), which contains all the sub-surfaces except the one belonging to ZD-tension. The parameter c_{op} controls the amount of permanent deformation and the parameters S_1, S_2 and m are associated with the damage

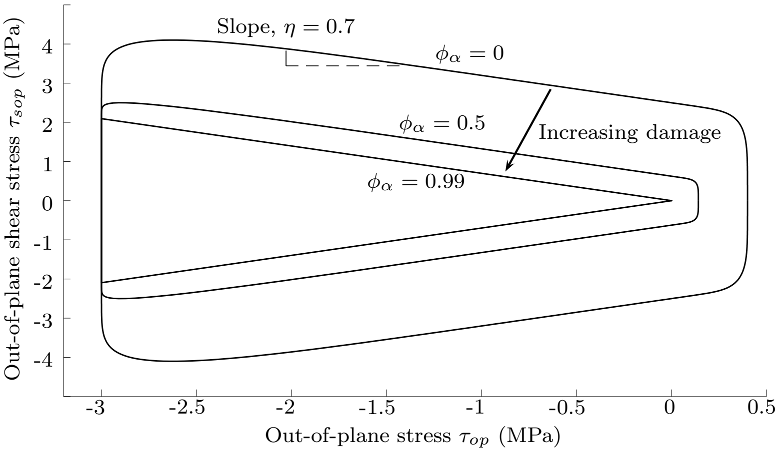

Figure 1: A projection of the yield surface $f = 0$ for different value of damage $\phi_\alpha \in \{0, 0.5, 0.99\}$. The damage variables changes proportionally, i.e. $\phi_\alpha = \phi_1 = \phi_2$.

evolution. The H_2 is a step function which takes τ_{op} is argument and is defined as 1 when $\tau_{op} > 0$ and zero otherwise. Non-associative evolution laws are assumed and are given by

$$\begin{aligned}
\boldsymbol{d}^p &= \dot{\lambda}\frac{\partial g}{\partial \boldsymbol{\tau}} &&= \sum_{\gamma\in\Omega_\nu} \chi^{(\gamma)} \frac{\dot{\lambda}2k\Lambda_\gamma^{2k-1}}{\tau^{(\gamma)}} \mathrm{sym}(\boldsymbol{n}_s^{(\gamma)}) + c_{op}\chi^{(8)} \frac{\dot{\lambda}2k\Lambda_8^{2k-1}}{\tau^{(8)}} \mathrm{sym}(\boldsymbol{n}_s^{(8)}) \\
\dot{\kappa}^{(\nu)} &= \dot{\lambda}\frac{\partial g}{\partial K^{(\nu)}} &&= -\chi^{(\nu)} \frac{\dot{\lambda}2k\Lambda_\nu^{2k}}{\tau^{(\nu)}} \\
\dot{\phi}_1 &= \dot{\lambda}\frac{\partial g}{\partial Y_1} &&= \dot{\lambda}H_2\left(\frac{Y_1}{S_1}\right)^m, \qquad \phi_1 < \phi_1^{max} \\
\dot{\phi}_2 &= \dot{\lambda}\frac{\partial g}{\partial Y_2} &&= \dot{\lambda}\left(\frac{Y_2}{S_2}\right)^m, \qquad \phi_2 < \phi_2^{max}
\end{aligned} \tag{30}$$

The proposed form for the damage variables follows the format proposed in i.e. Lemaitre (1985). Note that damage evolution will only take place as long as the damage variables are less than a threshold value ϕ_α^{max}. Once the damage threshold is reached, the evolution of the damage variable is suppressed, $\dot{\phi}_\alpha = 0$. The ϕ_α^{max} are needed to obtained numerically stable results and finite elements that do not degenerate.

In addition to (30), the eulerian plastic spin also need to be chosen, and it is chosen in a similar format as in Borgqvist *et al.* (2015),

$$\boldsymbol{\omega}^p = \sum_{\gamma\in\Omega_\nu} \chi^{(\gamma)} \frac{\dot{\lambda}2k\Lambda_\gamma^{2k-1}}{\tau^{(\gamma)}} \mathrm{skew}(\boldsymbol{n}_s^{(\gamma)}) + c_{op}\chi^{(8)} \frac{\dot{\lambda}2k\Lambda_8^{2k-1}}{\tau^{(8)}} \mathrm{skew}(\boldsymbol{n}_s^{(8)}), \tag{31}$$

motivated from a simple shear load situation. To evaluate the capabilities of the model, it has been implemented in a finite element code and compared to experimental results.

The software ABAQUS, Abaqus User's Manual (2013) has been utilized with the user material subroutine, UMAT to implement the model. The constitutive model has been numerically integrated using the backward Euler scheme. Details regarding the numerical implementation of the model is provided in Borgqvist *et al.* (2015).

5 Single element out-of-plane simulations

To verify the qualitative performance of the model, uniaxial tests in the out-of-plane directions have been performed with a single element. The in-plane material properties and out-of-plane compression test been calibrated to uniaxial measurements according to Borgqvist *et al.* (2015) and Borgqvist *et al.* (2014). The simulations in this section will provide results where damage is approximated as being smeared out over the entire element (since only one element is used). Experimental data from a tensile test in the out-of-plane direction and results from simulations are shown in Fig. 2.

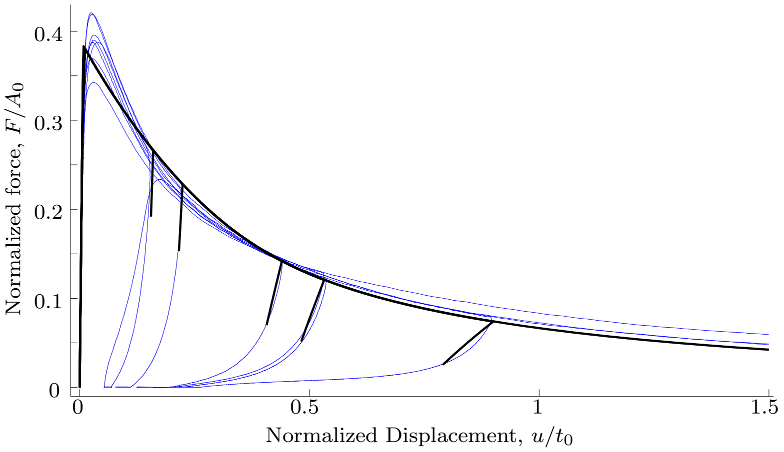

Figure 2: Experimental data (blue lines) and simulated response (black line) of a tension test in ZD. The simulation has been performed with a single element. The displacement is normalized with the initial thickness, t_0, and the force is normalized with the initial cross section area A_0.

Similarly, simulations in out-of-plane shear has been performed, cf. Fig. 3a and b. In Fig. 3b, simulations of shearing with a super-imposed normal pressure in ZD is shown. The experimental measurements are however limited in this direction, cf. i.e. Stenberg *et al.* (2001) and therefore no experimental measurements are shown. A good agreement between the measured and simulated response is seen in Fig. 3a. From the measurement, it is observed that the initial post-peak loading of the curve has failed to be recorded. This is likely due to instability triggered by the localization of failure. In Fig. 3b, a frictional type behavior is obtained, where increasing shear stresses are obtained as the normal pressure increases.

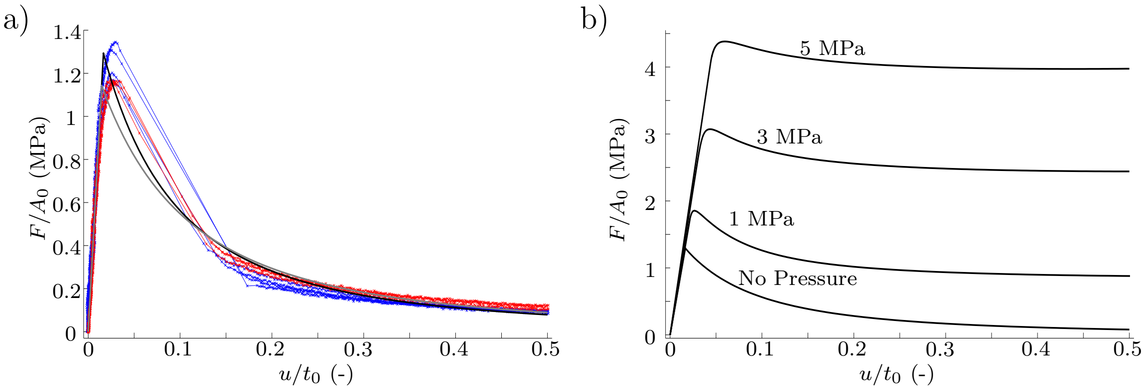

Figure 3: Out-of-plane shear test of paperboard a) in MD-ZD (blue: experimental data, black: simulated response) and CD-ZD (red: experimental data, grey: simulated response) direction and b) with a superimposed out-of-plane compression stress. The displacement is normalized with the initial thickness, t_0 and the force is normalized with the initial cross section area, A_0. The simulations have been performed with a single element.

6 Creasing and Folding

The introduction of damage does introduce a pathological mesh sensitivity. The remaining simulations of the creasing and folding process will therefore be performed on a fixed mesh. Alternatives to reduce the mesh-dependency are for instance to introduce non-local internal variables as in e.g. Pijaudier-Cabot and Bažant (1987) and Strömberg and Ristinmaa (1996) or modify the parameters associated with the softening according to the mesh size, Bažant and Oh (1983). A length parameter that is related to the width of a localization zone typically needs to be introduced and for paper-based materials one possible choice could be the thickness of the fiber. In this work no explicit length scale parameter is used, instead a fixed mesh size of 25 elements through the thickness are used in the simulations. This element size is in the same order as the thickness of a fiber. The out-of-plane material parameters related to the softening have been fitted to creasing and folding response for the given mesh.

To evaluate the quality of paperboard, simplified testing setups are commonly adopted in the industry. Two such testing setups are the line creasing and line folding operations. The results obtained from these tests are commonly correlated to the performance of the paperboard in the converting operations. One indicator correlated to the success of forming a package, is the maximum bending moment. The large local deformations generated during creasing and folding have been investigated using the proposed model. The adopted creasing setup is sketched in Fig. 4.

The web-tension is applied by introducing a prescribed displacement, u_w, as shown in Fig. 4, such that a certain initial force is obtained. An initial web-force of 58 N, corresponding to a web-tension of 1.5 kN/m, has been adopted in this work. After the application of the web-tension, the male die die presses the paperboard into the groove of the female die. The displacement of the male die is defined as zero when the male die is

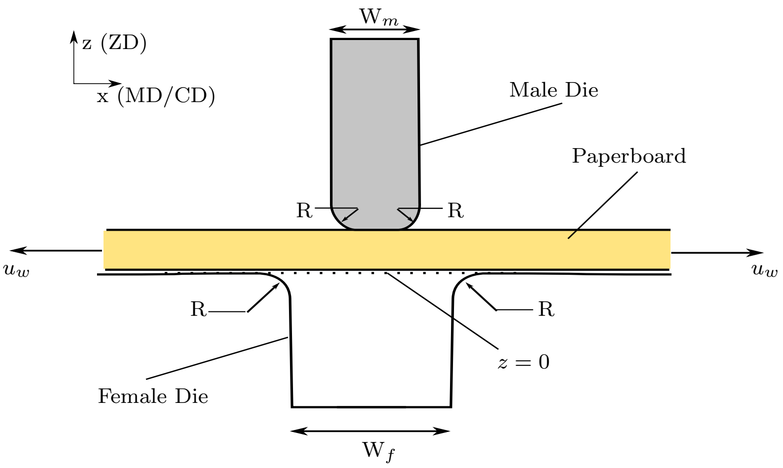

Figure 4: Schematic of the creasing process, showing the geometry of the simulated setup.

aligned with the female die (indicated by the dotted line in Fig. 4). The width of the male die is W$_m$ = 0.9 mm and the width of the female die is W$_f$ = 1.7 mm. The board is 110 mm long, 38 mm wide and 0.39 mm thick. The radius R on the male and female tools in Fig. 4 has been chosen as 0.1 mm. The reaction force of the male die and the displacement has been recorded during the test. The process is called a MD-crease when the x-direction in Fig. 4 is co-linear with MD and with similar definition for CD-crease.

After the creasing operation, the paperboard is folded according to the setup sketched in Fig. 5. In the setup for the line-folding operation, the paperboard is clamped at one

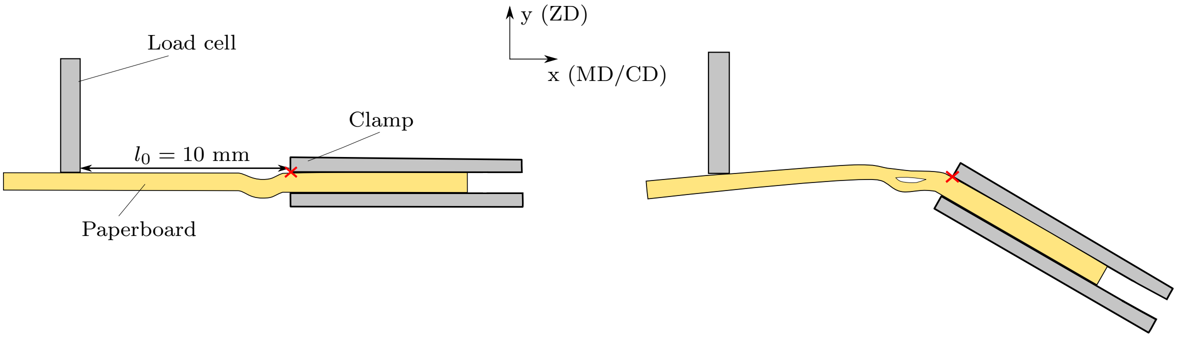

Figure 5: Schematic of line folding operation of a creased paperboard. The rotation center is marked with a red cross.

side with a pressure of 0.2 MPa whereas the other side is constrained by a load-cell acting as a rigid support. A bending moment is applied by rotating the clamps. The distance between the clamps and the load cell is 10 mm and the paperboard is folded until an angle of 90 degrees is reached and then unloaded. During the test, both the force as well as the bending angle are measured. The L & W creasability tester (AB Lorentzen & Wettre, Stockholm, Sweden) has been utilized in this work. Snapshots of the folding of creased paperboard in MD at a depth of 0.15 mm for different folding angels are shown in Fig. 6. Delamination is clearly visible in the images in Fig. 6 and significant damage has been introduced in the board.

Figure 6: Folding of creased paperboard. The bending angles are approximately (from left to right) 10, 20 and 60 degrees.

7 Simulations of creasing and folding

The folding process has been numerically simulated using the presented material model. In the numerical simulations, the paperboard is assumed to be homogeneous and therefore possess constant material parameters through the width and thickness.

The problem is modeled using 2d, fully integrated plane strain bi-linear continuum elements. All tools have been modeled as rigid analytic bodies and static Coloumb coefficient of friction equal to 0.3 between the tools and the paperboard is adopted. The standard ABAQUS-direct solver is utilized, with a quasi-static solution procedure. Paperboard creased and folded in both MD and CD have been tested and simulated.

The reaction force and displacement obtained from the experimental tests are compared to the simulation results in Fig. 7. As seen in Fig. 7, the overall shape of the macroscopic force-displacement curves can be captured in both MD and CD. The peak forces predicted by the model correspond well to the experimental results, with a slight overestimation of the peak force in MD.

The deformed shape of the paperboard at a crease depth of 0.18 mm and after it has been unloaded are shown in Fig. 8. The threshold values for the damage have been taken as $\phi_1^{max} = 0.7$ and $\phi_2^{max} = 0.4$. Significant damage is induced in the paperboard during creasing, cf. Fig. 8a. The shear damage starts to develop at a displacement of around -0.35 mm in the simulations, which can be compared to the global force-displacement curves in Fig. 7 where a drop in stiffness can be observed around the same displacement. The magnitude and distribution of ϕ_2 are similar when comparing Fig. 8a and 8b. The shear damage has reached ϕ_2^{max} close to the corners of the male and female tools. During the unloading phase, damage related to ZD-tension, i.e. ϕ_1, starts to develop at the bottom of

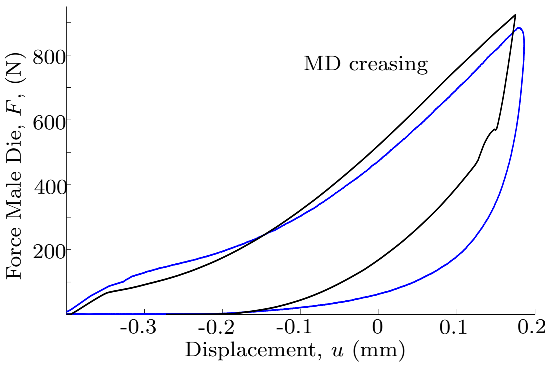

Figure 7: Reaction force vs displacement of male die in the creasing operation. The blue curves indicates experimental data and the black curves the simulation predictions. Both MD and CD creasing are shown.

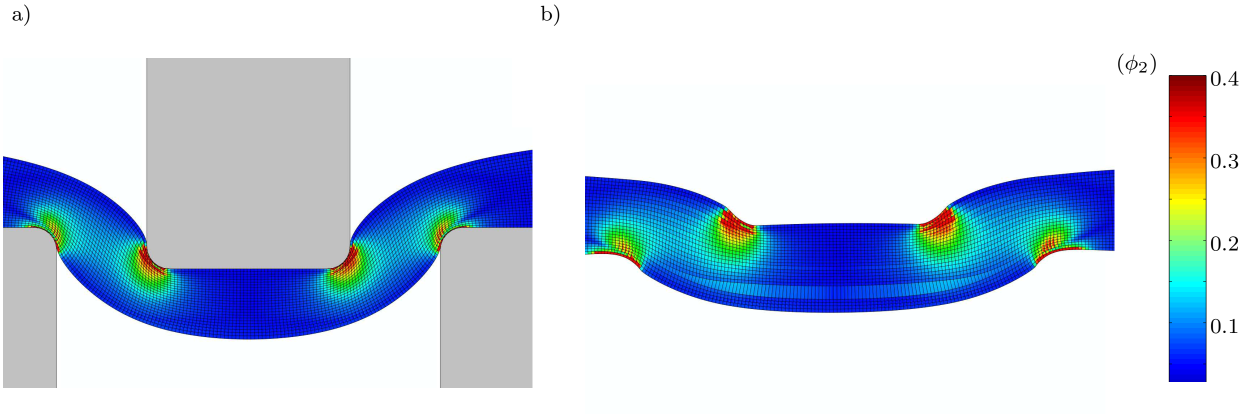

Figure 8: a) MD creasing of paperboard at a crease depth of 0.18 mm and b) after it has been unloaded. The damage variable ϕ_2 is indicated by the color contours.

the board. This was not observed in the measured response and might be a consequence of that homogeneous material properties are assumed through the thickness in the modeling.

The response during folding for creased and uncreased paperboard are shown in Fig. 9. The general shape of the global force-bending angles curves are captured by the model, both in MD and CD. The reaction force obtained from the folding simulation of uncreased paperboard corresponds well with the measured data in CD, but is slightly underestimated in MD. The shape is more serrated in the simulations compared to the measured data, which can be correlated to the formation of shear bands. Examining the folding response of the creased paperboard in MD, it is observed that the simulations predict a change in stiffness around a bending angle of 5 degrees. This change occurs earlier in the simulations compared to the measured data. It is also noted that the reaction force is lower in the simulations than the measured data for bending angles less than 50 degrees. The reaction force is continuously increasing in the simulations, while in the measurements the force is

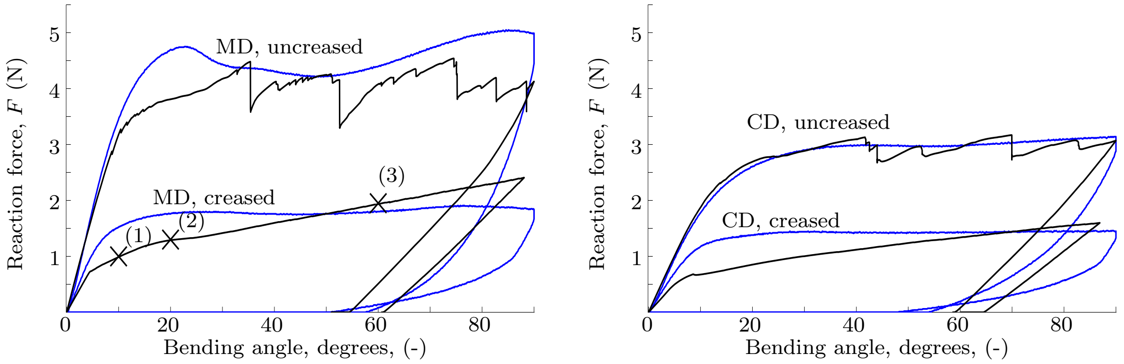

Figure 9: Response during folding of creased and uncreased paperboard in MD and CD. The blue curves indicates experimental data and the black curves the simulation predictions. The bending angle vs the reaction force at the load cell is shown.

nearly constant after a bending angle of around 10 degrees. The creased folding curve in CD has similar tendencies as MD, but the reaction force is lower.

For the three load levels marked in the MD-creased curve in Fig. 9, the deformation pattern of the paperboard has been examined in detail, cf. Fig. 10. To visualize the shear deformation, the accumulated effective plastic shear, defined from

$$\dot{\kappa}^s_{eff} = \sqrt{(\dot{\kappa}^{(9)})^2 + (\dot{\kappa}^{(10)})^2 + (\dot{\kappa}^{(11)})^2 + (\dot{\kappa}^{(12)})^2}, \tag{32}$$

is shown in Fig. 10 together with the damage ϕ_1.

In Fig. 10, it can be observed that some elements are stretched several hundreds of percent, indicating a deformation similar to that of delamination. The damage ϕ_1 starts to develop at a bending angle of around 5 degrees, i.e. slightly before load level (1) at 10 degrees. At this load level, the bending stiffness has become lower compared to the initial bending stiffness. As the paperboard is further folded, cf. load level (2) and (3), the damage is increasing. As seen in Fig. 8b, not only the damage in ZD is significant, but also the shear deformation is continuously increasing.

The final shape of the paperboard obtained from the experimental test and the simulation after the folding process is compared in Fig. 11. Large localized deformation in the elements at the center of the paperboard is observed, resembling the delamination seen in Fig. 11b. The permanent deformations appears however to be overestimated in the model and the paperboard is thicker compared with the measurements.

As large shear deformations appears to be present in the folding of creased paperboard, a sensitivity analysis with respect to the parameter η has been performed, cf. Fig. 1. Note that η determines how much the shear strength increases under super-imposed ZD-compression (i.e. a friction parameter), but it also determines the amount of dilation in the ZD-direction during plastic shear deformation due to the choice of flow rules. The force-displacement response for the values $\eta \in \{0.35, 0.7, 1.4\}$ are shown in Fig. 12.

As seen in Fig. 12, the η parameter has a significant effect on the response. The reaction

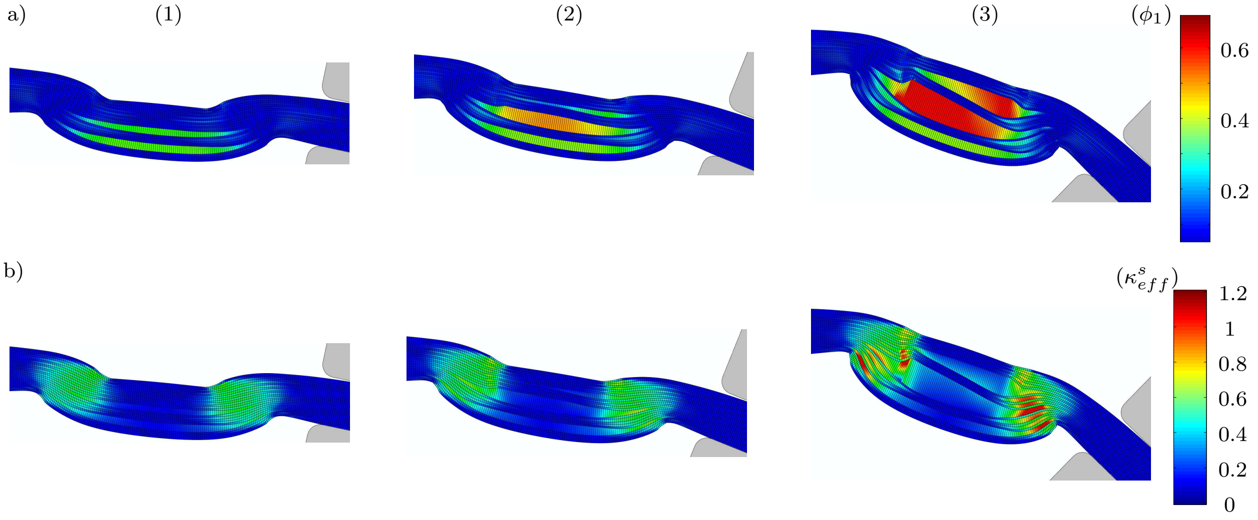

Figure 10: The deformation during folding of creased paperboard. The images are taken at the load-levels marked in Fig. 10. In a), the magnitude of ϕ_1 is shown and in b) the accumulated plastic shear, κ_s^{eff}.

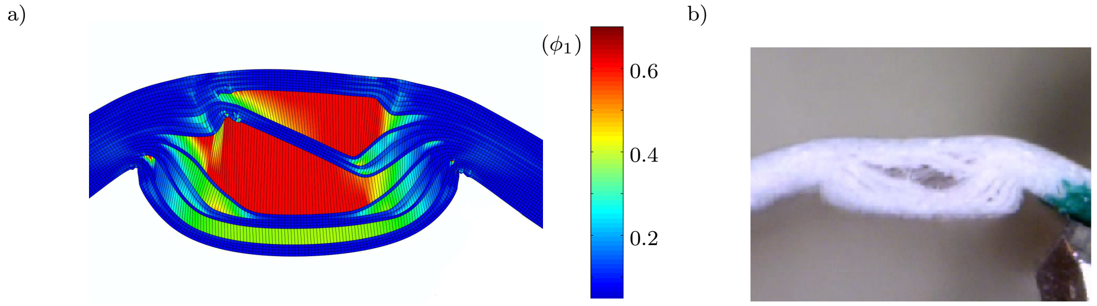

Figure 11: The final shape of the creased paperboard in MD compared with the observed deformation.

force becomes larger as the slope η increases. The deformed shape of the paperboard is also significantly different as η is changed, which is illustrated in Fig. 13. Higher value of η implies increased curvature of the lower boundary of the crease zone, cf. Fig. 13. As the value of η decreases, the shape of the crease is more rectangular which is in better agreement with experimental observations. It can also be noted that fewer elements expand in the ZD-direction at the corners of the crease zone as η increases. The properties related to out-of-plane shearing therefore appears to be of importance for folding of creased paperboard.

Finally, simulations have been performed where the damage evolution is suppressed to illustrate the effect of introducing damage. The force-displacement curves with and

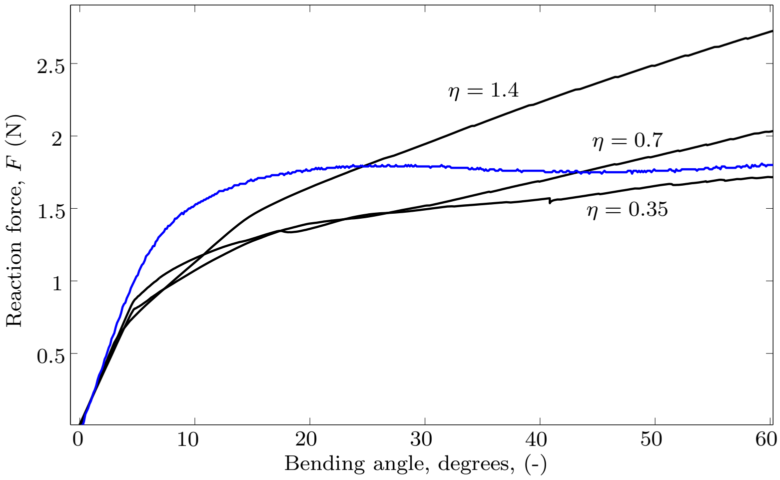

Figure 12: Folding of creased paperboard in MD for different values of the paper friction parameter η. The blue curve indicates experimental data and the black curves the simulation predictions. The bending angle vs the reaction force at the load cell is shown.

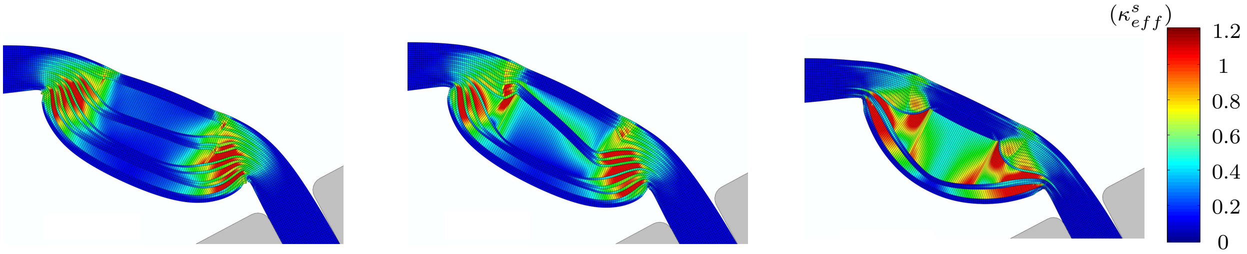

Figure 13: Deformed shape of paperboard at a bending angle of 60 degrees for different values of η. The values are (from left to right) $\eta = 0.35$, $\eta = 0.7$ and $\eta = 1.4$.

without damage are shown in Fig. 14. As expected, the damage reduces the predicted reaction force, cf. Fig. 14. The reaction force is continuously increasing at a higher rate when no damage is included in the model.

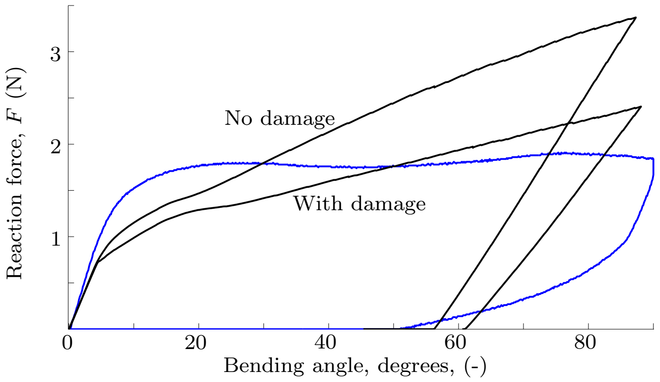

Figure 14: Bending angle vs the reaction force for folding curves of creased paperboard where the damage has been suppressed (dashed line) and when damage is included (solid line). The blue line indicate the measurements.

8 Conclusions

An anisotropic material model has been established. The model has been developed in a thermodynamic setting, fulfilling the dissipation inequality. The directional dependence is modeled by the introduction of director vectors and a normal vector that represent the characteristics directions of the material, MD, CD and ZD. A yield surface that hardens and softens distortionally has been used to model permanent deformations. Two scalar damage variables have been introduced to model the softening associated with out-of-plane tension and shear deformations. The material model has been applied to paperboard and it is shown that the model can capture the uniaxial response.

The model has been used to simulate the creasing and folding operations. The deformation and global force-displacement curves have been compared to measured data. The simulated deformation patterns and the force-displacement curves are in qualitative agreement with the measured data. It is shown that the introduction of damage variables are necessary to reduce the reaction force in bending.

The parameters associated with the softening have been fitted for a fix mesh in the creasing and folding operations. The deformation pattern is highly complex and involves several deformation modes. It has been observed that both out-of-plane tension and out-of-plane shear are important deformation mechanisms in folding creased paperboard. The out-of-plane shear-friction parameter η has a significant influence on the folding response and it can be concluded that the strength in out-of-plane shear is therefore important for forming packages. The simulated folding response matches qualitatively the measured data, but there are some differences. The reaction force is initially underestimated by the model, but then a continuous increase in the force is predicted while the measured data indicates approximately constant force after a bending angle of approximately 10 degrees. The permanent deformation in the out-of-plane direction are overestimated in the model. Nevertheless, adopting continuum for predicting the full field behavior of paperboard appears to be a viable approach, but more work remains to obtain better correspondence with the measured data.

A Material parameters

The material parameters used in this work are presented in Tables. 1, 2 and 3. The non-zero components of $N_{ij}^{(\nu)}$ are summarized in Table. 1. The exponent $k = 3$ has been used in (21). The density of the paperboard is 780 kg/m^3.

Stress-state,	Subsurface, ν	Subsurface component $N_{ij}^{(\nu)}$ (-)
MD-tension	1	$N_{11}^{(1)} = 0.925, N_{22}^{(1)} = -0.379$
CD-tension	2	$N_{11}^{(2)} = -0.215, N_{22}^{(2)} = 0.977$
MD-CD shear	3	$N_{12}^{(3)} = 0.7071, N_{21}^{(3)} = 0.7071$
MD-compression	4	$N_{11}^{(4)} = -1$
CD-compression	5	$N_{22}^{(5)} = -1$
MD-CD shear	6	$N_{12}^{(6)} = -0.7071, N_{21}^{(6)} = -0.7071$
ZD-compression	7	$N_{33}^{(7)} = -1$
ZD-tension	8	$N_{33}^{(8)} = 1$
MD-ZD-shear	9	$N_{33}^{(9)} = 0.704, N_{13}^{(9)} = 0.502$
MD-ZD-shear	10	$N_{33}^{(10)} = 0.704, N_{13}^{(10)} = -0.502$
CD-ZD shear	11	$N_{33}^{(11)} = 0.704, N_{23}^{(11)} = 0.502$
CD-ZD shear	12	$N_{33}^{(12)} = 0.704, N_{23}^{(12)} = -0.502$

Table 1: Numerical values of the in-plane subsurface parameters

Elastic parameter	Value
A_1	1690 (MPa)
A_2	292 (MPa)
A_3	28.4 (MPa)
A_4	1333 (MPa)
A_5	110 (MPa)
A_6	0.365 (MPa)
A_7	11.5 (-)

Table 2: Numerical values of the elastic parameters.

Subsurface , ν	Initial yield, K_0 (MPa)	Hardening a_ν (MPa)	Hardening b_ν (-)
1	20.4	12.2	690
2	11.7	5.10	435
3	9.91	6.63	334
4	29.1	-	-
5	21.0	-	-
6	9.91	6.63	435
7	1.00	49	-
8	0.5	-	-
9	2.5	-	-
10	2.5	-	-
11	2.5	-	-
12	2.5	-	-

Table 3: Numerical values of the plastic parameters

Damage parameter	Value
n	3.15 (-)
n_t	0.85 (-)
n_s	1.5 (-)
n_c	1 (-)
S_1	0.1 (MPa)
S_2	25 (MPa)
c	0.1 (-)
m	0.39 (-)

Table 4: Numerical values of the damage parameters.

References

Abaqus User's Manual (2013). Dassault Systemes. Abaqus Inc providence, RI, USA, 6.13 edition.

Al-Rub, R. K. A. and Voyiadjis, G. Z. (2003). On the coupling of anisotropic damage and plasticity models for ductile materials. *International Journal of Solids and Structures*, **40**, 2611–2643.

Bažant, Z. P. and Oh, B. H. (1983). Crack band theory for fracture of concrete. *Materials and Structures*, **16**, 155–177.

Beex, L. A. A. and Peerlings, R. H. J. (2009). An experimental and computational study of laminated paperboard creasing and folding. *International Journal of Solids and Structures*, **46**, 4192–4207.

Beex, L. A. A. and Peerlings, R. H. J. (2012). On the influence of delamination on laminated paperboard creasing and folding. *Philosophical transactions of the Royal Society*, **370**, 1912–1924.

Besson, J. (2010). Continuum models of ductile fracture: A review. *Int. J. Damage Mechanics*, **19**, 3–52.

Borgqvist, E., Lindström, T., Tryding, J., Wallin, M., and Ristinmaa, M. (2014). Distortional hardening plasticity model for paperboard. *International Journal of Solids and Structures*, **51**, 2411–2423.

Borgqvist, E., Wallin, M., Ristinmaa, M., and Tryding, J. (2015). An anisotropic in-plane and out-of-plane elasto-plastic continuum model for paperboard. *Composite Structures*, **126**, 184–195.

Cavlin, S. (1988). The unique Convertibility of Paperboard. *Packaging Technology and Science*, **10**, 77–92.

Chaboche, J.-L. (1981). Continous damage mechanics - a tool to describe phenomena before crack initiation. *Nuclear Engineering and Design*, **64**, 233–247.

Ciarlet, P. G. (1988). *Mathematical Elasticity.* Elsevier Science Publishers B.V.

Coleman, B. D. and Gurtin, M. E. (1967). Thermodynamics with internal state variables. *Journal of Chemical Physics*, **47**, 597–613.

Dafalias, Y. F. (1998). Plastic spin: necessity or redundancy? *International Journal of Plasticity*, **04**, 909–931.

Garbowski, T., Maier, G., and Novati, G. (2011). On calibration of orthotropic elastic-plastic constitutive models for paper foils by biaxial tests and inverse analyses. *Structural and Multidisciplinary Optimization*, **46**, 111–128.

Giampieri, A., Perego, U., and Borsari, R. (2011). A constitutive model for the mechanical response of the folding of creased paperboard. *International Journal of Solids and Structures*, **48**, 2275–2287.

Hagman, A., Huang, H., and Nygårds, M. (2013). Investigation of shear induced failure during sct loading of paperboards. *Nordic Pulp & Paper Research Journal*, **28**, 415–429.

Harrysson, M. and Ristinmaa, M. (2007). Description of evolving anisotropy at large strains. *Mechanics of Materials*, **39**, 267–282.

Harrysson, M., Harrysson, A., and Ristinmaa, M. (2007). Spatial representation of evolving anisotropy at large strains. *International Journal of Solids and Structures*, **44**, 3514–3532.

Huang, H., Hagman, A., and Nygårds, M. (2014). Quasi static analysis of creasing and folding for three paperboards. *Mechanics of Materials*, **69**, 11–34.

Isaksson, P., Hägglund, R., and Gradin, P. (2004). Continuum damage mechanics applied to paper. *International Journal of Solids and Structures*, **41**, 4731–4755.

Kachanov, L. M. (1958). Rupture time under creep conditions. *Izv. Akad. Nauks SSSR Otd. Tech. Nauk*, **8**, 26–31 (In russian). English translation: *Rupture time under creep conditions.* International Journal of Fracture, Vol. 97, No 1–4 , pp. xi–xviii, 1999.

Lemaitre, J. (1985). A continuous damage mechanics model for ductile failure. *Journal of Engng. Mat. and Tech.*, **107**, 83–89.

Mandel, J. (1971). *Plasticite Classique et viscoplasticity.* CISM course No.97. Udine.

Nagasawa, S., Fukuzawa, Y., Yamaguchi, T., Tsukatani, S., and Katayama, I. (2003). Effect of crease depth and crease deviation on folding deformation characteristics of coated paperboard. *Journal of Materials Processing Technology*, **140**, 157–162.

Nygårds, M., Just, M., and Tryding, J. (2009). Experimental and numerical studies of creasing of paperboard. *International Journal of Solids and Structures*, **46**, 2493–2505.

Pijaudier-Cabot, G. and Bažant, Z. (1987). Nonlocal damage theory. *Journal of Engineering Mechanics*, **113**, 1512–1533.

Stenberg, N. (2002). *On the Out-of-Plane Mechanical Behaviour of Paper Materials*. Ph.D. thesis, Department of Solid Mechanics, Royal Institute of Technology, Stockholm, Sweden.

Stenberg, N., Fellers, C., and Östlund, S. (2001). Plasticity in the thickness direction of paperboard under combined shear and normal loading. *Journal of Engineering Materials and Technology*, **123**, 184–190.

Strömberg, L. and Ristinmaa, M. (1996). FE-formulation of a nonlocal plasticity theory. *Computer Methods in Applied Mechanics and Engineering*, **136**, 127–144.

Tjahjanto, D., Girlanda, O., and Östlund, S. (2015). Anisotropic viscoelastic–viscoplastic continuum model for high-density cellulose-based materials. *Journal of the Mechanics and Physics of Solids*, **84**, 1–20.

Xia, Q. S. (2002). *Mechanics of inelastic deformation and delamination in paperboard*. Ph.D. thesis, Massachusetts Institue of Technology.

Xia, Q. S., Boyce, M. C., and Parks, D. M. (2002). A constitutive model for the anisotropic elastic-plastic deformation of paper and paperboard. *International Journal of Solids and Structures*, **39**, 4053–4071.